Advanced Vehicle Power Technology Alliance Fiscal Year 2017 (FY17) Annual Report

(1 Oct 2016 – 30 Sep 2017)

Department of the Army

(RDTA-COS)

Department of Energy

8 February 2018

Mr. Michael Berube
Director, Vehicle Technologies Office, Department of Energy-Energy Efficiency and Renewable Energy (DOE-VTO-EERE).

Dr. Paul Rogers
Director, United States Army Tank Automotive Research, Development and Engineering Center (TARDEC), United States Army Research Development and Engineering Command (RDECOM), United States Army Materiel Command (AMC).

OPSEC #29887

This Page Intentionally Blank

ACKNOWLEDGEMENTS

The Advanced Vehicle Power Technology Alliance (AVPTA) between the Department of Energy (DOE) and the Department of the Army (DA) was publicly announced in July 2011. The Alliance underscores the urgency for energy security; in particular, an emphasis on developing advanced technologies that enable military ground vehicles to become significantly more energy efficient. Individually and collaboratively, the DOE and DA have a long history of successfully developing innovative vehicle technologies. The Alliance is chartered to accelerate the conceptualization and transition into deployment of inventive and creative energy-saving concepts that the Nation needs to achieve energy security.

This report summarizes the sixth year of technical effort and output of the Alliance's Technology Focus Area (TFA) working groups. The TFAs are respectively led by DOE and DA Subject Matter Experts (SMEs) that jointly recommend and oversee project portfolios in areas of interagency mutual technical interest.

We acknowledge the significant contributions of the DOE and DA administrative and technical personnel who in six years have grown the Alliance from a notional concept into a self-sustaining and highly-productive entity. Work product generated by the Alliance has migrated into commercial and military applications through industry partners. In parallel with ongoing activities, DOE and DA personnel have extended the AVPTA enterprise into new areas of engagement including the Office of the Secretary of Defense Operational Energy Plans and Programs (OSD/OEPP)-sponsored "Increasing the Fuel Efficiency of the Current Ground Tactical Fleet" (IFECGTF) Program; the project portfolio of which includes autonomy-enabled, vehicle electrification and powertrain technology-related activities.

We specifically acknowledge Mr. William Haris, who as TARDEC Technical Liaison resident at DOE Headquarters collocated within the VTO from 2012 to 2016, provided invaluable insight and facilitated inter-agency communication, coordination and collaboration to the Alliance.

Mr. Michael Berube
Director, Vehicle Technologies Office, Department of Energy-Energy Efficiency and Renewable Energy (VTO, DOE-EERE).

Dr. Paul Rogers
Director, United States Army Tank Automotive Research, Development and Engineering Center (TARDEC), United States Army Research Development and Engineering Command (RDECOM), United States Army Materiel Command (AMC).

This Page Intentionally Blank

CONTENTS

Appendix

This Page Intentionally Blank

EXECUTIVE SUMMARY

The AVPTA Mission is to leverage “resources to improve transition of technologies into both the commercial and military marketplace,” and “industrial research and development (IRAD) involving commercial automotive and defense ground vehicle manufacturers to transition technologies and increase precompetitive research and development.”

The following summaries document the work product of twenty-six (26) projects contained within the AVPTA portfolio. Project performers include Automotive Industry Original Equipment Manufacturers (OEMs) and Tier 1 / 2 Suppliers, Defense Industry OEMs and Suppliers, DOE National Laboratories, DOD Research Laboratories, Contract Research Organizations, Universities and Colleges, Small and Other Category Businesses.

Some of the projects reported upon herein were among the seven (7) original projects that formed the Alliance’s foundation and enabled its rapid start-up. In many instances, DOE and DA mutually leveraged respective ongoing projects by infusing personnel, contributing resources, and providing mutual experience/expertise. This quickly expanded the Alliance technical network and reach, and provided access to activities beyond those directly funded by the Alliance. An example is TARDEC SME engagement in the VTO Annual Merit Review (AMR) during which TARDEC personnel are exposed to the complete VTO project portfolio including participating/contributing as review panel members. Joint participation in the AMR helps to formulate areas of mutual technical interest (AOIs) that contain the description, scope and deliverables for future new-start projects.

Also reported upon herein are projects that were jointly selected for start-up in preceding Fiscal Years. The Alliance has developed and instituted a sustainable, new-start project review and selection process based upon VTOs annual Funding Opportunities Announcements process and timeline. The process leverages DOE’s National Energy Technology Laboratory Contract Office to rapidly obligate and efficiently track project funding by individual performer.

Since its inception, DOE and DA have jointly contributed a total of $122.5M[a] to the Alliance. The result has been a level of effort/output that neither agency would have realized without the interagency collaboration.

Report Prepared by:

Scott Schramm, Technical Advisor, Chief of Staff Office, TARDEC/RDECOM/AMC

Gurpreet Singh, Program Manager, DOE-VTO, EERE

[a] NOTE: A total of $142.6M was erroneously reported within the AVPTA FY16 Annual Report. The correct amount was $118.6M.

This Page Intentionally Blank

INTRODUCTION

There are two high level drivers that led to the development of the AVPTA. The first is the elevation of energy efficiency and security as points of emphasis throughout the Army and the Department of Defense (DOD) as a whole. For the Army, a major milestone in this was the development of the Army Energy Security Implementation Plan (AESIP) in 2009. Within the AESIP goal to Increase Energy Efficiency across Platforms and Facilities, there was an objective to increase the efficiency of tactical equipment. At the DOD level, the Operational Energy Strategy is a principle-guidance document for the Department's approach to ensure energy security for operational forces.

The second was a call by the DOD for strengthened interagency partnering. This was set forth in its 2010 Quadrennial Defense Review. Energy security was identified as an excellent opportunity area for such a partnership. To this end, the DOE and DOD worked to craft a Memorandum of Understanding (MOU) to establish a partnering framework to enhance national energy security. This MOU is included as Appendix A. The MOU calls for the Departments to work together in a wide range of technical areas; including efficient transportation and overall energy efficiency.

DA and DOE worked together under the auspices of this MOU to develop a charter for working together in a wide range of vehicle technologies. This charter describing the Alliance was originally signed by the Honorable Daniel B. Poneman, Deputy Secretary of Energy and the Honorable Joseph W. Westphal, Under Secretary of the Army; and in 2016 was renewed/extended for five (5) additional years under the signatures of the Honorable Elizabeth Sherwood-Randall, Deputy Secretary of Energy and Honorable Patrick J. Murphy, Under Secretary of the Army (see Appendix B).

DOE's Office of Energy Efficiency and Renewable Energy (EERE) supports early-stage research of energy efficiency and renewable energy technologies that enhance energy affordability, reliability, and resilience and strengthen U.S. energy security, economic growth, and environmental quality. A critical step in any new technology development is having it accepted and deployed in the marketplace. Teaming with DOD provides an attractive pathway for early utilization of the novel energy-saving ideas coming from the DOE research portfolio. These agencies strategic goals are summarized in the following table:

Remainder of Page Intentionally Blank

DOD & DOE Strategic Goals

DOD Operational Energy Strategy	DOE Vehicle Technologies Office
Reduce Energy Demand: − Reduce: • Overall Operational Energy Demand • Mission Risks & Costs − Improve Energy Usage Efficiency	Improve Energy Efficiency of the Transportation Sector
Expand & Secure Energy Supply: − Diversify Energy Sources − Protect Energy Supply Access	Increase Domestic Energy Security Reduce Petroleum Consumption Reduce Operating Cost for Consumers and Business
Integrate Operational Energy Considerations Into: − Planning Activities and Force Development	Improve Global Competitiveness of U.S. Industry Improve Domestic Manufacturing

With strong support from senior leadership, the agencies collaborated at the Executive and SME Levels to identify AOIs that are the founding principles for describing each of the Alliance’s Technology Focus Areas (TFAs). The respective TFA descriptions follow.

Remainder of Page Intentionally Blank

TECHNOLOGY FOCUS AREA (TFA) DESCRIPTIONS

TFA1: Advanced Combustion Engines & Transmissions

Advanced air-fuel management systems and novel combustion regimes have the potential to dramatically increase efficiency and power density, while at the same time reducing emissions. Meeting the challenge of developing and optimizing the combustion of common petroleum fuels, including Jet Propellant-8 (JP8), or biofuels in advanced engines requires a new level of the understanding of the physical and chemical phenomena of the Direct Injection (DI) diesel engine, which will be strongly affected by the different fuel properties which in turn affect fuel/air mixture preparation, combustion and emissions.

Advanced transmissions can allow the engine to operate more frequently in regions of high efficiency and transmit more torque while maintaining drivability. Of particular interest for further Research & Development (R&D) are approaches and devices to increase launch-assist device efficiency, and to increase the number of gear ratios. Among possible options for investigation are higher gear count automatic transmissions, Dual Clutch Transmissions (DCT), wet and dry clutch launch devices, multi damper torque converters, Continuously Variable Transmissions (CVTs), and binary transmissions.

TFA2: Lightweight Structures & Materials

Reduction of vehicle gross weight is an effective approach to reduce energy consumption during the vehicle usage, regardless of their energy sources (e.g., liquid fuels or electric batteries). Lightweight materials such as aluminum (Al) alloys, magnesium (Mg) alloys, high-strength steel, and carbon-polymer composites have been considered to replace low carbon steels conventionally used in automotive components. Challenges exist, however, to integrate components made of these lightweight materials into vehicle structures to achieve maximum weight reduction, while maintaining structural rigidity, crash safety, production quality and cost parity.

TFA3: Energy Recovery & Thermal Management

In current vehicles, approximately 60% of the chemical energy of fuel is lost in the form of waste heat, dissipated by the exhaust and cooling systems. The former offers high-grade heat that approaches temperatures of 800^{o}C while the latter is a considerably more modest heat source at approximately 120^{o}C. Of significant interest are exhaust heat recovery systems, including Organic Rankine cycles, as well as mechanical and electrical turbo-compounding. In addition, through the development of cost-competitive advanced second generation thermoelectric (TE) devices for vehicle applications vehicle fuel efficiency, performance, and emissions can be improved. Thermo-electric devices can convert engine waste heat to useful electrical power, to be used either assisting propulsion or for powering hotel loads. By integrating high Figure of Merit TE devices in the vehicle architecture, thermal management of vehicles can become significantly more efficient.

TFA4: Alternative Fuels & Lubricants

Alternative fuels and lubricants can facilitate or enhance conventional engine technology, as well as advanced combustion regime engine operation such as Homogeneous Charge Compression Ignition (HCCI) or Low Temperature Combustion. For alternative fuels, the focus should be on drop-in fuels or blend stocks that displace petroleum-derived fuels in vehicle applications without significant infrastructure changes or requirements. New developments in base oil and additive packages can reduce viscosity while maintaining temperature requirements, thereby improving engine and transmission efficiency.

TFA5: Electrified Propulsion Systems

Electric drive options range from mild battery-alternator systems to full parallel and series systems or all electric drive, and require engineering trade-offs between fuel consumption benefit and system complexity, reliability and cost. However, to achieve efficient solutions, electrical materials and devices will require higher conversion efficiencies and power/energy densities than are currently possible. The next generation electric drive vehicles will benefit from improved and lower cost batteries, novel electric motors, thermoelectric waste heat recovery, and power electronic devices and electrical topologies that are capable of handling increased loads and multiple combinations of sources and accessories. Activities focus on hybrid system power electronics and electric machines.

TFA6: Energy Storage & Batteries

Stakeholders desire to improve existing battery chemistries, develop advanced battery technologies (high power and high energy systems), and conduct ultra-capacitor research. Military goals are to improve the availability of onboard power, reduce energy demand/consumption, expand the energy supply to military operations and build energy security into future forces in the specific areas of: silent watch capability, electromagnetic armor and starting/lighting/igniting (SLI). Civilian/commercial goals are to reduce the petroleum demand and promote US economic competitiveness in advanced hybrid electric vehicles and electric vehicles. Advanced lead-acid batteries, ultra-capacitors, lithium-ion batteries, lithium sulfur and lithium-air batteries are joint areas of interest. Both agencies are also interested in improving on-board safety, developing battery test protocols and promoting codes and standards.

TFA7: Analytical Tools (Modeling & Simulation)

Diverse fuel sources, advanced combustion modes, hybrid/electrified powertrains, energy harvest/waste heat recovery technologies, and using lightweight materials substantially elevate the complexities of efficient vehicle powertrain systems and impose critical challenges for system integration and control. These efficient vehicle powertrain sub-systems, with new characteristics and strongly interactive dynamics, necessitate research on system integration and advanced control strategies. An integrated and analytical systems approach ensure that the various sub-systems of the vehicle work seamlessly, reliably and synergistically to optimize coordination so as to maximize vehicle energy efficiency, power density and emission reduction potential in real-world applications. Through state-of-the-art modeling and analysis, concepts and strategies can be screened during the vehicle design stage, and most promising candidates and key pathways to bring them to realization in an effective time frame can be identified. Critical components and/or systems needing specific development can also be identified and analyzed with simulation tools.

TFA9: Autonomy-enabled Technologies

Autonomy-enabled technologies have the promise to significantly decrease fuel consumption through a variety of mechanisms. For example, platooning, where vehicles travel close to each other in order to reduce aerodynamic drag at high speeds, can only be achieved through connectivity and automation. A significant source of excess fuel consumption comes from vehicle operators driving in a sub-optimal manner, such as exceeding optimal speeds and accelerating and decelerating too quickly. Intelligent systems can help increase fuel efficiency by providing information to the driver to improve operational behavior, by determining more efficient routes based on topography or traffic conditions, or by taking control of certain vehicle functions. An automated traffic management system, implemented through a system of autonomous vehicles connected with intelligent roadway infrastructure, could greatly reduce vehicle start/stops and slowdowns, optimizing traffic flow, and improving mobility in urban driving. Preliminary research by the National Renewable Energy Laboratory (NREL) indicates that platooning could increase fuel efficiency by 10%, eliminating driver inefficiencies another 15%, and completely automating the vehicle transportation system could yield a 40% improvement. However, these estimates are based on a limited number of experiments, which may not include the full range of variability that a real world system would experience, nor potential second-order effects, such as an increase in vehicle miles traveled. Accordingly, additional analysis and targeted experimentation are needed to more fully explore the limitations that these autonomy-enabled technologies may have in regards to increasing fuel efficiency across the transportation system.

TFAE: "Extended Enterprise" Activities

"Extended Enterprise" Activities projects are technically 'endorsed' by the DOE Vehicle Technologies and/or Fuel Cell Technologies Office(s) (DOE-VTO, FCTO), but because the project scope of work ***does not directly align*** with a VTO or FCTO Funding Opportunities Announcement Area of Interest (FAO-AOI), DOE does not contribute project funds. TARDEC funds the projects to which VTO and FCTO representatives have meeting access and about which receive technical reports.

PROJECT TECHNICAL REPORTS

(Start on Page 15)

AVPTA Technology Focus Area 1: Advanced Combustion, Engines & Transmissions

DOE-VTO TFA Lead: Gurpreet Singh
TARDEC TFA Lead: Dr. Peter Schihl

There was no project activity under this TFA during FY17.

Remainder of Page Intentionally Blank

This Page Intentionally Blank

AVPTA Technology Focus Area 2: Lightweight Materials and Structures

Light Weight Vehicle Structure (LWVS)

DOE-VTO TFA Lead: Sarah Ollila
TARDEC TFA Lead: Ravi Thyagarajan

Principal Investigators:
Dr. Richard Gerth and
Mr. Scott Hodges
U.S. Army TARDEC
Product Lifecycle Engineering - Materials

Project Start: Oct 2013
Project Completed: Q3FY17

Objectives:

- Design, manufacture, and evaluate lightweight, multi-material military vehicle structure that is both affordable and 30%+ lighter in weight.
- Evaluate commercial defense barriers to lightweight material technology adoption.

Strategic Context:

- Evaluation structure of the Light Armored Vehicle (LAV)-25 turret. Technologies and lessons learned may be transferable to new turrets, such as Combat Vehicle Prototype (CVP), Next Generation Combat Vehicle (NGCV), and Future Fighting Vehicle (FFV).
- The target design is a multi-material turret (Figure 1), which is a technology explicitly mentioned in the Lightweight Combat Vehicle Science and Technology Campaign (LCVSTC)
- The turret will provide insight to guide future Research & Development (R&D) directions necessary to overcome barriers to adoption of the light-weighting technologies.

Accomplishments:

- Gun Fire Testing successfully completed.
- Ballistic impact evaluation successfully completed.
- Cold and hot weather storage testing successfully completed.
- Lifting test successfully completed.
- Results presented and published at NATO meeting.

Introduction:

Vehicle light-weighting is a priority for the US. Army (Polsen, et al., Lightweight Combat Vehicle Science and Technology Campaign, 2014, [1]). The future force must be more expeditionary and agile to the ever changing global threat environment. Due to increased survivability requirements, additional protection measures have been added to vehicles, which has typically increased their weight. The increased weight has resulted in decreased fuel economy, decreased reliability and associated vehicle availability, and in some cases, decreased swim, fording, and transport capability. Further, as vehicle weight increases through the Engineering Change Proposal (ECP) process, operational capability may degrade [2].

A true multi-material structure for a military vehicle has not yet been produced for production. The Future Combat Systems Advanced REconfigurable Spaceframe (FCS ARES) was a hybrid monocoque / space frame architecture that was predominantly aluminum and composites (Pike & Filar, 2009). It was a multi-material structure which demonstrated the state of the art. The LWVS program is not designed to show the state of the technical art, but rather the state of the commercial art. In other words, it is not a study in how much weight can technically be eliminated through material optimization, but rather how much weight can be eliminated from a current military vehicle using commercially available and affordable technologies. The project tests the hypothesis that multi-material technologies developed for the commercial automotive industry can be adapted for military applications to significantly reduce vehicle weight for an acceptable cost. The ultimate goal of the project, if successful, is to transition the adapted technologies into a current military vehicle through a future upgrade program.

Approach:

The LWVS program is not designed to show the state of the technical art, but rather the state of the commercial art. In other words, it is not a study in how much weight can technically be eliminated through material optimization, but rather how much weight can be eliminated from a current military vehicle using commercially available and affordable technologies. The project tests the hypothesis that multi-material technologies developed for the commercial automotive industry can be adapted for military applications to significantly reduce vehicle weight for an acceptable cost. The ultimate goal of the project, if successful, is to transition the adapted technologies into a current military vehicle through a future upgrade program.

The demonstration platform for the LWVS was the Marine Light Armored Vehicle (LAV-25). The LWVS program was a multi-year program structured in three Phases:

I. Trade Study and Technology Development (14 months)
II. Detailed Design and Manufacture (18 months) of a composite/steel turret
III. Test and Evaluation (12 months).

Program results for Phase I, Phase II, and limited Phase III results were published in prior year AVPTA reports (Davis & Rogers, Advanced Vehicle Power Technology Alliance FY14 Annual Report, 2015) [3,4], as well as several open literature publications [5] [6]. While this report focuses project activities during FY17, some of the information published previously will be repeated for context and understanding.

Results and Discussion:

One of the primary tasks for FY17 was completing all testing and evaluation of the multi-material turret (Figure 1), and documenting the final results. The list of tests that were conducted over the whole project were:

TARDEC Physical Simulation & Testing Lab:

- High Temperature (Storage)
- High Temperature (Operation)
- Cold Temperature (Storage)
- Cold Temperature (Operation)
- Vibration
- Center of Gravity
- Turret Lift Test

Element Materials Technology Lab:

- Contamination by Fluids
- Solar Radiation (Sunshine)
- Humidity
- Fungus
- Salt Fog
- Sand and Dust
- Freeze-Thaw
- Flammability

Army Testing Center, Aberdeen:

- Gunfire Shock
- Weapon Accuracy
- Ballistic Shock

Results Summary:

- Gunfire tests were performed to provide a degree of confidence that the system could structurally and functionally withstand the relatively infrequent, short-duration transient, high-rate repetitive shock input encountered in operational environments during the firing of guns.

- The composite turret passed every test that it was subjected to, with no failures. There was no damage and the structure was intact after the testing.
- Testing issues:
    - Unable to finish the durability testing
        - This is a low concern since the strains were extremely low and not trending towards any concern.
    - The accuracy test of the main gun was not completed due to range size limitation, and not related to the capability of the turret
        - There was nothing to indicate that it would fail this test if performed.

The second task for the year was to develop an Affordability/Cost Report for 6 different production scenarios. The Rough-Order-of-Magnitude (ROM) production cost gathered was to cover two different volumes (150 and 300) over a one, three, or five year period. The breakdown of all production scenarios is shown below. The pricing for the production scenarios covered the cost of removal and teardown of the existing turret, manufacturing and installation of the composite turret, performance acceptance testing, and maintenance for a 15 year turret life (Table 1).

The cost estimates were for planning purposes only and did not reflect firm price of future requests for proposals related to this project. Additional Non-Recurring Engineering (NRE) that could result from lessons learned or future optimization was not included in this ROM estimate. Costs were gathered similar to an RFP process, but competitive bidding was not explored.

The third FY17 task was for GDLS to share their previous findings on Implementation challenges for composite applications in combat vehicles. The study listed the following typical barriers:

- Environmental: can be further broken down to 6 categories. Chemical, Thermal, Thermal/Chemical combines, Ballistic, Durability, Corrosion). Some are issues and need to be addressed.
- Joining: not a major issue.
- Business Case: Will the customer pay more for less weight? This is a barrier.
- Design Allowables: Testing costs are high, but not a technical issue, still needs to be addressed.
- Repairability: repaired sections may have reduced mechanical properties. Needs to be addressed.
- Raw Material Cost: Cost can be as high as $17.50 per lb. saved. This is an inherent issue.
- Processing Cost: usually is not an issue.
- Toxicity: There are design workarounds, and not a major issue.
- Employee involvement: Is there a corporate culture that mandates and/or incentivizes lightweighting? This continues to be a major issue.

- The Unknowns: There could be a new load case in the future that was not considered in the original design. This is an issue but outside the influence of the designer.
- Knowledge of failure initiation: Due to the somewhat unpredictable nature of composite test-to-failure, post-test diagnoses and model correlations are more difficult. This is an issue.

The last task was for General Dynamics Land Systems (GDLS) to rebuild the original turret to the vehicle so that it could be returned to the program office. The Final Presentation held on 27 June 2017 was attended by both TARDEC and Program Manager/Program Executive Office (PM/PEO) engineers. This included a walk-around by all the attendees around the composite turret which was hoisted up on a display stand. The lightweight composite turret on the stand, and explanatory posters were also displayed during the 2017 Ground Vehicle Systems Engineering and Technology Symposium (GVSETS) at the Suburban Showplace in Novi, MI on Aug 18-10. The capabilities of the project were well received by leadership as well as all the attendees.

Conclusions:

- The Lightweight Vehicle Structure project has amply demonstrated that it is possible to design and manufacture a multi-material turret that is significantly lighter and meets performance requirements. The composite-steel monocoque turret provides the same or better performance while reducing weight by approximately 380 lbs (39% of the original turret structural mass of 987 lbs), well above the stated goal of 339 lbs (Table 2).
- One major difference between this program and other previous weight savings programs is that rather than creating a structure from a single material, this project utilizes a combination of the most effective materials that meets the need for each component.
- Future work would have to determine whether resin composite materials are competitive from a cost and performance point of view to be utilized by a defense prime to meet light-weighting needs of a military vehicle. This would not only be a function of production cost and product performance, but also of testing and repairability cost.
- It is anticipated that testing and repairability costs could be a significant barrier to adoption. Therefore, any future expansion of this project would have to address the question of how to reduce the test and evaluation cost of a hypothetical upgrade program involving a composite turret to the point that testing costs are equivalent to those for the baseline monocoque metallic turret. The testing issue is primarily an issue for upgrade programs. It would not be as much of an issue for new start programs, as they have to evaluate the complete vehicle regardless.
- The barriers to implementation of such light-weighting opportunities have been clearly enumerated, and must be examined by the concerned decision-makers to enable incorporation into future programs.

The final detailed “FOUO/Distribution C” report [7] for this project is available from the PIs or the TFA Leads listed for the project.

References:

[1] E. Polsen, L. Krogsrud, R. Carter, W. Oberle, C. Haines and A. Littlefield, "Lightweight Combat Vehicle Science and Technology Campaign," US Army Tank Automotive Research, Development, and Engineering Center, Report # 25940, Warren, 2014.

[2] R. J. Gerth and R. A. Howell, "What is a Ton of Weight Worth?," in *Ground Vehicle Survivabilty Training Symposium*, Ft. Bening, GA, 15-17 Nov., 2016.

[3] P. Davis and P. Rogers, "Advanced Vehicle Power Technology Alliance Fiscal Year 2014 Annual Report," Department of Army and Department of Energy, Warren, MI, 2015.

[4] D. Howell and P. Rogers, "Advanced Vehicle Power Technology alliance Fiscal Year 2015 Annual Report," Department of the Army; Department of Energy, Warren, MI, 2016.

[5] R. J. Gerth, "Trade Study of a Lightweight, Multi-Material Military Vehicle Structure," in *2013 NDIA Ground Vehicle Systems Engineering and Technology Symposium, 21-22 August 2013.*, Troy, MI, 2013.

[6] R. J. Gerth, "A Lightweight, Multi-Material Turret Structure," in *NATO AVT-264/RSM-043 Specialist's Meeting on Design, Manufacturing and Application Of Metallic Lightweight Material Components For Military Vehicles*, Tallinn, Estonia, 2016.

[7] Chad Osburn, James Pytleski, Bangalore A. Suresh, Karl Buter, Joshua Malberg, Zach Shofestall, “LWVS Technology Development: Composite Turret Structure Demonstrator EWD 002 Final Report”, June 14, 2017, Document Number R&D_LAV_A003-005, IAW CDRL A003 of Contract W56HZV-13-C-0261, LIGHT WEIGHT VEHICLE STRUCTURES.

Figures and Tables Start on Next Page

Figures and Tables:

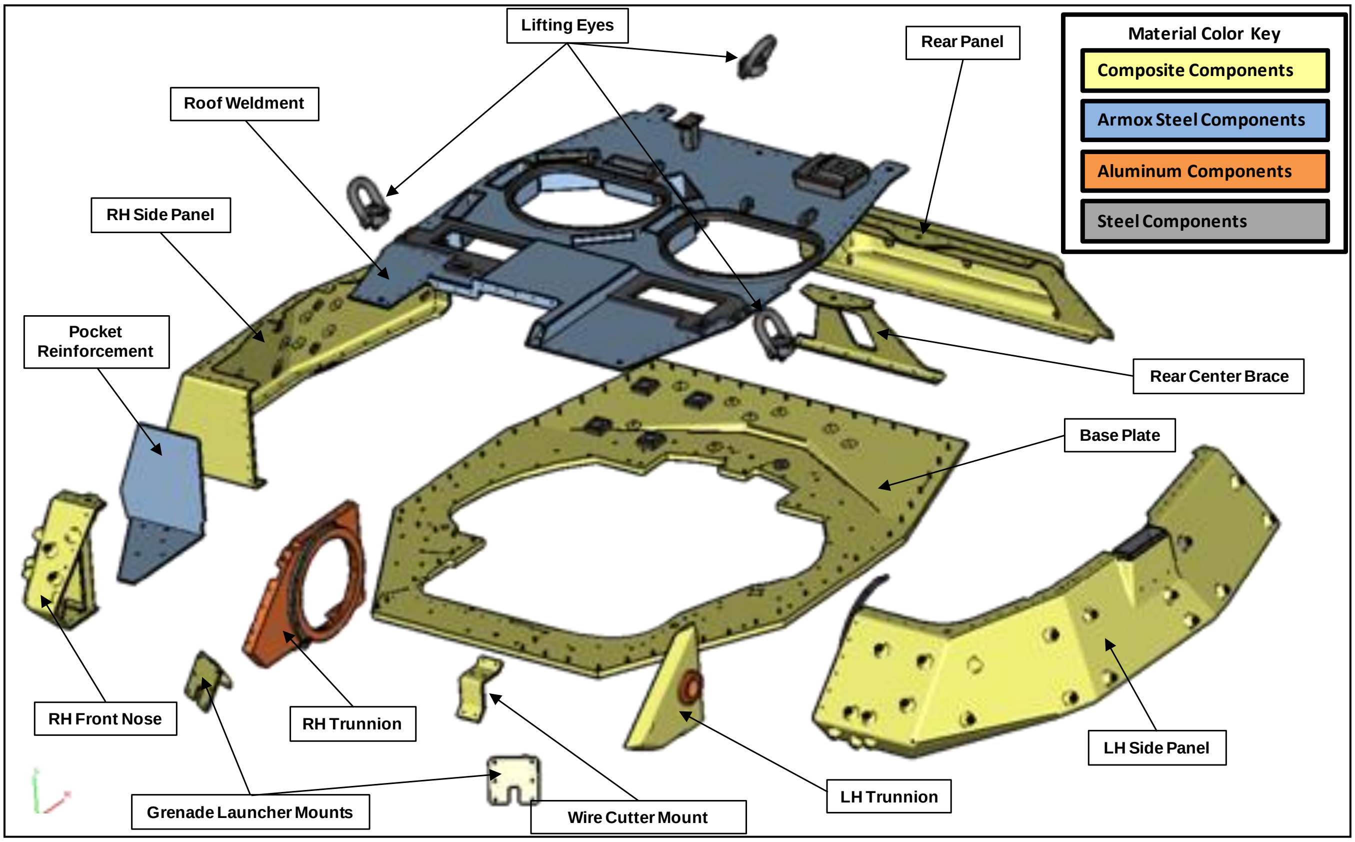

Figure 1. Exploded View of Turret Structure

Years	Volume	Price
1	150	$43,200,000
1	300	$82,600,000
3	150	$43,300,00
3	300	$83,100,000
5	150	$44,800,000
5	300	$83,600,000

Table 1: Pricing for different production scenario volumes

Description	Legacy (lbs)	Target (lbs)	PDR Estimate (lbs)	CDR Estimate (lbs)	Actual (lbs)
Structure Weight	987	568	446	521	527
Armor Weight	426	506	506	506	506
Total Weight	1,413	1,074	952	1,027	1,033
Total Reduction	-	339	403	386	380
Margin to Target	-	-	64	47	41

Table 2: Weight History of the Turret Design

Remainder of Page Intentionally Blank

Multi-Material Joining (MMJ) - Thermal Friction Stir Welding

DOE-VTO TFA Lead: Sarah Ollila
TARDEC TFA Lead: Ravi Thyagarajan

Principal Investigators:
Mr. Martin M. McDonnell
U.S. Army TARDEC
Product Lifecycle Engineering - Materials

Mr. Eugene Creed
Affiliation: Focus: HOPE – Manufacturing & Research
1200-C Oakman Blvd., Detroit, MI 48238

Project Start: Jan 2015
Project Completed: Q4FY17

Objectives:

- Develop the process, fixtures, tooling and testing of Thermal Friction Stir Welding (TFSW) of up to 36-inch long, 0.5-inch deep, bimetallic, production representative joints.
- Optimize the friction stir process parameters to achieve the best possible mechanical and metallurgical properties between aluminum alloy 6061 and high hardness armor steel.
- Perform mechanical testing and metallurgical analysis to characterize the joint.

Strategic Context:

- Falls under TARDEC Thrust area: Light-weighting/Multi-material joining, and Sub-area: Army Vehicle Light Weighting Campaign
- TSFW will be used by new Programs of Record (PORs) that require welding of steel to aluminum.
- The technology directly supports the TARDEC Strategy as a leap-ahead capability. It will also help ensure that newer lightweight requirements can be met without loss of performance.
- The project work product can easily transition to military stakeholders for utilization on new programs where dissimilar material joining is required. The technology also helps TARDEC's continual growth as the Joining Center of Excellence for the Department of Defense (DOD).

Accomplishments:

- A successful tool was designed that can produce the 36-in bimetallic welds.
- The observed mean and standard deviation of the bend test results were:
    Flexure load at break, 1.496 ± 0.815 kN (336.3 ± 183.2 lbf)
- The observed mean and standard deviation of the tensile results were:
    Yield stress, 123.09 ± 8.78 MPa (17.85 ± 1.27 ksi)
    Breaking stress, 139.23 ± 9.50 MPa (20.19 ± 1.39 ksi)
    Breaking strain, 4.47% ± 1.17%

Introduction:

Friction Stir Welding (FSW) is a metal fabrication process used to join separate pieces of metal and is a specific application of the friction stir process. However unlike traditional fusion welding processes which use electrical or heat energy to melt the adjoining surfaces of the metal pieces to fuse the material together, FSW is a solid state process where the frictional heat of a rotating machine tool warms the metal/alloy to a temperature that is below its melting/solidus temperature yet softens the metal to a state of plasticity where it can be easily deformed. During the FSW process, the rotating FSW tool stirs the warmed metal of the adjoining surfaces to mix the softened materials thereby welding the pieces together. Figure 1 depicts general features, terminology, and process parameters of a simple friction stir process. Similar heated stir processes which are fundamentally identical to friction stir processes but use other heating methods include laser, oxyacetylene, induction, and ultrasonic. Heated stir processes are also used as a method to create a metal matrix composite surface layer by introducing metallurgic additives, or to simply refine the grain structure of an alloy.

Figure 2 provides a time-based graphical representation of a typical friction stir process by simultaneously comparing several friction stir process parameters. To begin, the spindle motor rotates the Friction Sir Processing (FSP) tool at an initial rate which is usually significantly higher than the in-process rotation speed and the machine Computer Numerical Control (CNC) system moves the spindle to the start position where it is oriented at the proper tilt angles. The rotating tool is slowly lowered (plunged) into the start point of the joint along the plunge axis which is the resultant angle of the back and side tilt of the tool axis. When the FSP tool reaches its final plunge axis weld position, the rotating tool is held at the position for a specified dwell period to fully heat the material. The rotational speed of the FSP tool during the dwell period may remain at the initial speed, lower to a mid-range speed, and/or lower to the final in-process spindle speed. At the end of the dwell, the machine begins to move the rotating FSP tool along the joint axis. Depending on material, design, and fixture configuration, the parameters may be varied during the traverse process. Upon completion of the tool traverse, the tool is withdrawn from the material leaving an exit hole.

Because the microscopic structure of a metal is significantly changed after it undergoes a melting and resolidifying transition, the material strength of a fusion weld joint is significantly reduced—as much as 80% for some structural metal alloys. Because it is a solid-state process occurring below an alloy's solidus temperature, a heated stir process avoids the deleterious microstructural transformations that are common with liquid-state fusion welding and virtually eliminates the material porosity inherent with liquid alloy processes. Also, because less heat is input to the material during a heated stir process, the volume of material affected by the process heat is substantially lower than that of heat-intensive fusion processes. Another secondary benefit of heated stir joining processes is their capability of joining dissimilar metals which cannot be welded using traditional fusion welding. Because melting temperatures often promote chemical reactions between different material compounds, bimetallic fusion welding i.e. aluminum-steel, aluminum-titanium, titanium-steel is difficult, if not impossible. However because heated stir processes avoid the high temperatures causing these adverse effects, they are more applicable to joining dissimilar alloys.

Approach:

Friction Stir Tools:

- Design – For the experiments in this project, four different tool design configurations (Tool A: 12.5 degree taper angle with single pass welds, Tool B: 12.5 degree taper angle with double pass welds, Tool C: 25 degree taper angle single pass welds and Tool D: 36 degree taper angle single pass welds) were prepared as shown in Figure 3.
- Material Selection – The tools were made from tungsten-based material W-25%Re, which exhibited the best durability in the earlier C-0721 project [5].

Process Parameter Optimization Experiments:

As part of the second phase of this project, the new fixture (Figure 4) was used to conduct a series of friction stir weld design of experiments to study the tool geometries and further optimize process parameters (i.e. tool rotation speed, tool travel speed, and tool orientation) as required. For these experiments, four different tool design configurations (Tool A: 12.5 degree taper angle with single pass welds, Tool B: 12.5 degree taper angle with double pass welds, Tool C: 25 degree taper angle single pass welds and Tool D: 36 degree taper angle single pass welds), as shown in Figure 5, were readied. After initial trial of process parameters, L-9 Taguchi design of experiment method was used for optimization study.

All experiments were run with machine positional control with the vertical (Z) and transverse (X) axes zeroed for each run which compensated for varying work piece dimensions and tool probe length. For many coupons, multiple sets of parameters were used on a single coupon. For example, one section of the joint was fabricated with a traverse speed of 40 mm/min, and without stopping, the following section was produced with a slightly slower 30 mm/min.

Remainder of Page Intentionally Blank

Results and Discussion:

The friction stir joints were first made using trial process parameters for all four tools. The trial process parameters were based on prior experience of staff with the friction stir machine and tool combinations. Figure 4 shows the resulting welds from the four tools.

The trials showed that Tool A produced the best joint. In the next step, an L-9 Taguchi matrix was designed to further study and verify the optimal process parameters for Tool A. A preliminary Welding Procedure Specification (pWPS) sheet was completed at the end of this experimental study. At the same time, Tool A was selected for preparation of 18" and 36" long joint coupons in the next steps of this project.

Issues and Obstacles:

- Tool material wear due to processing on extremely hard steel (500 Brinell)
- Maintaining design tolerances on the angled joint surface while machining the high hardness steel bars. The issue intensifies with the length of the steel bar.
- Thermal management of the process-induced friction heat within the bimetallic joint coupons and fixture.
- The custom made friction stir machine sometimes produces tool path errors or suffers other breakdowns.

Metallurgical Analysis:

a) Base Material AA6061-T6511 – Aluminum 6061 is a precipitation hardening aluminum alloy, containing magnesium and silicon as its major alloying elements. The chemical composition of AA6061 plate used in the present study is listed in Table 1. During precipitation heat treatment, silicon combines with magnesium to form Mg2Si precipitate and contributes to the age-hardening process. AA6061 may be formed in the T4 temper (solution heat-treated) and T6 temper (solution heat-treated followed by precipitation heat-treated). AA6061 has good formability, weldability, machinability, and corrosion resistance, with medium strength.

Figure 5 shows the Scanning Electron Microscope (SEM) micrographs of as-received Al 6061-T6511 material. The average grain size in the as-received material was found to be about 200 μm.

b) Base Material MIL-DTL-46100 Steel – This alloy is quenched and tempered hard armor (HRA) wrought steel plate for lightweight armor applications for recommended thickness up to 2-inches. Rolled Homogeneous Armor (HRA) steel plates have been used to build armored combat vehicles and vessels due to good ballistic behavior accompanied by weight reduction in the armored structure as a consequence of the plate's high mechanical strength. The chemical composition of MIL-STD-46100 HRA used in the present study is listed in Table 2.

Plates of this material were received in quenched and tempered condition (water quenched from 1660°F and air tempered at 425°F for 71 min). SEM micrographs of the as-received material revealed typical tempered martensitic microstructure that was created due to water quenching and tempering. Low magnification SEM images (figure 6a-c) do not exhibit the presence of cementite particles in the micrographs. However, high magnification image (figure 6d) revealed the presence of very fine carbide particles. This observation implied that the as-received steel plate was very lightly tempered. Due to the low tempering temperature (425°F), it can be expected that the martensitic structure got mainly stress-relieved with little tempering.

c) Aluminum Nugget Zone – Figure 7a shows SEM of the Al-Steel interface microstructural morphology. It revealed sharp joint interface between Al and Steel. Since the rotating tapered pin just touched the faying surface of the steel plate during welding, large plastic mixing of Al and steel was not expected. Only few steel flakes came out from the faying steel surface embedded in the Al matrix in the nugget zone as shown in figure 7b. Figures 7c-d show the presence of very fine equiaxed microstructure of Al in the stir zone. The fine microstructure got created due to dynamic recrystallization during FSW. The SEM investigation also revealed that the grain size in the nugget zone got reduced to about 5-15 μm.

d) Heat Affected Zone (HAZ) of steel plate – In case of similar material joints, a non-consumable rotating tool with a specially designed pin and shoulder traverses along the joint lime. Consequently, in the nugget zone, both plates undergo intense plastic deformation at strain rates of 2–12 s-1 at elevated temperature. For the dissimilar material joints prepared in this study, the rotating tool pin only traversed through the Al plate and just touched the faying surface of the steel plate. So the steel plate was not severely deformed compared to Al plate. Only the faying surface of the steel plate got deformed due to rubbing action of the rotating tool pin. However, because of the heat generation due to friction between rotating tool and steel plate, and plastic deformation in the Al plate, the steel plate experienced some thermal excursion during welding. This is the HAZ in the steel plate. Figure 8 shows typical tempered martensitic microstructure in the HAZ. High magnification SEM image (figure 8d) exhibits the presence of cementite particles which formed due to the tempering of martensite during welding.

e) Micro-Hardness Measurement – Micro-Hardness measurements were carried out on the transverse cross-section of the weld at mid-height along red line shown in figure 9a.

Figure 9b exhibits the micro-hardness distribution from steel to Al across the joint interface. Hardness results revealed a sharp change in hardness across the steel-Al joint interface because of no plastic mixing of steel and Al at the joint interface. Hardness gradually increased in steel plate from 470 HV at the interface to about 540 HV over a distance of 25 mm from the interface. Similarly, in Al plate hardness gradually increased from 50 HV at the interface to about 120 HV over a distance of 25 mm from the interface. The substantial hardness decrease in the weld nugget and heat affected zone is related to the dissolution or coarsening of strengthening Mg2Si precipitates in the Al matrix during welding. As-received Al 6061-T6511 was fully hardened by Mg2Si precipitates, however due to the heat generated during welding, Mg2Si precipitates partially dissolved or coarsened in the aluminum matrix resulting hardness decrease in nugget and heat affected zone. Also, the hardness of the steel plate near the interface (HAZ) was reduced to about 470 HV from the parent material hardness of 550 HV. This decrease of hardness in the HAZ of steel plate is attributed to tempering of martensite in the HAZ due to thermal excursion during welding. Microstructural investigation has also revealed the presence of tempered martensitic microstructure in the HAZ.

f) X-Ray Diffraction (XRD) Investigation – Figure 10a shows the XRD pattern of Al 6061 at the stir zone, HAZ, and 40 mm away from the joint interface (base material). Figure 10b exhibits the magnified view of figure 10a. The intensity of the Mg2Si strengthening precipitates was found to be relatively high in the HAZ compared to stir zone and base material. This is most probably due to the coarsening of Mg2Si precipitates in the HAZ. Figure 12c exhibits the X-ray Diffraction pattern of steel at HAZ and 40 mm away from the joint interface (base material). The scan displays the presence of only α-Fe in the HAZ and base material. However, microstructural investigation revealed the presence of tempered martensitic microstructure of steel near the joint interface (HAZ). Hence, cementite (Fe3C) must be present in the α-Fe matrix as X-ray Diffraction method is unable to detect very fine carbide (Fe3C) particles in α-Fe matrix. A Transmission Electron Microscope (TEM) investigation is required to identify the size and distribution of fine carbide (Fe3C) particles.

g) Energy Dispersive X-ray Spectroscopy (EDS) investigation – EDS was carried out to identify elemental distribution in the stir zone and at the Al-Steel joint interface. Figure 13 shows the elemental maps at the joint interface, and reveals the presence of very thin (≈1μm) diffusion layer of aluminum and iron at the joint interface. In addition, Al was diffused to about 5 to 10 μm into the steel plate in severely deformed regions. The steel surface near the joint interface was plastically deformed in the micron scale as shown in figures 11b and 11d. However, no physical mixing of steel and Al at the joint interface was observed.

Mechanical Load Tests:

- Specimen Preparation – Tensile and bend test samples were cut out from 18 inch long Al-Steel joint plates made using optimal tool and process parameters found in this project. A slow feed EDM process was used for minimal heat effect on the test samples. The samples were designed to meet ASTM E8 and ASTM E290 test standards respectively. Figure 12 shows a sketch of the test samples used in this study.

  Al 6061 is a heat treatable alloy and so heat treatment can have considerable effect on the bimetallic joint strength. Our past study (C-0721 contract) has shown that an aging heat treatment of 347 deg. F for eight hours provides better joint strength compared to as-welded and T6511 conditions. Therefore, in this project too, we did the same aging heat treatment on all mechanical test samples before testing.

- Bending – Figure 13 shows the bend plots of the several samples tested. The observed mean and standard deviation of the results were:
    - Flexure load at break, 1.496 ± 0.815 kN (336.3 ± 183.2 lbf)
- Tensile – Figure 14 shows the tensile plots of the several samples tested. The observed mean and standard deviation of the results were:
    - Yield stress, 123.09 ± 8.78 MPa (17.85 ± 1.27 ksi)
    - Breaking stress, 139.23 ± 9.50 MPa (20.19 ± 1.39 ksi)
    - Breaking strain, 4.47% ± 1.17%

Conclusions:

Investigation was performed where the usage of four different Tungsten-Rhenium (W-Re) FSW tool geometries for bimetallic friction stir welding of 0.5” thick 6061 aluminum alloy with 0.5” thick high hardness armor steel, and found that good welds of up to 36” length are doable. The observed challenges in the process are a) rapid tool wear, b) maintaining of tolerances during machining of high hardness armor steel coupons- especially as the length of the coupon increases from 18” to 36” and c) welding machine’s ability to withstand loads resulting from the process.

After completing all the experiments and analyzing the results, we have concluded that one of the four tools (Tool A), produces better extended-length joints than the others. Sets of 18” and 36” long joint samples made with Tool A were delivered to TARDEC as production representative demonstration. In addition, metallurgical properties and strength of resulting joints were studied in detail.

References:

[1] E. Polsen, L. Krogsrud, R. Carter, W. Oberle, C. Haines and A. Littlefield, "Lightweight Combat Vehicle S&T Campaign," U.S. Army Tank Automotive Research, Development, and Engineering Center, Warren, 2014.

[2] C. Dauer, "Military Vehicles Must Balance Weight, Protection Considerations," 11 NOV 2011. [Online]. Available: http://www.idga.org/vehicles/articles/army-vehicles-must-balance-weight-protection-consi. [Accessed 16 SEP 2016].

[3] W. M. Thomas, E. D. Nicholas, J. C. Needham, M. G. Murch, P. Templesmith and C. J. Dawes, "Friction Stir Butt Welding". Patent G.B. Patent Application No. 9125978.8, DEC 1991.)

[4] W. M. Thomas, "Friction Stir Butt Welding". Patent U.S. Patent No. 5,460,317, 1995.

[5] R. Miller and M. McDonnell, "Bimetallic Friction Stir Joining of AA6061 and High-Hardness Steel," 2013.

[6] "Wisconsin University, Robotics Engineering," [Online]. Available: http://robotics.engr.wisc.edu/cgi-bin/wikiwp/wp-content/uploads/2011/11/frictionStirWelding_detailSchematic.png. [Accessed 2016].

[7] B. Justusson, "Microstructural Investigation And Evaluation Of Mechanical Properties In Friction Stir Welded Joints," U. S. Army Research Labortory, Aberdeen Proving Grounds, 2011.

[8] M. Grujicic, B. Pandurangan, A. Arakere, C.-F. Yen and B. A. Cheeseman, "Friction Stir Weld Failure Mechanisms in Aluminum-Armor Structures Under Ballistic Impact Loading Conditions," Journal of Materials Engineering and Performance, vol. 22, no. 1, pp. 30-40, 2013.

[9] M. A. Sutton, A. P. Reynolds, D.-Q. Wang and C. R. Hubbard, "A Study of Residual Stresses and Microstructure in 2024-T3 Aluminum Friction Stir Butt Welds," Journal of Engineering Materials and Technology, vol. 124, pp. 215-221, 2002.

[10] K. A. Dannemann, S. Chocron, A. E. Nicholls and D. L. Wagar, "Mechanical Characterization of Aluminum 2195-BT for Determination of Johnson-Cook Constitutive Constants," U.S. Army RDECOM-TARDEC, 2009.

[11] B. Thompson, K. Doherty, C. Niese, M. Eff, T. Stotler, Z. Pramann, J. Seaman, R. Spencer and P. White, "Friction Stir Welding of Thick Section Aluminum for Military Vehicle Applications," Army Research Lab, 2012.

[12] R. S. Mishra and Z. Y. Ma, "Friction stir welding and processing," Materials Science and Engineering, vol. 50, pp. 1-78, 2005.

[13] K. A. Dannemann, R. P. Bigger, N. L. Scott, C. Weiss and A. J. Carpenter, "Deformation Response Comparison for Gas Metal Arc Welds (GMAW) vs. Friction Stir Welds (FSW)," Southwest Research Institute, San Antonio, 2014.

[14] K. J. Doherty, B. Thompson, T. Stotler, S. Vaze and C. Niese, "Ballistic Shock Testing of 2139-T8 Alumiunm Friction Stir Welds," U.S. Army Research Laboratory, Aberdeen Proving Ground, 2010.

Figures and Tables:

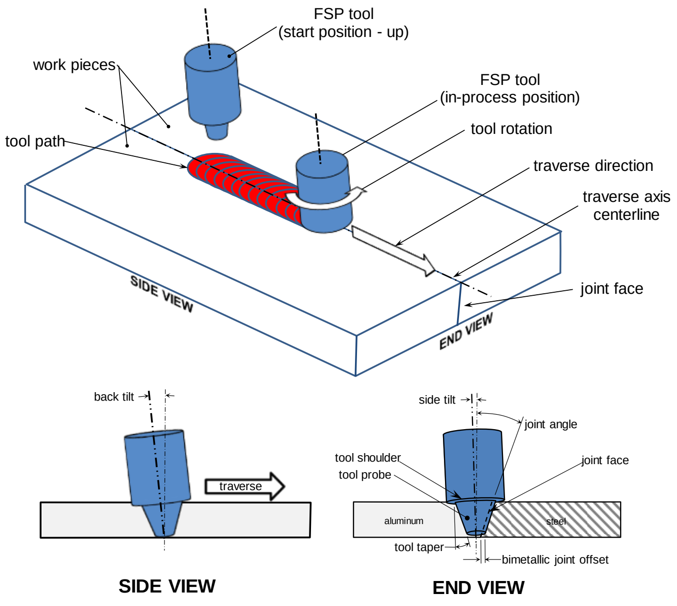

Figure 1 – FSP Terminology

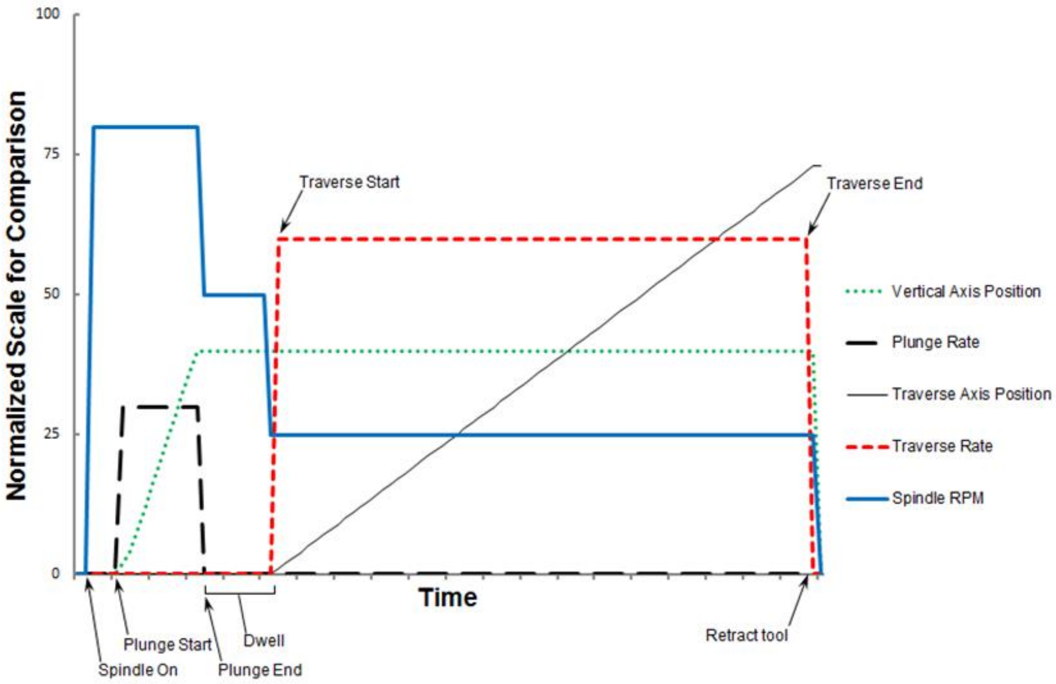

Figure 2 – FSP Process Graph

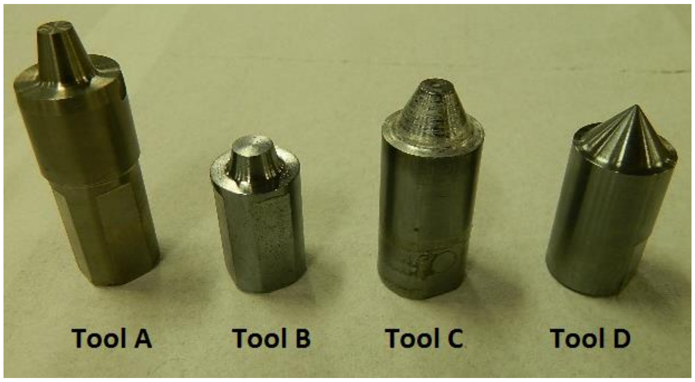

Figure 3 – FSW Tool designs

Figure 4 – Trial bimetallic joints made with Tools A, B, C and D

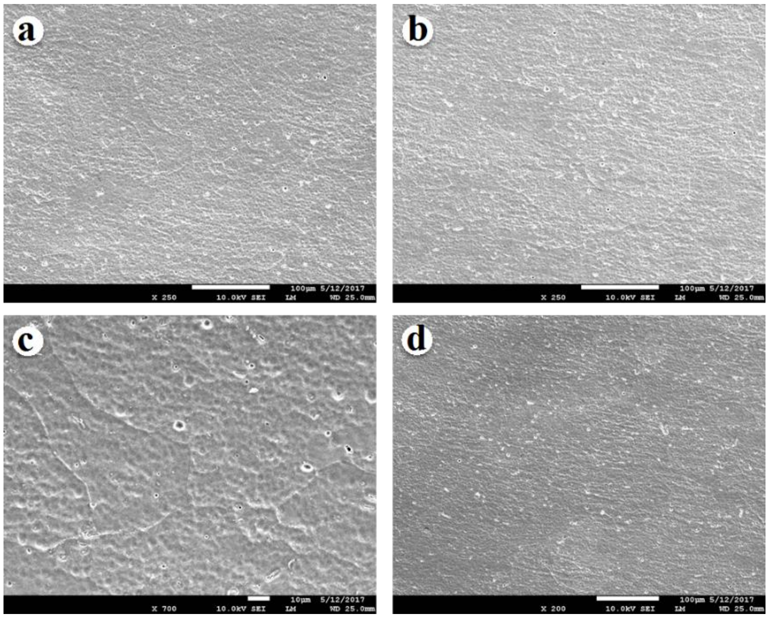

Figure 5 – (a-d) Scanning electron micrographs of as-received Al 6061-T6511 plate.

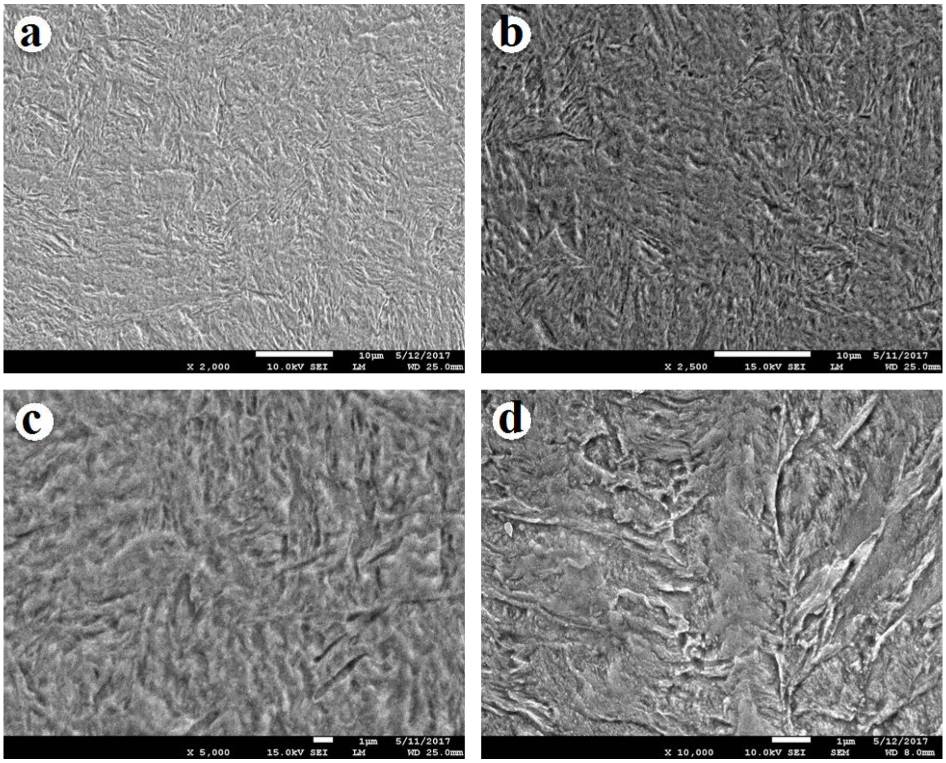

Figure 6 – (a-d) Scanning electron micrographs of as-received MIL-STD-46100 steel plate.

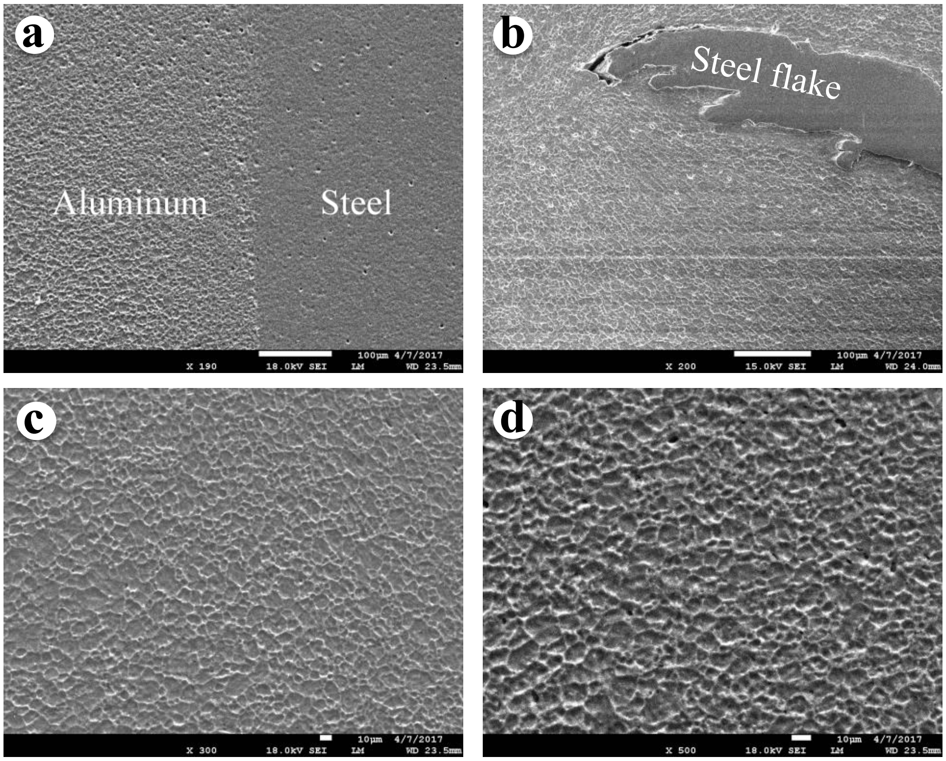

Figure 7 – Scanning electron micrographs exhibit (a) Al-Steel interface, (b) steel flake embedded in Al matrix close to the weld interface, (c-d) nugget zone micrographs.

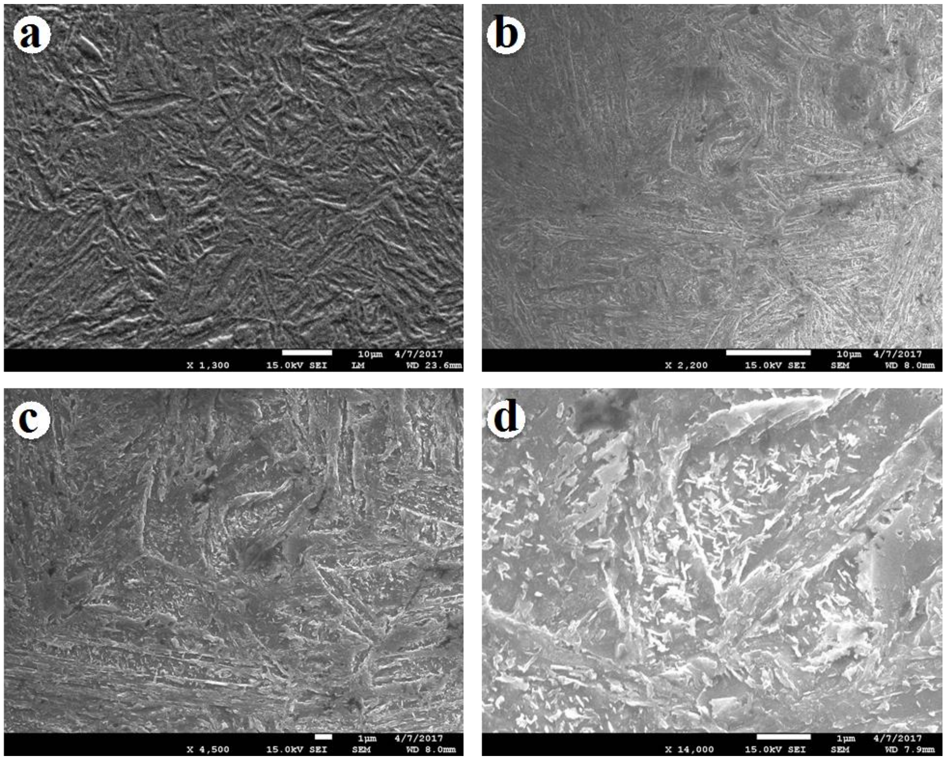

Figure 8 – Scanning electron micrographs showing tempered martensitic microstructure in the steel HAZ.

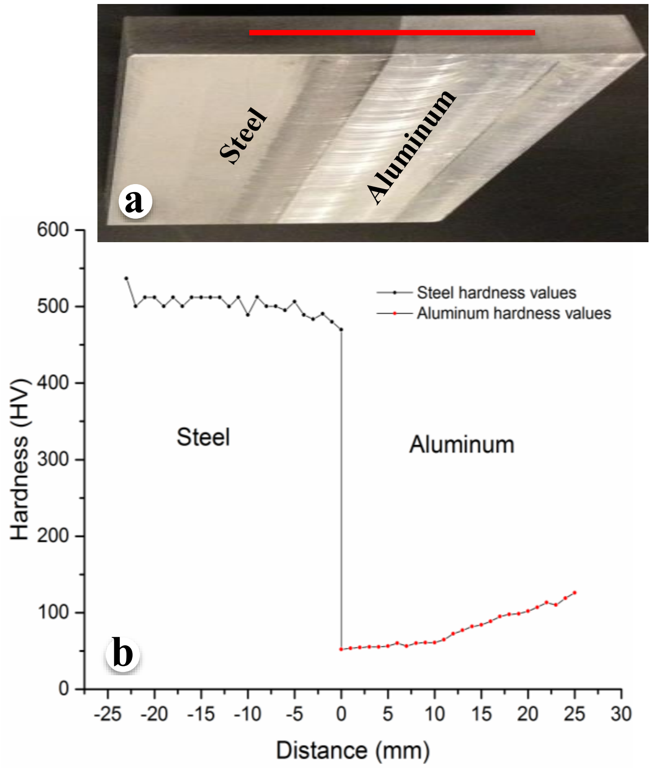

Figure 9 – (a) Al-Steel bimetallic friction stir weld made with optimized process parameters. (b) Microhardness distribution from Steel to Al on transverse cross-section at mid-height along red line shown in (a).

Figures Continued on Next Page

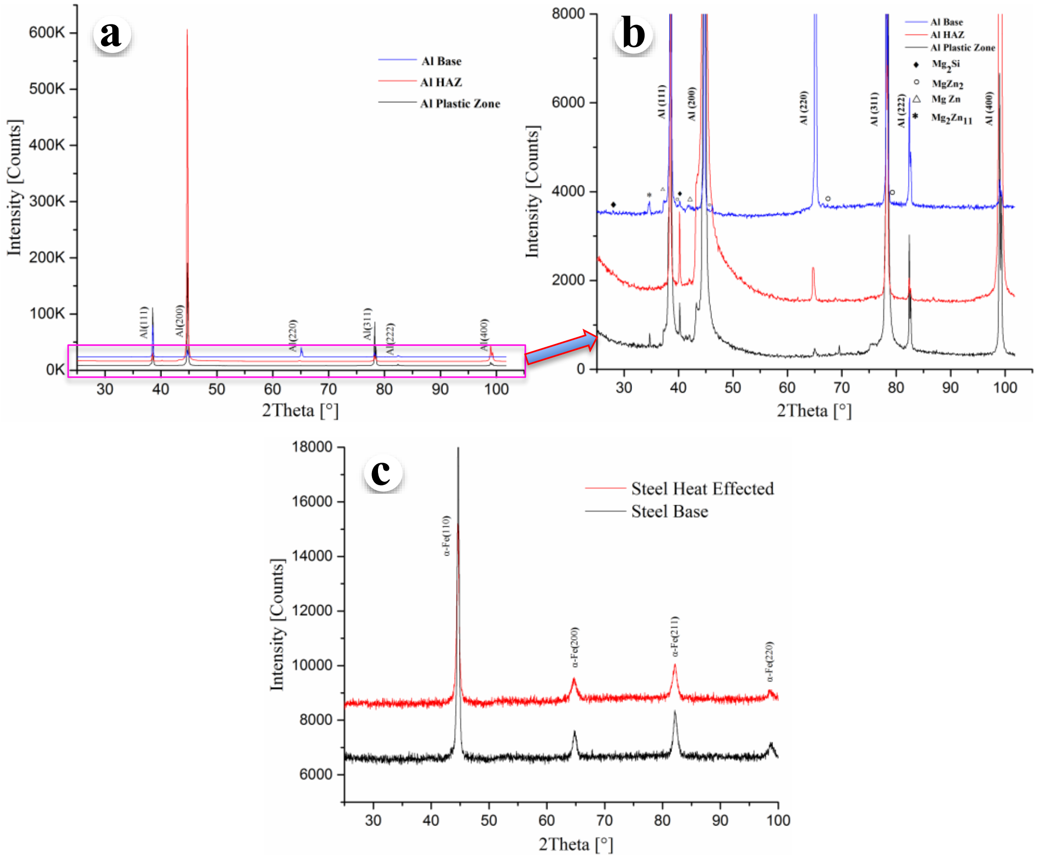

Figure 10 – X-ray Diffraction patterns of Al-Steel weld at different locations. (a) Al at stir zone, HAZ, and 40 mm away from the joint interface (base material), (b) Magnified view of figure (a), and (c) Steel at HAZ and 40 mm away from the joint interface (base material).

Figures Continued on Next Page

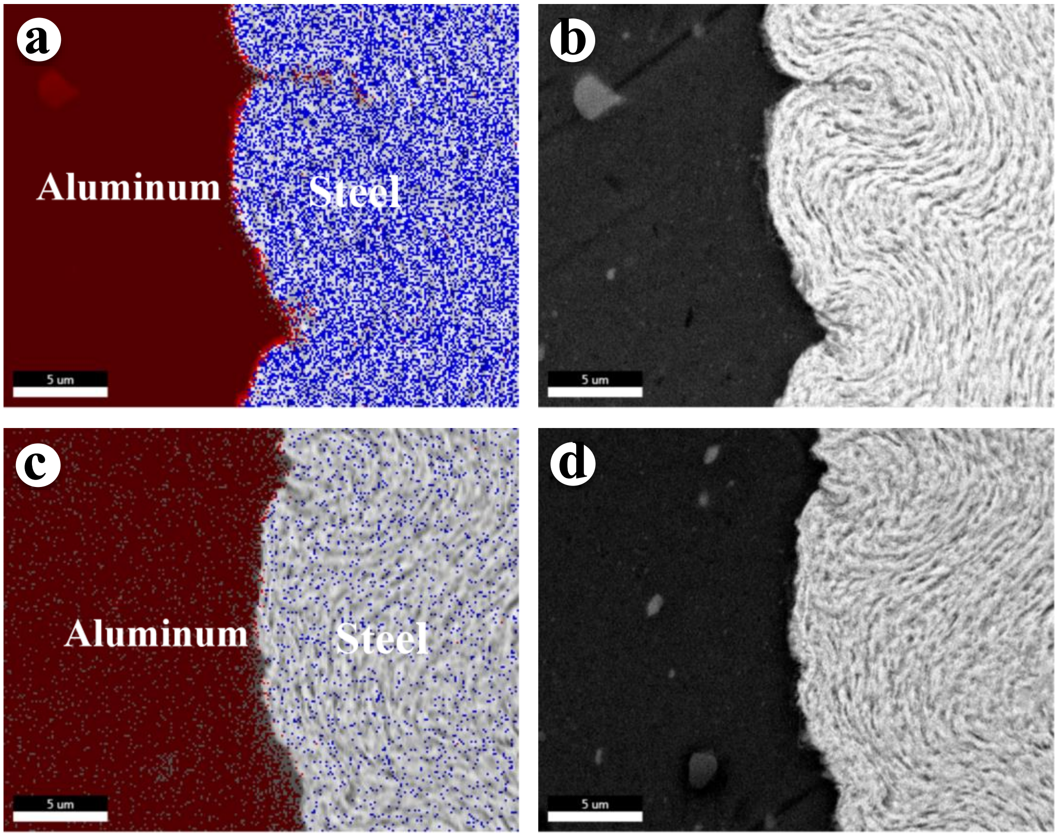

Figure 11 – EDS elemental maps across the Al-Steel weld interface at (a) upper part of the weld and (c) lower part of the weld. (b) and (d) exhibit the SEM micrographs of joint interface at top and bottom part of the weld.

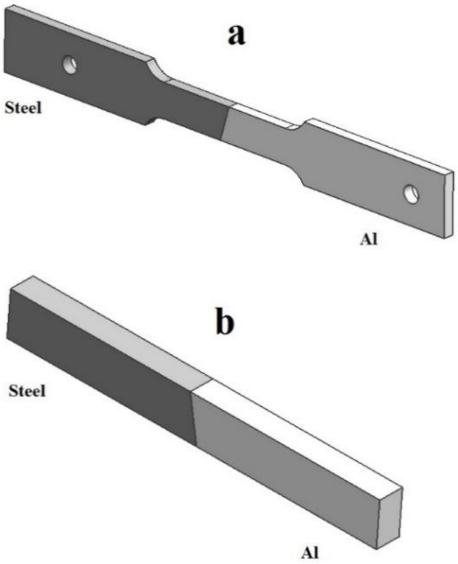

Figure 12 – Steel-Al weld mechanical test samples. (a) Tensile and (b) Bend.

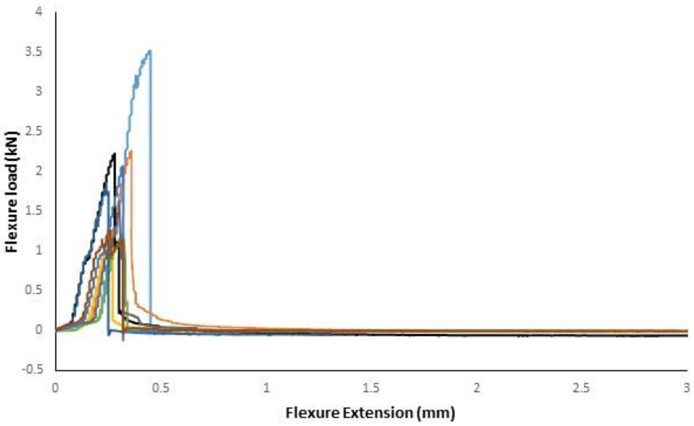

Figure 13 – Bend test plots.

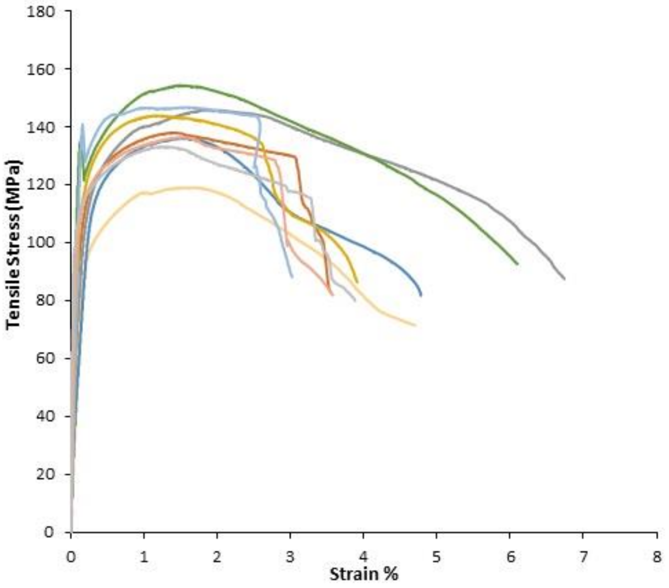

Figure 14 – Tensile test plots

Table 1 – Chemical Composition of AA6061-T6511 Plate

Element	Al	Si	Fe	Cu	Mn	Mg	Cr	Zn	Ti	Other Each	Others Total
Wt. %	Bal.	0.40-0.80	0.7	0.15-0.40	0.15	0.8-1.2	0.04-0.35	0.25	0.15	0.05 max	0.15 max

Table 2 – Chemical Composition of MIL-STD-46100 Steel Plate

Element	Fe	C	Mn	P	S	Si	Cu	Ni	V	Al	Cr	Mo	Ti
Wt. %	Bal.	0.28	0.87	0.011	0.003	0.45	0.05	0.4	0.01	0.041	0.5	0.21	0.045

This Page Intentionally Blank

Multi-Material Joining (MMJ) – Weld Wire Characterization in Welding Advanced High-Strength Steels (AHSS)

DOE-VTO TFA Lead: Sarah Ollila
TARDEC TFA Lead: Ravi Thyagarajan

Principal Investigator:
Mr. Matthew Rogers
U.S. Army TARDEC
Product Lifecycle Engineering - Materials

Project Start: Oct 2013
Estimated Completion: Q4FY18

Objectives:

- Understand the joint quality and welding process efficiency of welded armor steels
- Establish weld wire selection criteria for the new MIL-Standard on the welding of armored steel
- Provide practitioners a point of comparison between current joining practices and future welding practices.
- Create validation data for ballistic and blast models of welded armor plates.

Strategic Context:

- The project data will transition and be used by both TARDEC engineers and vehicle manufacturers to further optimize vehicle designs. The data will identify optimal weld wire / material combinations to maximize weld filler material properties. The information will be transitioned to OEMs and suppliers through the military weld standard.
- The project supports TARDEC's Value Stream 2, Support Systems Across the Acquisition Lifecycle, by providing PMs with data and standards for improving weld quality for all steel vehicles. The same data and standards can be transitioned to the automotive industry.
- The project continues to build on the AVPTA MMJ investments in making TARDEC a joining center of excellence. The level of detail and fidelity of study speaks to TARDEC's in-depth expertise in welding.
- Future plans are to expand the study to include aluminum materials (2xxx, 5xxx, 6xxx, and 7xxx).

Accomplishments:

- Phase 1 Testing 50% Complete
- Phase 2 Testing 75% Complete
- Phase 3 Testing 100% Complete

Introduction:

The chemical and mechanical properties of armor steel used by the U.S. Army are similar to advanced high strength steels used in the automotive industry. The ultimate tensile strength ranges from 150 ksi to 300 ksi depending on the armor grade selected. The last MIL standard for welding armor was canceled in 1998 and replaced with the Ground Combat Vehicle Welding Code (GCVWC)-Steel, which has never been updated and has no engineering guidance for the selection of weld wire. Additionally, neither the old MIL standard nor the GCVWC-Steel include any recommendations based on newer armor grades and new welding techniques. There are also no published industry guidelines for welding of advanced high strength steels, which the government could use to weld armor. This has led to a proliferation of welding techniques by the defense contractors, which in turn has led to a general decrease in weld quality and the proliferation of defects, such as cracks induced by hydrogen embrittlement.

Performance of welded joints is critical to the performance and reliability of ground vehicles. The performance depends on many factors associated with the welding. One key factor is the type of weld wire, of which there are many. A weld wire is classified by weld process and tensile strength. The preferred process for welding plate armor in ground vehicles is Gas Metal Arc Welding (GMAW) pulse. Weld wire tensile strength ranges from 70 ksi to 120 ksi; some ground vehicle manufacturers have even used austenitic stainless steel filler metals. Unfortunately, the weldments made from these wires in combination with modern armor materials have not been characterized. There is also a general lack of knowledge of the mechanical and ballistic performance, in terms of joint efficiency, of these wires. Joint efficiency is defined as the ratio of the properties of the welded armor to the properties of the base metal armor. If the joint efficiency of each weld wire is known, then proper filler metal selection criteria can be established and implemented through a the new weld standard.

In addition to establishing selection criteria for the welding of armor steel, the data obtained in this study will be used to validate material models for ballistic and blast modeling and simulation. This data can be used by both TARDEC engineers and vehicle manufacturers to further optimize vehicle designs.

Remainder of Page Intentionally Blank

Approach:

The project is divided into three phases:

Phase 1: Investigate the mechanical and metallurgical properties of welded armor using various weld wires.
Phase 2: Perform high strain rate events using a ballistic shock test with a welded H-plate.
Phase 3: Perform penetration testing to determine magnitude of vulnerability.

Phase 1: Involves robotically welding MIL-DTL-12560 class1, MIL-DTL-46100 class1, and ASTM A514 Grade A to themselves in 14” x 21” x 1/2” single V-groove sample. Filler materials are solid wire, stainless steel, and metal core filler. Various tensile strengths ranging from approximately 70ksi-140ksi will be used. All samples will be welded internally at TARDEC/Center for System Integration (CSI). The samples will then undergo tensile, hardness, fatigue, charpy impact, hydrogen embrittlement (see Figure 6). Once this is complete, the samples will be ranked for performance. The highest performers will move to Phase 2.

Phase 2: This phase involves taking the highest filler performers from Phase 1 and robotically welding them into a 3’ x 3’ x 1/2” H-plate configuration. The same single V-Groove configuration will be used throughout this test as well. Once the plates are welded and radiographically tested they will be sent over to the TARDEC SABL lab for Ballistic Shock testing (see Figure 2). If the samples pass, they will be used for Phase 3

Phase 3: This phase involves taking the performers from Phase 2 and robotically welding 2’ x 2’ x 1/2” single V-groove plates. Penetration testing will determine the joint efficiency as defined by the magnitude vulnerability (see Figure 3). These tests are performed with a high speed camera and flash x-ray to record the dynamic deformation during the ballistic shock test. Understanding the dynamic deformation response is crucial to improving our understanding of weld responses to high strain rate events.

Results and Discussion:

In the first year, the overall study plan was completed and the welding material and weld wires procured. In addition, it was necessary to develop an automated manner to weld standard I-plates and H-plates for testing. Figure 1 & 2 shows the hardware fixture that was developed to robotically weld the large sample of I- and H-plates. Figure 1 shows a completed I-plate weld, and Figure 2 shows how an H-plate looks by comparison.

One issue that was not anticipated was that the MIL-DTL-46100 (high hard) material became highly magnetic from the shoot penning cleaning process. This required the additional step of demagnetizing the material before welding to prevent arc blow (see Figure 4).

Phase 1: Welding of the I-plates has been completed. Figure 5 shows a sample hardness scan of a completed weld zone. Figure 6 shows how all the weld characterization samples are cut from a single plate. Three samples will be cut from different plates for each weld wire/parent material combination to obtain statistical validity of the results. Phase 1 is currently about 50% complete. For the tensile samples, one of the four sets of tensile bars for every combination has been complete. We currently have data to understand what the trends look like. As tensile strength goes below 80ksi or above 120ksi ultimate tensile strength yield strength properties begin to change. It is too early to tell but it is believed that they will be a level that will be acceptable ranging from 80ksi to 100ksi

Phase 2: Currently is at 75% complete. Obtaining range time to complete this task is difficult. The range has about 25 H-Plates left to shoot. Digital Imaging Correlation (DIC) software/ analysis was added to the testing in order to better understand the deflection on the steel at high strain rate. Completion for this is expected to be no later than May 2018.

Phase 3 is 100% complete and the final report is being completed. Final report due early 2018.

Conclusions:

The Phase 1 plates will be tested and analyzed. The remaining Phase 2 plates will take approximately 9 months to weld. The data that was collected, has been provided for input to the new MIL-STD-3040 for welding. MIL-STD-3040 has utilized the data and testing criteria to develop mechanical acceptance criteria.

This data will transition and be used by both TARDEC engineers and vehicle manufacturers to further optimize vehicle designs. This data will transition to Industry, PMs, Depots, and Arsenals through the new welding MIL standard, by creating filler metal selection charts. The data from this project will also be easily transitioned to help industry, such as the automotive and heavy equipment companies, in the selection of weld filler materials for their types of AHSS due to the similarities in properties. The data obtained in this study will also be used to refine material models for modeling and simulation (M&S).

References:

[1] MIL-STD-3040
[2] AWS D1.1
[3] AWS A2.4
[4] ASTM A514
[5] MIL-DTL-46100
[6] MIL-DTL-12560
[7] Matthew Rogers, “Quantifying Hydrogen Induced Cracking (HIC) Susceptibility of Welding Filler Wires Used in the Welding of Armor Steel”, Nov 2016, https://www.dtic.mil/dodtechspace/docs/DOC-25241

Figures and Tables Begin on Next Page

Figures and Tables:

Table 1: Phase 1 Test, Test Location and Timeframe

Test	Locations	Time Frame
Robotically welded samples	TARDEC CSI weld area	FY14
Tensile Testing	TARDEC Metallurgical Lab	FY14/FY15/FY17/FY18
Hardness Testing	TARDEC Metallurgical Lab	FY14/FY15
Charpy Impact	TARDEC Metallurgical Lab	FY14/FY15/FY17/FY18

Table 2: Phase 2 Test, Test Location and Timeframe

Test	Locations	Time Frame
Robotically welded samples	TARDEC CSI weld area	FY14/FY15
Radiographic Test	ANAD	FY15
Ballistic Shock Test	TARDEC GSS SABL	FY15/FY16/FY18

Table 3: Phase 3 Test, Test Location and Timeframe

Test	Locations	Time Frame
Robotically welded samples	TARDEC CSI weld area	FY15
Radiographic Test	Outside Contractor	FY16
Penetration Test	TARDEC GSS SABL	FY16

Figure 1: Fixture for Robotic Welding of Phase 1 plate

Remainder of Page Intentionally Blank

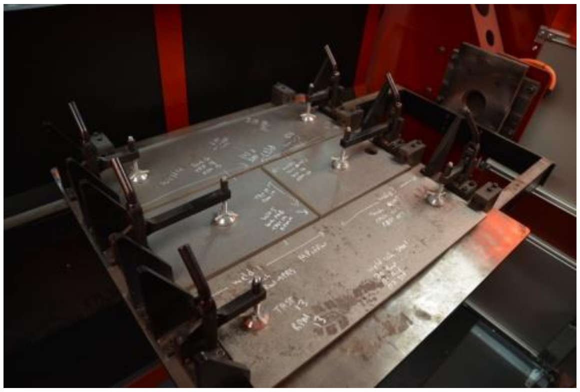

Figure 2: Phase 2 H-plate Clamped and Ready for Welding

Figure 3: Penetration Testing Phase 3

Remainder of Page Intentionally Blank

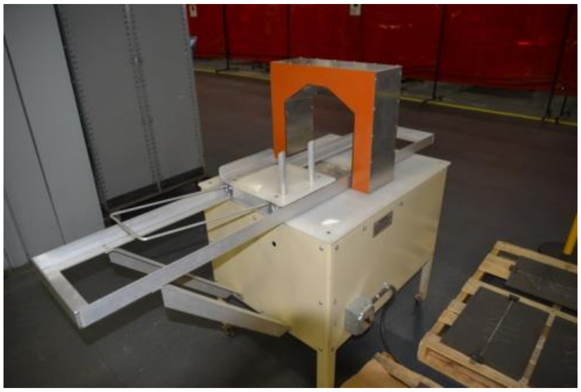

Figure 4: Demagnetizing Process

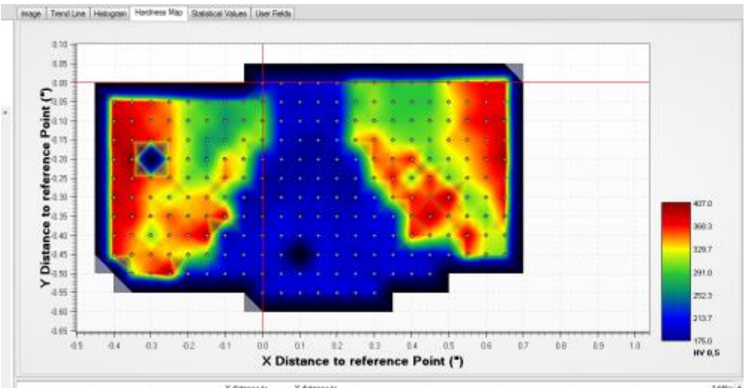

Figure 5: Sample of Micro hardness profile

Figure 6: Phase 1 I-plate Marked Samples for Standardized Weld Characterization Tests

Remainder of Page Intentionally Blank

This Page Intentionally Blank

AVPTA Technology Focus Area 2: Lightweight Structures & Materials

Multi-Material Joining (MMJ) – High Strength Weld Wire Development Suitable for High Strength 6XXX Aluminum Alloys

DOE-VTO TFA Lead: Sarah Ollila
TARDEC TFA Lead: Ravi Thyagarajan

Principal Investigator:
Mr. Matthew Watson
Arconic
100 Technical Drive
Alcoa Center, PA 15069-0001

Project Start: May 2014
Estimated Completion: Q3FY18

Objectives:

- Develop a weld wire for welding high strength aluminum plate, particularly 6055; such that the weld joints exhibit improved mechanical properties and corrosion resistance over the incumbent weld wire material.
- Refine the chemistry of the weld wire in an effort to optimize the corrosion and mechanical properties of the resulting weld joint.
- Fusion weld aluminum alloy materials (5083 and 6055) with the newly developed high strength filler wire.
- Develop a weld wire for 7085 that will pass the Army's ballistic shock test requirement.

Strategic Context:

- Permits the light weighting and improved performance of new vehicles, as well as increased protection for the Warfighter, due to a 20% strength increase in 6xxx alloys
- Improves the maintainability and repairability of legacy vehicles.
- Provides a cost effective solution and enables design flexibility in material choices for high performance combat and heavy transport vehicles.
- Attractive for commercial transportation applications to cost effectively save weight.
- 7085 if, when welded will be suitable in high strain rate environments, would be a viable alternative alloy for other, more costly alloys

Accomplishments:

The production of small volumes (50-100 lbs.) of filler wire for initial Gas Metal Arc Welding (GMAW) evaluations, including weldability and mechanical property evaluations, has been accomplished which has proven to be a complex, time-consuming activity that involves 5 steps and multiple vendors. Also the following were successfully achieved:

- Cast ~100 lb. billets (Alcoa) of C138H and C139H
- Billets were homogenized (Alcoa), cropped and scalped, and cut to length
- An annealing practice will be developed for C138H and C139H
- An extrusion practice was developed based on the composition of the material and capabilities of the extrusion press
- The technical information package and quoting materials was completed to place Alcoa Forging and Extrusion (AFE) Pimalco (Chandler, AZ) under contract to extrude our C138H and C139H filler alloy billets.
- All billets were milled, sawn and marked according to Pimalco’s requirements, and shipped.
- Tests were performed to ensure Environment, Health and Safety (EH&S) compliance
- Extrusion dies were designed and ordered
- Extrude billets to 0.75" rods (Pimalco)
- The 0.5” rods will be drawn down to 0.118” wire and coiled (Beneke)
- The 0.118” wire will be drawn down to the final 0.062" diameter by Hobart
- Written report on the progress to date with the 5k/6k weld wire development focusing on the technical difficulties encountered

In July 2017, 7085 weld wire development was added to the Scope of Work (SOW) and the period of performance extended to June 2018.

- Large diameter filler material of new weld wire material was used to perform weldability evaluations
- Drawing the weld down to final gauge is in process, GMAW Metal Inert Gas (MIG) weldability evaluations will start once enough final gauge material is on hand

Introduction:

High strength aluminum alloys, such as 6055 and 7085, have approximately 20% higher strength than currently used aluminum alloys. They offer the potential to significantly improve performance and reduce weight and cost. However, when welding high strength aluminum alloys, the only commercially available filler wires that can be used to weld these alloys without cracking produce welds with limited shear strength and ductility [1], which in turn limits their capability to withstand blast type of loads. Because the joints produced with these filler wires are so much weaker than the parent material, the full benefits of the high strength alloys cannot be realized. As such, the thickness of the components must be designed to compensate for the weakness of the joining method used, resulting in parasitic materials and increased weight. The increase in weight results in an increase in fuel consumption, an increase in drive train and suspension requirements, and a loss in performance. In addition, when welding these high strength alloys to 5XXX (e.g. 5083) parts, the use of 4XXX type filler leads to formation of brittle MgSi2 at the fusion zones of the welds with the 5XXX parent metals. On the other hand, when welding such high strength 6XXX/5XXX alloy combinations with Mg based 5XXX filler alloys (e.g. 5556, 5356, 5183), the formation of Mg/Cu low melting eutectics at the fusion zones of the welds leads to their cracking. Similarly, the currently available weld wire available for the 7085 alloy has not passed a ballistic shock test. Improved joining methods are therefore needed so that these high strength materials can be joined in a fashion that optimizes the vehicle manufacturing system. To address this need, Alcoa is developing a number of weld wires that would result in higher strength weld joints over the incumbent weld wires.

Approach:

In the past, the extrusion step was performed at an Alcoa facility on an extrusion press that was recently shut down. As such, Alcoa has been working to identify an alternative supplier for extruding the four prototype billets that were cast in 2015. Extrusion trials have been performed at an outside vendor and at another Alcoa location but with less than desired turnaround times and/or quality. FY16 milestones are being repeated here for continuity.

During FY17, the 5xxx/6xxx weld wire development was paused and the 7085 weld wire development initiated. Billets of new alloys have been produced and extruded to 0.375” dia. As of Oct-17 the material was at Hobart for final draw down to 0.062” dia. This processing should be completed by mid-January.

Results and Discussion:

The C138H and C139H compositions are significantly higher in certain alloying elements than traditional aluminum 5XXX filler wire [2] alloys. Therefore, the flow stress (yield strength) of the material is higher than that of traditional filler alloys. These compositions also work harden more than traditional 5XXX alloys, leading to high tensile stresses during the drawing process. It is due to the higher strength and work hardening of these compositions that the processing from billets to useable weld wire has been so fraught with difficulties. A more conservative approach (less reduction in each drawing pass) has been proposed.

Due to delays with the Government’s clarification of requirements and the availability of funding, what was expected to be a one or two month pause in the project became nearly a full calendar year. Similarly, the ballistic shock testing that was to be funded and performed by TARDEC’s Ground Vehicle Survivability & Protection (GVSP) organization was delayed from Sep-17 to May-18, which has resulted in Alcoa plant lowering the priority of processing the new material. This is, however, expected to be completed in Jan-18 and ballistic shock test panels ready for testing in May-18.

Remainder of Page Intentionally Blank

Conclusions:

Development of the 5xxx/6xxx filler alloy has been shelved for the time being. The 7085 weld wire development has been initiated but delayed. With the expected test dates now at the end of May-18, there are no further delays anticipated. Project accomplishments are listed on the first page of this report.

References:

[1] http://www.dtic.mil/dtic/tr/fulltext/u2/a622461.pdf
[2] http://www.azom.com/article.aspx?ArticleID=2804 (example)

Figures and Tables:

None

Remainder of Page Intentionally Blank

AVPTA Technology Focus Area 2: Lightweight Structures & Materials

Multi-Material Joining (MMJ) Bolted Composite Joint Strength and Fatigue

DOE-VTO TFA Lead: Sarah Ollila
TARDEC TFA Lead: Ravi Thyagarajan

Principal Investigators:
Mr. Riley Woodham
Seemann Composites
12481 Glascock Dr, Gulfport, MS 39503-4639

Mr. Ted Campbell
Material Sciences Corporation

Project Start: Oct 2010
Project Complete: Q4FY17

Objectives:

- Assess how an applied load is distributed between a metallic (17-4PH stainless steel) component and intermediate modulus carbon fiber reinforced composite component joined by a series of bolts.
- Determine the effect of bolt hole size and bolt-hole pattern on the performance of a composite component bolted to a metallic component.
- Determine the potential failure modes for joints comprised of a composite component bolted to a metallic component.

Strategic Context:

- Work directly contributes to the design and development of a mid-span hinge joint for a composite bridge being designed for potential use on a current assault bridge program of record.The Army's Product Manager for Bridging has shown interest in further development of this bridge to address the capability of military bridges to accommodate the growing weights of military vehicles such as the Abrams tank
- Knowledge gained from this work can also be applied in other applications where stainless steel is bolted to an intermediate-modulus carbon fiber composite

Remainder of Page Intentionally Blank

Accomplishments:

- A fourth bolt bearing and by-pass test was performed to assess the performance of design changes made to the joint since the completion of the third bolt bearing and by-pass test
- Fabrication-level drawings for the full-scale Composite Assault Bridge mid-span critical bridge element test article were completed, incorporating lessons learned from the completed assessment of the capability of the full bridge to carry Military Load Class 120 loads and previous bolt bearing and by-pass tests. These drawings were provided to TARDEC prior to the end of the contract, along with a 3-D printed scale model of the test article. A test plan was also drafted for testing of this article.
- Fatigue testing was completed for five different composite laminate designs, representative of the laminates being used on the sidewall, tension rail, built up tension rail and face sheets of the bridge. Testing was completed at various load levels, with a maximum load level of 75% of Ultimate Strength.
- Phase 1 of corrosion testing, consisting of coupon and sub-component testing, was completed during this fiscal year. This testing helped to identify design features, implemented for corrosion prevention, to test further in Phase 2 and design features to eliminate from consideration.
- Corrosion Test Phase 1.2, which tested corrosion performance with respect to how tight a fit exists between the bolt and the bolt hole, and Phase 2, which tested the corrosion performance of a simulated full-scale joint, was started. Phase 1.2 and Phase 2 specimens experienced a total of approximately 109 and 116 cycles at the time the contract ended.

Introduction:

The Composite Assault Bridge is a composite bridge being designed for potential use on a future Product Manager Bridging assault bridge program of record. One of its design elements is a mid-span joint consisting of a stainless steel hinge bolted to an intermediate modulus carbon fiber composite tension rail. The bridge's mid-span sees the highest amount of load during bridge crossing, making it the most critical component of the structure and a candidate for risk reduction. Unknowns exist with respect to how load is actually distributed between the metal and composite when connected using bolts, as well as the failure modes which may result. To resolve these unknowns, a test program was started to assess the behavior of joints comprised of intermediate modulus carbon fiber composite components bolted to stainless steel components.

Approach:

In lieu of building a full scale structure, it was decided to exercise the critical behavior of the joint through component testing utilizing associated fixturing. Figures 1-2 shows the test article design and its derivation from the full Composite Assault Bridge design. The test article consists of a stainless steel hinge fitting bolted to an intermediate modulus carbon fiber composite tension rail. These components are then placed into a steel box used to approximate the joint's boundary conditions in the overall bridge structure. Based off of the results of Test 1 in April 2013, a simulated bulkhead was added to the steel box in October 2013 to provide additional resistance to vertical loads. Figure 3 shows the test specimen inside of the test box with the simulated bulkhead installed.

A finite element model was run to simulate the test results prior to each test. To run the model, assumptions were made with respect to the following aspects of the specimen:

- Fit of the tension rail in the slotted fitting and associated friction
- Fit of bolts in normal prep holes and minimal torque
- Fit of pins in multi-lug hole and associated friction
- Geometric variations within practical tolerances
- Clearance of side walls away from the box structure and of assembled test specimen from steel box bottom plate/ rails (areas where bearing on steel is possible)
- Clamp up forces at minimum torque.

The model also included displacements which were imposed to test frame interfaces.

Figure 4 shows the full test specimen placed onto a 3000-kip Southwark-Emery universal testing machine at the University of Illinois Urbana-Champaign's Talbot Laboratory. The steel box attached to the testing machine through the use of a pair of loading tangs and a link adapter which were originally designed for the Advanced Modular Composite Bridge (AMCB), a previously completed program performed by Seemann Composites.

The test machine applies an axial tension load to the test article, and the test box reacts this load to the test specimen through a double shear, bolted connection. Within the test box, the test specimen is oriented at an angle of approximately 4 degrees with respect to the pull load to more accurately simulate the loads seen in the full bridge. This orientation also introduces an out-of-plane load to the specimen.

Each test consisted of seven test runs performed at the following load levels:

- Run 1: Up to 70 kips for System Checkout
- Run 2: 50% design load (175 kips)
- Run 3: 100% design load (350 kips)
- Run 4: 150% design load
- Run 5: 180% design load
- Run 6: 200% design load
- Run 7: Load specimen to failure

Visual inspections of the specimen were performed after each run. Cracking and other audible events were also listened for throughout testing. Strain, load and displacement were measured and recorded for each test.

Potential galvanic corrosion issues resulting from the joining of the carbon fiber reinforced polymer composite to a 17-4PH stainless steel plate using super-alloy A286 fasteners was also assessed in this effort. These materials are representative of the materials being used for the center joint of the bridge. Corrosion testing consisted of three phases: Phase 1, Phase 1.2, and

Phase 2. For Phase 1, a total of 51 samples were tested, consisting of the following three sample types:

- Type I – Bolt Plate (5 total)
- Type II – Flat Gap Coupon Assembly (40 total)
- Type III – Glass Veil Coupon Assembly (6 total)

Figures 6-8 show an illustration of each sample type. Type I samples were tested in accordance with ASTM G71, while Type II and III samples were tested in accordance with GMW14872. 120 cycles were performed for all sample types.

Phase 1.2 further investigated the galvanic corrosion performance associated with the fit of bolts within the bolt hole. Test specimens for this phase look similar to that shown in Figure 5, but include only tight and normal fits, as well as various treatments for the holes. In this phase, a carbon panel and an e-glass panel, which is used as a control panel, were tested. Figure 8 shows a schematic of the carbon fiber test panel, while Figure 9 shows a picture of the actual carbon test panel. The e-glass panel does not include any coatings in the holes. Immersion testing of these panels was performed in accordance with ASTM G71, with the panels tilted 10 degrees from vertical to ensure that the loose bolt slugs touch the hole wall. Salt-spray testing performed in this phase was done in accordance with GM14872, with the panels tilted at 30 degrees from horizontal.

Phase 2 of the corrosion investigation aimed to look at the corrosion performance of the multi-material system in an assembly made to simulate the joint assembly within the Composite Assault Bridge design. Similar to Phase 1.2, carbon fiber test articles were fabricated, along with an e-glass article which was used as the control. The carbon fiber test articles were either preloaded to 70,000 lbs. while making up the bolts or unloaded. Figure 10 shows a schematic of each test article, while Figure 11 shows the actual carbon test article. All test articles in this phase were tested in accordance with GM14872, with the panels tilted 30 degrees from horizontal.

Results and Discussion:

During FY17, work continued to progress on the development of the center joint of the bridge. A test was performed in December 2016 on a modified Military Load Class (MLC) 85 test article. This test article is of similar design to that shown in Figure 3, but also included a number of design changes to address lessons learned from the previous center joint tests. The test article also includes design changes made to accommodate MLC 120 loads, but scaled down to fit the MLC 85 test article. The composite behaved as predicted and did not show any evidence of damage when loaded up to overload (1.33 times the design load) or ultimate load (1.5 times the design load), while the steel began to show the onset of yielding at ultimate load. The specimen eventually failed at a load of 788 kips due to net section failure of the composite tension rail. However, failure occurred where the specimen bolts into the steel box fixture, not at any of the detailed design features of the hinge assembly. Post-test inspections performed after disassembling the test specimen found the following:

- Permanent deformation of ½ inch bolts due to shear and bending, indicating that ultimate shear failure was close to occurring
- Modest indication of shear yielding in 5/8 inch bolts
- Limited bearing degradation in composite bolt holes
- Minimal steel bolt hole elongation
- Tension rail/ side wall delamination

While failure modes of the hinge assembly design were not determined from this test, this test demonstrated the strength of a number of design elements and identified a number of implications relative to accommodating the higher MLC 120 load. Fatigue testing was also performed on laminates being considered for the bridge design. All panels were tested in the 0 degree primary fiber direction, while side wall laminates were also tested in the 90 degree direction. Specimens were tested at various load levels, ranging from 40% of the maximum ultimate strength to 75% of the maximum ultimate strength. It was observed that the specimens generally bowed outward in the gage region prior to experiencing fiber failure.

After this test, work began on the design of a center assembly test article. This test article, shown in relation to the overall bridge length in Figure 12, is approximately 57% of the total bridge length and differs from the previous test articles in that it not only tests the center hinge design, but also tests the interfaces between the center hinge and other critical elements of the bridge design. Design of the test article was completed just prior to the completion of the contract. Test article drawings and CAD files were delivered to the Government, as well as a 3-D printed model of the test article.

Work also continued on the investigation of potential galvanic corrosion issues associated with the joining of composites to 17-4PH steel using A286 fasteners. Phase 1 of the corrosion study, which consisted of coupon-level testing, completed early in FY17. From this test, the following observations were made:

- Little material loss results for uncoated A286 fasteners in loose contact with uncoated carbon fiber composite surfaces under both salt spray and submerged conditions
- A286 experiences some material loss under both salt spray and submerged conditions in tight fit holes. The material loss was attributed to the combination of the A286 surfaces not being passivated and the breaking down of the epoxy coating, used to coat the carbon fiber holes, in a high temperature environment.
- Polymeric coatings on the bolts did not perform as well as expected, with respected to corrosion prevention
- 17-4PH steel exhibited galvanic corrosion when placed in contact with carbon fiber composites without a glass veil, but did not exhibit galvanic corrosion when the carbon fiber composite had a glass veil on its surface.

Phase 1.2, which consisted of the testing of Bolt Gap Corrosion panels, and Phase 2, consisting of Full-Scale Joint test articles, was also performed during FY17. Articles for each phase were scheduled for exposure for a total of 120 days. However, due to delays associated with design and fabrication of the test article, testing was unable to be completed before the end of the contract. Shown in Figures 13-14 are Phase 1.2 and Phase 2 test articles after 60 days of exposure. At this time, it was believed that the 17-4PH was the cause of the majority of the oxidation observed in the test articles, due to it being the most anodic of the materials. It is noted that these tests include more than 2 different materials in the galvanic reaction process

Conclusions:

Based upon the work performed in FY17, the following conclusions can be made:

- Multi-material component assemblies, consisting of carbon fiber composites and steel, have the potential to be able to carry a high load, making them useful for various applications such as bridging
- How well a bolt fits into a bolt hole will affect the galvanic reaction results observed when exposed to a corrosive environment
- Glass veil surface treatment on carbon fiber composites may help to prevent galvanic corrosion effects from occurring on steel

The contract for this effort ended at the end of FY17. No future work is planned.

References:

[1] Test Report, MSC TPR 21836/IN45, CJAB Critical Joint Test Report – Round 4, February 2017

[2] Status Report, MSC SAR010-17, CJAB Center Assembly Test Article Design, 31 March 2017

[3] Test Report, MSC SAR004-17, CJAB Fatigue Testing Summary for Defined Laminates

[4] Status Report, Composite Joint Assault Bridge, Contractor’s Progress Status and Management Report for April 2017, 8 May 2017

[5] Status Report, Program Status Update, 27 July 2017

[6] Status Report, CJAB Corrosion Study Phases 1.2 and 2 60-cycle Status Update, 28 August 2017

Figures and Tables:

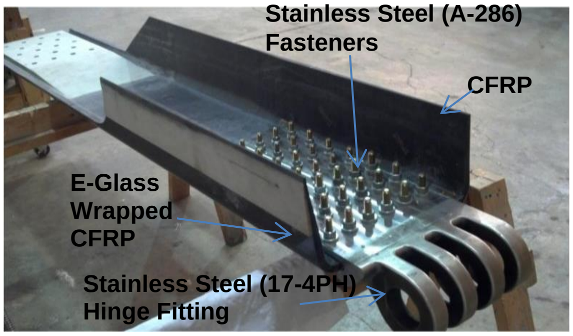

Figure 1: Joint Test Specimen

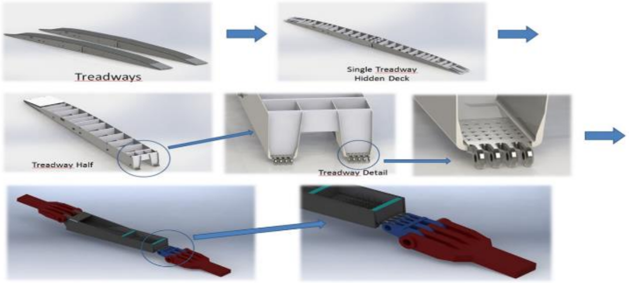

Figure 2: Derivation of Test Specimen from Bridge Design

Figure 3: Joint Test Specimen within Steel Box

Figure 4: Test Specimen Installed In Test Machine

Figures Continue on Next Page

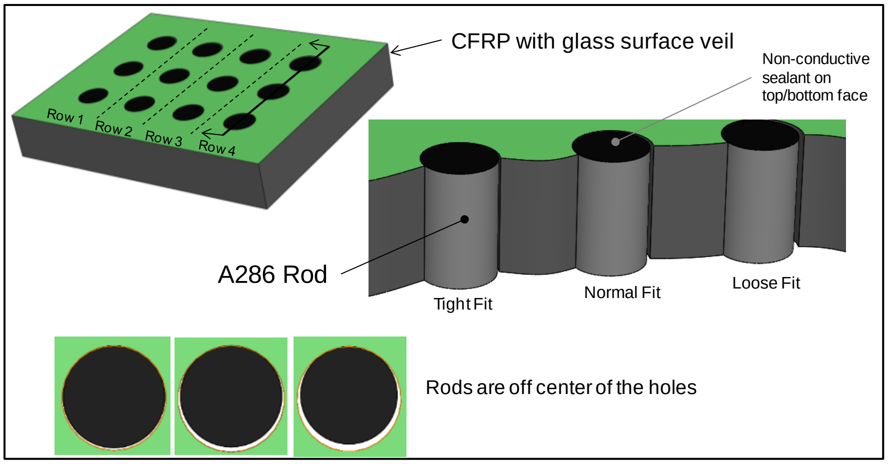

Figure 5: Type I - Bolt Plate Corrosion Test Sample

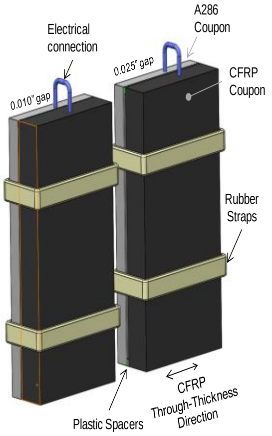

Figure 6: Type II - Flat Gap Coupon Assembly

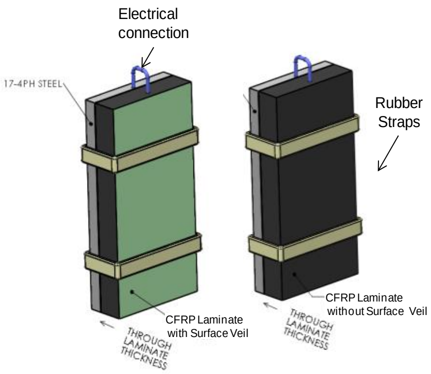

Figure 7: Type III- Glass Veil Coupon Assembly

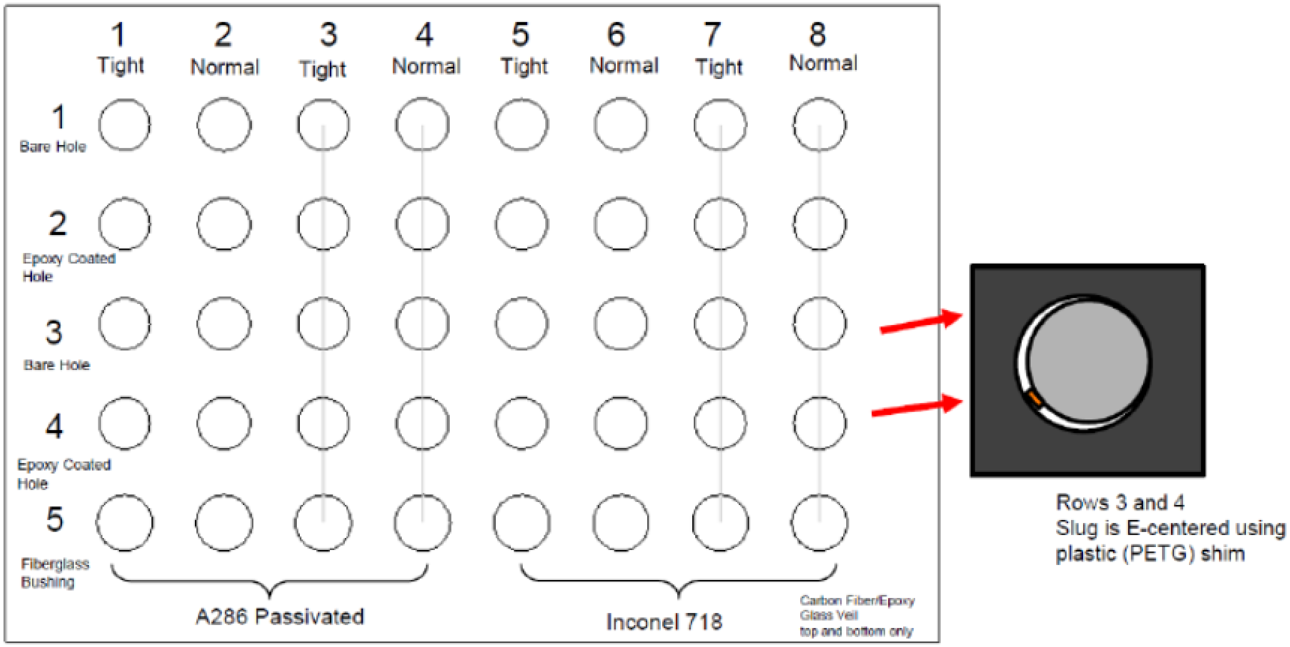

Figure 8: Corrosion Test Phase 1.2 Carbon Fiber Test Article Schematic

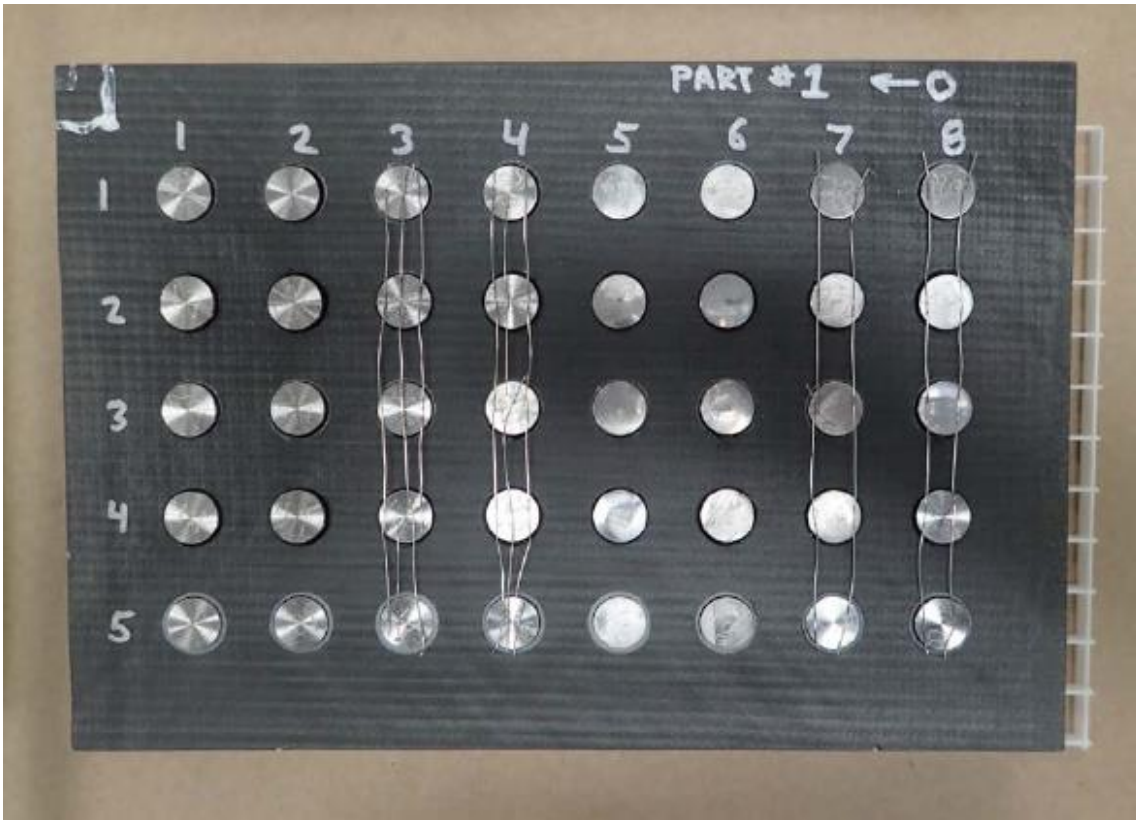

Figure 9: Corrosion Test Phase 1.2 Carbon Fiber Test Article

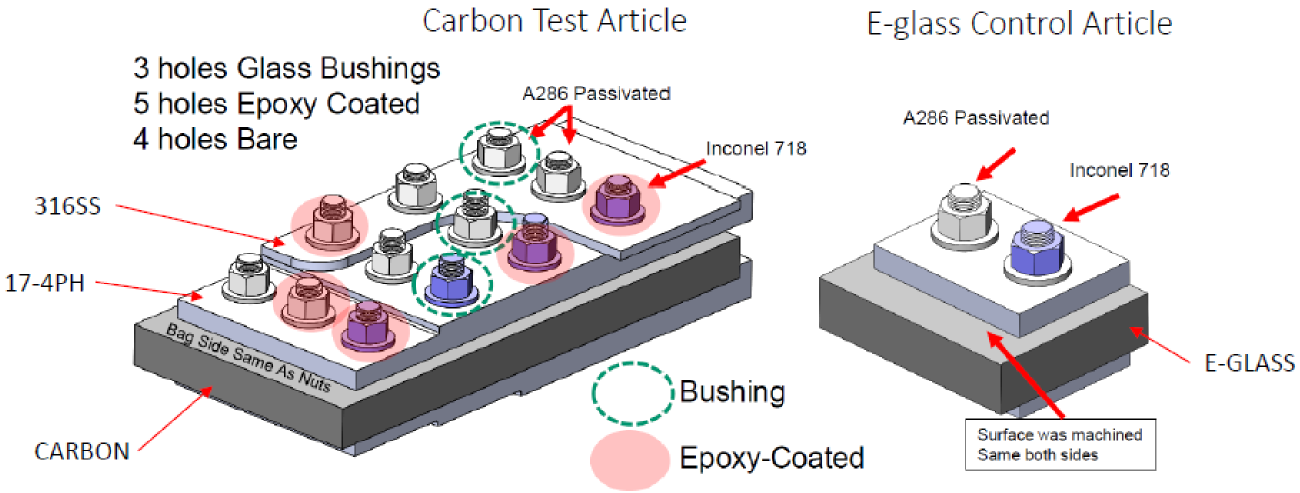

Figure 10: Phase 2 Corrosion Test Article Schematic

Figure 11: Carbon Fiber Phase 2 Corrosion Test Article

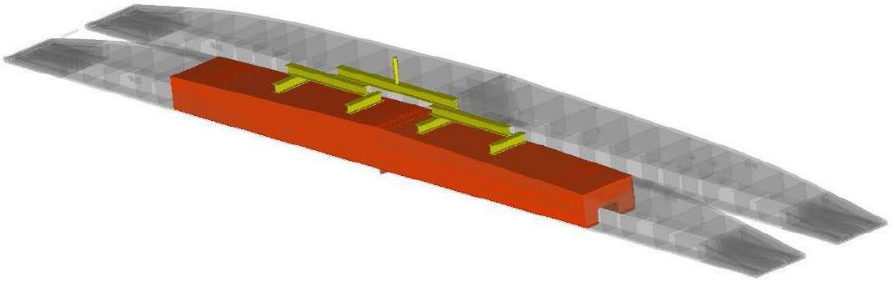

Figure 12: CJAB Critical Element Test Article, Shown Relative to the Full-Length of the Bridge

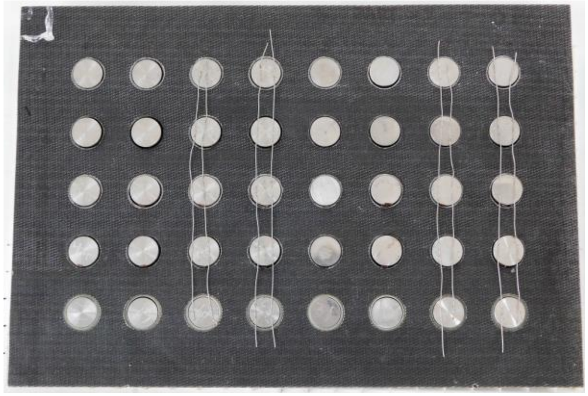

Figure 13a) Immersion Test Article After 60 Days Exposure

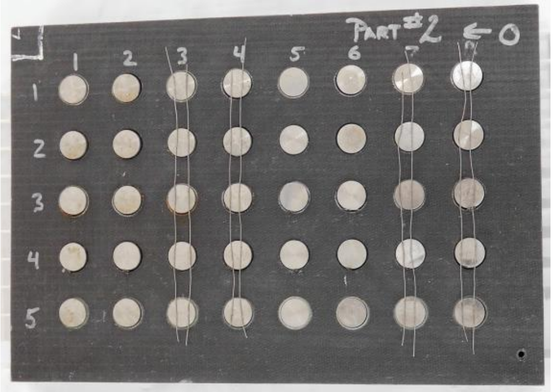

Figure 13b) Salt Spray Test Article After 60 Days Exposure

Figures Continue on Next Page

Figure 14: Corrosion Test Phase 2 Test Article After 60 Days Salt Spray Exposure

Remainder of Page Intentionally Blank

AVPTA Technology Focus Area #2: Lightweight Structures and Materials

Breakthrough Techniques for Dissimilar Material Joining - Thick Section Scribe for Dissimilar Aluminum-Steel Joints

DOE-VTO TFA Lead: Sarah Ollila
TARDEC TFA Lead: Ravi Thyagarajan

Principal Investigator:
Dr. Scott Whalen
Pacific Northwest National Laboratory
902 Battelle Blvd.
P.O. Box 999, MSIN K2-03
Richland, WA 99352

Project Start: Nov 2015
Estimated Completion: Q1FY19

Objectives:

- Develop solid-phase technologies that enable joining of Rolled Homogeneous Armor (RHA) to Blast Grade Aluminum for lightweight armor applications.
- Improve joint strength compared to conventional fusion and state-of-the-art friction stir approaches that rely exclusively on intermetallic bonding as the only joining mechanism.
- Utilize novel temperature control algorithms and spray-cooled thermal boundary conditions to tailor material properties of the joint.
- Reduce tool cost by orders of magnitude compared to current friction stir approaches.
- Characterize process window and repeatability to ultimately define a specification.

Strategic Context:

- This strategic input area directly addresses two of the eight areas from the Training and Doctrine Command's (TRADOC) Science and Technology (S&T) "Big 8" capabilities. Combat Vehicles (CVs) and Advanced Protection are two of the areas. This project pertains to those areas in the context that multi-material joining is a key enabler to light-weight CVs without diminishing protection.
- This input area could also be applied to Expeditionary Mission Command, Future Vertical Lift and Robotics and Autonomous Systems (RAS) capabilities.
- The Army's modernization priority of mobility, lethality and protection of brigade combat teams is another strategic input area that this technology can also be applied to.

Accomplishments:

- Invented a new process for joining aluminum to steel, called "Friction Stir Dovetailing (FSD)", which combines mechanical interlocking with metallurgical bonding. US Patent Application 15,694,565 "System and Process for Joining Dissimilar Materials and Solid-State Interlocking Joint with Intermetallic Interface Formed Thereby".
- Developed novel and inexpensive FSD tooling and process conditions for 1) creating mechanical interlocks between RHA (MIL-DTL-12560J) and aluminum (AA6061-T6) which are 2) rereinforced by thin metallurgical bonds formed in situ to the process.
- Implemented simultaneous force and temperature control algorithms to reduce heat input and control thickness of deleterious FeAl intermetallics to less than 200 nanometers.
- Achieved superior lap shear strength and strain-at-failure in thick sections compared to conventional fusion and state-of-the-art friction stir approaches.
- Demonstrated FSD for aluminum thicknesses up to 2.0" in AA6061-T6.
- Joined over 10 linear feet of 0.5" RHA to 1.0" AA6061-T6 in a lap configuration without visible signs of FSD tooling wear.
- Implemented spray cooling at University of South Carolina to minimize degradation of material properties in the aluminum Heat Affected Zone (HAZ).
- Performed corrosion study at Oregon State University using Scanning Vibrating Electrode Technique (SVET) and determined that thin intermetallic layers reduce galvanic corrosion between RHA and AA6061-T6.
- Multi-pass FSD joints achieved failure into the HAZ of the bulk aluminum.
- Published: Reza-E-Rabby, K. Ross, S. Whalen, Y. Hovanski, M. McDonnell, "*Solid-State Joining of Thick-Section Dissimilar Materials Using a New Friction Stir Dovetailing (FSD) Process*," Friction Stir Welding and Processing IX, 67-77, 2017. Paper presented at TMS annual conference.

Introduction:

Reducing the weight of military vehicles to increase energy efficiency, agility, and mobility [1] can be accomplished by replacing steel components with aluminum (Al). This requires the ability to join metals with vastly different material properties and has led to the investigation of numerous alternative joining techniques [2]. Joining Al to steel is particularly difficult due to large differences in material properties such as melting temperature, density, coefficient of thermal expansion, and flow stress that govern fusion and friction-based welding. In addition, a high chemical affinity with limited solubility also encourages the formation of intermetallic compounds (IMCs), which typically result in brittle failure of the joined parts [3]. Although a large body of work exists for metallurgical friction-based joining of Al to steel, only a few studies report data for Al or steel thicknesses exceeding 6 mm [4-6]. This is primarily because 1) friction techniques for joining thin sheets do not generally scale well for thick plates and 2) these approaches suffer from uncontrolled growth of FeAl intermetallics which result in brittle failure modes [7-9]. Cost is also an issue with exotic tool materials having complex features being required for friction stir approaches. The challenges for joining Al to steel are magnified when thick structures are required, such as those utilized in military combat vehicles and mobile structures. In light of these challenges, FSD has been developed as a new technique for low cost joining thick section aluminum to steel.

Approach:

In FSD, mechanical interlocks are formed between the Al and steel, which are further reinforced by metallurgical bonding created in situ during joining [10]. In this work, FSD is demonstrated for AA6061-T651 joined to Rolled Homogeneous Armor (RHA) MIL-DTL-12560J [11] in a lap configuration. During FSD, Al is extruded into dovetail grooves pre-machined on the surface of the underlying steel forming a mechanical joint, while engagement of a Tungsten-Carbide (WC) tip along the Al-RHA interface results in metallurgical bonding within the dovetail. To achieve this dual effect, a specialized FSW tool is utilized that 1) promotes plastic deformation of Al into the dovetail groove while 2) simultaneously heating the Al-RHA interface to drive interdiffusion and formation of an interlayer.

Figure 1 illustrates the FSD technique in a lap configuration with a single dovetail groove cut into the RHA. The H13 tool contains a WC insert embedded within the tool tip and type-k thermocouples are soldered at the locations indicated for the purpose of controlling temperature to limit intermetallic formation. Threads on the pin are designed to force material into the dovetail while scrolled features on the shoulder gather material to avoid formation of surface defects and interior wormholes.

RHA was cut into individual plates measuring 150 mm x 300 mm and dual disc ground to a thickness of 12.70 mm. These plates were then machined with dovetail and rectangular trench grooves. Dovetail grooves had a tail width of 14.22 mm, depth of 2.54 mm, and 60° root angle along the entire 300 mm length of the RHA plate. Rectangular trench grooves had a width of 11.73 mm and depth of 2.54 mm. Al plates were machined to 150 mm x 300 mm x 12.70 mm. RHA and Al plates were then clamped in a lap configuration to the work deck of a Transformation Technologies, Inc. (TTI) ultra-high precision friction stir welding machine. FSD was preformed using a tool made from H13 tool steel hardened to 45-48 HRC. The tool consists of a convex scrolled (3.18 mm/revolution) shoulder (38.1 mm diameter) and a frustum shaped (6.1°) threaded (2.12 mm/revolution) pin (15.85 mm diameter near the shank and 11 mm length) with 3 flats (120^0 apart). A two flatted WC insert (7.94 mm diameter, cylindrical) was embedded within the pin and extends 3.18 mm from the tip. An example of the FSD tool geometry and thermocouple locations are shown in Figure 2. Even in small batches of 10 tools per order, these FSD tools cost just $500 dollars each including thermocouple instrumentation. Four joining trials (A, B, C, and D, as described in Table 1) were investigated to determine the impact of geometry and process variables on lap shear strength and interlayer formation. All trials were performed in electronic displacement control mode at a constant welding speed of 76.2 mm/min. The temperature at the WC tip was controlled at ~470°C by dynamically modulating the spindle torque using a temperature control algorithm [12]. The tool plunge depth was precisely controlled in order to regulate contact between the WC and RHA. Figure 3 shown the lap joint configuration and path of tool travel.

Table 1 summarizes the primary process parameters for the four different joining trials. For trial A, engagement between the WC insert and RHA was intentionally avoided to prevent formation of an interlayer, thereby isolating the effect of mechanical interlocking (i.e., no metallurgical bonding). For trial B, the WC tip engaged the RHA plate, without a dovetail, to isolate the effect of metallurgical bonding (i.e., no mechanical interlocking). The configuration of trial B is similar to the popular Al-steel lap joint approaches found in the literature [8-10] and is used for comparison in this study. For trial C, the effects of mechanical interlocking and metallurgical bonding are combined by engaging the WC tip with the RHA along the base of the dovetail groove. Trial D is similar to trial C, except a rectangular trench is utilized rather than the dovetail geometry. The process parameters used in trials B–D were developed to limit interfacial layer formation in order to reduce joint embrittlement. Tanaka et al. reported an exponential increase in joint strength as IMC thickness decreased, with IMCs <100 nm exhibiting the highest tensile strength for AA7075/mild steel FSW butt joints [3]. As such, process parameters were optimized to achieve IMC thicknesses in the 100 nm range.

The AL-RHA plates from each joining trial were sectioned perpendicular to the tool path via water jet to produce 13 mm wide lap joint specimens with a gage length of 127 mm as shown in Figure 4. Room temperature lap shear tensile testing was performed on six specimens from each joining trial at an extension rate of 2.54 mm/min using a 50 kip MTS test frame. Metallographic specimens from neighboring faces were then prepared via sectioning and epoxy mounting with a final surface finish established using 0.05 µm colloidal silica. Initial investigation of interfacial layer formation was performed using a JEOL 7600 field emission scanning electron microscope (SEM). A low angle Back-Scatter Electron (BSE) detector was utilized to examine the joint interfaces at various regions across the sample in low kV (5–8kV and a small probe) mode. Utilizing low kV, BSE analysis allowed for examination of the interface such that interlayer formation could be readily observed.

Results and Discussion:

Scanning Electron Microscope (SEM) montages and high resolution images showing the joint cross section and Al-RHA interface are visible in Figure 5 for all four joining trials. The joint overview images confirm that Al is fully extruded into the dovetail (trials A and C) and rectangular trench grooves (trial D). SEM micrographs in the interface overview, taken near the centerline of the Al-RHA interface, show distinct differences between the joining trials. For trial A, no metallurgical bonding is observed at the Al-RHA interface as evidenced by the ~45 µm gap between the Al and RHA. For trials B, C, and D, the SEM micrographs show a well-bonded interface with minimal interlayer formation. When present, interlayer formation for trials B and C exhibit non-uniform island-like growth with a maximum thickness of ~150 nm. The interfacial region of trial D shows no evidence of interlayer formation or banding of second phase dispersions. Partially formed layer structures as well as the absence of interlayer formation following friction stir joining have been reported in prior works [13, 14]. For regions where a distinct interlay is not observed, closure of the mated surfaces appears to be a result of local plastic deformation at elevated temperature, which has promoted interdiffusion across the interface. Given that the WC tip temperatures were nearly identical for all joining trials, this work supports the assertion of prior studies, that contact and engagement between the FSW tooling and steel is critical to controlling formation of metallic interlayers [15], likely due to the elevated temperature exposure of clean, un-oxidized steel resulting from intense local mixing at the interface.

The effect of mechanical interlocking and interlayer formation on joint strength was characterized by lap shear tensile testing. In Figure 6, the load-displacement curves for the four joining trials are shown with each curve representing the average of six specimens. The y-axis shows load normalized to the thickness of each specimen (i.e., load per unit weld length) and the x-axis shows linear displacement. The macro images below the graph show the failure morphology corresponding to each of the four joining trials. In these experiments, Al was tensioned to the left and RHA to the right.

Some general observations can be made from the data in Figure 6. Trial A has the lowest strength of the four trials and failed at the corner of the Al within the dovetail. For trial B, the maximum strength increased due to interfacial bonding compared to trial A, but exhibited more brittle behavior with significantly lower extension at failure. For trial C, combining a dovetail interlock (trial A) with a metallurgical bond (trial B) results in a significant increase in strength and extension, with failure in the Al occurring far from the Al-RHA interface. For trial D, the groove geometry was changed to a rectangular trench and exhibited somewhat lower performance than trial C. Clearly, the combined effect of mechanical interlocking and metallurgical bonding (implemented in trials C and D) results in higher strength and greater extension at failure than metallurgical bonding alone (trial B), which is the most popular approach to Al-steel friction stir welding. For trials C and D, regions where the WC insert did not contact the RHA near the groove corners are observed to pull up during lap shear testing due to a lack of metallurgical bonding. Table 2 summarizes the maximum load, extension at maximum load, and extension at fracture for the four joining trials. One standard deviation is indicated as ± in the table. Extension at fracture is defined as when the load has dropped to 70% of the maximum load.

Comparing trial B relative to trial A; the maximum load increases by 57% but the extension at fracture decreases by 60%, which is consistent with brittle interfacial bonding. For trial C, the maximum load increases by 109% and 34% compared to trials A and B, respectively, while extension at maximum load increases by 92% and 229%, respectively. Trial D has decreased strength and extension at failure compared to trial C, suggesting that the small amount of interlocking provided by Al in the corners of the dovetail grooves contributes substantially to joint performance. IMC layers were not resolvable by SEM for trial D and the interface exhibited a sharp transition between the Al and RHA. Novel temperature control algorithms that allow for precise control of the Al-RHA interface temperature is a key development toward limiting the formation of brittle intermetallic layers in this study. The FSD approach offers the potential for improved joint strength and extension compared to typical Al-steel friction stir joints, which suffer from unregulated formation of thick Inter-Metallic Compound (IMC) layers.

Due to the superior performance of trial C, a detailed Transmission Electron Microscope TEM investigation of the interlayer was performed to better understand the structure and composition profiles present across the Al-RHA interface. Overview Scanning Transmission Beam Microscopy Bright Field (STEM BF) images of the specimen (see Figure 7) reveal the presence of a refined dispersion of second phase material that extends ~1.5 µm into the aluminum layer from the Al-RHA interface. STEM EDS across the interface illustrates the formation of a locally enriched Si-layer along the interface. This Si-rich layer, as measured via TEM, was found to have an average thickness of 40–70 nm in thickness. The composition of the layer was measured to be 76.4 at% Al, 18.4 at% Fe, and 5.2 at% Si (63.8 wt% Al, 31.8 wt% Fe, and 4.5 wt% Si).

STEM Annular Dark Field (ADF) imaging at elevated magnification indicates the structure of the IMC layer is polycrystalline. This observation was confirmed using Selected Area Diffraction (SAD). Due to the refined length scale of the IMC, SAD patterns appear to incorporate through thickness diffraction from multiple grains, in addition to super-lattice reflections. This observation is in contrast to prior studies on Al-steel systems that have reported the formation of an amorphous IMC layer [5]; however, it is consistent with multiple efforts that have revealed the presence of an $FeAl_3$ intermetallic formation at layer thicknesses greater than 0.5 µm [7]. The compositional information obtained in this work suggests the interlayer formation may be an $FeAl_3$ intermetallic layer with local silicon enrichment.

A key enabled for suppressing FeAl IMC growth is the ability to maintain a prescribed constant temperature at the WC tip (i.e. RHA-Al interface). Figure 8 shows typical data for shoulder temperature, WC tip temperature, and rpm as a function of tool traverse distance. It is seen that rpm (and thus torque) fluctuates in order to maintain a constant temperature. Some leveling of the control algorithm occurs at the beginning of the process but temperatures become quite stable after the first few inches. It has also been shown that multi-pass joint drive failure into the HAZ of 0.5” thick Al (Figure 9). Models are currently being developed and validated for use in predicting how thick of Al can be support depending on dovetail geometry and number of passes. The strength of the metallurgical bond has been tested via mini-tensile specimens cut by Electron Discharge Machining (EDM) from the dovetail joint as shown in Figure 10. A total of 21 specimens were tensile tested and all specimens failed on the bulk aluminum, likely O-tempered after processing, within the dovetail joint. No failures occurred at the metallurgical bond and this result has been used to justify the assumption of “tied” nodes at the RHA-Al interface for modeling purposes. A paper based on these mini-tensile tests, modeling, and experimental validation is forthcoming.

Corrosion testing was performed by Oregon State University for the purpose of determining if the presence of a metallurgical bond impacted corrosion rate. Corrosion testing via the Scanning Vibrating Electrode Technique (SVET) was conducted on dovetail specimens with a 1 micron metallurgical bond thickness (Sample B), 2-3 micron metallurgical bond thickness (Sample C) and no metallurgical bond present (Sample A). In short, the presence of a metallurgical bond reduced current density in the aluminum (i.e. corrosion rate) compared to when no metallurgical bond was present. A final report describing the details of the corrosion study is prepared and available upon request. A summary of the results is shown in Figure 11.

In addition to FSD, an additional process called Friction Stir Interlocking [16] has been developed as an alternative means of joining dissimilar materials using strictly mechanical interlocking. In FSI, aluminum or steel pins are embedded within the RHA that is contained by a C-shape aluminum piece. A conventional FSW tool either 1) processes an aluminum pin as part of the C-shaped aluminum piece (Figure 12) or 2) processes an aluminum plug to retain the steel pin within the assembly (Figure 13). Figure 14 shows data for the aluminum and steel pin approaches. The advantage of such an approach compared to bolting is that 1) many joints can be formed simultaneously and 2) corrosion can be greatly decreased because the RHA-Al joint can be sealed from electrolyte imbibition. Such sealing is not possible with conventional bolting.

Conclusions:

Based on the mechanical and microstructural data, it can be concluded that FSD is a promising new technique for joining thick section Al-steel. SEM and TEM results of the Al-RHA interface have confirmed the presence of a sub-micron interlayer formation, likely $FeAl_3$. The ability to inhibit the growth of IMC layers during joining has been demonstrated, and is in contrast to popular friction stir approaches that suffer from unregulated formation of thick intermetallic layers at the Al-steel interface. As a result, the simultaneous mechanical interlocking and metallurgical bonding leads to improved strength and a large increase in strain-at-failure. Tools have been developed with the potential for low cost, even in small quantities. Novel temperature and force control algorithms are enabling technologies for realizing the FSD process. A simple Friction Stir Interlocking (FSI) technique may also be useful for applications such as bridges and other heavy-duty structures.

References:

[1] E. Polsen, L. Krogsrud, R. Carter, W. Oberle, C. Haines, A. Littlefield, Lightweight Combat Vehicle S and T Campaign, US Army TARDEC/Ground System Survivability Warren United States, 2014.
[2] K. Martinsen, S. Hu, B. Carlson, CIRP Annals-Manufacturing Technology 64(2) (2015) 679-699.
[3] T. Tanaka, T. Morishige, T. Hirata, Scripta Materialia 61(7) (2009) 756-759.
[4] T. Nishida, T. Ogura, H. Nishida, M. Fujimoto, M. Takahashi, A. Hirose, Science and Technology of Welding and Joining 19(7) (2014) 609-616.
[5] T. Ogura, Y. Saito, T. Nishida, H. Nishida, T. Yoshida, N. Omichi, M. Fujimoto, A. Hirose, Scripta Materialia 66(8) (2012) 531-534.
[6] E.E. Patterson, Y. Hovanski, D.P. Field, Metallurgical and Materials Transactions A 47(6) (2016) 2815-2829.
[7] K. Kimapong, T. Watanabe, Materials transactions 46(4) (2005) 835-841.
[8] R.P. Mahto, R. Bhoje, S.K. Pal, H.S. Joshi, S. Das, Materials Science and Engineering: A 652 (2016) 136-144.
[9] Y. Wei, J. Li, J. Xiong, F. Zhang, Journal of materials engineering and performance 22(10) (2013) 3005-3013.
[10] K.Ross, Scott Whalen, Md Reza-E-Rabby, Yuri Hovanski, US Patent Application No. 15/694,565, Systems and Process for Joining Dissimilar Materials and Soli-State Interlocking Joint with Intermetallic Interface Formed Thereby, Battelle Memorial Institute, 2017.
[11] U.S. Army Research Laboratory, Weapon and Materials Research Directorate, Materials and Manufacturing Technology Branch, MIL-DTL-12560K(MR), Armor Plate, Steel, Wrought, Homogeneous (For use in Combat-Vehicles and for Ammunition Testing), Specifications and Standards Office, Aberdeen Proving Ground, MD, 7 Dec. 2013.

[12] K. Ross, C. Sorensen, Friction Stir Welding and Processing VII, Springer2013, pp. 301-310.
[13] H. Springer, A. Kostka, J. Dos Santos, D. Raabe, Materials Science and Engineering: A 528(13) (2011) 4630-4642.
[14] R. Marstatt, M. Krutzlinger, J. Luderschmid, M. Zaeh, F. Haider, Formation of a diffusion-based intermetallic interface layer in friction stir welded dissimilar Al-Cu lap joints, IOP Conference Series: Materials Science and Engineering, IOP Publishing, 2017, p. 012002.
[15] A. Elrefaey, M. Gouda, M. Takahashi, K. Ikeuchi, Journal of materials engineering and performance 14(1) (2005) 10-17.
[16] Scott Whalen, Md Reza-E-Rabby, Ken Ross, Aashish Rohatgi, US Patent Application No. 15/794,687, Friction Stir Interlocking of Dissimilar Materials, Battelle Memorial Institute, 2017.

Figures and Tables:

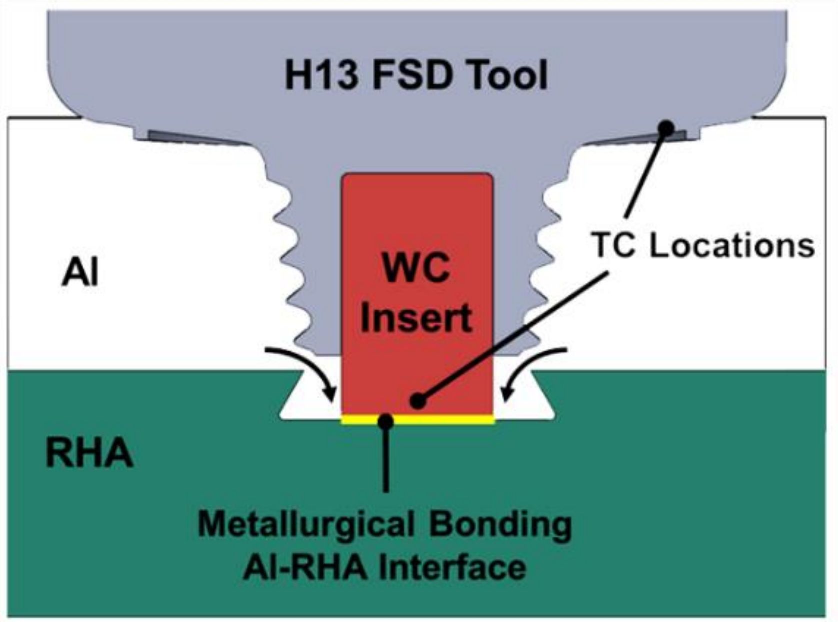

Figure 1. Illustration of FSD technique and tooling showing mechanical interlocking and metallurgical bonding in a dovetail groove.

Figures Continue on Next Page

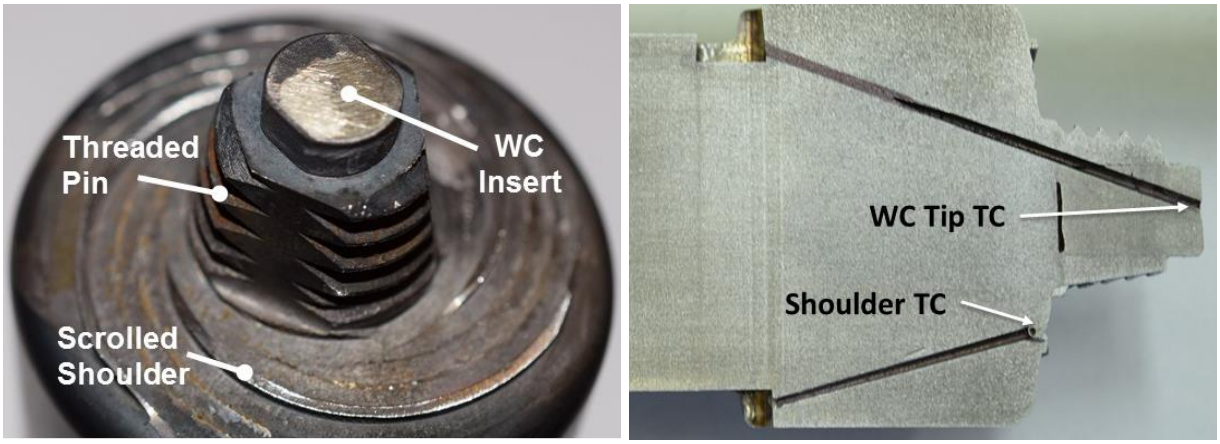

Figure 2. FSD tool showing threaded pin, 120 degree offset flats, scrolled shoulder, and tungsten-carbide insert for forming metallurgical at the RHA-Al interface within the root of the dovetail.
Thermocouple locations in the WC tip and shoulder are also shown.

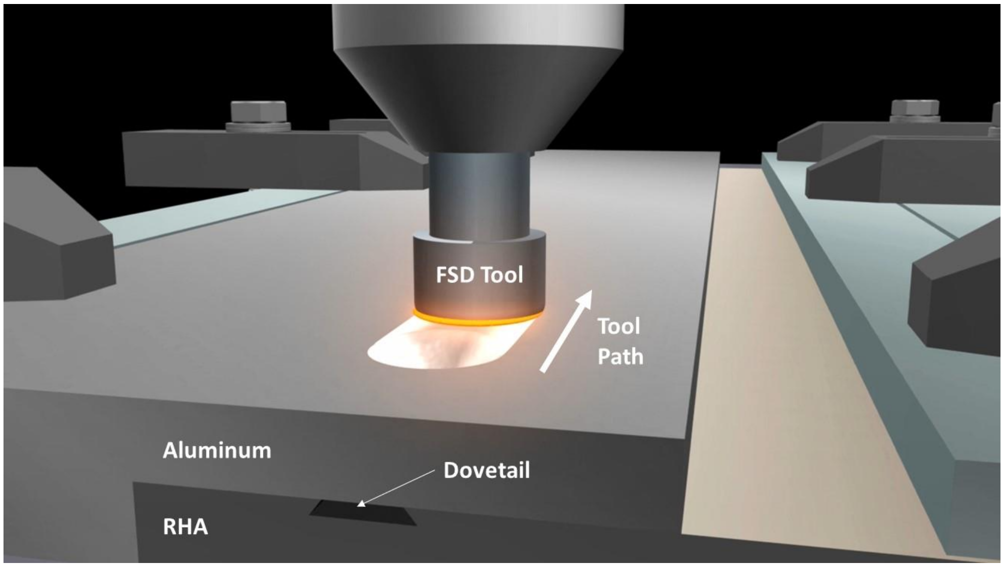

Figure 3. FSD lap joint configuration showing direction of tool path. As the tool traverses, the dovetail pre-machined into the RHA is 1) filled with aluminum to form a mechanical interlock while 2) simultaneously forming a thin metallurgical bond at the RHA-Al interface within the root of the dovetail.

Figures Continue on Next Page

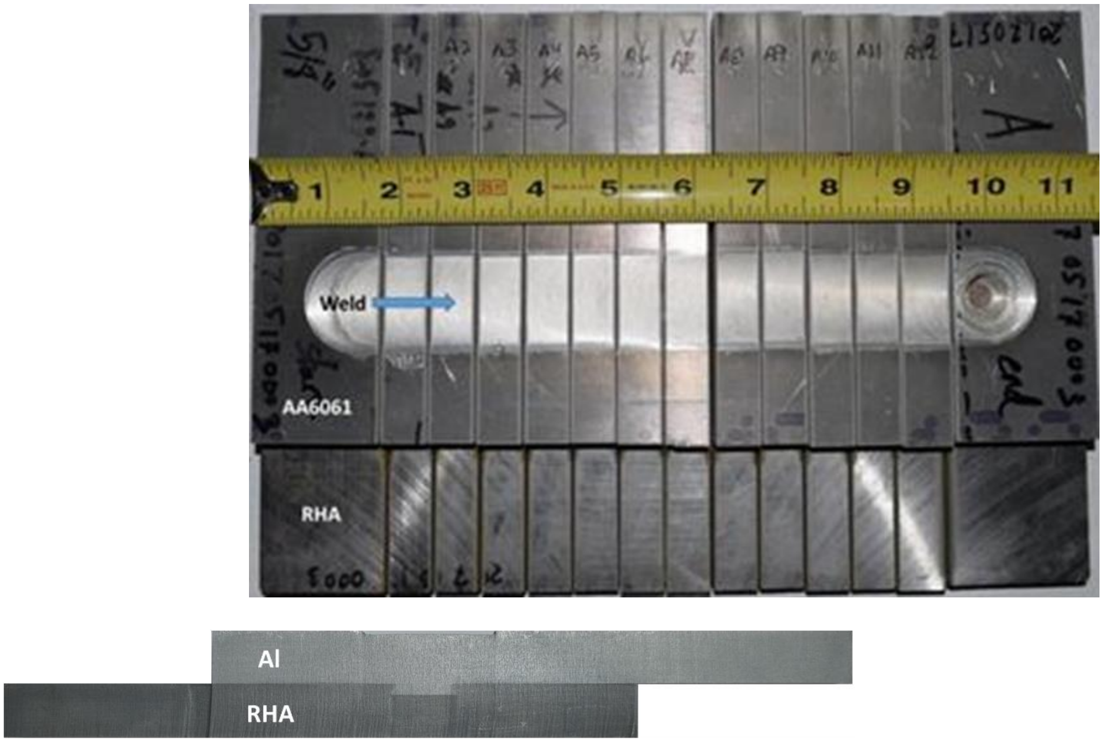

Figure 4. Lap shear specimen cut by water jet having a thickness of 13mm in the tool traverse direction.

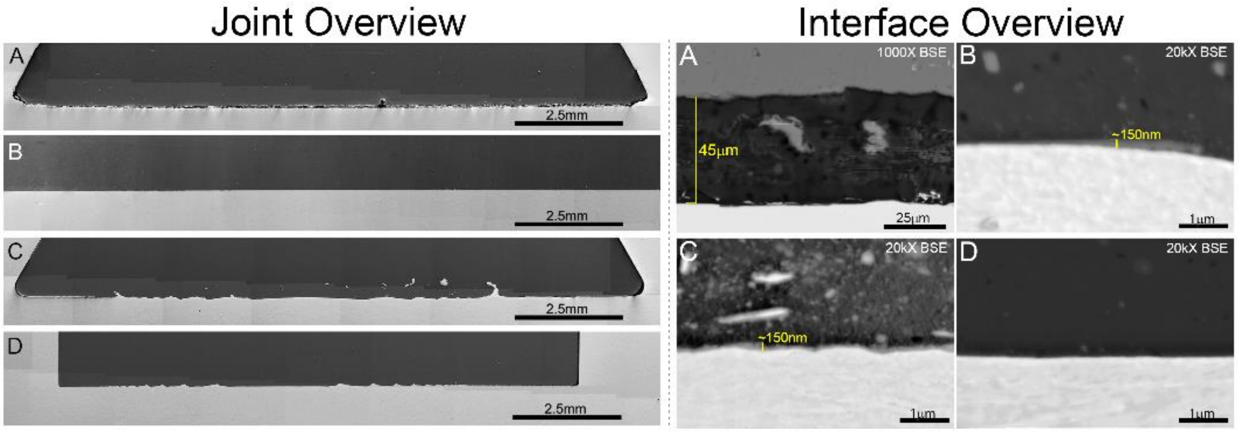

Figure 5. Transverse section SEM montage images of the joint region for trial A–D (left) and high resolution SEM micrographs along the Al-RHA interface (right).

Figures Continue on Next Page

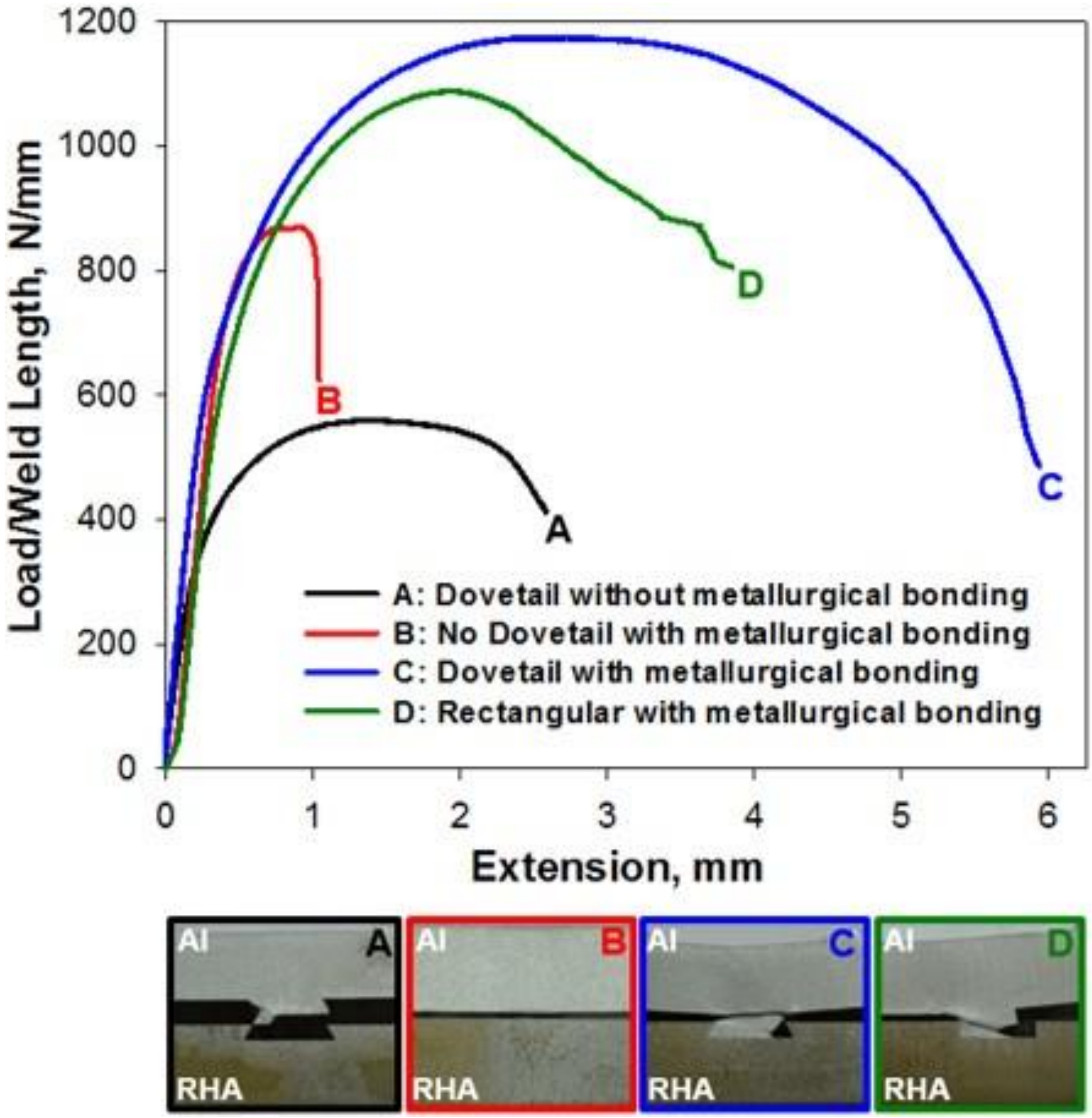

Figure 6. Load per unit joint length vs. extension for joining trials A, B, C, and D, along with their corresponding failure morphology.

Figures Continue on Next Page

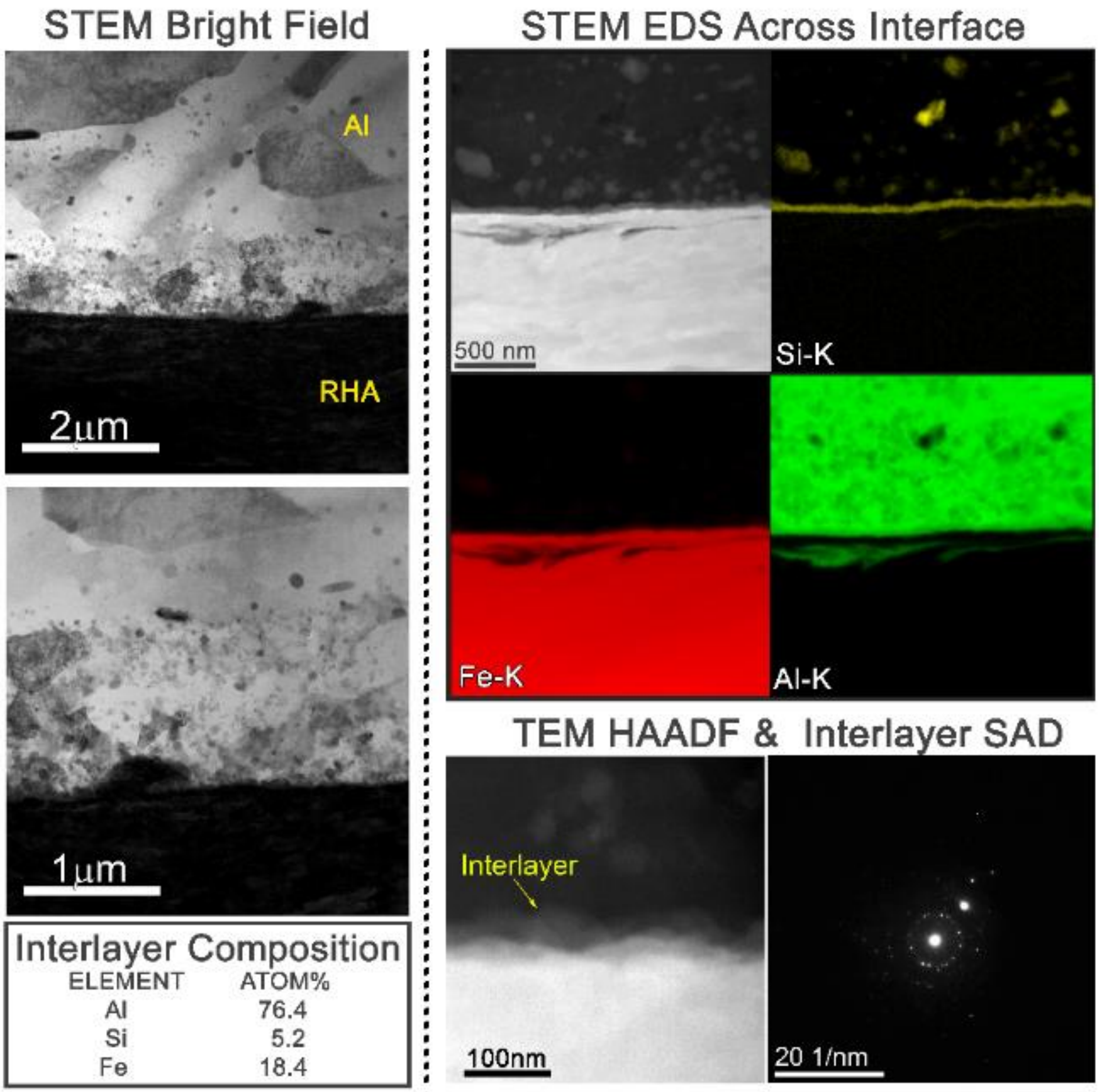

Interlayer Composition

ELEMENT	ATOM%
Al	76.4
Si	5.2
Fe	18.4

Figure 7. STEM results obtained from the Al-RHA interface show a banded layer of refined, Si-rich, second phase dispersoids along the interface extending ~1.5 µm into the Al layer. Formation of a crystalline, Si-rich intermetallic layer averaging 40–70 nm in thickness is also observed at the Al-RHA interface.

Figures Continue on Next Page

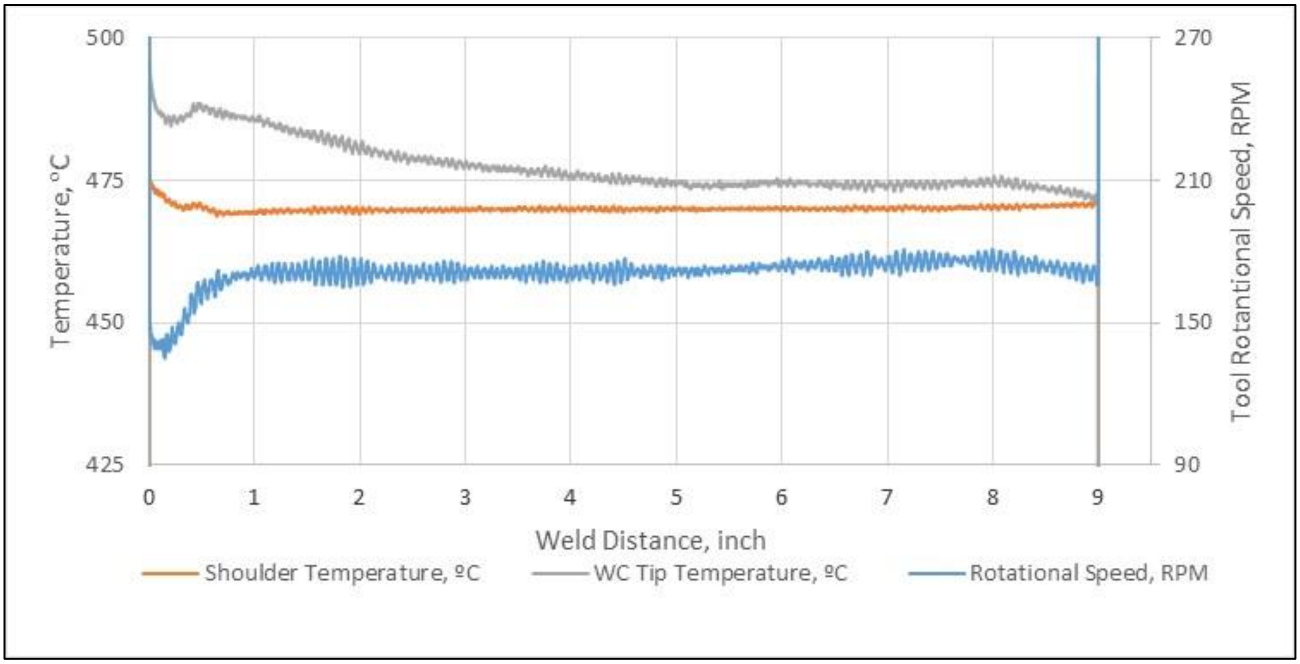

Figure 8. Example of data showing FSD tool tip and shoulder maintaining fairly constant temperature after the first three inches of joining.

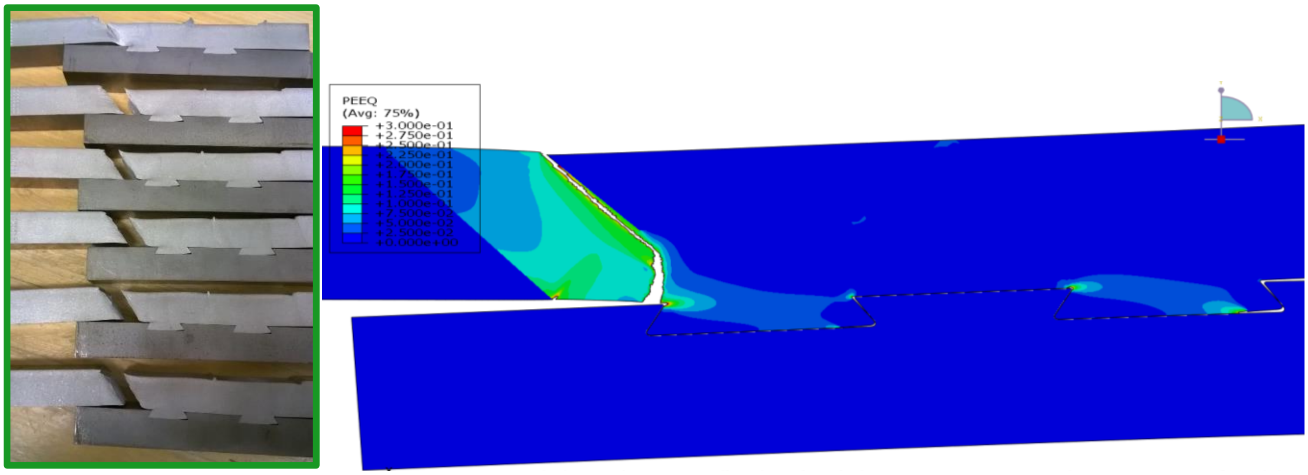

Figure 9. Multi-pass dovetail joints failing in HAZ of Al along with preliminary modeling results showing the same.

Figures Continue on Next Page

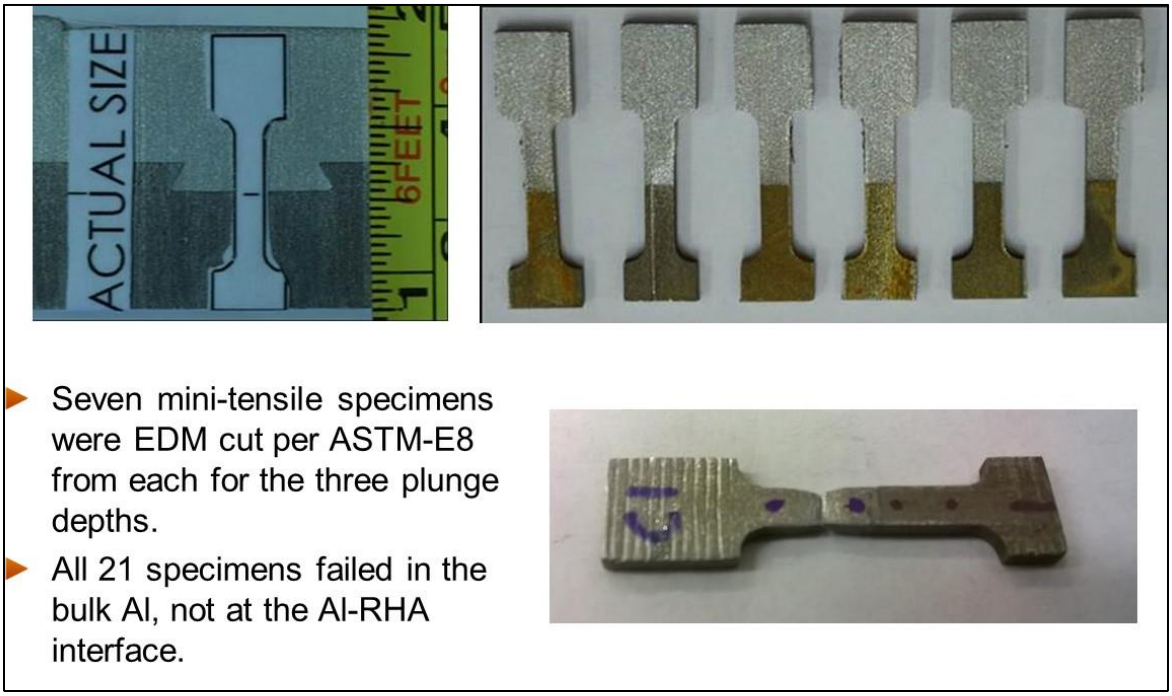

- Seven mini-tensile specimens were EDM cut per ASTM-E8 from each for the three plunge depths.
- All 21 specimens failed in the bulk Al, not at the Al-RHA interface.

Figure 10. Min-tensile test specimens of metallurgical bond showing that failure always occurs in the bulk aluminum within the dovetail joint.

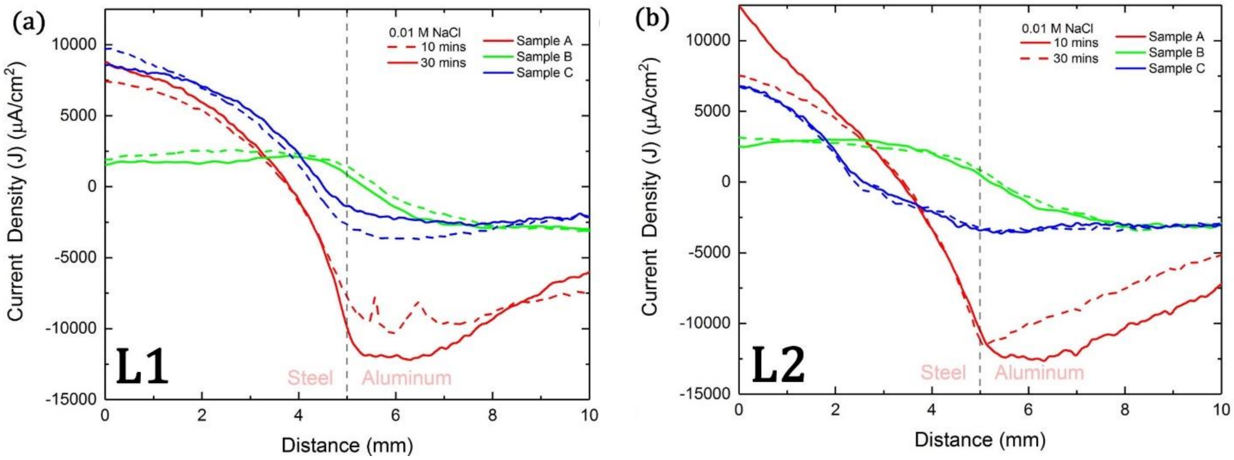

Figure 11. SVET scans showing lower corrosion current in the aluminum with the metallurgical bond present (i.e. samples B and C compare to A).

Figures Continue on Next Page

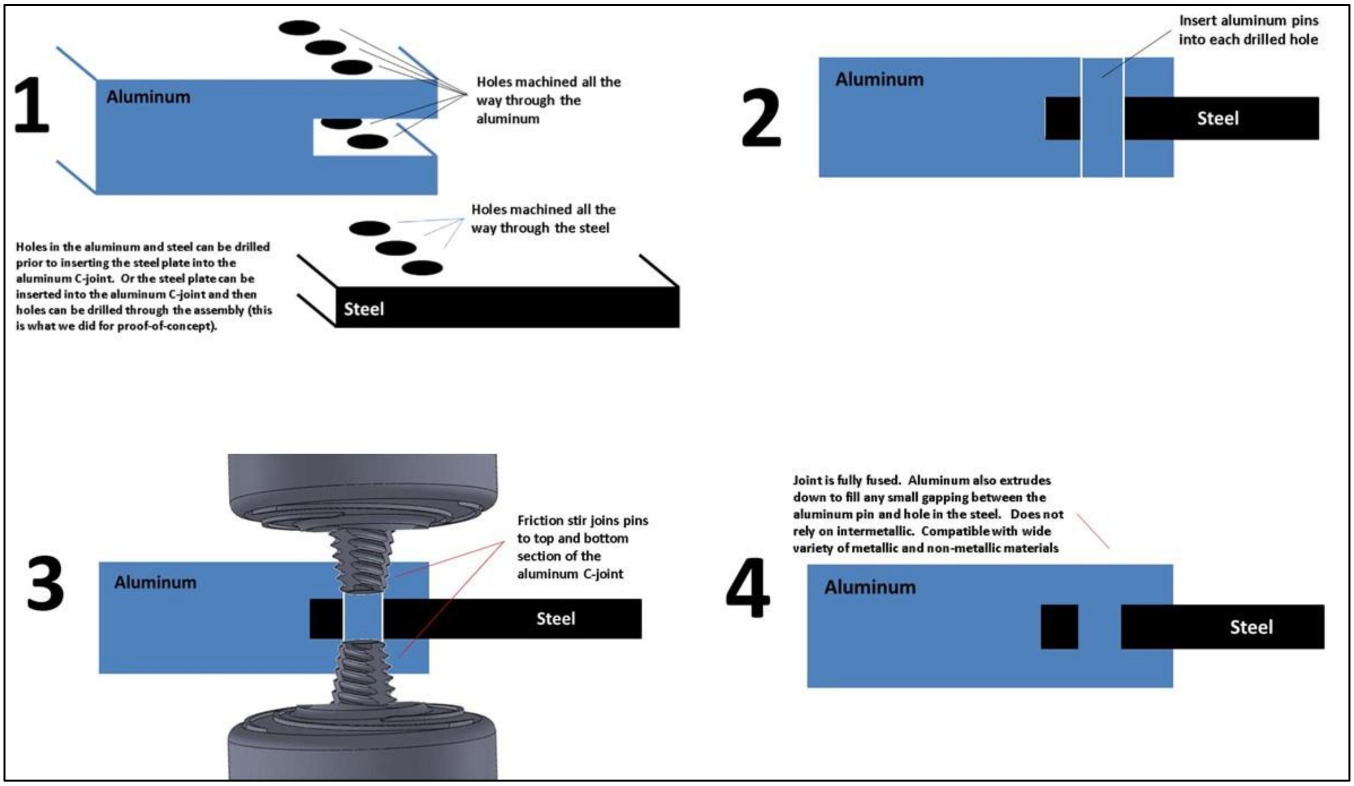

Figure 12. FSI with aluminum pin approach.

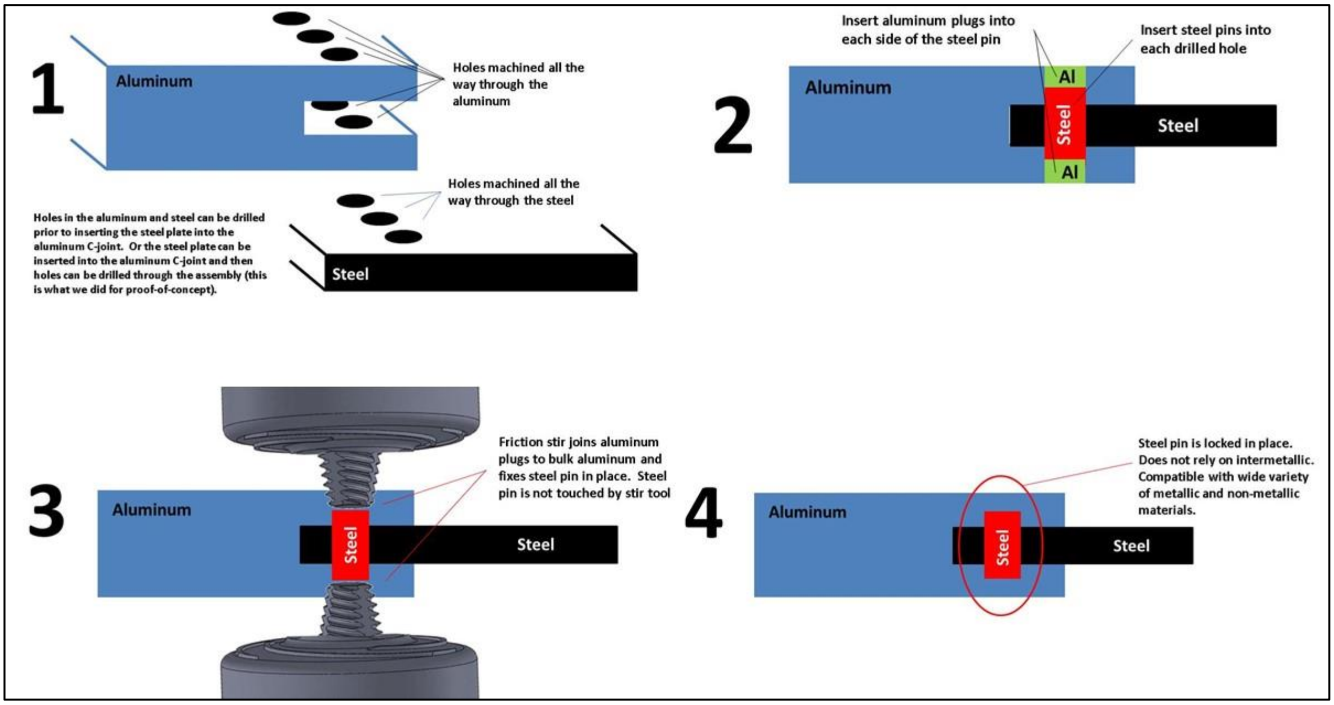

Figure 13. FSI with steel pin approach.

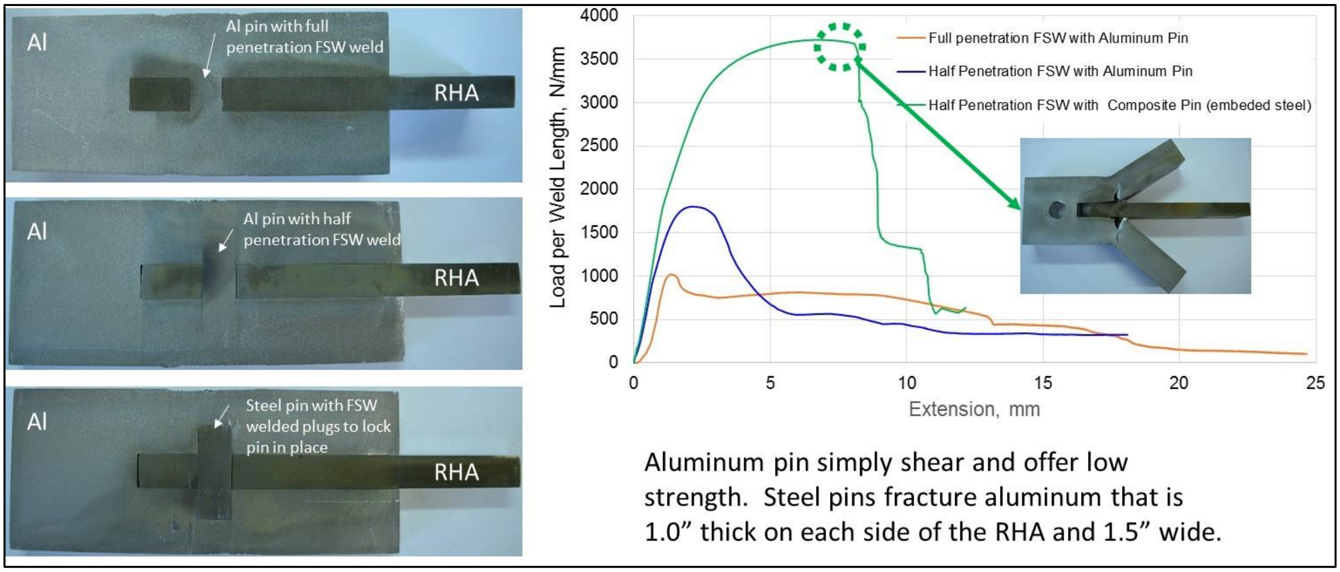

Aluminum pin simply shear and offer low strength. Steel pins fracture aluminum that is 1.0” thick on each side of the RHA and 1.5” wide.

Figure 14. FSI with steel pin approach.

Table 1. Process parameters for four different FSD joining trials.

Joining Trial	Lap Joint Configuration	Plunge Depth of WC into RHA	WC Tip Temperature	Tool Rotational Speed
	Interlock Geometry: Type	mm	°C	RPM
A	Dovetail: Mechanical Interlocking	-0.220	475	165
B	Flat Interface: Metallurgical Bonding	0.051	460	125
C	Dovetail: Interlocking + Bonding	0.051	485	150
D	Trench: Interlocking + Bonding	0.051	480	185

Table 2. Summary of lap shear tensile test data for joining trials A, B, C, and D.

Joining Trial	Maximum Interlayer Thickness	Maximum Load	Extension at Maximum Load	Extension at Fracture
	nm	N/mm	mm	mm
A	0	560 ± 6	1.42 ± 0.04	2.58 ± 0.05
B	~150	880 ± 23	0.83 ± 0.10	1.04 ± 0.13
C	~150	1175 ± 36	2.73 ± 0.26	5.94 ± 0.32
D	0*	1092 ± 33	2.03 ± 0.22	3.85 ± 0.46

*Maximum thickness of 0 indicates an interfacial layer was not visible via scanning electron microscopy

Breakthrough Techniques for Dissimilar Material Joining – Brazing Dissimilar Metals with a Novel Composite Foil

DOE-VTO TFA Lead: Sarah Ollila
TARDEC TFA Lead: Ravi Thyagarajan

Principal Investigator:
Dr. Timothy P. Weihs
Johns Hopkins University
3400 N Charles St.
Baltimore, MD 21218

Project Start: Oct 2014
Estimated Completion: Q1FY18

Objective:

- To develop, characterize, and assess novel reactive foils that are based on reduction-oxidation (redox) chemical reactions for use in dissimilar alloy bonding applications.

Strategic Context:

- This technology will be applied to future Programs of Record (PORs) requiring dissimilar material lap joints.
- The technology supports the TARDEC Strategy enabling new capability in the design and application of dissimilar material lap joints.
- A patent application has been submitted with the intent of licensing the technology to a materials manufacturer, who will then sell to the automobile industry.
- Follow-on activities may include further AVPTA interest to investigate increasing joint strength, reducing cost and/or developing foils for other material combinations. TARDEC-specific follow-on may include lap joint ballistic shock evaluations.

Accomplishments:

- Investigated the use of Ti:2B reaction system to produce hot, molten scaffold to minimize porosity and enable braze to flow.
- Characterize the effect of milling parameters on the microstructure of Ti:2B system.
- Microstructurally analyzed length scales of Redox Foils to compare with Finite Element Modeling (FEM) heat dissipation models.

- Reduced mass loss in Cu_2O via heat treatment.
- Investigated use of Ti-C-Cu system as alternative to $Al{:}Cu_2O$:Diluent thermite system.

Introduction:

Reactive materials have been used to join metals for over 100 years ever since Hans Goldschmidt discovered that reactive aluminum and iron oxide could produce molten iron capable of joining railroads [1,2]. This was called the thermite process, where aluminum reduces a metal oxide creating molten metal, alumina, heat, and often gaseous products. Initial joining use of these chemistries involved powdered mixtures and a mold so that the molten braze created can flow into joints. More recently, reactive multilayer foils using intermetallic formation reactions have been used as a heat source [3-5]. These joints do not produce their own braze, and therefore require pre-wetting of solder or braze layers to enable joining. Reactive joining provides a fast, efficient bonding approach, allowing one to use high temperature brazes that cannot be used on certain alloys.

This project aims to combine the concepts of the two types of reactive joining described above. By utilizing a thermite composition, the exothermic reaction can create its own braze without requiring any pre-coated solder or braze layers on the components. Further, by creating a fully dense foil, the joint can be formed without any mold or complicated fixture. The braze is created at the location of the joint as shown in Figure 1 and does not need to flow into the joint area, as is the case with typical thermite joining. To reduce the amount of gas produced by thermite reactions, the mixture is diluted with excess metal. Adding diluent decreases the reaction velocity, decreases the total amount of heat, and decreases the reaction temperature. Adding diluent also has the benefit of increasing the quantity of molten metal braze in the products as compared to undiluted thermites [6].

The chemistry and microstructure of the Redox Foil determines how the foil will propagate. The chemistry also determines the characteristics of the braze that is formed. By engineering the reaction properties of the foil, we can tailor the reaction to join many dissimilar metal combinations. Because the reactions propagate quickly (on the order of 1 m/s), the heat is produced for a short period of time, and very locally. This allows for brazing of dissimilar combinations that cannot be joined with traditional furnace brazing (such as joining steel to magnesium alloys).

Approach:

To develop a Redox Foil capable of joining dissimilar metals, we have produced two different types of foils. The first foil is made by mechanically processing constituent powders (Redox Foil)[6,7] and the other by Vapor Phase Deposition (PVD). The Redox Foil, is the economical solution that can be easily scaled for automotive applications. PVD foils, on the other hand, have well-defined geometries for scientific inquiry. These ideal microstructures are critical for understanding the processes that occur during propagation, and aid in engineering the necessary microstructure which we emulate in the Redox Foils. In the past, we determined that the Al:Cu_2O system is the most promising system for joining, with the diluent typically Cu, but some Ag dilutions have been prepared, as will be described.

The Redox Foil fabrication process involves three steps. First constituent powders are ball-milled to produce nanocomposite powders. This step was added in FY15 to reduce the reactant spacing between the aluminum fuel and the oxide. Initially only the Al and metal oxide were milled together producing thermite composites (these foils are labeled BM). However, due to analysis from the PVD foils in FY16, it was determined that the diluent needs to be more uniformly incorporated into the final structure, therefore the diluent was added to the ball milling process (BM+D). After milling, the powders are packed into a tube and then compacted by swaging, a radial reduction technique. Finally, the swaged tubes are rolled flat and the tube encasing removed leaving the fully dense Redox Foil.

The PVD foils are made using magnetron sputtering. The sputtering chamber contains three targets, Al, Cu2O-Cu, and Cu. Inside of the chamber, substrates are rotated past each target producing layered foils of a planar geometry.

To analyze the materials a variety of techniques were employed. To understand characteristics of propagating reactions in the foils, high speed videography coupled with emission spectroscopy is used. High speed videos allow us to determine propagation velocity, a key metric for how fast the reaction is producing heat. The emission spectroscopy is used to identify if vapor species are produced by the reactions, as well as to approximate reaction temperatures. Slow heating experiments, including Differential Scanning Calorimetry (DSC) and Thermo-Gravimetric Analysis (TGA), were also used to characterize the thermal properties of reactive materials and resulting braze. Finally, the Redox Foils are used to join Al 3003, Mg AZ31, and Hot Stamped Boron Steel (HSBS), and the shear strengths of resulting bonds are tested.

Results and Discussion:

Microstructurally analyzed length scales of Redox Foils to compare with FEM heat dissipation models:

Image analysis was performed on Al:Cu_2O:Cu BM Redox Foils to understand the length scales present in the microstructure. The results are summarized in Figure 2 where the ratio of thermite to diluent is plotted vs the thermite length scale. Larger ratios correspond to smaller levels of dilution. The size of the circle corresponds to the area fraction of length scales within a given ratio. In addition, FEM heat transfer simulations determined the critical thermite lengths and ratios that are required to suppress Cu gas formation during propagation, as summarized in Figure 3. Based on these simulations it was determined that for 20wt%, and 30wt% cases, which produce Cu vapor, over half of the foil area was capable of producing vapor using the analysis from the simulations. The 40wt% sample, with fewer dangerous microstructural length scales, did not produce any vapor. Therefore, to produce gasless propagation, only BM+D foils, which have a finer spacing and more homogenous distribution of diluent in the microstructure, should be used moving forward.

Evaluated the use of Ti:2B scaffolds for enhanced braze flow and reduced porosity:

Ti:2B ball-milled powders have the advantage of a higher adiabatic temperature than thermites and higher melting temperatures for the final TiB_2 compound product that forms. This means that these powders quickly enter the solid phase after reaction. We combine the Ti:2B pellets with our traditional thermite powder systems and leverage the best qualities of both reactive systems. The Ti:2B has a high heat output upon reaction, forming TiB_2, which creates a hot, porous, and solid matrix. The thermite acts as an additional heat source while providing molten braze material that solidifies at temperatures approximately 2000^oC below the melting point of TiB_2. These metallic products (Cu and Ag) are able to flow into the hot pores of the TiB_2 matrix, decreasing porosity and increasing the degree of connectivity of the metal braze throughout the bond thickness. More molten metal is contributed from the local heating of the substrates (Al 3003), which allows for further pore filling. We have fabricated tri-layer pressed pellets with thermite outer layers and a Ti:2B core, as depicted in Figure 4 (a). We have demonstrated the ability to produce joints with such tri-layers as shown in Figure 4.

Mass losses have been observed for the Ti:2B ball-milled powders that we have fabricated. TGA scans of the elemental starting powders (Figure 5) showed that the Boron powder experiences a mass loss of nearly 8% within the first 150 °C of heating. This mass loss has been attributed to water vapor adsorbed to the Boron surface as Boron has well known hygroscopic properties. The release of this vapor upon reaction is in competition with the infiltration of molten metal into the porous TiB_2 structure (Figure 6). Therefore, it is advantageous to process the Boron powder prior to ball milling. The powders were annealed in an inert atmosphere to remove the adhered water, as well as packed into ball milling vials in an inert atmosphere in order to bypass the possibility of re-adsorption of water.

Bonding of Al and steel substrates was attempted using various combinations of thermite and Ti:2B powders. Results of bonding trials using annealed Cu_2O thermite have yielded low bonding strengths (Figure 7, red dots). This has been attributed to use of sub-optimal Ti:2B powder (i.e. over-milled or in need of further processing) leading to an inability to provide effective wetting of the substrate metal surface. Additions of diluent metal in various stages of processing, annealing of boron powder to reduce vapor generation, and variation of the thickness and distribution of thermite and Ti:2B layers was investigated to improve bond strengths but bond strengths remained low.

Investigated use of Ti-C-Cu system as alternative to Al:Cu2O:Diluent thermite system:

New Ti-C-Cu powders were synthesized using ball milling. To understand the effect of braze dilution, a Cu-rich 0.63CuTiC and a Cu-lean 0.44CuTiC composition was synthesized. Table 1 depicts the atomic percentages of the individual elements for a given composition. For initial testing, we milled 60g of powders with 1/4th-inch stainless steel balls with a ball to powder mass ratio (BPR) of 3 and milling time of 90 min using Retsch Planetary Mill PM400.

To understand the effect of milling, we cross-sectioned the ball milled powders mounted in epoxy and obtained Back-Scatter Electron (BSE) Scanning Electron Microscopy (SEM) images to determine the degree of incorporation of Ti and C into the Cu matrix as shown in Figure 8. The contrast in the SEM images is due to the difference in the atomic number of the elements, heavier elements like copper are brighter when compared to Ti or C. The atomic number for carbon is significantly lower than that for both Cu and Ti; as a result, imaging C inclusions with the back-scattered detector is challenging. The SEM images show poor incorporation of Ti into Cu matrix for both the compositions. Also, these images show that the milled powders are flake-like and elongated. We gauged the reactivity of the ball milled powders by heating them to 1400°C at 20°C/min using a simultaneous TG/DTA system under argon. Figure 9 depicts the typical heat flow vs. temperature for the milled powders. Both the ball milled powders have poor heat release below 600°C, followed by a large heat flow spike. Though the net heat from the formation reaction is high, the poor low temperature heat release is typical from poorly milled powders. With better incorporation, we expect sub 600°C heat release to improve significantly.

The Cu-rich 0.63CuTiC ball milled powders were pressed into 12.7 mm diameter by 1 mm pellets using a Carver press. With a max load value of 15,000 lbs, we obtained pellets with an average TMD of 40%. These pellets have poor integrity and de-laminate with relative ease upon handling. However, the consolidated fragments ignite when initiated by an electrically heated coil. Figure 10 images (a) through (c) depict the ignition and propagation of the reaction front, while image (d) depicts the longtime cooling of the fragment. Even with a poorly incorporated composite, we observe powder compacts to be reactive. For the Ti-C-Cu system, the formation of Cu-Ti intermetallics is undesirable. We used X-ray diffraction to identify the composition of the reaction products that formed during low heating rate experiments (DTA) and faster heating during fragment ignition. The X-ray patterns show peaks for the TiC and Cu products from both modes of heating as shown in Figure 11. Even with a poor incorporation of Ti/C in Cu, we observe the formation of TiC and not Cu-Ti intermetallics.

Conclusions:

To produce strong joints, the braze produced by propagating Redox Foil should have low porosity and mass ejection. FY17 efforts focused on identifying the length scales present in the microstructure of BM and swaged Al:Cu_2O:Cu system. The length scale ratio of thermite to diluent vs. thermite length scale determines the degree of homogeneity in a given region. Large ratios correspond to smaller levels of dilution resulting in thermite rich regions that are prone to produce hot-spots that are the source for gas evolution and mass ejection. For different synthesized compositions, the volume fraction of these poorly mixed regions determines the degree of porosity in the bonds. FEM heat transfer simulations determined the critical thermite lengths and ratios that are required to suppress Cu gas formation. Using this insight, we determined the thermite system with 40% dilution had fewer poorly mixed zones resulting in less porous bonds.

To overcome the gas evolution and enhance braze flow, we investigated the use of Ti:2B reactive scaffolds to provide a heated framework to improve bonding strengths. Early efforts focused on optimizing the milling parameters to obtain reactive Ti:2B composites. While optimizing the synthesis, we observe ~8% mass loss during TG/DTA scans. We attribute the weight loss to the loss of adsorbed water on the surface of Boron. This volatile mass enhances porosity and mass ejection during bonding, resulting in reduced mechanical strengths. Due to these powder processing hurdles, we decided to leverage the carbide formation reactions to melt the braze instead of a redox reaction based reactive braze. The preliminary effort focused on synthesizing Ti-C-Cu based reactive braze wherein, TiC formation reaction results in melting the braze. Current efforts are underway to optimize the milling conditions and identifying the braze volume fraction that will provide us with higher bond strengths than the previous systems.

References:

[1] Goldschmidt, H. Process of Joining Metal Pieces. Google Patents January 6, 1903.

[2] Wang, L. L.; Munir, Z. A.; Maximov, Y. M. Review Thermite Reactions: Their Utilization in the Synthesis and Processing of Materials. *J. Mater. Sci.* 1993, *28*, 3693–3708.

[3] Wang, J.; Besnoin, E.; Duckham, A.; Spey, S. J.; Reiss, M. E.; Knio, O. M.; Weihs, T. P. Joining of Stainless-Steel Specimens with Nanostructured Al/Ni Foils. *J. Appl. Phys.* 2004, *95* (1), 248–256.

[4] Duckham, A.; Spey, S. J.; Wang, J.; Reiss, M. E.; Weihs, T. P.; Besnoin, E.; Knio, O. M. Reactive Nanostructured Foil Used as a Heat Source for Joining Titanium. *J. Appl. Phys.* 2004, *96* (4), 2336.

[5] Weihs, T. P. *Fabrication and Characterization of Multilayer Films and Foils*; 2014.

[6] Kinsey, A. H.; Slusarski, K.; Woll, K.; Gibbins, D.; Weihs, T. P. Effect of Dilution on Reaction Properties and Bonds Formed Using Mechanically Processed Dilute Thermite Foils. *J. Mater. Sci.* 2016, *51* (12), 5738–5749.

[7] Woll, K.; Gibbins, J. D.; Slusarski, K.; Kinsey, A. H.; Weihs, T. P. The Utilization of Metal/metal Oxide Core-Shell Powders to Enhance the Reactivity of Diluted Thermite Mixtures. *Combust. Flame* 2016, *167*, 259–267.

[8] Zhou, L.; Piekiel, N.; Chowdhury, S.; Zachariah, M. R. Time-Resolved Mass Spectrometry of the Exothermic Reaction between Nanoaluminum and Metal Oxides: The Role of Oxygen Release. *J. Phys. Chem. C* 2010, *114* (33), 14269–14275.

Figures Begin on Next Page

Figures and Table:

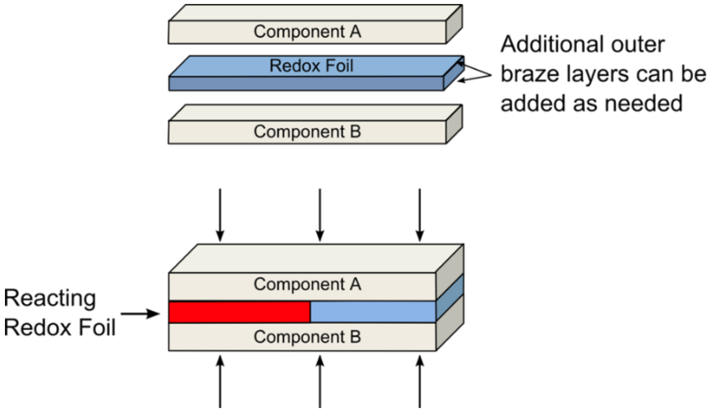

Figure 1: Schematic of the joining process with Redox Foil. As the reaction propagates molten braze is produced.

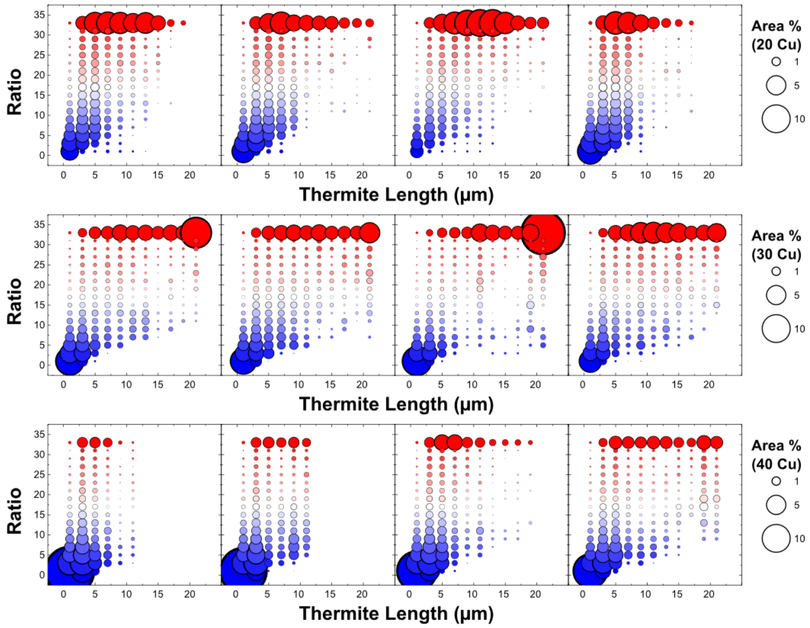

Figure 2: Microstructural analysis of BM Redox Foils. Each graph represents analysis on a different region of foil. Top row is 20wt% Cu; middle row is 30wt% Cu; and bottom row is 40wt% Cu.

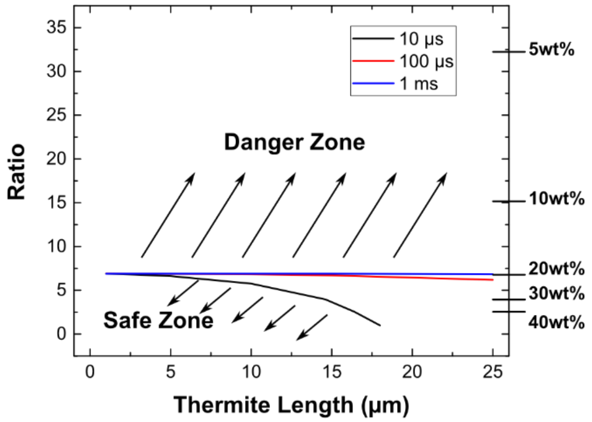

Figure 3: Results from FEM simulations determining what ratio and length scales are required in order to suppress gas formation

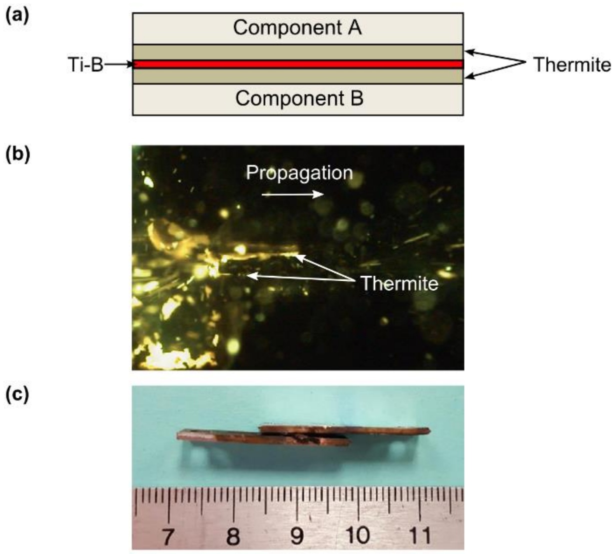

Figure 4: (a) Schematic representation of bonding with a tri-layer pellet and (b) video of such a pellet propagating between two Al 3003 substrates producing the joint shown in (c).

Figures Continue on Next Page

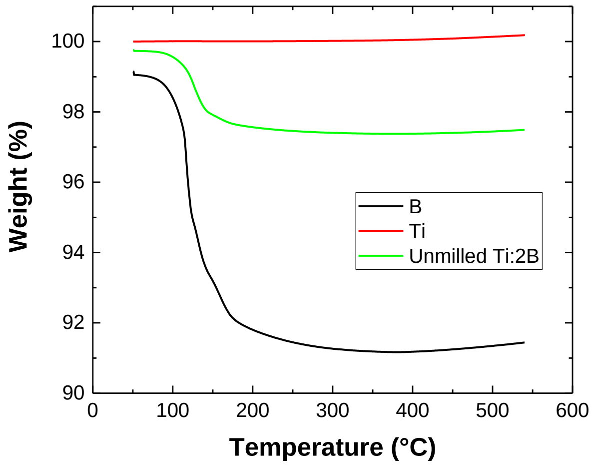

Figure 5: TGA signals showing the mass loss associated with elemental starting powders comes solely from Boron.

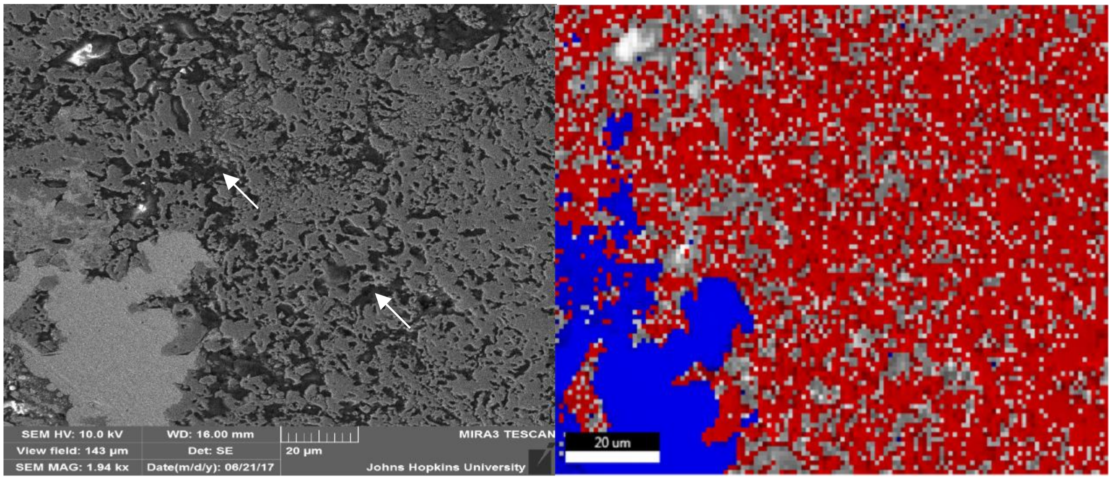

Figure 6: (Left) SEM image of reacted Ti:2B/Al:Cu2O pellet. White arrows indicate porosity in TiB2. (Right) EDAX scan of area revealing TiB2 region (red) and Cu region (blue).

Figures Continue on Next Page

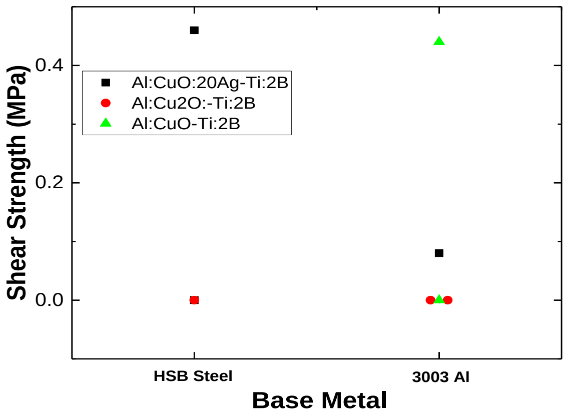

Figure 7: Preliminary bonding results for various Combinations of thermite and Ti:2B powders.

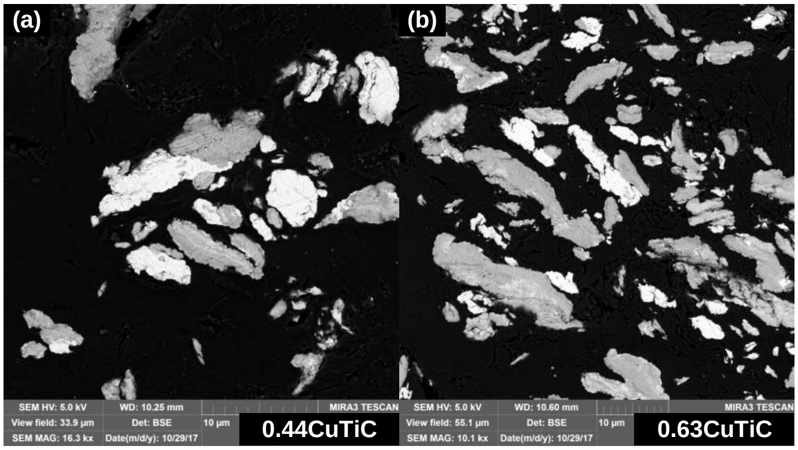

Figure 8: Cross-sectional back scatter SEM images of
(a) 0.44CuTiC and (b) 0.63CuTiC powders ball milled for 90 min.
(b) The dark (black) background is the epoxy, the grey particles
(c) are “Ti” and the higher atomic number “Cu
(d) is depicted by the light grey particles.
(e) “C” with its low atomic number is hard to image
(f) and obtain a contrast in SEM images.

Figures Continue on Next Page

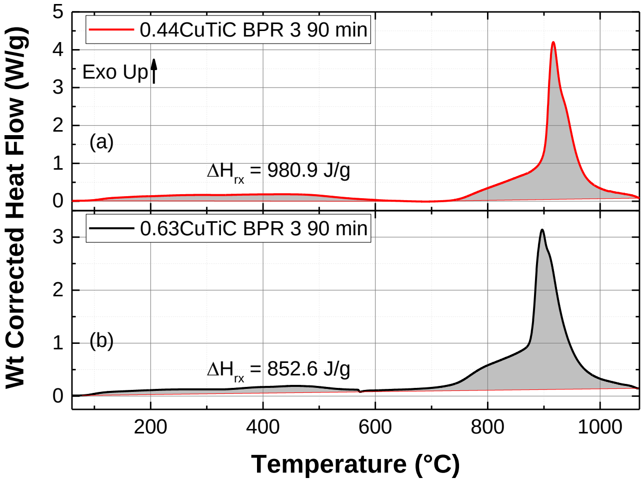

Figure 9: DTA traces of (a) 0.44CuTiC and (b) 0.63CuTiC ball milled powders heated at 20°C/min up to 1400°C in argon.

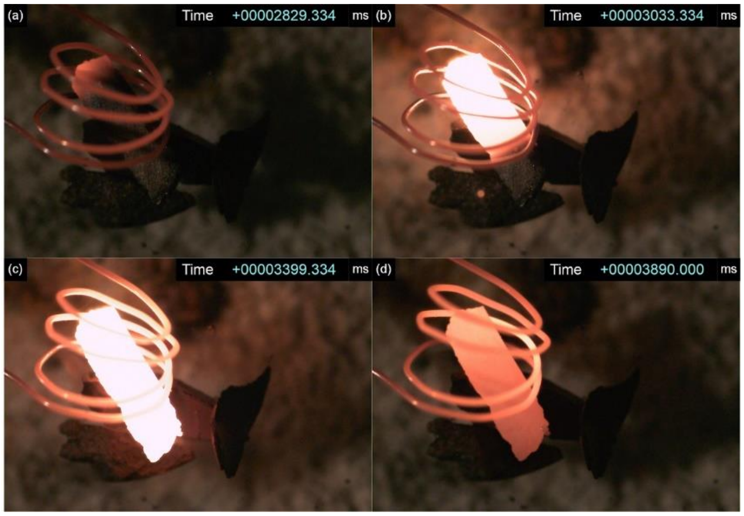

Figure 10: Ignition and propagation of consolidated 0.63CuTiC fragment with a heated coil. Images a through d depict the propagation and cooling of the reactive braze.

Figures Continue on Next Page

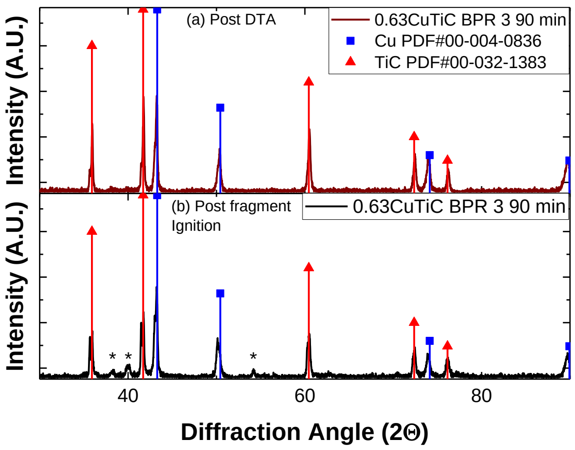

Figure 11: XRD scans showing peaks for the Cu and TiC products formed during (a) DTA heating and (b) during consolidated fragment ignition.

Table 4: Atomic composition of the milled powders.

Composition	Ti at%.	C at%.	Cu at%.
0.63CuTiC	38	38	24
0.44CuTiC	41	41	18

Remainder of Page Intentionally Blank

Bi-metal Brake Development

DOE-VTO TFA Lead: Sarah Ollila
TARDEC TFA Lead: Ravi Thyagarajan

Principal Investigator:
Dr. Adam Loukus
Reliable, Exact and Logical Equipment (REL) Inc.,
57640 North 11th Street,
Calumet, MI 49913

Project Start: Oct 2013
Project Completed: Q1FY17

Objectives:

- Develop lightweight bi-metal rotors for the High Mobility Multipurpose Wheeled Vehicle (HMMWV) platform which shall provide comparable weight, but increased durability and performance.
- Determine whether new advanced materials, advanced manufacturing techniques and thorough testing of prototype units shall improve the performance of the HMMWV.

Strategic Context:

- Reliable, Exact and Logical's (REL) bi-metal technology combined with functional reinforcement gradient technology will be employed to overcome the previous limitations of alternative brake materials.
- REL has vertically integrated the Metal Matric Composite (MMC) rotor process, is delivering MMC brake rotors to the motorcycle market and is expanding the deployment of this technology into automotive markets.
- REL is leveraging their knowledge obtained in developing MMC brake products to develop rotors for the HMMWV application. The goal of the Bi-metal Brake Development project is to rapidly modify a HMMWV braking system to improve stopping performance, handling, safety, and durability throughout the range of vehicle weights.

<u>Remainder of Page Intentionally Blank</u>

Accomplishments:

- Bi-metal HMMWV prototype rotors have been manufactured and tested.
- The prototypes are selectively reinforced aluminum metal matrix composite rotors with a nickel surface, and manufactured through squeeze casting, machining, and nickel plating.
- Testing results show that the prototype brake rotors have superior cooling and friction capabilities when compared to original equipment HMMWV rotors and pads, and can replace a stock HMMVW rotor.

Introduction:

Vehicle light-weighting is a priority for the U.S. Army and the future force must be more expeditionary and agile to the ever changing global threat environment [1]. Due to increased survivability requirements, additional protection measures have been added to vehicles, which has typically increased their weight. The increased weight has resulted in decreased fuel economy, decreased reliability and in mobility as well as transportability. Light-weighting efforts in Army ground vehicles are imperative to reverse this trend, and MMC brake rotors offer one such opportunity.

REL's bi-metal technology combined with functional reinforcement gradient technology will be employed to overcome the previous limitations of alternative brake materials. REL has vertically integrated the MMC rotor process, and is delivering MMC brake rotors to the motorcycle market and is expanding the deployment of this technology into automotive markets. REL is leveraging their knowledge obtained in developing MMC brake products to develop rotors for the HMMWV vehicle.

The goal of the Bi-Metal Brake Development is to rapidly modify a HMMWV braking system to improve stopping performance, handling, safety, and durability throughout the range of vehicle weights. the adapted technologies into a current military vehicle through a future upgrade program.

Approach:

REL produced a bi-metal aluminum metal matrix composite rotor that can be used in the current configuration of the HMMWV braking system. Merging MMC technology with REL's bi-metal developments allows for the production of a bi-metal lightweight brake rotor. An in-house dynamometer allowed REL to test brake rotors and brake friction materials while evaluating performance of the baseline HMMWV rotor against the bi-metal option.

Many of the tasks needed to develop a bi-metal brake system were accomplished concurrently, with their results being combined following completion. Key tasks were as follows:

- Define geometry of bi-metal rotor
- Analysis of rotor design
- Develop and optimize manufacturing methods for HMMWV MMC rotor casting
- Adapt current rotor bi-metal surface technology to HMMWV MMC rotor
- Manufacture molds and support tooling for rotor casting
- Cast, machine, and surface initial rotors to prove out manufacturing process

- Performance testing and analysis on initial rotors
- Manufacture final prototypes.

Prototype Rotor:

The bi-metal HMMWV prototype rotor is comprised of two metal MMC blades, connected by an aluminum alloy hub and aluminum alloy venting structure. The rotor has a nickel coating to increase rotor durability. A diagram of the rotor is shown in Figure 1. A Non-Asbestos Organic (NAO) brake pad was chosen to be compatible with the rotor. Because of the unique materials used in the rotor, a suitable brake pad is necessary for operation.

Manufacturing:

The manufacturing process of a prototype rotor consists of three main steps: casting, machining, and nickel plating. A salt core placed between two ceramic preforms creates a MMC rotor. This setup is place in a die along with molten aluminum alloy. The setup is shown is Figure 2. The die is then subjected to high pressure to create a rotor casting. The casting die and press are shown in Figure 3. The casting then is machined to the correct size. A chemical process applies the nickel coating to the rotor. An uncoated rotor is shown in Figure 4 and a nickel coated rotor is shown in Figure 5, respectively.

Results and Discussion:

Figure 6 shows the temperature over the entirety of the twelve-stop integrity test. Rotor evaluations were done on the prototype rotor. The rotor was found to be without layer separation between aluminum alloy and MMC layers, or any visible cracking and warping. Surface integrity was determined to be acceptable with NAO brake pads. Figure 7 shows a prototype rotor after integrity testing.

Rotor Cooling Testing:

Rotor durability testing provides insight into the capabilities of a rotor under heavy braking. Rotor cooling testing shows how a rotor recovers after braking. The original equipment rotor were be evaluated for comparison. Results from testing help in evaluation of rotor cooling. A component level test was performed in a dynamometer within REL, and the test samples were prototype bi-metal HMMWV rotors and Original Equipment (OE) HMMWV rotors. The test criteria was rotor cooling cycle until below 100°F.

Rotors are heated to a temperature above 500°F through a braking cycle. The rotors are then spun at 40 mph (equivalent speed) until rotor temperatures reach near environmental temperatures. Thermocouples implanted in the rotors monitor and record temperatures.

Figure 8 shows the results of the prototype cooldown test along with the original equipment cooldown test. Table 1 also shows the results in tabular form. From the results of the cooldown test, it can be seen that the prototype rotor cools much faster than the original equipment rotor. From 500°F to 200°F the prototype rotor cools about two times faster. This difference in cooling will allow the rotor to have cooler operational temperatures than stock cast iron rotors.

Friction Event Testing:

While the rotor durability and cooling testing evaluated important features of the rotor, a friction event test helps to evaluate a composite of the two, while testing the braking critical feature, friction. In a friction event test, a brake rotor is put through a cycle of braking and cooling. Data from the test provides the amount of friction that was available at each braking event. This test gives the composite performance of a brake rotor and brake pad.

Along with evaluating rotor performance, the friction event test is used to evaluate brake pad friction performance. Once a baseline has been established with the original equipment HMMWV brake rotors and pads, other pads can be used to test their compatibility and performance with the bi-metal rotor. An assembly level test was performed in a dynamometer within REL, and the test samples were prototype bi-metal HMMWV rotors, OE HMMWV rotors and pads, and various other pads. The test criteria was Rotor braking and cooling cycles to evaluate friction and temperature.

Four different brake rotor and pad combinations were tested: OE rotors and pads, OE rotors and NAO pads, MMC rotor and OE pads, and MMC rotor and NAO pads. Each combination was put through a 10 stop dynamometer test. Rotors were spun to 50 mph equivalent speed (654 rpm) with an inline cooling wind matching the equivalent speed. Thermocouples placed in the blade of each rotor recorded temperature data.

Figure 9 shows the temperature of each rotor/pad combination during the friction event test. Figure 10 shows the coefficient of friction during the test for each rotor/pad combination. From the results of the tests, the different pad/rotor combinations can be compared. From the temperature graph, the MMC rotor/NAO pad combination had the highest operating temperature. The stock rotor/NAO pad combination had a similarly high maximum test temperatures but generally lower operating temperatures. The original equipment setup of stock rotors/stock pads also had the second lowest operating temperature, but had a lower coefficient of friction. Less braking energy was being transferred to the rotor, ending in less heat being measured. Form the coefficient of friction graph, the stock rotor/stock pad setup had a much higher Coefficient of Friction (COF) than the other three combinations. The prototype setup of MMC rotors/NAO pads had a slightly better average COF than the OE stock rotor/stock pad setup.

Conclusions:

- Bi-metal HMMWV prototype rotors were manufactured from selectively reinforced aluminum metal matrix composite rotors with a nickel surface using squeeze casting, machining, and nickel plating.
- Testing results show that these prototype brake rotors have superior cooling and friction capabilities when compared to original equipment HMMWV rotors and pads, and can replace a stock HMMVW rotor.

Remainder of Page Intentionally Blank

Reference:

[1] E. Polsen, L. Krogsrud, R. Carter, W. Oberle, C. Haines and A. Littlefield, "Lightweight Combat Vehicle Science and Technology Campaign," US Army Tank Automotive Research, Development, and Engineering Center, Report # 25940, Warren, 2014.

Figures and Table:

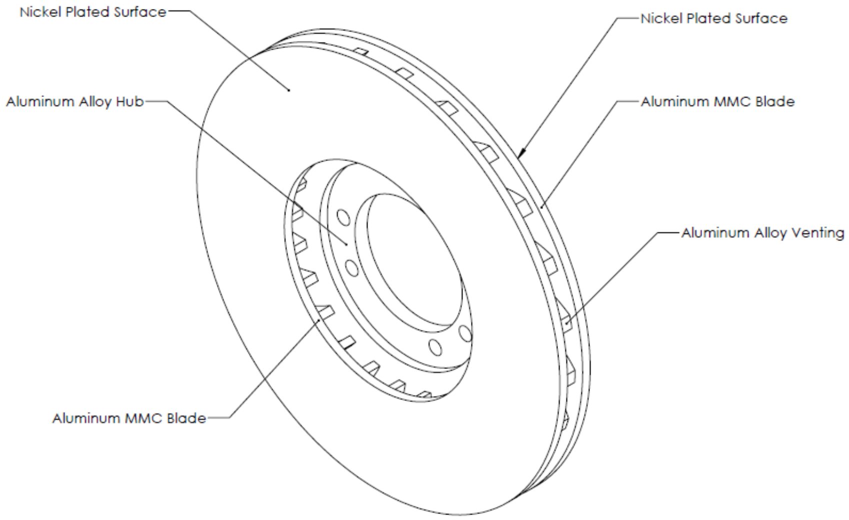

Figure 1. Bi-metal Prototype Rotor

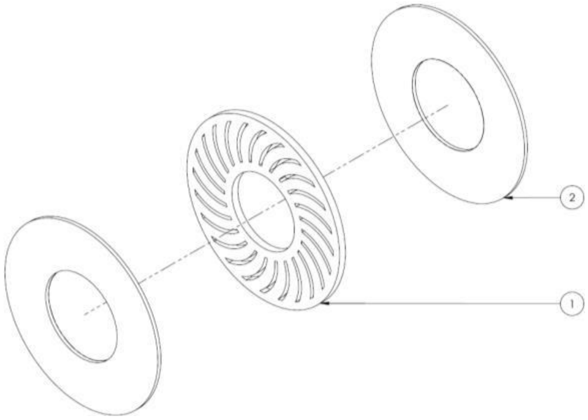

Figure 2. Salt Core and Ceramic Preforms

Figures Continue on Next Page

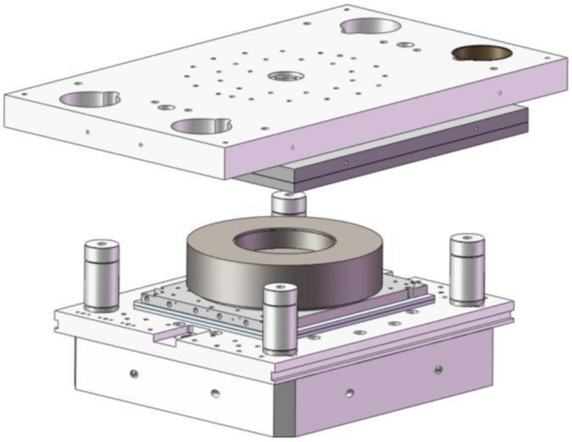

Figure 3. Casting Equipment

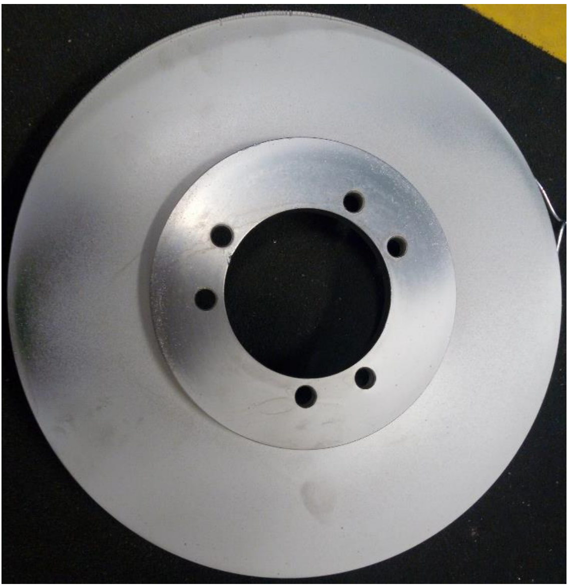

Figure 4. Uncoated Prototype Rotor

Figure 5: Nickel Coated Rotor

Figures Continue on Next Page

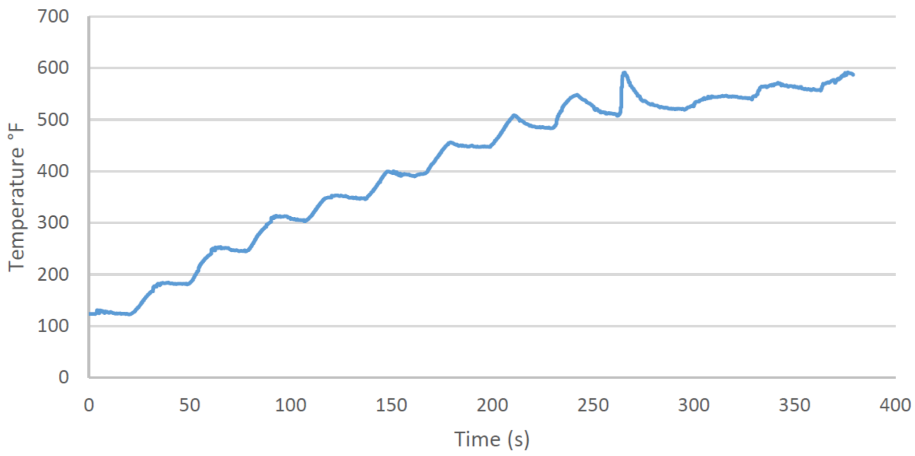

Figure 6. Integrity Test

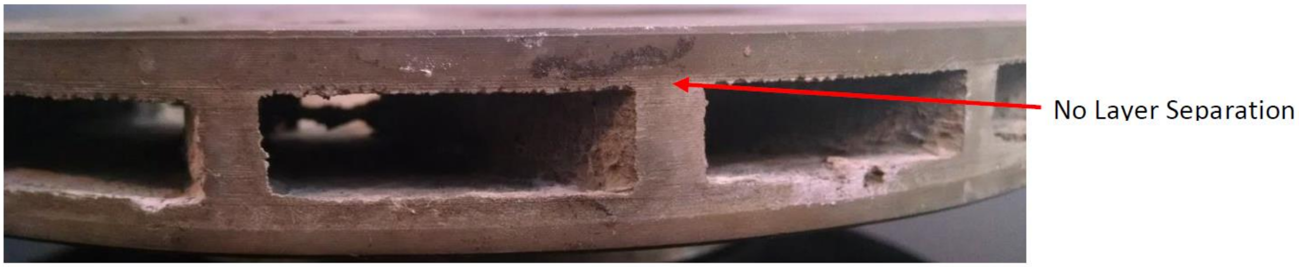

Figure 7. Rotor after Integrity Testing

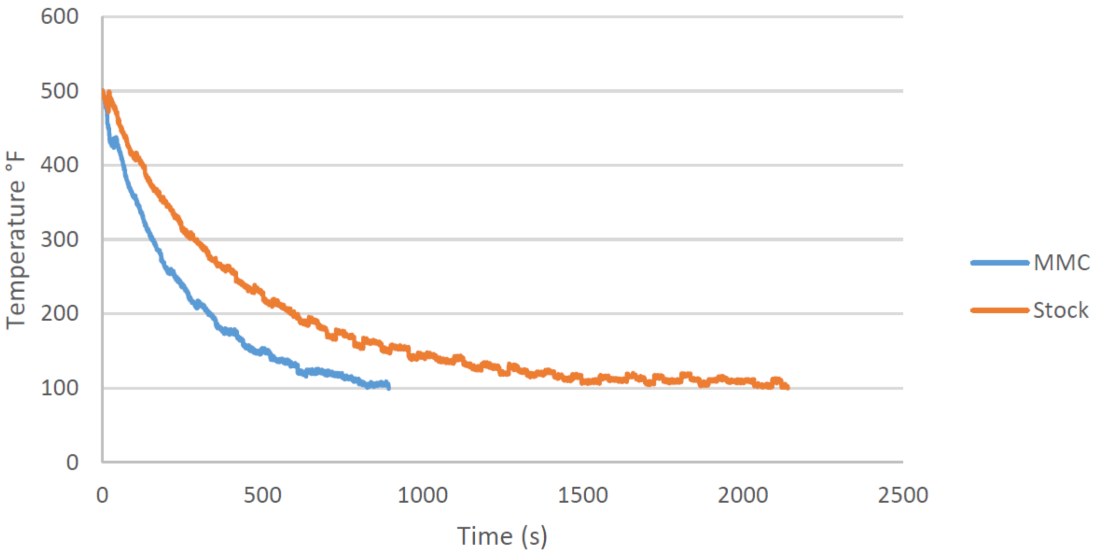

Figure 8. Cooldown Test Curves

Prototype

Temperature Range °F	500-400	400-300	300-200	200-100
Start Time (s)	0	66	155	593
End Time (s)	66	155	332	894
Total Time (s)	66	89	177	302

OE

Temperature Range °F	500-400	400-300	300-200	200-100
Start Time (s)	0	126	286	593
End Time (s)	126	286	593	2140
Total Time (s)	126	159	307	1548

Table 1: Cooldown Test Results

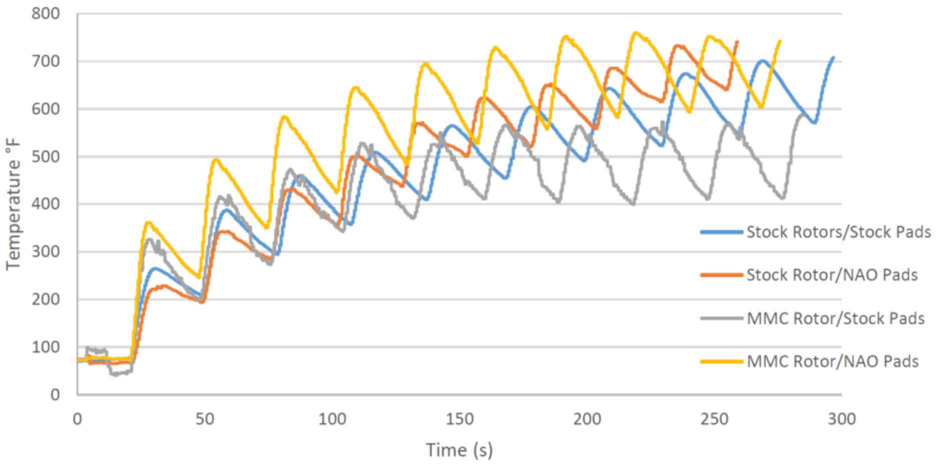

Figure 9. Friction Event Test -Temperature Comparison

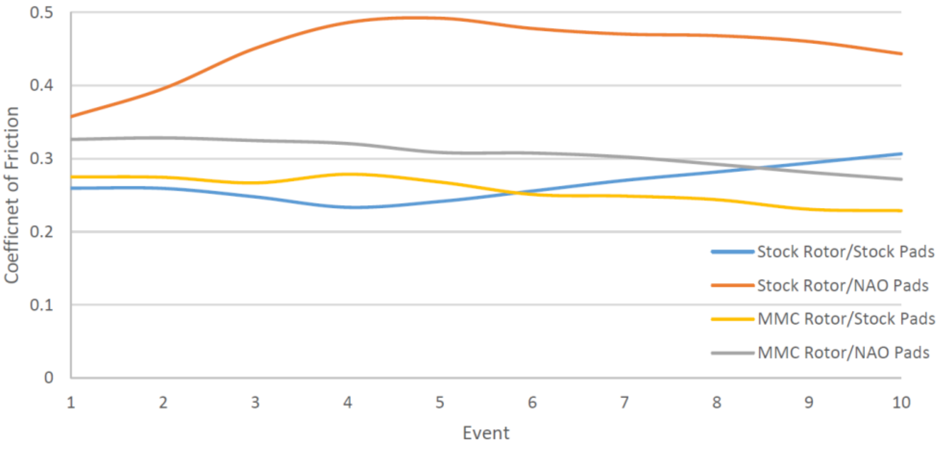

Figure 10. Friction Event Test - Coefficient of Friction Comparison

AVPTA Technology Focus Area 3: Energy Recovery & Thermal Management

DOE-VTO TFA Lead: Steven Boyd
TARDEC TFA Lead: Mary Goryca

There was no project activity under this TFA during FY17.

Remainder of Page Intentionally Blank

This Page Intentionally Blank

Lubricant Formulations to Enhance Fuel Efficiency
Polyalkylene Glygol (PAG) based Lubricant for Light & Medium Duty Axles

DOE-VTO TFA Lead: Dr. Michael Weismiller
TARDEC TFA Lead: Dr. Jay Dusenbury

Principal Investigators:
Dr. Arup Gangopadhyay
Mr. Chintan Ved
Ford Motor Company
Ford Research and Innovation Center
2101 Village Road, MD 3629, Room 3217
Dearborn, MI 48121

Project Start: Oct 2013
Estimated Completion: Q3FY18

Objectives:

- Develop novel axle lubricant formulation
- Improve vehicle fuel efficiency by at least 2% without adverse impacts on vehicle performance or durability

Strategic Context:

- Supports TARDEC's goals to extended vehicle range and reduced frequency of resupply
- Supports TARDEC's goals to research and develop lubricants to simplify life-cycle logistics and improve reliability, availability and maintainability of military ground systems

Accomplishments:

- Developed a new co-base stock formulation (i.e., mixture of petroleum base oil and Oil Soluble PAG – {OSP}) which uses more environmentally preferable OSP
- New co-base stock formulation passes industry standard performance tests including ASTM D5704 (Oxidation and Thermal Stability), ASTM D6121 (Low Speed/High Torque Load Carrying Capacity), ASTM D7038 (Corrosion Resistance) and ASTM D7452 (High Speed/Shock Loading – Load Carrying Capacity)

Introduction:

In this project Ford Motor Company ("Ford") is developing novel lubricant axle oil formulations that are expected to improve the fuel efficiency of light-duty, medium-duty, commercial and military vehicles by at least 2% over currently used SAE 75W-140 axle lubricants (improvement based on comparative results from chassis dynamometer testing or track testing, e.g., SAE J1321) without adverse impacts on vehicle performance or durability.

Approach:

Ford, in cooperation with Dow Chemical Company and Argonne National Lab is developing a Poly-Alkylene glycol (PAG) based axle oil, taking advantage of PAG's natural lubricity, high viscosity index, and excellent oxidation and shear stability. They've completed bench testing to identify formulations with the greatest potential to meet the project objectives and completed industry standardized component level testing to validate candidate fluid performance. Next steps are to complete Ford internal testing for gear wear, axle efficiency, and vehicle fuel economy on a final formulation.

Results and Discussion:

In previous years Ford developed several candidate axle lubricant formulation using only PAG for its base stock. Ford decided to abandon a pure oil soluble PAG (OSP) formulation in favor of a co-base oil formulation of petroleum and OSP after storage stability testing revealed an incompatibility issue with the OSP and the performance additive package resulting in the formation of an unwanted precipitate and performance degradation in key bench tests. After successfully completing bench scale testing, the co-base oil formulation was tested in industry standardized tests including test for thermal oxidation (L-60-1), moisture corrosion (L-33-1), shock-load testing (L-42) and load carrying capacity (L-37). Unlike previously tested pure OSP formulations, the co-base oil formulation successfully past all the industry standardized tests. These industry tests are major requirements of SAE J2360, the standard used by most major Original Equipment Manufacturers (OEMs) and the military to qualify axle lubricants for service and factory fill applications.

Conclusions:

Ford developed a co-base oil formulation using petroleum and OSP which has shown excellent results in industry standardized tests. Next steps in the project include conducting a Ford internal tests to measure co-base oil formulation efficiency improvements over a baseline 75W-140 fluid, a Ford proprietary gear wear test, and full vehicle fuel economy testing.

References:

[1] Ford Motor Company Quarterly Progress Reports, DOE Award DE-EE0006430

Figures and Tables:

None

AVPTA Technology Focus Area 4: Alternative Fuels & Lubricants

Lubricant Formulations to Enhance Fuel Efficiency
A Novel Lubricant Formulation Scheme for 2% Fuel Efficiency Improvement

DOE-VTO TFA Lead: Dr. Michael Weismiller
TARDEC TFA Lead: Dr. Jay Dusenbury

Principal Investigator:
Dr. Q. J. Wang
Northwestern University
2145 Sheridan Road
Tech A219
Evanston, IL 60208-3109

Project Start: Oct 2013
Estimated Completion: Q2FY18

Objectives:

- Develop novel lubricant formulation that reduces boundary friction and promotes temporary shear-thinning when viscous losses are the dominate mechanism for energy dissipation
- Improve vehicle fuel efficiency by at least 2% without adverse impacts on vehicle performance or durability.

Strategic Context:

- Supports TARDEC's goals to extended vehicle range and reduced frequency of resupply
- Supports TARDEC's goals to research and develop lubricants to simplify life-cycle logistics and improve reliability, availability and maintainability of military ground systems

Accomplishments:

- Successful synthesis of a di-block copolymer viscosity modifier
- Molecular dynamics simulation of Friction Modifiers (FMs) in the presence of base oil
- Hot-stop friction testing of new cyclen friction modifiers result in reduced friction compared to fully formulated 5W-30 engine oil
- Slide/roll and high temperature reciprocating testing demonstrates the ability of cyclen friction modifiers to reduce boundary friction without affecting hydrodynamic lubrication
- Oil soluble Polyalfaolefin-Poly(isodecyl)methacrylate (PAO-PiDMA) di-block Viscosity Modifiers (VMs) developed
- Completed testing of di-block viscosity modifiers with varying degrees of coiled structure

- Completed molecular dynamic simulations on the effects of chain length on the performance of the new friction modifiers

Introduction:

The project goats are to (1) reduce friction due to asperity rubbing in start-up and low-speed operations during which boundary friction controls energy dissipation, and (2) temporarily reduce the lubricant viscosity (temporary shear-thinning) in medium- to high-speed cruise operations during which viscous loss is the dominant mechanism for energy dissipation. The proposed research is expected to result not only in a 2% fuel efficiency improvement, but also enhanced performance of the powertrain/drivetrain components.

Approach:

Northwestern University in collaboration with Argonne National Lab developed three generations of heterocyclic friction modifiers and functionalized B_2O_3 nanoparticles which significantly lower boundary friction. Northwestern University also synthesized temporary shear-thinning di-block copolymer VMs that yield low friction under stress.

Results and Discussion:

Pin-on-disk testing conducted by Northwestern University was completed for randomly branched PE viscosity modifier. Testing showed randomly branched PE viscosity modifiers provided approximately 20% reduction in friction compared to commercial Olefin Co-Polymer OCP based viscosity modifier. A di-block copolymer viscosity modifier was successfully synthesized and oil soluble PAO-PiDMA di-block viscosity modifier demonstrated enhanced thermo-thickening and shear-thinning performance. Additional synthesis and testing of different di-block VMs with varying degrees of coiled structure versus branched was conducted and the well coiled di-block VMs reduced the coefficient of friction by ~65% to ~90% in the hydrodynamic regime. Hot-stop friction tests at 200°C demonstrate that cyclen friction modifiers reduce friction by 50% compared to a fully formulated 5W-30 engine oil. Slide/roll and high temperature reciprocating testing demonstrated the ability of cyclen friction modifiers to reduce boundary friction without affecting hydrodynamic lubrication. Cyclen friction modifiers added directly to a 5W-30 fully formulated oil reduced friction coefficient by 20%. Molecular dynamic simulations were conducted on the effects of chain length on the performance of the new FMs that helped develop an understanding of the surface adsorption/desorption enhancement of the cyclen FMs in agreement with tribological test results which provided further confirmation that the C18Cyc cyclen FM has consistently been the best boundary lubrication performer among all of the heterocycles studied in the present research.

.

Remainder of Page Intentionally Blank

Conclusions:

Northwestern University successfully synthesized novel friction modifiers and a novel viscosity modifier. Bench testing and molecular dynamic simulations have been completed to better understand the mechanisms of these additives. Next steps include the formulation of an optimized fully formulated lubricant based on the heterocyclic FMs, di-block copolymer VMs, and functionalized nanoparticles. Additional evaluations of high temperature-high shear performance and shear stability will be completed, as well as, fuel economy testing.

References:

[1] Northwestern Quarterly Progress Reports, DOE Award DE-EE0006449

Figures and Tables:

None

Remainder of Page Intentionally Blank

This Page Intentionally Blank

AVPTA Technology Focus Area 4: Alternative Fuels & Lubricants

Lubricant Formulations to Enhance Fuel Efficiency
Improved Fuel Economy through Formulation Design and Modeling

DOE-VTO TFA Lead: Dr. Michael Weismiller
TARDEC TFA Lead: Dr. Jay Dusenbury

Principal Investigator:
Dr. Gefei Wu
Valvoline, a Division of Ashland Inc.
3499 Blazer Parkway
Lexington, KY 40509-1850

Project Start: Oct 2013
Estimated Completion: Q1FY18

Objectives:

- Develop fuel efficient engine, transmission and axle lubricants and verify using SAE J1321 testing
- Improve vehicle fuel efficiency by at least 2% without adverse impacts on vehicle performance or durability

Strategic Context:

- Supports TARDEC's goals to extended vehicle range and reduced frequency of resupply
- Supports TARDEC's goals to research and develop lubricants to simplify life-cycle logistics and improve reliability, availability and maintainability of military ground systems

Accomplishments:

- Completed SAE J1321 – Fuel Consumption Test Procedure - Type II testing of three engine oils, three axle oils and two transmission oils

Introduction:

This project focused on developing lubricant formulations that are expected to improve the fuel efficiency of medium-duty, commercial and military vehicles by at least 2% (improvement based on comparative results from engine dynamometer testing, chassis dynamometer testing or test track, e.g., SAE J1321) without adverse impacts on vehicle performance or durability. This was accomplished through engine, transmission and axle lubricant formulation design, modeling and testing.

Approach:

Valvoline applied its extensive experience in the formulation of engine, transmission and axle lubricants to develop improved fuel economy through the optimization of engine, transmission and axle lubricants using advanced base oils and additive technology, including a bio-based base oil, and industry best practices.

Results and Discussion:

In previous years Valvoline used its experience developing heavy-duty diesel engine oils, transmission, and axle lubricants to formulate state-of-the-art candidate lubricants at lower viscosity and using advanced friction modifiers. They conducted bench scale and physical and chemical testing and input these results into computer models developed to predict fuel economy benefits. In this final year of their project they focused on validating there candidate fluids in industry standardized testing, including fuel economy testing in accordance with SAE J1321. Valvoline developed a 5W-30 and 5W-20 heavy-duty diesel engine oil which, in engine dynamometer testing, resulted in a fuel economy improvement over a 15W-40 baseline of 1.6% and 1.8%, respectively. For axle lubricants, Valvoline developed two candidate 75W-90 grade oils and conducted axle efficiency testing with resulting efficiency improvements between 0.63 and 1.36% under demanding conditions. For the transmission Valvoline developed two candidate formulations meant to improve upon a baseline TES-295 fluid. J1321 fuel consumption testing was conducted by the Transportation Research Center (East Liberty, OH) using four Class-6 trucks and seven test segments. Four different candidate oil combination led to fuel economy benefits greater than 2% with the greatest benefit being 2.58%. Candidate engine and gear oils resulted in the greatest improvement above baseline fluids.

Conclusions:

By judiciously selecting base oil and additives Valvoline developed candidate engine, transmission, and axle oils which resulted in significant improvements in fuel economy that were validated in both dynamometer tests and full vehicle testing. The best combination of engine, transmission and axle candidate lubricants improved fuel economy when tested in accordance with SAE J1321 test standard by 2.58%. A final report is pending.

References:

[1] Valvoline Quarterly Progress Reports, DOE Award DE-EE0006427

Figures and Tables:

None

Remainder of Page Intentionally Blank

AVPTA Technology Focus Area 4 Adjunct: Tire Efficiency

Improved Tire Efficiency through Elastomeric Polymers Enhanced with Carbon-based Nanostructured Materials

DOE-VTO TFA Lead: Roland Gravel
TARDEC TFA Lead: Dr. James Dusenbury

Principal Investigator:
Dr. Georgios Polyzos
Oak Ridge National Laboratory (ORNL)
Oak Ridge TN 37831-6054

Project Start: Dec 2015
Estimated Completion: Q1FY18

Objectives:

- Reduce hysteretic losses for reduction of rolling resistance
- Sharply enhance the wear resistance of the tire without compromising its viscoelastic properties.
- To uniformly disperse well-defined structures of self-assembled graphene layers in the rubber matrix
- 4% improvement in fuel efficiency

Strategic Context:

- Reduce fuel consumption and logistics burden in operational theaters
- Increase Power Density and Energy Efficiency resulting in increased vehicle range, endurance and operational tempo.
- Increase fuel efficiency of ground vehicles to Reduce Life Cycle Costs
- Incorporate into Tactical Vehicles currently using Commercial Tires
- Leverage technology to develop for military specific tires

Accomplishments:

- Defined the silica nanofiber volume fraction in order to increase the tear resistance.
- Determined the graphene nanoplatelets volume fraction in order to achieve 4% fuel savings.
- Demonstrated the feasibility to fabricate composite rubber materials with reduced hysteretic losses sufficient to achieve at least 4% fuel savings and improve tear strength.

Introduction:

In materials science of elastomers the influence of manufactured nanomaterial filler particles is of utmost significance for the performance of innovative rubber products, i.e., passenger and commercial tires with ultralow rolling resistance but high traction. Advances in both performance areas are imperative for the development of improved tire efficiency to meet Department of Energy's (DOE) fuel consumption reduction target of 4%, all while maintaining or improving wear characteristics of the tire. The unique geometrical configuration of the graphene fillers makes them the most promising carbon based fillers for breakthrough reduction of the rolling resistance.

Approach:

The approach capitalizes on the recent advances in nanomaterial and graphene synthesis and functionalization to suggest a promising avenue for the amalgamation of cutting-edge nanotechnologies that can be utilized towards DOE's technical targets. Recent research efforts focus mainly on the development of composite tires based on carbon black and silica. The project goal is to replace existing fillers (such as carbon black and silica) with higher performance materials (viz., graphene and silica nanofibers). This project will be conducted in collaboration with Michelin Americas Research Company.

Results and Discussion:

The graphene nanoplatelets showed good dispersion in the elastomer. Silica nanofibers were successfully synthesized at ORNL using electrospinning process. The combination of the graphene nanoplatelets and silica nanofiber fillers improved the mechanical performance of the elastomer. It is feasible to achieve 4% reduction in the fuel efficiency and at the same time to enhance the mechanical performance of the tire. The target tangent delta value is 0.3. ORNL non-crosslinked composites exhibit tangent delta values of 0.13 (see Figure 1) and also improved the mechanical properties of the elastomer up to 20%.

Conclusions:

High performance materials (graphene nanoplatelets and silica nanofibers) were generated for this project. ORNL demonstrated the feasibility to fabricate composite elastomer materials with reduced hysteretic losses (sufficient to achieve at least 4% fuel savings), and also improved tear strength.

Figure on the Next Page

Figure:

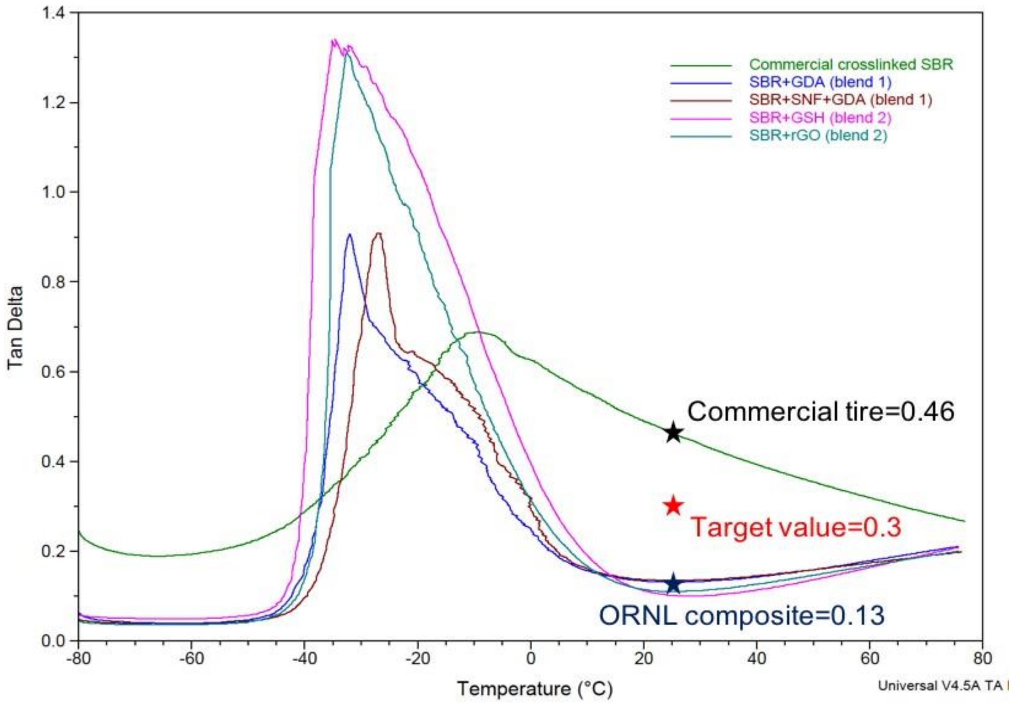

Figure 1: Tangent Delta of Synthesized Composites

Remainder of Page Intentionally Blank

This Page Intentionally Blank

AVPTA Technology Focus Area 4 Adjunct: Tire Efficiency

Advanced Truck and Bus Radial Materials for Fuel Efficiency

DOE-VTO TFA Lead: Dave Ollett
TARDEC TFA Lead: Dr. James Dusenbury

Principal Investigator:
Dr. Lucas Dos Santos Freire
PPG Industries, Inc.
Monroeville Technical Center
440 College Park Drive
Monroeville, PA 15146

Project Start: Oct 2014
Estimated Completion: Q2FY18

Objectives:

- Develop a novel surface-modified silica technology and demonstrate 4-6% improved fuel efficiency of Truck and Bus Radial (TBR) tires built from the technology.
- Proposed fuel efficiency increase will be achieved while maintaining or improving tear strength and tread wear.

Strategic Context:

- Reduce fuel consumption and logistics burden in operational theaters
- Increase Power Density and Energy Efficiency resulting in increased vehicle range, endurance and operational tempo.
- Increase fuel efficiency of ground vehicles to Reduce Life Cycle Costs
- Incorporate into Tactical Vehicles currently using Commercial Tires
- Leverage technology to develop for military specific tires

Accomplishments:

- Optimized silica tread compound formulation at the bench scale.
- Experimental Tire build (1st iteration).
- Developed prototype silica fillers with improved dispersion and lower tan delta values which correlate to 16% lower rolling resistance

Introduction:

Fuel-efficient silica fillers were adopted for passenger tires over 20 years ago. However, similar fuel-efficient benefits have not been realized for truck and bus radial tires. This project is focused on modifying silica to create an affinity for natural rubber as well as synthetic rubbers so that new, fuel-efficient truck and bus radial tires with optimized wear and tear properties result.

If half of the Class 8 vehicles on the road were to increase fuel efficiency by 4%, a potential 1.5 billion gallons of diesel, corresponding to $5.8B and 15 million metric tons of $C0_2$ emissions, could be saved.

Approach:

This project begins with the team systematically and thoroughly investigating the properties that enable uniform dispersion of silica in both natural and synthetic rubbers. This knowledge will drive custom silica synthesis. Once novel silicas are developed that can be uniformly dispersed throughout multiple rubber types, the team will develop new TBR tread compound formulas. The formulas will be tested at bench scale to predict performance with the best performers being built in actual tires so that on-tire testing can be completed. Two rounds of formulation and tire builds will be conducted during the project to confirm viability. At the conclusion of the project, the team will deliver prototype fuel-efficient tires and control tires. These tires will be evaluated at the Tank Automotive Research Development and Engineering Center (TARDEC).

This project will be conducted in close collaboration with Bridgestone Americas Tire Operations. Bridgestone’s technical lead is Mr. Paul Hamilton.

Results and Discussion:

Three silica parameters were evaluated on a Bridgestone tread formulation and optimized for lowest rolling resistance, similar hardness as control, processing, abrasion and tear strength. (See Table 1.)

PPG developed 2 prototype silicas which were used to produce tires at Bridgestone in the 295/75R22.5 size. Test results for the tires show that hardness and tear targets were achieved. See Table 2. The silica compound tires resulted in lower rolling resistance values of 14% and 16% versus the control. See Table 3.

Conclusions:

From the silica optimization studies, the tread formulation needs to contain 100% natural rubber for maintain tear resistance. The prototype silica used in the Bridgestone tire build produced up to 16% lower rolling resistant tires. Further adjustment to the compound formulation in the second tire build are needed to achieve the target value of 20% lower rolling resistance.

Tables Start on Next Page

Tables:

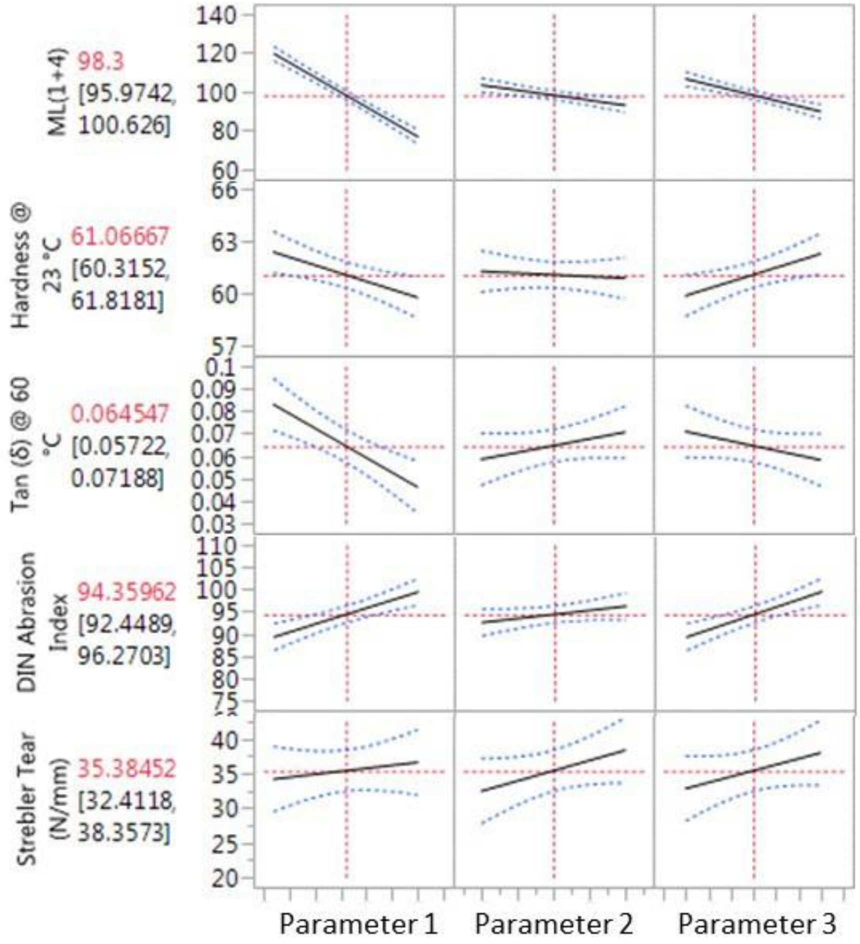

Table 1: Silica Parameter Optimization on Bridgestone Tread Formulation

Tables Continue on Next Page

	Parameter	CB control	BXR-990	BXR-991
Viscosity	ML1+4	100	112	114
Scorch	T50	100	82	82
	T90	100	96	91
Tensile at 25°C	Mod300	100	102	90
	Elongation	100	101	105
	Tensile	100	102	103
Temp. sweep	Tan δ @ 0°C	100	84	78
	E' @ 30°C	100	104	119
	Tan δ @ 60°C	**100**	**53**	**60**
Wear	Index	**100**	**90**	**93**
Hardness	Index	**100**	**108**	**109**
Tear at 25°C	Load	**100**	**95**	**108**

Table 2: Tread Compound Data

Test	Target	BXR-990	BXR-991
Hardness	± 10 %	108	109
Tear strength	± 10 %	95	108
RR	≤ 80 %	84	86
Lab wear	± 10 %	90*	93*

*Preliminary abrasion test

Table 3: Silica Tread Formulation Testing Results

Remainder of Page Intentionally Blank

Non-Rare-Earth Integrated Starter Generator

DOE-VTO TFA Lead: Susan Rogers
TARDEC TFA Lead: Dean McGrew

Principal Investigators:
Joshua Tylenda,
Joe Heuvers and
Dean McGrew
U.S. Army TARDEC
Ground Vehicle Power & Mobility

Project Start: Q1FY13
Estimated Completion: Q4FY18

Objectives:

- The TARDEC Advanced Propulsion Team, in collaboration with the DOE Vehicle Technologies Office, is working to develop and demonstrate two Integrated Starter Generators (ISG) without rare-earth permanent magnet materials suitable for onboard vehicle power generation.
- Most high-performance electric machines in hybrid electric applications use rare-earth magnets (NdFeB & SmCo) to achieve the required power and torque densities.
- This effort will additionally explore alternate electric machine topologies to achieve its targets and other specifications, Tables 1 through 3.

Strategic Context:

Through the Non-Rare Earth ISG project, TARDEC's strategy is to develop the following:

- Ability of the motors to meet the specified performance without the use of rare-earth magnetic materials.
- Ability to perform according to schedule given issues and delays that have emerged.
- Ability to minimize audible noise signature of the Switched Reluctance (SR) generator topology.

To help manage risks, weekly status meetings are held to allow issues to be surfaced in a timely manner and mitigations put in place to resolve them in order to maintain schedule. Additional contract actions are planned to address audible noise of the SR topology.

Accomplishments:

- The University of Akron completed the design, build and testing of the *Task 3* Switched Reluctance (SR) ISG optimized design with windowing and the *Task 4* SR ISG optimized design with skewing.
- The baseline Remy SR ISG was re-characterized for comparison with the optimized designs, and the modeling was improved to correlate acoustic noise in test versus in simulation. An acoustic chamber was built for test as well to isolate the sound produced by the SR ISG from external sources.
- The initial trade study for novel SR ISG designs was reopened to provide a more promising design for the third design optimization for the *Task 5* design, which shows potential in simulation for further reduction of acoustic noise beyond the skewed and windowed SR ISGs with an optimized distributed airgap design.
- The contractor presented at the Ground Vehicle Systems Engineering & Technology Symposium (GVSETS) in August 2017 on the topic of optimization methods for noise reduction in SR ISGs.
- The Non-Rare Earth effort is being augmented with an Army Small Business Innovation Research (SBIR) Phase II contract with Continuous Solutions to develop a 100kW inverter with active torque ripple mitigation to pair with a 100kW SR ISG. Threshold/objective goals include a decrease in 25%/50% of acoustic noise and torque ripple. Modeling and simulation, prototyping at a 15kW level, militarized build for shock, vibration and high temperature operation have been completed and are going into performance testing in Q1FY18. Scaling and performance validation of an additional unit sized at 100kW will occur later in FY18.

Introduction:

The Non-Rare-Earth ISG project has the opportunity to reduce the cost of high-performance power generation hardware. This project seeks alternatives to rare earth designs in case of a supply disruption of rare-earth permanent magnet materials similar to events in 2010-2011. In July 2010, China cut its exports rare earth minerals by 72%. In September 2010, China temporarily cut rare earth exports to Japan due to a maritime dispute. In 2011, China had cut exports further and raised export tariffs for rare earths. The world remains almost completely dependent on China for rare earths.

In 2010, The Department of Energy had published a Critical Materials Strategy, ranking Neodymium and Dysprosium among the most critical from an importance and supply risk perspective. Both materials are used in the highest performance Neodymium Iron Boron (NdFeB) permanent magnets available today, Figures 1 and 2.

Approach:

The project commenced with trade studies to identify the two most promising ISG architectures without rare-earth permanent magnets and to identify permanent magnet materials which could be leveraged for this effort. The two ISG architectures which were down-selected include the SR and Spoke Interior Permanent Magnet (Spoke IPM), Figure 3. The SR architecture does not include permanent magnets. The Spoke IPM is leveraging ferrite magnets which have approximately 1/10 the energy product of high performance rare earth magnets.

A study on permanent magnets revealed that ferrite and Alnico permanent magnets are the only non-rare-earth permanent magnets available in sufficient quantities to achieve the program goals, Figure 4. Due to the low coercivity of Alnico magnets, ferrite was determined to be the most promising choice for the design.

The SR ISG has emerged as the more promising of the two designs evaluated and now being built under the effort. The SR topology is more cost effective than any other known generator architecture - approximately 1/3 the cost of comparable rare earth permanent magnet based designs.

Results and Discussion:

Performance projections for the two ISGs based on Finite Element Analysis are shown in Figures 5 and 6.

Tasks 1 & 2 were closed out, with SR ISG and Spoke IPM builds, optimizations and testing completed.

The SR ISG resulted in better performance, and was chosen for *Tasks 3-5* for building additional ISGs with optimization for reducing audible noise as identified in the trade study.

The *Task 3* design used through windowing in the stator and rotor, as shown in Figure 7.

The *Task 4* design used skewing in the stator and rotor, and optimized at the skew angle of 13.75 degrees to maximize torque production while minimizing torque ripple. Models of this design are shown in Figure 8, as well as the machine's performance, Figure 9.

These tasks have both successfully completed build and test. The experimental noise result for the three ISGs is presented below at the rated condition of 800rpm, 1000Nm, which is the worst-case point for acoustic noise during operation, Figure 10.

The plot contained within Figure 11 shows the 800rpm, 600Nm point comparison, which shows more of a difference between machines, with a maximum 6-7dB decrease between the baseline SR ISG and the windowed SR ISG, and then again between the windowed SR ISG and the skewed SR ISG.

During test, it was discovered that tests results were not correlating as well as expected when compared to the simulations; upon further investigation, it was determined that adding radial force factor to the models significantly increased the fidelity of those models. If the windowed and skewed SR ISGs were to be redesigned, acoustic noise would likely be further reduced by using radial force in optimizing the design.

Conclusions:

Build and validation of the *Task 3* windowed SR ISG and the *Task 4* skewed SR ISG were completed in FY17. In comparison with the baseline, both SR ISGs improved upon the acoustic noise output, with the skewed SR ISG being more effective than the windowed SR ISG. *Task 5* for a distributed airgap rotor optimization has been awarded and will complete CDR in Q2FY18.

Future Direction:

Using lessons learned from the previous two SR ISG optimizations, this design is expected to reduce acoustic noise output further than the other optimizations. Build and test of the SR ISG will be completed near the end of FY18.

Figures and Tables:

	Objective	*Threshold*
Machine Dimensions		
Housing Outside Diameter	< 558 mm (22 inches)	
Overall Active Length	100 mm	120 mm
Power Supply		
Nominal Voltage:	600 V ± 35 V	
Thermal Requirements		
Liquid cooling	WEG / PWG	
Inlet Temperature	110°C	105°C
Cold Start Initial Condition	-50°C	
Maximum Flow Rate	< 30 LPM (8 GPM)	
Maximum Pressure Drop	16 PSI	
Operating Air Temperature	-50°C to 125°C	

Table 1. Technical Targets

	Objective	Threshold
Target performance		
Continuous Power	100 kW	
Max Operating Speed	4250 RPM	3200 RPM
Base (corner) Speed	800 RPM	1100 RPM
Continuous Torque (0-800 RPM)	1200 Nm	
Peak Torque (0-800 RPM)	1800 Nm	
Duration of Peak Torque	30 sec	
Torque Density		
Volumetric Torque Density	80 Nm/L	50 Nm/L
Gravimetric Torque Density	11 Nm/kg	7 Nm/kg
Power Density		
Volumetric Power Density	8 kW/L	5 kW/L
Gravimetric Power Density	1.2 kW/kg	0.8 kW/kg

Table 2. Performance Targets

Other
Compatible with SAE#1 Bell-housing. Designed for integration between Caterpillar C9 engine and Allison 3200SP transmission.
Waterproof (per 3.5.1.2 from MIL-S-3785E(AT))
Conform to MIL-STD-461F (EMC)
Resolver control hall-effect redundancy

Table 3. Other Specifications

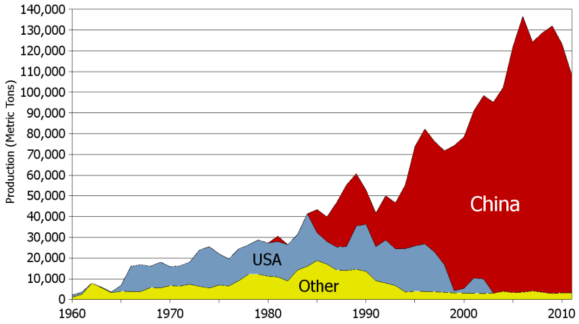

Figure 1. World-Wide Production of Rare-Earth Materials

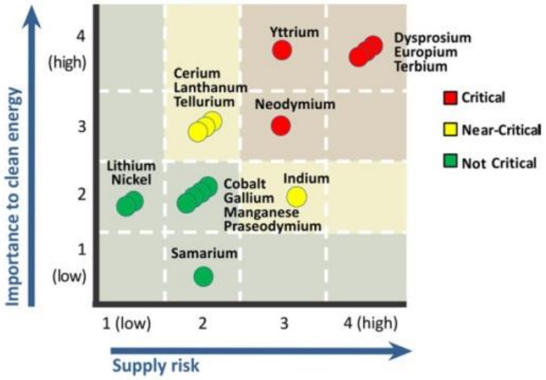

Figure 2. Department of Energy
Critical Materials Strategy

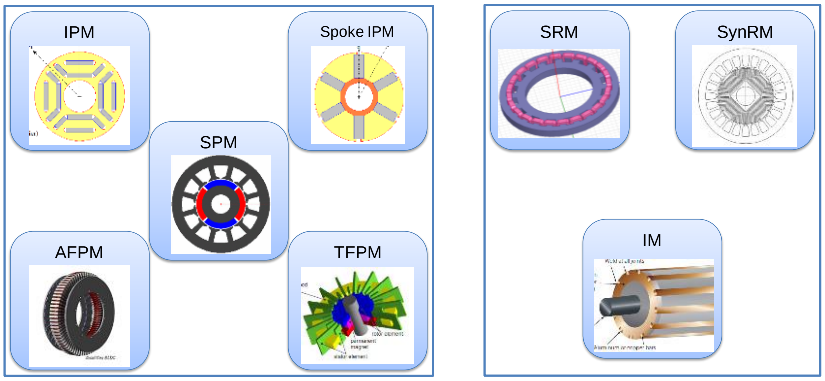

Figure 3. ISG Architectures

Remainder of Page Intentionally Blank

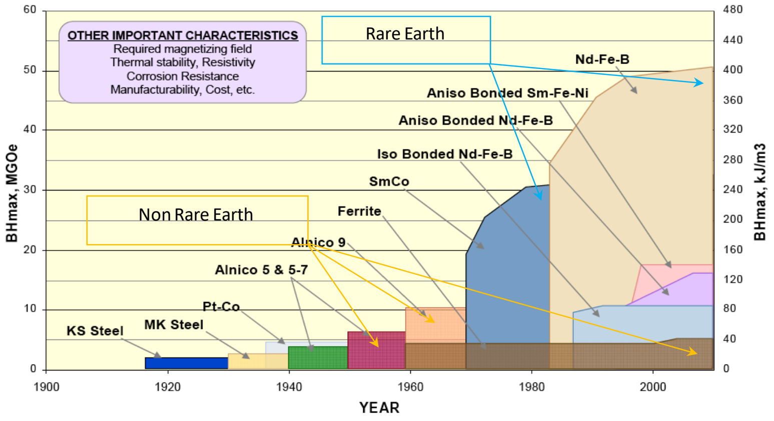

Figure 4. Non-Rare-Earth Permanent Magnet Quantities

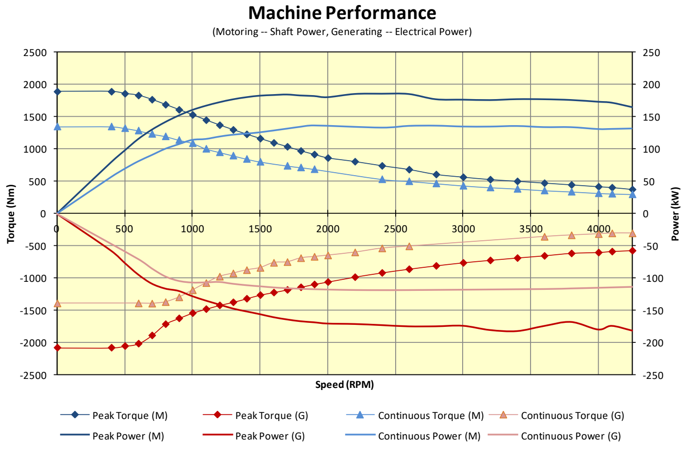

Figure 5. Characteristic Machine Performance

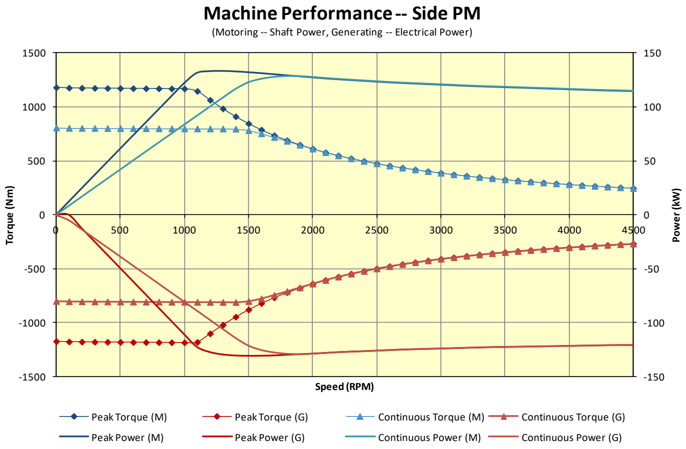

Figure 6. Side PM Machine Performance

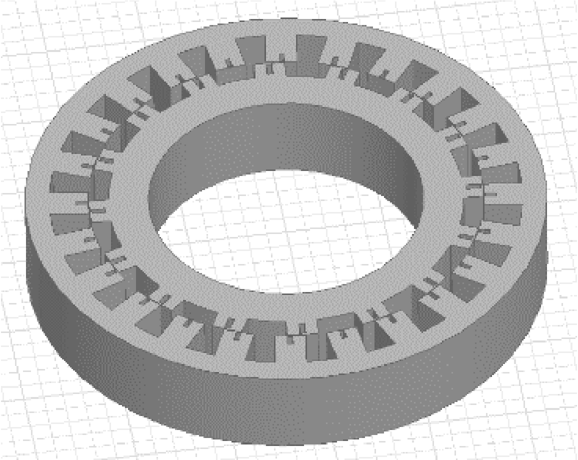

Figure 7. Windowed Stator and Rotor Design

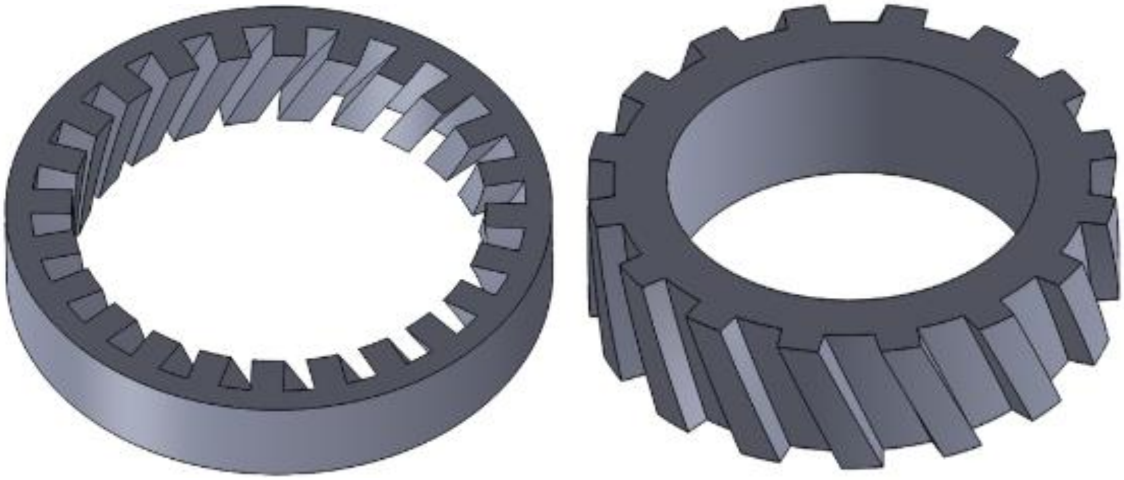

Figure 8. Skewed Stator and Rotor Designs

Remainder of Page Intentionally Blank

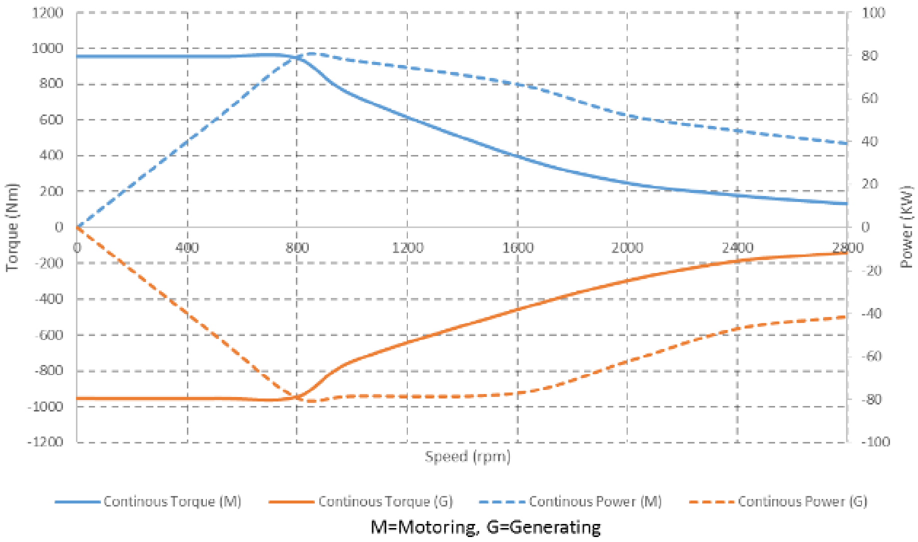

Figure 9. Performance of Skewed Stator and Rotor Design

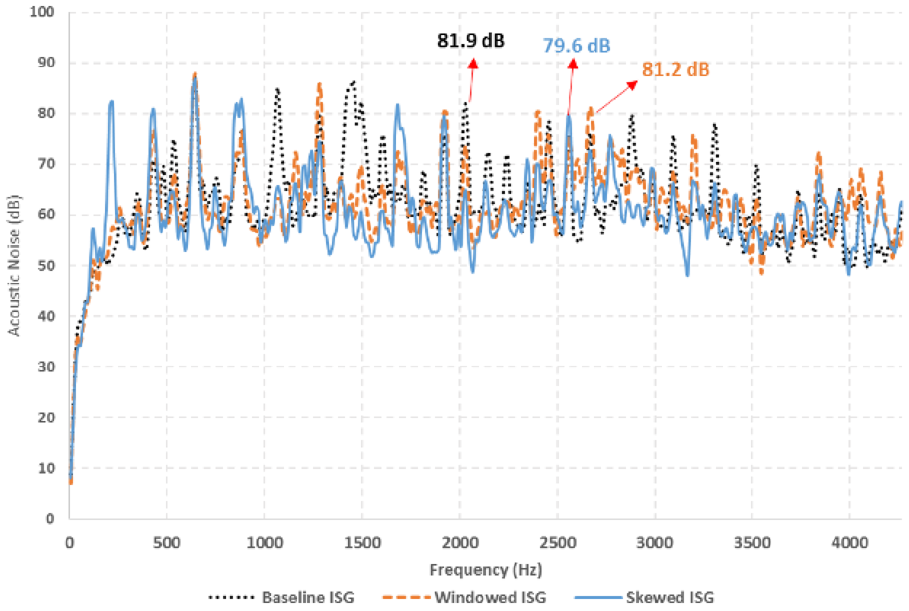

Figure 10. Experimental Noise Result for Three ISGs at 800 rpm and 1000Nm.

Figures Continue on Next Page

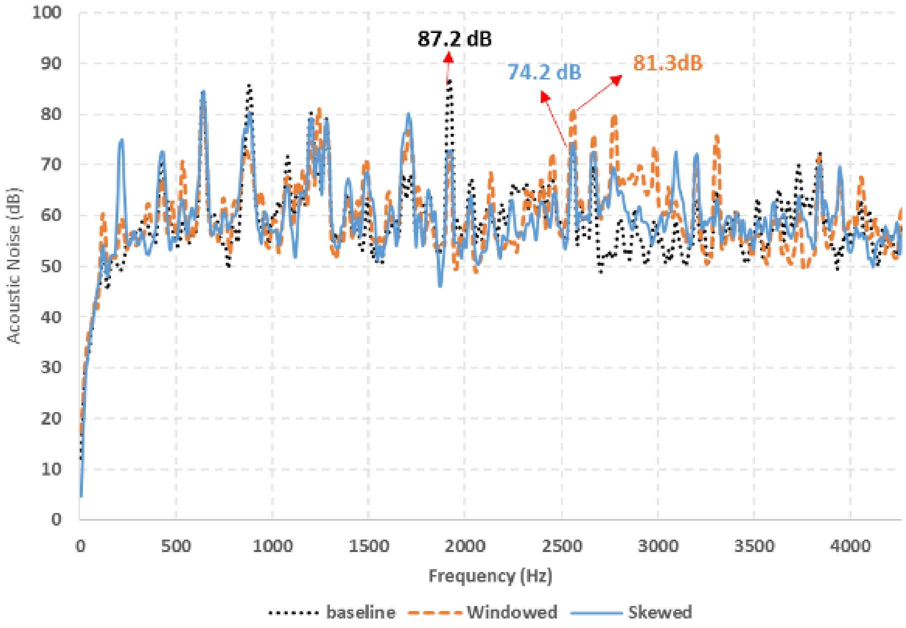

Figure 11. 800 rpm and 600 Nm Comparison Point Showing 6-to-7 dB Decrease between Baseline and Windowed SR ISGs.

<u>Remainder of Page Intentionally Blank</u>

AVPTA Technology Focus Area 6: Energy Storage & Batteries

Efficient Safety & Degradation Modeling of Automotive Li-Ion Cells & Packs

DOE-VTO TFA Lead: David Howell
TARDEC TFA Lead: Laurence Toomey

Principal Investigator:
Dr. Chao-Yang Wang
EC Power, LLC
341 Science Park Road,
State College, PA 16803

Project Start: Oct 2013
Project Completed: Q3FY17

Objectives:

- Develop an efficient pack-level safety and abuse model;
- Develop mechanism-based, fundamental models for accurately predicting degradation of Li-ion batteries under user-specified and wide-ranging temperatures and operating conditions;
- Perform co-simulation of our software with structural mechanics software via the Open Architecture Standard, developed by Oak Ridge National Laboratories;
- Perform testing and validate the cell and pack–level safety models and degradation models over wide-ranging temperature and operating conditions;
- Expand extensive materials database by experimentally characterizing and adding commercially-relevant cathode material; Lithium-Nickel, Cobalt and Aluminum-oxide (NCA), to our materials database including materials such as; Lithium-Nickel, Cobalt and Manganese-oxide (NCM).

Strategic Context:

- Key barriers to more widespread adoption of hybrid and electric platforms include challenges in the design of large-format Li-ion cells and packs related to performance, safety, life, and abuse.
- In this project, we are developing and refining commercial physics-based software tool that is directly aimed at helping cell manufacturers, the military, and automakers overcome these design challenges and barriers through an accurate and fast computer aided engineering tool.

Accomplishments:

- Completed cell and pack nail penetration tests
- Developed a nail penetration model and finished cell and pack model validation
- Completed cycle life tests of NCM111 and NCM622 cells for both high power and high energy types
- Developed a comprehensive cycle life model by incorporating the new crack formation-growth mechanism and completed model validation against four types of cells with both high power and high energy and two cathode materials, NCM111 and NCM622.
- Completed overcharge tests for both NCM and NCA cells
- Developed a new battery overcharge model and performed model validation against NMC/C cell data

Introduction:

This is an overall synopsis of the activities and accomplishments of the EC Power Computer-Aided Engineering of Batteries Phase 2 (CAEBAT2) project over the course of four years. The reader is referred to the previously submitted quarterly reports, review presentations, and Department of Energy Vehicle Technologies Office Annual Merit Review (AMR) presentations for further technical details. As highlighted by the numerous results shown herein and the volume and quality of the publications and presentations made in the course of this project, we feel that we have made a strong impact in the community.

Approach:

General model description:

Basic operating principles of a Li-ion battery

A Li-ion cell consists of three main components – a negative composite electrode (also known as the “anode”), separator, and a positive composite electrode (also known as the “cathode”). The basic cell structure and operating principle of a Li-ion battery. For illustration purposes, a Li-ion battery with graphite (Li_xC_6) anode and iron phosphate (Li_yFePO_4) cathode is shown.

During discharge, Li+ ions de-intercalate from Li_xC_6 solid particles in the negative electrode, travel through the liquid electrolyte across the separator into the positive electrode, and then intercalate into active material particles in the positive electrode, such as Li_yFePO_4. Electrons, blocked by the separator, are forced to travel an opposite route from Li+ ions and pass through an external circuit. Electronic current is collected from the electrodes and sent to the battery terminals via a copper foil attached to the negative electrode and an aluminum foil attached to the positive electrode. During charging of the cell, the opposite process occurs, with Li+ ions traveling from the positive electrode to the negative electrode, through the electrolyte. Full cells are built by either spirally winding long thin sheets into a cylindrical/prismatic shape or alternately stacking anode and cathode plates into prismatic shape.

The electrochemical reaction occurring at the solid/electrolyte interface of the negative electrode Li_xC_6 particles is

$$Li_xC_6 \underset{ch}{\overset{dis}{\rightleftharpoons}} Li_0C_6 + xLi^+ + xe^- \quad (1)$$

while the corresponding reaction at the solid/electrolyte interface of the positive electrode particles (e.g. $LiFePO_4$) is

$$FePO_4 + yLi^+ + ye^- \underset{ch}{\overset{dis}{\rightleftharpoons}} Li_yFePO_4 \quad (2)$$

The electrodes are porous, with active material (solid particles) for storing the Li+ ions. The solid particles are surrounded by either a liquid or gelled electrolyte solution responsible for transporting Li+ ions across the separator to the opposite electrode. Cell performance during discharge and charge of Li-ion cells is dictated by kinetics of Li+ intercalation/de-intercalation at active material particle surface, Li+ diffusion inside solid particles, electrolyte transport under concentration gradients, and electron transport in the electrodes. Owing to inefficiencies associated with electrochemical reaction and transport processes, heat is generated during cell operation that needs to be effectively dissipated from cell surface during operation. As thermal feedback has a strong effect on the operating performance of Li-ion batteries – especially large-format Li-ion batteries – properly modeling this thermal feedback is essential for capturing, for example operation in sub-freezing environments [2] and safety events that lead to thermal runaway [3]. These types of automotive applications necessitate a Thermally Coupled Battery (TCB) approach to modeling Li-ion batteries.

Thermally Coupled Battery (TCB) model

EC Power has developed the AutoLion™ software suite based on the Electro-Chemical-Thermal (ECT) coupled modeling approach that we refer to as thermally coupled battery (TCB) modeling. The TCB modeling approach has its roots in the isothermal model of Doyle and Newman [4], and substantial extensions through the electrochemically and thermal couplings by Gu and Wang [5], Srinivasan and Wang [6], and Smith and Wang [7]. The TCB modeling approach includes the following physico-chemical phenomena: Li intercalation/de-intercalation reactions at the electrode/electrolyte interface, transport of charge in both solid materials and electrolyte, transport of species (both neutral and ionic) by migration, diffusion and/or convection with the latter possibly induced by electrolyte flow due to electrode volume change, solid-phase Li diffusion in active materials, and thermal behaviors.

In a Li-ion battery, the thermal effects are strongly coupled with electrochemical processes. As shown in Figure 1, the tight ECT coupling is a principal feature captured in AutoLion™ by the TCB modeling construct, and is critically important in being able to capture automotive-relevant simulations, such as the dynamics of cell shorting [3] and operation in subfreezing environments [2]. Figure 1 highlights how these two factors complement each other: the heat generated by the cell electrochemical processes feed directly into the thermal energy equation (via heat source term), and as temperature changes, it feeds back into to the electrochemical process via the temperature-dependent, physico-chemical properties. The successful implementation of the TCB modeling construct in AutoLion™ hinges on two critical factors: (1) an efficient and robust set of numerical algorithms to resolve strongly nonlinear couplings of the electrochemical and thermal equations, and (2) an accurate description of the battery's material properties over a wide range of conditions.

Governing equations

A brief summary of the ECT3D governing equations are described here. The solid-phase conservation of charge, electrolyte-phase conservation of charge, and electrolyte-phase Li+ species conservation equations are discretized in the three dimensions for the cell using a finite control volume approach. The active material Li species conservation equation is discretized in the radial direction of a representative active material particle. Further, in ECT3D, the energy equation is solved locally, as controlled by the macro thermal mesh, which includes discretization within the battery's anode/separator/cathode sandwich.

Using the TCB construct, there is no assumed or grossly approximated heat source. In the energy equation there are four heat sources: q_r is the reaction heat, q_j is the joule heat, qc is the heat generation due to contact resistance, and q_e is the entropic heat. The reaction heat, joule heat, and entropic heat are calculated based on the local electrochemical conditions across the anode/separator/cathode sandwich; the local heat terms themselves are directly related to the output of the electrochemical equations, such as solid and electrolyte potential, and electrolyte concentration. The contact heat is determined from user-defined contact resistance of the given cell. The entropic heat is a thermodynamic property of the active cell materials, and is given by the materials database or user-input properties. For further details, the reader is referred to [10]. Butler-Volmer and Tafel equations, as appropriate, are used to model the reaction rates and the corresponding species source terms, j_{Li}. Note that in AutoLion™, there is no simplified treatment (e.g. linearized analytical or quasi-analytical solution) of solid diffusion in the active material particles. A numerical solution to the non-linear solid-phase diffusion equation (with $D_s = f(c_s,T)$) is performed.

AutoLion™ is largely based on the work of Gu and Wang [5], Wang and Srinivasan [6], Smith and Wang [7], and Fang et al. [10]. The reader should see these references for additional modeling details. One major benefit of AutoLion™'s TCB model as opposed to most Pseudo-2D or Newman-type models is that AutoLion™ utilizes a *fully coupled* electrochemical and thermal method. As a result, AutoLionTM can capture the voltage recovery period often seen in battery discharge from subfreezing temperatures. The TCB approach is also essential for the simulation of, for example, low-temperature operation of Li-ion batteries [2] and safety events [3]. Under these conditions it is critical to account for the materials' strong coupling to temperature. This is shown in a discharge of an 18650 NCM/graphite cell at initial and ambient temperature of -25°C for several convection heat transfer coefficients, indicating different cooling conditions for the cell. An isothermal model is incapable of predicting the voltage recovery that is observed under cell self-heating conditions, let alone the substantial differences in discharge performance for different heat transfer conditions.

In order to realize efficient simulation of large-format Li-ion batteries and packs, ECT3D employs a three-grid mesh, comprised of a macro-grid, a meso-grid, and a micro-grid. The thermal field (equation 7) is solved on the macro-grid, the electrochemical transport phenomena (equations 3, 4, 5) is solved on the meso-grid, and the solid-state diffusion inside active material particles (equation 6) is solved on the micro-grid. Note that there is one representative active material particle present within each meso-grid control volume, where active material is present (in the anode and cathode regions). With the TCB modeling construct there is a great deal of information passed between various grids. For example, the meso-grid calculations pass the rates of heat generation to the macro-grid, and the macro-grid passes the resulting temperature value to the meso-grid calculations. Further, the meso-grid model passes the reaction current to the micro-grid, and micro-grid passes the surface concentration at the solid particle/electrolyte interface to the meso-grid.

The macro-grid takes into account all of the detailed geometries of components of the large-format cells and packs, including all coolant flow and related components in the battery pack. ECT3D internal algorithms automatically generate the meso and micro-grids from the macro-grid mesh with a simple zone numbering scheme outlined in the user guide. All the governing equations (equations 3 through 7) are solved at one time step. Equation 7 is solved by the Computational Fluid Dynamics (CFD) solver on the macro-grid level. Equations 3, 4, and 5 are solved on meso-grid level, and equation 6 is solved on the micro- grid level. All equations are solved using a finite-volume scheme. The thermal macro-grid mesh is generated by the user, to the appropriate resolution required by the cell and/or pack design. Using the AutoLion™ Graphic User Interface (GUI), the user can specify the number of control volumes used in the macro- and micro-grid meshes. Further details of the user control are given in the user's guide, section.

Materials database

EC Power has developed and implemented in ECT3D an extensive materials database for a wide range of materials commonly used in commercial applications, such as $LiCoO_2$ (LCO), $LiFePO_4$ (LFP), $LiNi_{0.33}Mn_{0.33}Co_{0.33}O_2$ (NCM), $LiMn_2O_4$ (LMO) cathode materials, and graphite (LiC_6) and $Li_4Ti_5O_{12}$ (LTO) anode materials, in addition to electrolyte properties. The material properties have been measured as a function of temperature (-30°C < T < 60°C) and electrolyte concentration.

For this project, we completed characterizing commercially widely-used NMC622 and NCA cathode materials (-40˚C < T < 60˚C) and added material properties to the previously developed extensive material database. We also added the anode material Si to the database after successful implementation of new performance and ageing model including effects of active material swelling.

Pack-level safety and abuse modeling:

Li-ion cell safety is one of the technological hurdles for the widespread use of large-format cells in automotive applications. ECT3D, owing to its thermally coupled battery modeling framework is ideally suited for comprehensive large-format cell safety simulations. Based on the previous version of ECT3D, which is capable of simulating full nail penetration, external short, and internal short in a cell with prismatic stacked electrode design, we have extended our safety capabilities to include a truly deterministic pack model safety simulation, where the user inputs nail/short properties, location, nail speed, etc., for a cell in the pack, and can use the tool to investigate how the safety event propagates though the pack both thermally and electrochemically. Completed cell and pack level safety simulation capability make ECT3D an attractive tool to cell/pack abuse testing.

Figure 2 outlines the cell/pack nail penetration experimental setup. We have obtained results from the nail penetration process for single cell and 1S3P[a] pack respectively. The validated simulation results reveal the reason that nail penetration of a 1S3P pack is much more dangerous than a single cell (Fig.3, 4, 5).

[a] Within 1S3P: S is the number of cells or pairs of cells within the battery pack, P is the number of cells in parallel within the series cells.

Overcharge Modeling:

Overcharge can occur if the control electronics of the Battery Management System (BMS) malfunction. It can also occur if there is severe cell imbalance in a battery pack. The thermal response of Li-ion cells during overcharge is largely determined by the cathode chemistry. Measurements of heat flow from the cells have shown that there is a rapid increase in heat generation when all of the lithium has been removed from the cathode. Overcharge may also cause plating of lithium in the graphitic anode, which not only leads to capacity loss but may also induce internal short-circuit due to the growth of lithium metal dendrite.

Safety associated with Li-ion cell overcharge is a very important issue for Hybrid Electric Vehicle (HEV) and Electric Vehicle (EV) applications. Tolerance to overcharge depends strongly on charge rate and battery chemistry, particularly the cathode chemistry. During charge, cathode oxide material is delithiated. Different cathode materials have different residual stoichiometry of Li at 100% State of Charge (SOC), e.g. $Li_{0.0}FePO_4$ and $Li_{0.48}Ni_{1/3}Co_{1/3}Mn_{1/3}O_2$. Further removing Li from cathode material may result in crystallographic changes in structure, releasing a large amount of heat and leading to cell thermal runaway. Overcharge of Li-ion cell triggers complex reactions, such as electrolyte decomposition and gas evolution, further leading to heat and pressure build-up within the overcharged cell. The present work simulates thermal and electrochemical consequences of overcharge. Two cells, NCM 2.0Ah and NCA2.8Ah, were tested at different charging rate and temperature. The experimental setup for all overcharge tests is shown Figure 6. The rest are the experimental and model predicted results. Overcharge model of maximum temperature and temperature dynamics show good overall match with the experimental data (Figures 7, 8, and 9).

Cell Life Testing:

Extensive cycling tests have been performed to collect data for NCM111 and NCM 622 cells for model validation. Testing procedures and setup are pictured in Figure 10. We used the 3-electrode cell to investigate the separate the contribution of positive/negative electrode to cell degradation. Li reference electrode works very well. In order to identify degradation mechanisms of NMC/graphite cells and investigate the effect of electrode loading (or thickness) on cycle life, both high energy and high power cells are tested. The sketches and features for high energy and high power cells are list in Figure 11 and12. For NCM 111 ($LiNi_{1/3}Co_{1/3}Mn_{1/3}O2$), mass capacity is 155 mAh/g rated at C/3. For NMC 622: ($LiNi_{0.6}Co_{0.2}Mn_{0.2}O2$), mass capacity is 172 mAh/g rated at C/3. The High energy cell has electrode mass loading ~20/12 (C/A) mg/cm^2. The High power cell has electrode mass loading ~10/6 (C/A) mg/cm^2.

Cell Life Modeling and Validation:

The AutoLion™ Cycle life modeling frame work includes the Solid Electrolyte Interphase (SEI) growth on anode, film growth on cathode, and active material isolation (detaching away from binder/filler matrix) on both anode and cathode. As active material particle swell and shrink with lithiation, active material particles cracks with cycling. This aging mechanism was not considered in the current frame work. Thus, in this work we have incorporated Electrode Structure Degradation (ESD) and its dependence on electrode loading or thickness. In this model, we assume that stress formation and development in thick electrodes, causing crack propagation in graphite particles. Lithium is lost due to formation of SEI layers on the newly cracked surfaces.

Our new model of degradation starts from prediction of stress evolution during battery cycling, estimation of crack propagation and the ensuing area of newly exposed surfaces, and then followed by determination of loss of active cyclable lithium. Representative comparisons of the model prediction with charge-discharge performance at the beginning of life are shown in Figures 13-18 for NCM111/C and NCM622/C (high energy and high power) cells. Excellent agreement is found under a wide range of operating conditions. Experimental validation of the new degradation model against NCM111/C and NCM622/C (high energy and high power) cell data are obtained. Again, good agreement is achieved in cycle life model validation.

This model along with previously developed SEI layer model and oxide film growth model provides a comprehensive degradation model that can predict the electrode thickness effect on battery cycle life.

Coupling of ECT3D with Structural Mechanics Model via Open Architecture Standard (OAS)

In this task, we used the solid DisplacementFoam solver (OpenFoam 2.3) to do the linear stress analysis for the battery. Through this co-simulation, we have investigated thermal stress/strain field due to volume change of active materials, studied effects of constraint boundary condition to assess any difference between soft pouch and hardcase prismatic cells.

Representative results from this simulation are shown in Figures 19 and 20. The rigid packaging causes 120 times more stress than soft packaging due to thermal expansion alone. Thus during the cell/pack design, reserving extra room for battery volume expansion is significantly important. As the cell manufacturer try to pack more energy into the cell/pack, the reserved room becomes smaller and smaller. If there is no enough space to accommodate cell expansion, the increase pressure within the cell might develop to separator puncture, leading to thermal runaway.

Results and Discussion:

In addition to the successful completion of the primary goals and tasks of this project, we were able to successfully apply previously validated safety model towards the project goal. First we study the soft and hard shorting during charging. Then we apply the battery safety model to discover a safer battery structure for large EV cells.

Additionally, numerous papers and presentations were made through this project, and we have listed those below in order to emphasize the impact of this project work.

Soft vs hard internal shorting during charging:

The recent Samsung Note battery incidents indicate that soft internal shorting could become a huge hazard in presence of battery charging (connected to a wall socket). Similar problems could occur in electric vehicles (garage charging overnight). We use the validated safety model to elucidate this problem and identify the map of safety. Here we simulate the internal shorting under the condition of Constant Current and Constant Voltage (CCCV) charging process. It is shown that two different scenarios might occur depending on the magnitude of the shorting resistance (i.e. soft shorting or hard shorting).

We illustrates the current flow path in the internal short-circuit process, where a Short-Circuit Object (SCO) is embedded within one electrode layer of the cell. The SCO creates a short circuit and current loop within the electrode layer where the SCO is located. This electrode layer not only discharges its energy to itself, it also serves as a load to the other electrode layers without a SCO inside.

We calculated the voltage evolution for 10 mΩ cases. It is found that the cell voltage is very low for the internal shorting only case. The charging voltage for the charging case is only slightly higher (around 170mV). This higher voltage is required in order to keep the 1C charging current. We looked at the current responses for 10 mΩ cases. The current is defined as the total current flow through the SCO in this study unless noted. The difference between the two current responses is very close to the 1C charging current (8A). The reason can be easily explained by looking at the current flow path for the internal shorting process with constant current charging for small shorting resistance (10 mΩ). Due to small charging voltage, all of the cell layers are in the discharging mode. The current flow path is the same as the internal short only cases. The charging current is superimposed on the internal-short process. The 1C charging current only flows through the SCO. Due to the additional charging current, the temperature at the shorted location for the charging case is 70K higher than that of the internal shorting only case.

We also studied the voltage evolution for 2Ω cases (when there is a loose contact during soft shorting). For the internal shorting only case, the cell voltage shows a typical discharge curve when the load resistance is relatively large. However, the cell voltage for the charging case shows a typical voltage response under CCCV charging process: the cell voltage increases with time initially, and then remains at a constant value (4.2V). Even during the internal shorting process, the cell still can be charged. The current flow through the SCO is about 1.6A for the internal shorting only case. The SCO current (around 2.1A) can be roughly estimated using the charging voltage and shorting resistance for the charging case. Like a normal cell charging process, the current flow pattern is totally different from patterns. Only part of the total charging current (around 2.1A) flows through the SCO. The rest of the charging current flows through the cell layers as the reaction current. With regard to the temperature evolutions for 2Ω cases, since the SCO current of the charging case is much larger than that of the case without charging, the temperature at the shorted location for the charging case is much higher than that of the internal shorting only case. It is seen that the maximum temperature in the case absent of charging is around 125˚C, perhaps still within the limit of battery safety without causing deformation of the separator and decomposition of the electrolyte. On the other hand, in the presence of charging, the maximum temperature rises above 170˚C, exceeding the limit of battery safety. Here lies a major difference in the consequence of soft shorting with and without charging current. Safety simulation appears to have explained the dramatic effect of charging current on a soft-shorting scenario of a Li-ion cell.

Safer cell structure for large EV cells:

A larger cell capacity leads to more dangerous conditions upon internal short, simply by having greater energy to be dissipated during the short. In our safer cell design concept, we divide the one single cell into multiple zones by coating the Positive Temperature Coefficient (PTC) material on the tabs. This zone defense mechanism will turn off the energy release from the neighboring zones when internal short occurs.

In order to validate the new design, we apply our battery safety model to a 32Ah NCM/C cell. The cell has dimensions of 150mm × 100mm × 11mm. It is found that the new design concept can successfully reduce the cell temperature to the safe level with a few seconds.

Conclusions:

Over the past 3+ years the EC Power-led CAEBAT2 team has worked to fulfill the goals laid out at the beginning of the project. The team has met and in some cases exceeded these goals. We have accomplished the following major milestones:

- Expanded extensive materials database by characterizing and adding NCM622 and NCA cathode materials and Si/C anode material.
- Completed cell and pack nail penetration tests.
- Completed development of a nail penetration model and finished cell and pack model validation.
- Completed cycle life tests of NCM111 and NCM622 cells for both high power and high energy types.
- Developed a comprehensive cycle life model by incorporating the new crack formation-growth mechanism and completed model validation against four cells with both high power and high energy types and two cathode materials, NCM111 and NCM622.
- Completed overcharge tests for both NCM and NCA cells.
- Developed a new battery overcharge model and performed model validation against NCM and NCA cell data.
- Completed coupling of ECT3D with structural mechanics model via Open Architecture Standard (OAS).
- Investigated the soft and hard shorting during charging using validated safety model.
- Validated a safer battery structure for large EV cells using validated safety model.

We feel that most importantly, the project has been successful in two aspects:

- The project and project funding has led to a more refined ***commercial Li-ion battery design software*** that cuts cost and time from the design phase of automotive Li-ion batteries and packs. It will continue to make an impact in the battery and automotive

community, well beyond the close of this project. Our ***commercial Li-ion battery design software*** with above-mentioned expanded capabilities is being used by defense and aerospace industries.
- The team has been active in ***publishing, presenting, and sharing the results*** from the project to the battery and automotive community at large, thereby making an impact on the ***progression of automotive large-format Li-ion battery technology***.

As these successes, in addition to the other successful activities and outcomes of the project, are in line with the overarching goals of the CAEBAT2 program, we feel that this project can be deemed a success.

References:

[1] M. Anderson, "Energy System for Large Displacement Unmanned Undersea Vehicle Innovative Naval Prototype (INP)," US Office of Naval Research Presentation, http://auvac.org/publications/view/158 (2011).
[2] Y. Ji, Y. Zhang, and C.Y. Wang, J. Electrochem. Soc., 160, A639 (2013).
[3] C.E. Shaffer, C.Y Wang, G. Luo, and W. Zhao, "Safety Analysis Design of Lithium-ion Battery EV Pack through Computer Simulation" Battery Safety 2012, Knowledge Foundation Conference, December 6-7, 2012, Las Vegas, NV
[4] M. Doyle, T.F. Fuller, and J. Newman, J. Electrochem. Soc. 140, 1526 (1993).
[5] W.B. Gu and C. Y. Wang, "Thermal and electrochemical coupled modeling of a lithium ion cell", in Lithium Batteries, ECS Proceedings, 99-25, 748 (2000).
[6] V. Srinivasan and C. Y. Wang, J. Electrochem. Soc., 150, A98 (2003).
[7] K. Smith and C. Y. Wang, J. Power Sources, 160, 662 (2006).
[8] Joan Lowy, The Boston Globe, "FAA set to lift grounding order on 787s", April 20, 2013.
[9] Yancheng Zhang, Chao-Yang Wang, Xidong Tang, Journal of Power Sources, 196 1513, 2011.
[10] W. Fang, O.J. Kwon, and C.Y. Wang, Int. J. Energy Res., 34, 107 (2010).
[11] Y.T. Cheng, M.W. Verbrugge, J. Power Sources 190 (2009) 453e460.

Figures Start on Next Page

Figures:

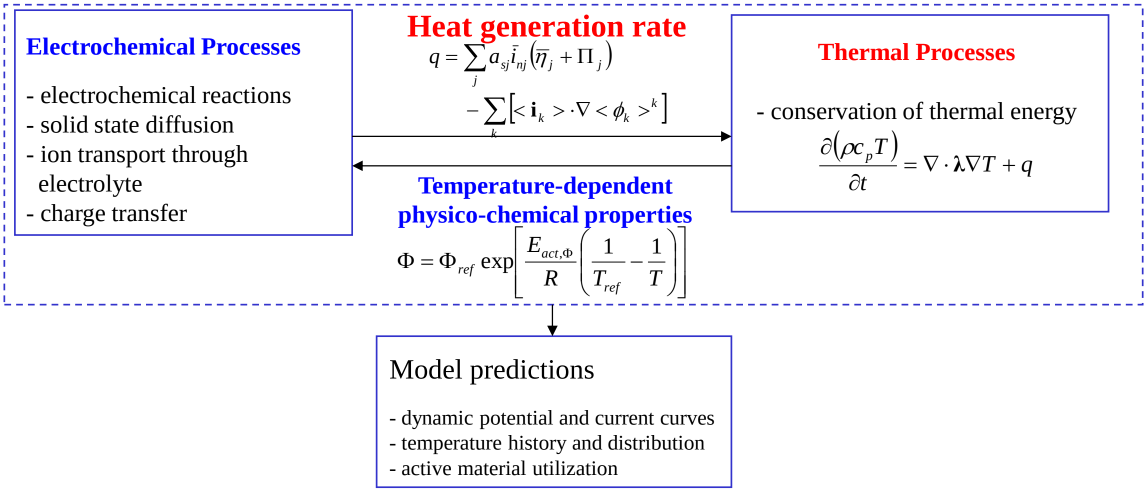

Figure 1. Summary of the thermally-coupled battery (TCB) modeling approach.

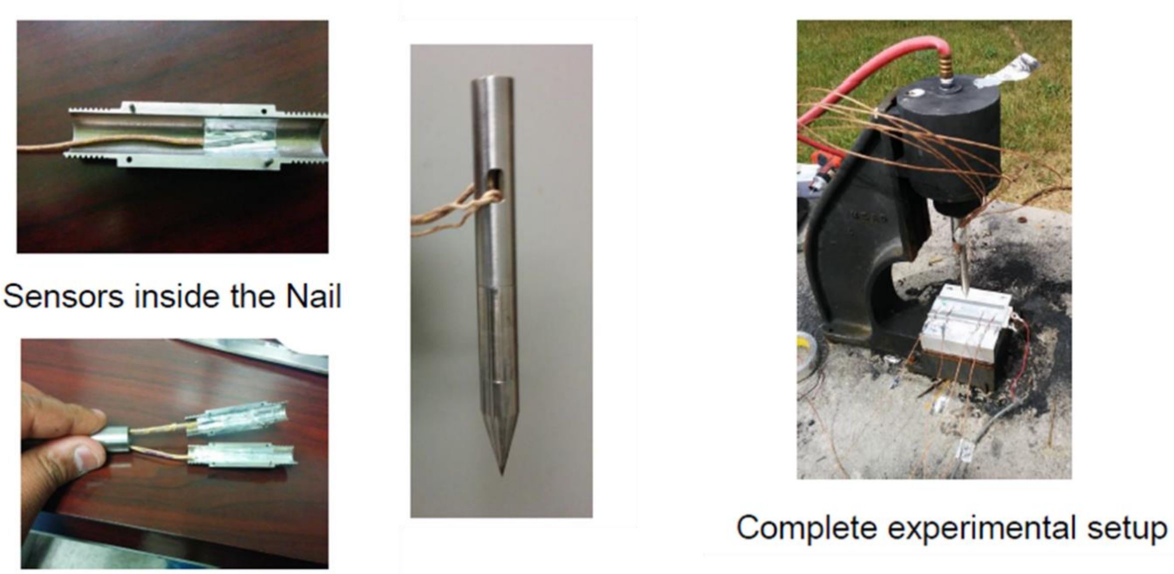
Sensors inside the Nail

Complete experimental setup

Figure 2. Cell/pack nail penetration setup

Figures Continue on Next Page

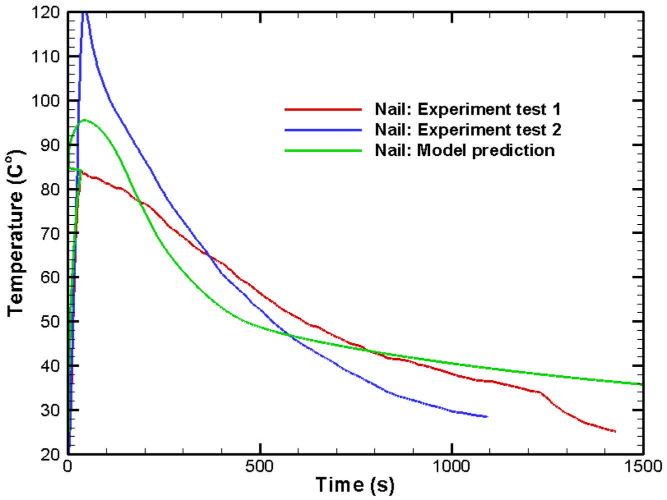

Figure 3. Predicted and measured temperature evolution for a single cell during nail penetration

Figures Continue on Next Page

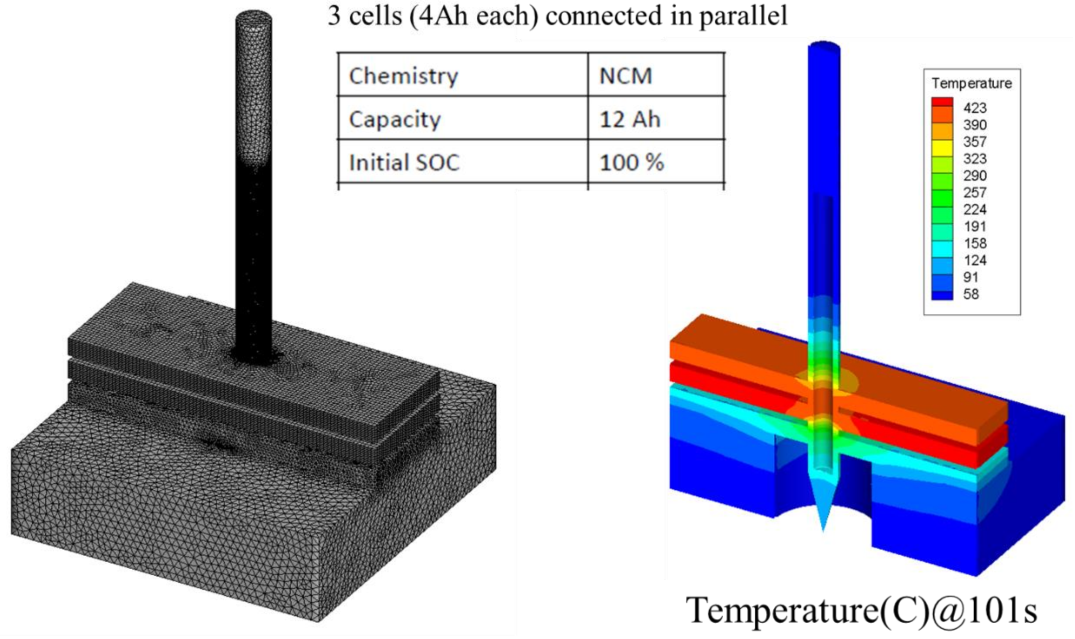

Chemistry	NCM
Capacity	12 Ah
Initial SOC	100 %

Figure 4. Nail penetration mesh setup and simulation results for a 3-cell pack

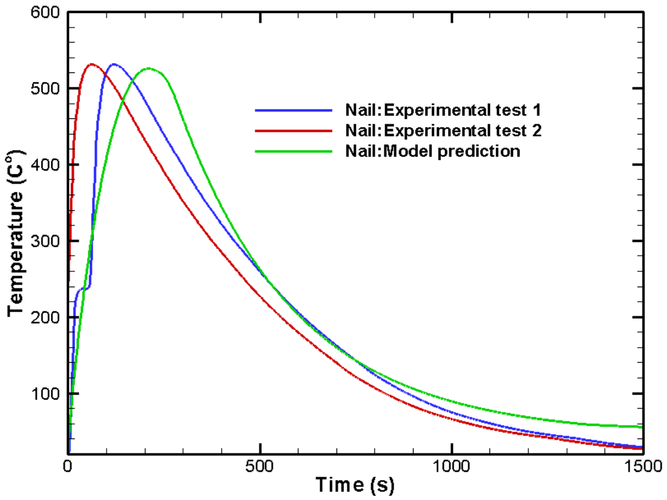

Figure 5. Predicted and measured temperature evolution for a single cell during nail penetration

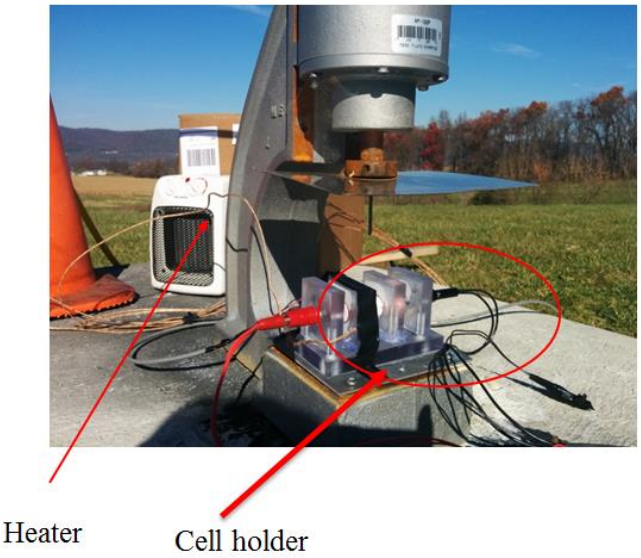

Heater was used to raise the temperature

Dry ice was used to reduce the temperature

Figure 6. Experimental setup for battery overcharge test

Figures Continue on Next Page

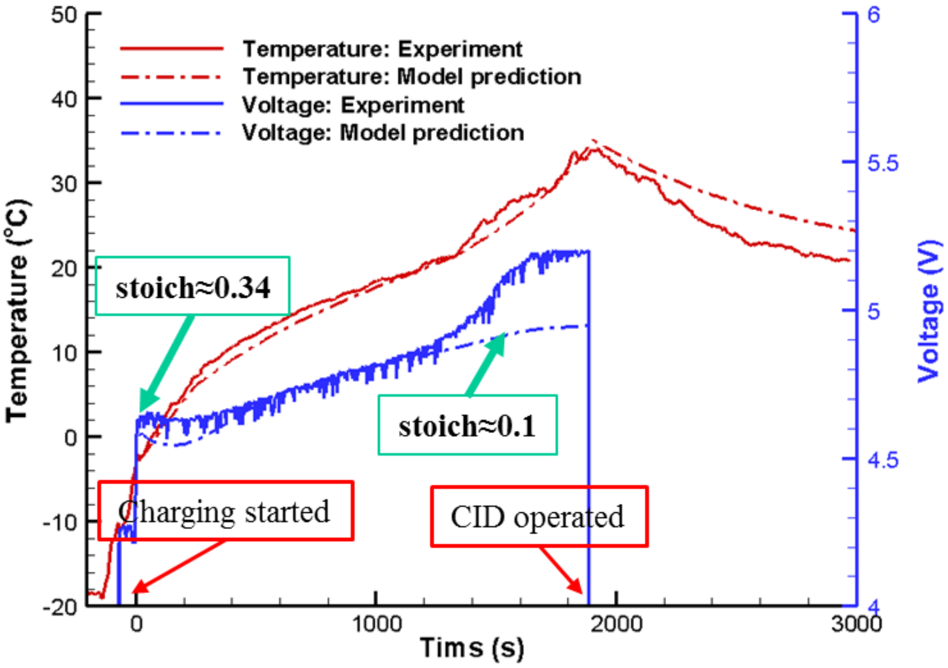

Figure7. Experimental and predicted overcharge results for NCM at -20ºC with 1C charging current

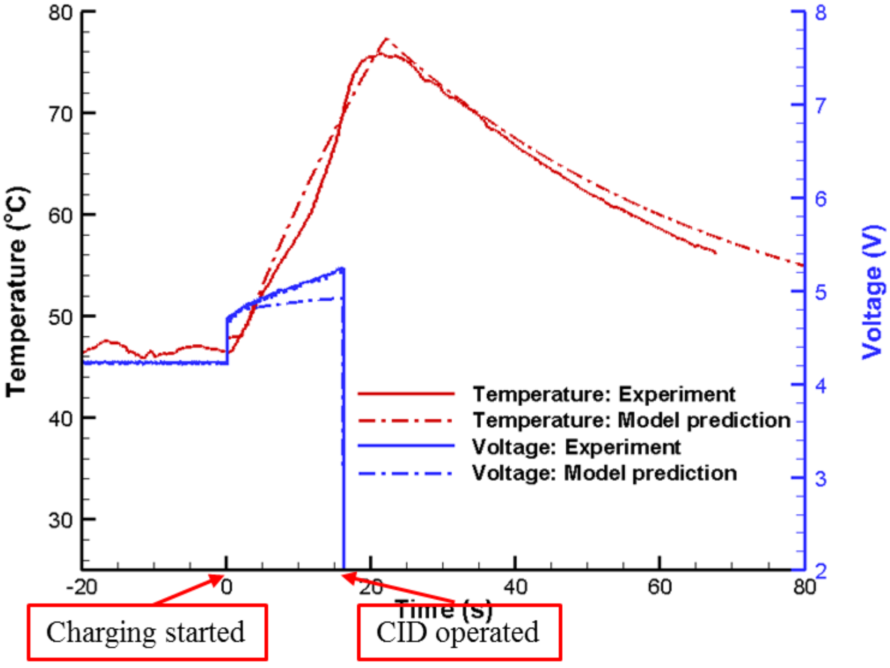

Figure 8. Experimental and predicted overcharge results for NCM at 45ºC with 10C charging current

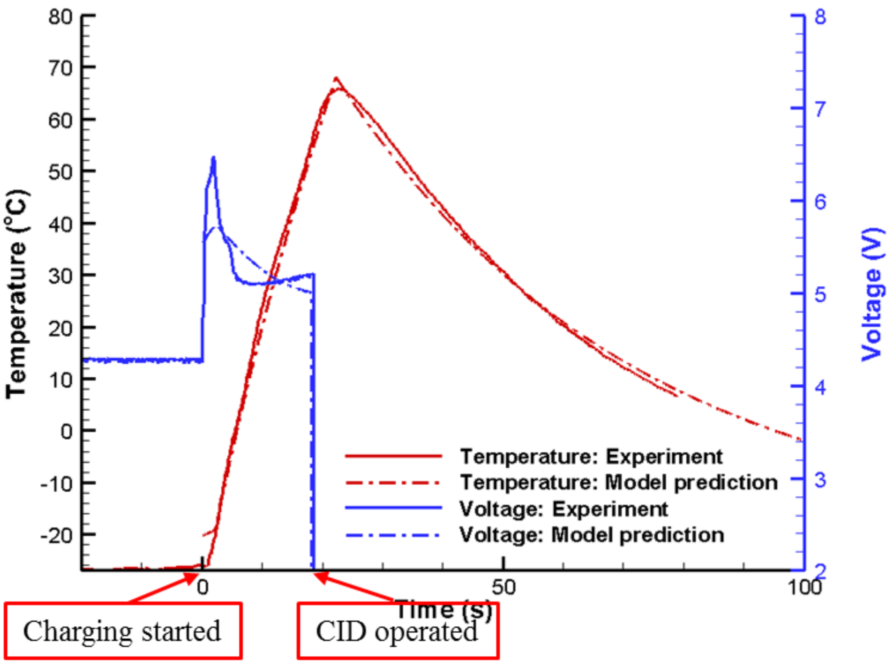

Figure 9. Experimental and predicted overcharge results for NCM at -20ºC with 10C charging current

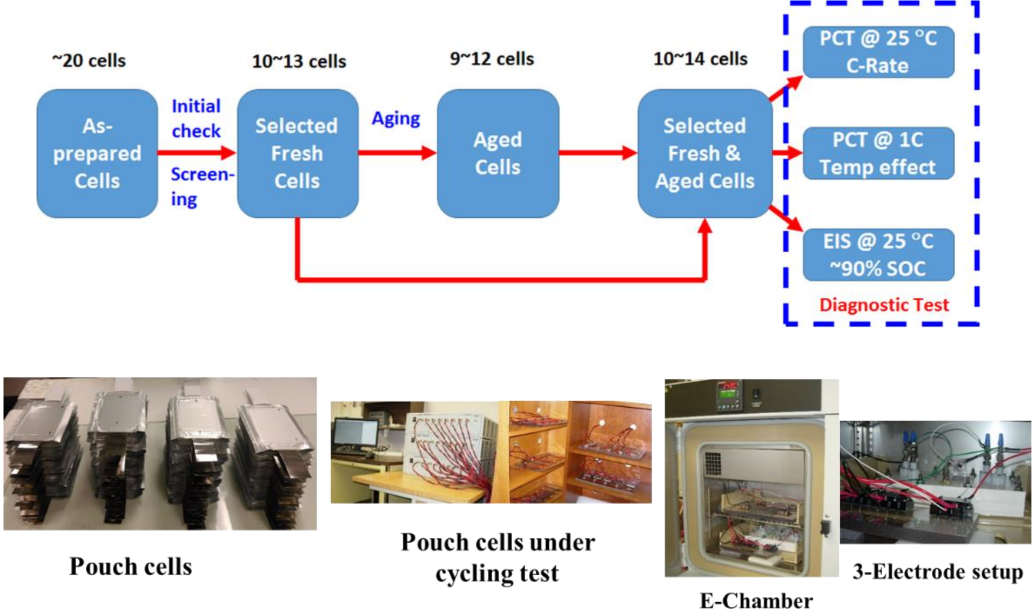

Figure 10. Experimental procedures for cycle life studies

Figures Continue on Next Page

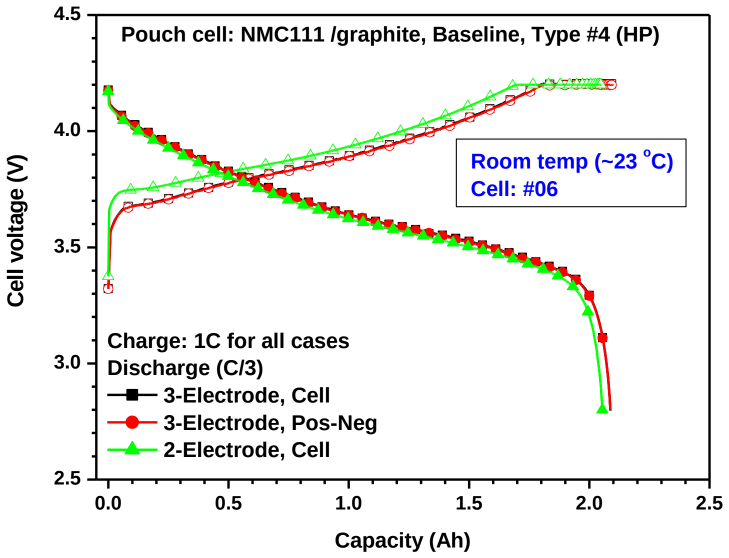

Figure 11. Cell performance curves for 2-electrode and 3-electrode cells.

- Thick anode and thick cathode
- Less non-active components
- High energy density
- Poor rate-capability

- Thin anode and thin cathode
- More non-active components
- High power density
- Good rate-capability

Figure 12. High energy and high power cell configuration.

Figures Continue on Next Page

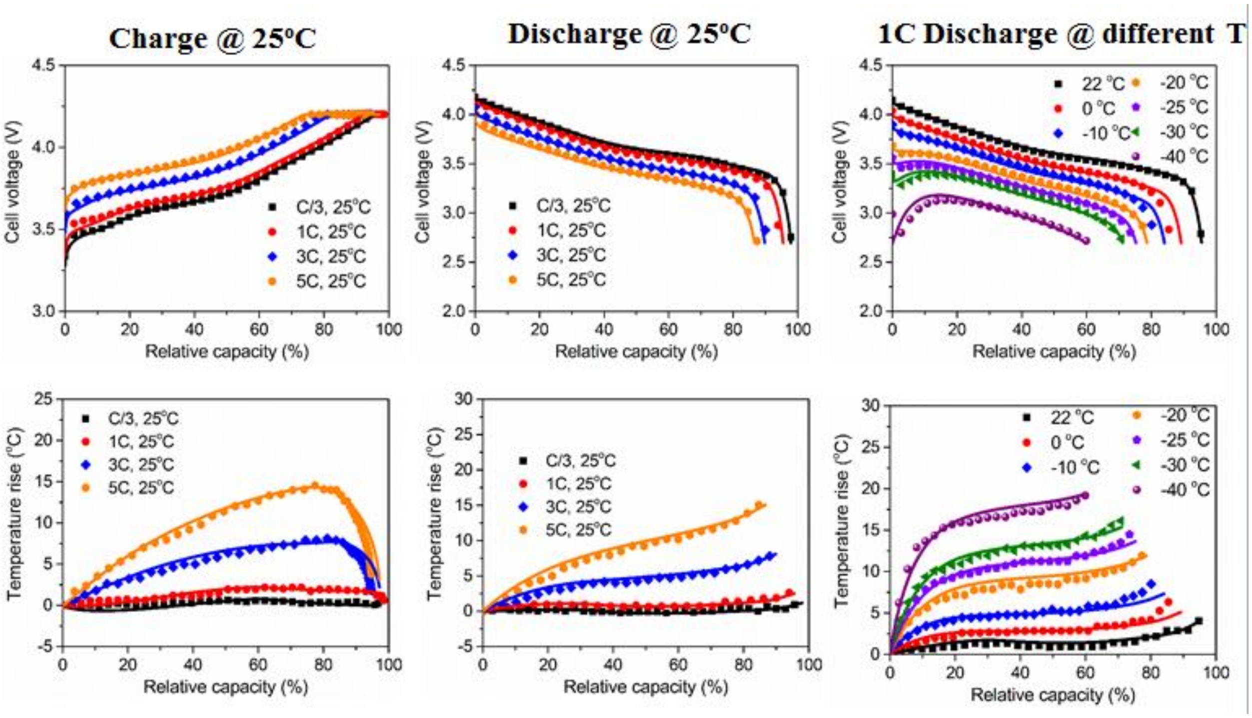

Figure 13. NMC622/C BOL performance: Model validation for high energy cell

Figures Continue on Next Page

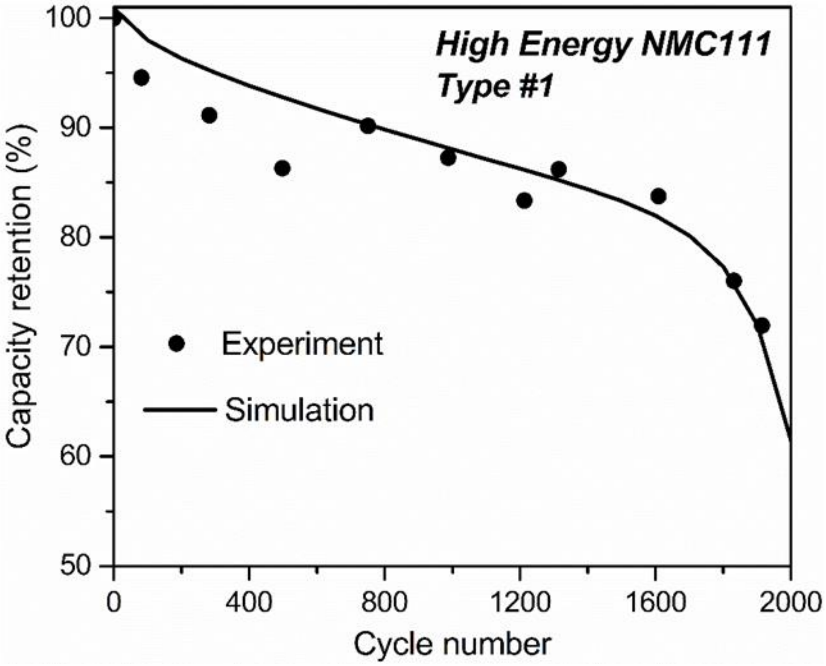

Figure 14. NMC111/C life model validation: C/3 capacity retention for high energy cell

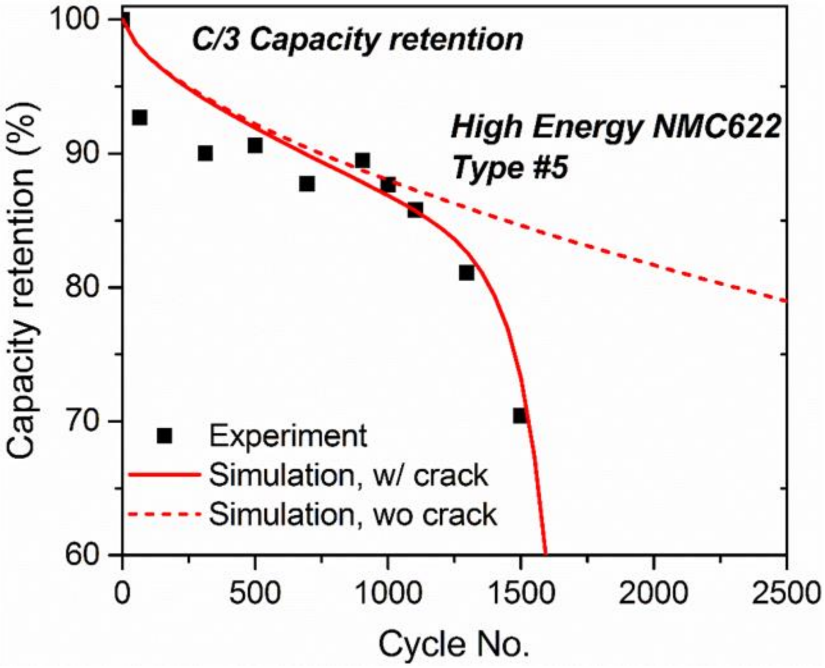

Figure 15. NMC622/C life model validation: C/3 discharge curves after various cycles for high energy cell

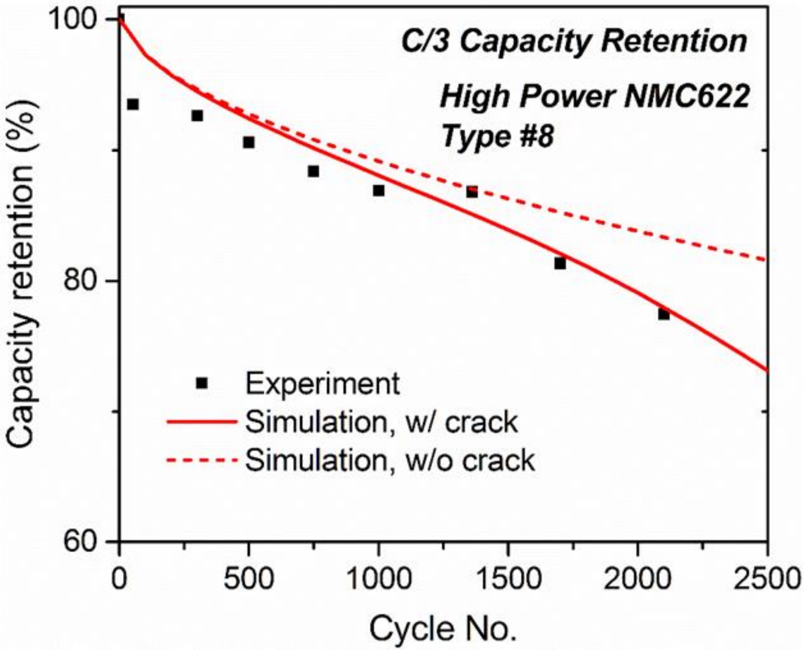

Figure 16. NMC622/C life model validation: C/3 discharge curves after various cycles for high power cell

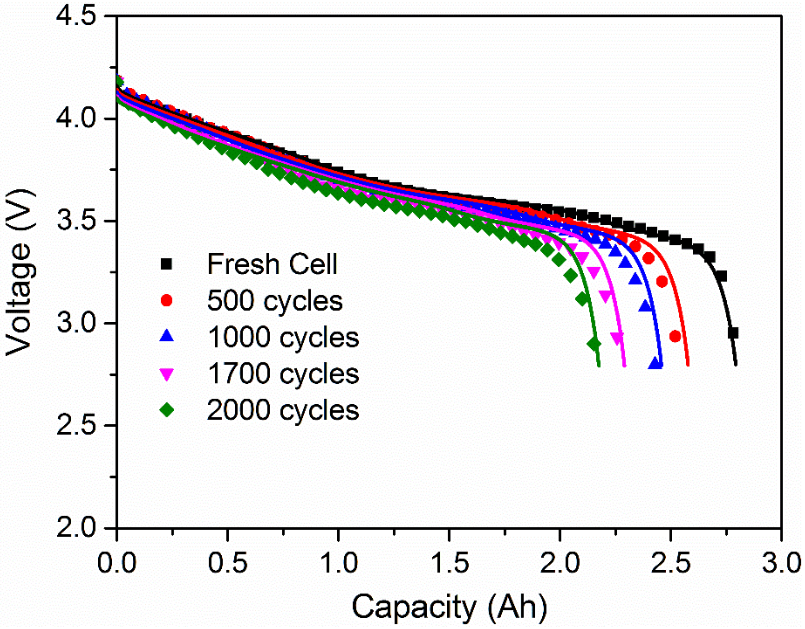

Figure 17. NMC6222/C life model validation: C/3 discharge curves after various cycles for high power cell

Figures Continue on Next Page

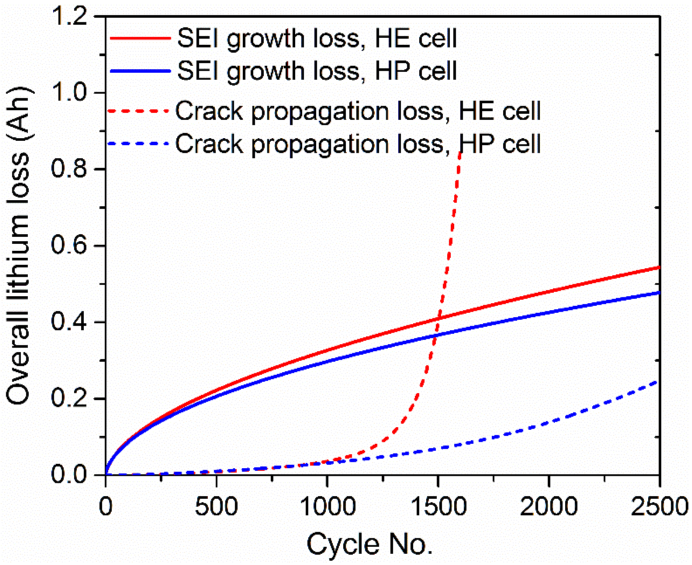

Figure 18. NMC6222/C life model analysis: capacity loss due to SEI growth and crack propagation for high energy and high power cells

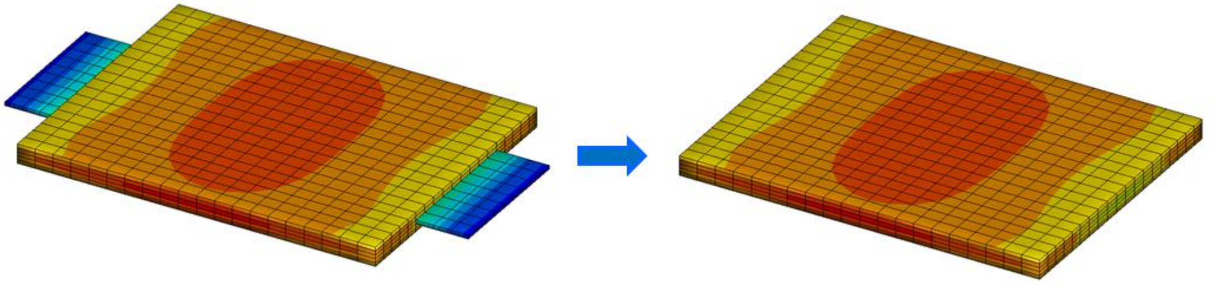

Ansys Fluent mesh (ECP software)

OpenFoam mesh created thru blockMesh

Figure 19. Mesh for EC Power software and solid Displacement Foam solver

Figures Continue on Next Page

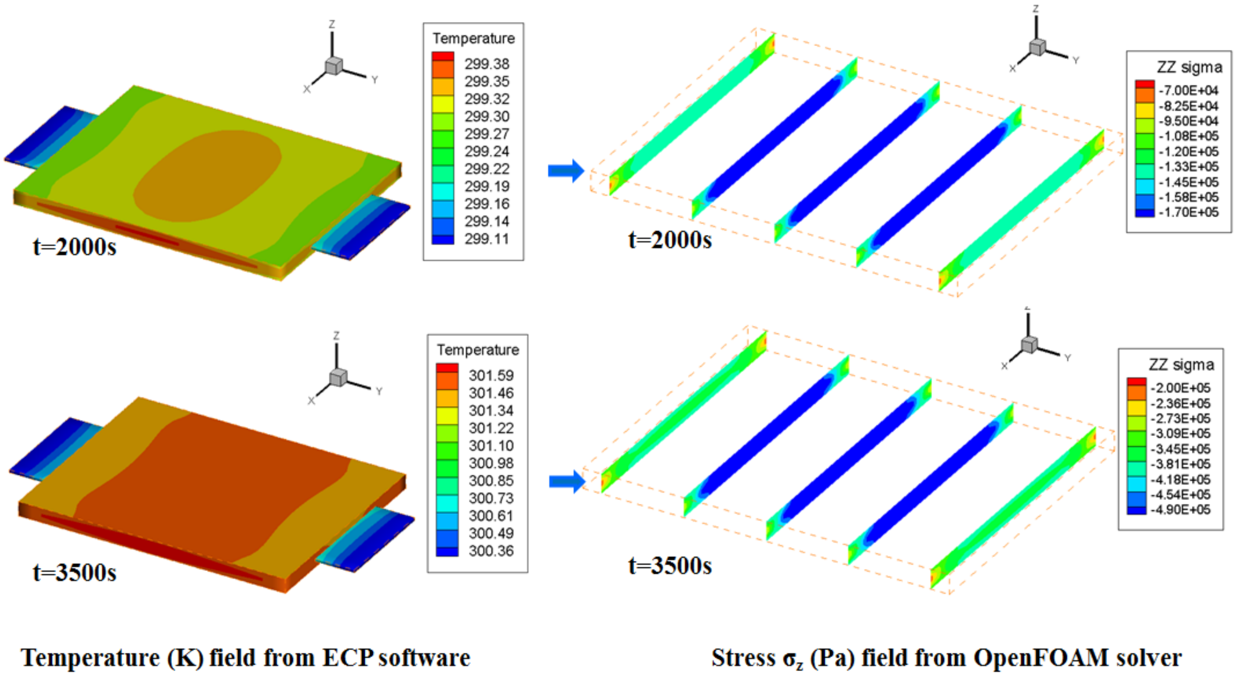

Temperature (K) field from ECP software

Stress σ_z (Pa) field from OpenFOAM solver

Figure 20. Simulation results for 1C discharge at two time instants, t=2000s and 3500s for rigid packaging

Remainder of Page Intentionally Blank

AVPTA Technology Focus Area 6: Energy Storage & Batteries

Multi-physics Computer-Aided-Engineering Tools for Performance, Life, and Safety Analysis of Li-Ion Battery Systems in Military Vehicle Applications

DOE-VTO TFA Lead: David Howell
TARDEC TFA Lead: Laurence Toomey

Principal Investigator:
Dr. Kandler Smith
National Renewable Energy Laboratory (NREL)
15013 Denver West Parkway, Golden, CO 80401

Project Start: Jul 2016
Estimated Completion: Q4FY18

Objective:

- Construct an integrated multi-physics simulation environment/tool for analysis of performance, safety and life of Li-ion battery module used in military vehicles.

Strategic Context:

- The energy efficiency and functionality of military vehicles through electrification can be improved through the adoption of Li-ion battery technology. Without significant testing, the cold temperature performance, safety and lifetime of Li-ion technology can be difficult to quantify, however. Computer-Aided Engineering (CAE) tools are capable of accelerating the development of safe, high-performance, and long-lasting Li-ion battery systems for military vehicle applications and reducing the need for time-consuming and expensive tests. NREL is developing a robust and efficient analysis tool for TARDEC by customizing NREL's in-house modeling tools and leveraging new functionalities being produced in ongoing Computer-Aided Engineering of Batteries (CAEBAT) projects. The model has the flexibility to adapt to new chemistries and designs.

Accomplishments:

- Provided an on-site training workshop
- Developed 3D model of 6T battery geometry and defined material thermal and mechanical properties
- Characterized battery electrochemical and aging sub-models from existing TARDEC data
- Developed plan for additional tests to complete model characterization and performance, aging, and safety validation studies

- Delivered preliminary ANSYS 3D thermal/electrochemical and LS-Dyna 3D ballistic safety simulation software to TARDEC for evaluation

Introduction:

Energy storage systems based on lithium-ion battery technology show great promise to improve the energy efficiency and functionality of military vehicles through electrification. CAE tools are able to accelerate development of safe, high-performance, and long-lasting lithium ion battery module for military vehicle applications. Physics-based models are adaptable as design changes occur over the life cycle of a military program.

As a CAEBAT program [1] performer, NREL supports DOE to develop numerical design tools to shorten design cycles and optimize batteries for improved performance, safety, long life, and low cost. NREL has played a leading role in numerical analysis of multiphysics behaviors of lithium-ion batteries. NREL's Multi-Scale Multi-Domain (MSMD) model overcomes the modeling challenges posed by the highly nonlinear multi-scale response of battery systems. The expandable, modular, and flexible architecture connects the physics of battery charge/discharge processes, thermal control, safety, and reliability in a computationally efficient manner.

The MSMD acts as the framework for the suite of tools being developed in this project. Performance-, life- and safety-component models will be customized and integrated as a user defined library in ANSYS Fluent, a computational fluid dynamics code in which MSMD model framework has been standardized. Ballistic simulations are performed using LS-Dyna, providing mechanical response of the battery to intrusion by bullet and providing the resulting internal short magnitude to ANSYS Fluent simulations for thermal runaway likelihood analysis. The user will further leverage enhanced capabilities being implemented in the ANSYS Fluent Battery Module as outcomes of other continued CAEBAT projects.

Approach:

The proposed CAE tool will be developed by customizing NREL’s in-house modeling tools and leveraging new functionalities being produced by continuing CAEBAT projects. NREL’s existing performance, life and safety model will be refined and integrated as a user defined library in ANSYS Fluent Battery Module [2], in which NREL’s MSMD battery modeling framework [3] has already become standard as a result of previous CAEBAT projects. The tool is being enhanced to integrate with NREL’s life model, so that battery lifetime tradeoffs can be assessed based on 3D thermal/electrical drive cycle simulations. Ballistic simulations are being built leveraging explicit mechanics and failure models in LS-Dyna and linked to ANSYS for safety evaluation. The functionalities of the CAE tool are being verified utilizing the 6T battery form factor.

Results and Discussion:

The existing capabilities of NREL’s battery performance, life and safety models were summarized and reported along with the development plan. These three component models are being integrated as a user defined library in ANSYS Fluent. One of the key challenges for model integration is the difference of temporal scales of life, performance and safety simulations. NREL is currently proposing an indirect coupling structure, as shown in Figure 1. There is no connection between the life and safety sub-models as their impact on each other is negligible.

The tool is aimed to support high performance parallel computing and simulation. NREL is evaluating the High-Performance Computing (HPC) performance of the ANSYS Fluent battery module. Figure 2 shows the comparison of simulation results utilizing four processors on a desktop computer and NREL's HPC system, Peregrine. The simulation condition is a 3S1P battery module under 4C constant-current discharge. With the Newman, Tidemann, Gu and Kim (NTGK) model implemented in Fluent battery module, an empirical electrode-domain model, identical results were obtained by the PC and HPC.

As part of the knowledge transfer activities, NREL held an on-site training workshop for TARDEC at the end of August, 2016 with two engineers from Analytic Department of TARDEC. This workshop helped TARDEC users get familiar with the battery modeling platform (Figure 3), current NREL modeling approaches and capabilities, and identified gaps that are being addressed under this project. During FY17, NREL developed 3D thermal and mechanical models of the 6T battery geometry and defined material properties (Figure 4). NREL further characterized battery electrochemical and aging sub-models from existing data (Figure 5). Example validation of the model for a single cell is shown in Figure 6. Figures 7 and 8 show thermal and electrical simulation results from the 3D electrochemical/ thermal model of the 6T battery in ANSYS Fluent. The 3D electrochemical/thermal model of the 6T battery is approximately 75% complete, awaiting the results of 6T battery calorimetry tests to be performed at NREL in the first half of FY18 to be used to validate the model. Life model integration with the 3D electrochemical/thermal model is ongoing.

To capture the mechanical-coupled failure modes of the 6T battery under ballistic threat, we developed a finite element procedure to simulate bullet penetration in LS-Dyna. Our approach is motivated by the observation that the 6T battery has multiscale features ranging from micrometers to centimeters. The traditional approach of solving the problem as the inversion of one big matrix imposes numerical challenges. The traditional approach requires long simulation times due to a large number of degrees of freedom and numerical stiffness stemming from the large in-plane element sizes (of the order of centimeters) versus the micron-sized through-plane dimensions. The proposed approach (Figure 9), uses a mathematical formulation that allows us to solve the high strain-rate problem across a section of the battery thickness in an initial step (e.g. the 6T battery case), then uses the velocity of the bullet at the exit point of the first section as the boundary condition for solving a similar high strain-rate problem across a second section of the thickness (e.g. the first cell), and so on, stepping through the battery layer-by-layer until the deformation problem has been solved across the complete geometry.

Figure 10 illustrates the preliminary results of bullet penetration through the 6T battery. After penetrating through the battery enclosure and plastic plate, the velocity of bullet decreased from 835 m/s to 827 m/s, indicating that about 2% bullet kinetic energy was absorbed by the enclosure and plastic plate (Figure 10 (a)). Importantly, the resultant velocity at the exit of the plastic plate serves as the initial boundary condition for the first battery cell. As shown in Figure 10 (b), the bullet velocity was reduced from 827 m/s to 825.9 m/s after penetrating through the first battery cell. Following the same procedure, one can readily determine the evolution of bullet velocity through the whole 6T battery. The proposed approach for high strain rate simulations saves computational time and successfully predicts the evolution of damage through the 6T battery. As a next step, the deformed geometry will be used to model the electrical short pathways inside the battery which will then be coupled to the 3D electrochemical/thermal model to simulate the internal short process, enabling model-based assessment of the likelihood of catastrophic battery thermal runaway.

Conclusions:

NREL and TARDEC are developing an integrated multiphysics simulation tool for analysis of performance, safety and life of military Li-ion battery systems, with application and validation for the 6T battery. The tool leverages previous electrochemical/thermal model developments under the CAEBAT program, applies them to the 6T battery system and also extends those models to capture 3D aging effects and ballistic response of the 6T battery system. At the end of FY17, the team delivered preliminary ANSYS 3D thermal/electrochemical and LS-Dyna 3D ballistic safety simulation software to TARDEC for evaluation. The team has developed a plan for additional tests to be conducted in FY18 needed to complete model characterization and conduct validation studies. The final validated model will be delivered in FY18 and NREL will conduct user training sessions at TARDEC.

References:

[1] Computer-Aided Engineering for Electric-Drive Vehicle Batteries (CAEBAT). (2016). Retrieved from http://www.nrel.gov/transportation/energystorage/caebat.html
[2] ANSYS Fluent Battery Module, Release 17.0, ANSYS Fluent Advanced Add-On Modules, ANSYS, Inc.
[3] G-H. Kim, K. Smith, K-J. Lee, S.Santhanagopalan, A. Pesaran, “Multi-Domain Modeling of Lithium-Ion Batteries Encompassing Multi-Physics in Varied Length Scales,” J. Electrochem Soc, Volume 158, Issue 8, pp. A955-A969 (2011)
[4] Chao Zhang, Shriram Santhanagopalan, Michael A. Sprague, Ahmad A. Pesaran, "A representative-sandwich model for simultaneously coupled mechanical-electrical-thermal simulation of a lithium-ion cell under quasi-static indentation tests", Journal of Power Sources, Volume 298, Pages 309-321, 2015.
[5] Chao Zhang, Shriram Santhanagopalan, Michael A. Sprague, Ahmad A. Pesaran, "Coupled mechanical-electrical-thermal modeling for short-circuit prediction in a lithium-ion cell under mechanical abuse", Journal of Power Sources, Volume 290, Pages 102-113, 2015.

Figures Start on Next Page

Figures:

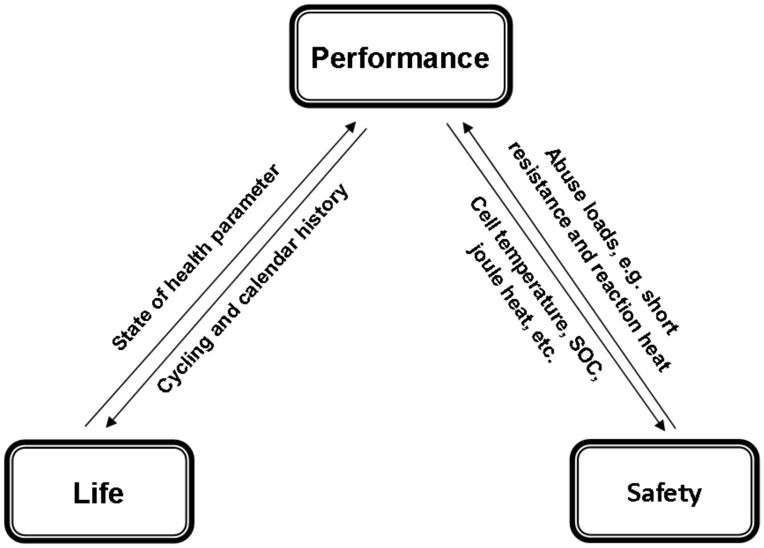

Figure 1. Indirect coupling between performance, life and safety

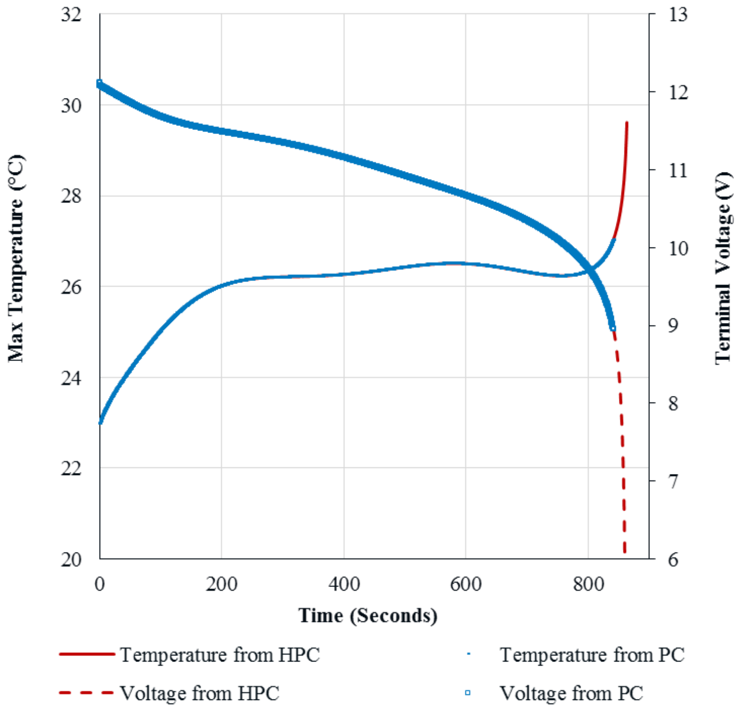

Figure 2. Comparison of simulation results of a 3S1P battery module under 4C constant-current discharge using PC and HPC

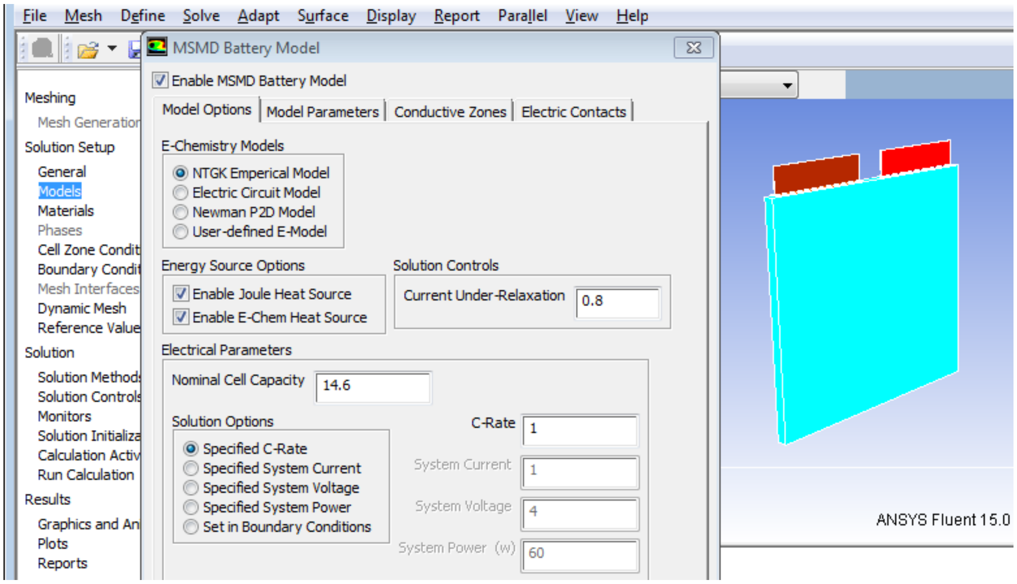

☑ Enable MSMD Battery Model

E-Chemistry Models

● NTGK Emperical Model
○ Electric Circuit Model
○ Newman P2D Model
○ User-defined E-Model

Energy Source Options

☑ Enable Joule Heat Source
☑ Enable E-Chem Heat Source

Solution Controls

Current Under-Relaxation: 0.8

Electrical Parameters

Nominal Cell Capacity: 14.6

Solution Options

● Specified C-Rate
○ Specified System Current
○ Specified System Voltage
○ Specified System Power
○ Set in Boundary Conditions

C-Rate: 1
System Current: 1
System Voltage: 4
System Power (w): 60

Figure 3. Graphical user interface of the MSMD battery model in ANSYS Fluent battery add-on module

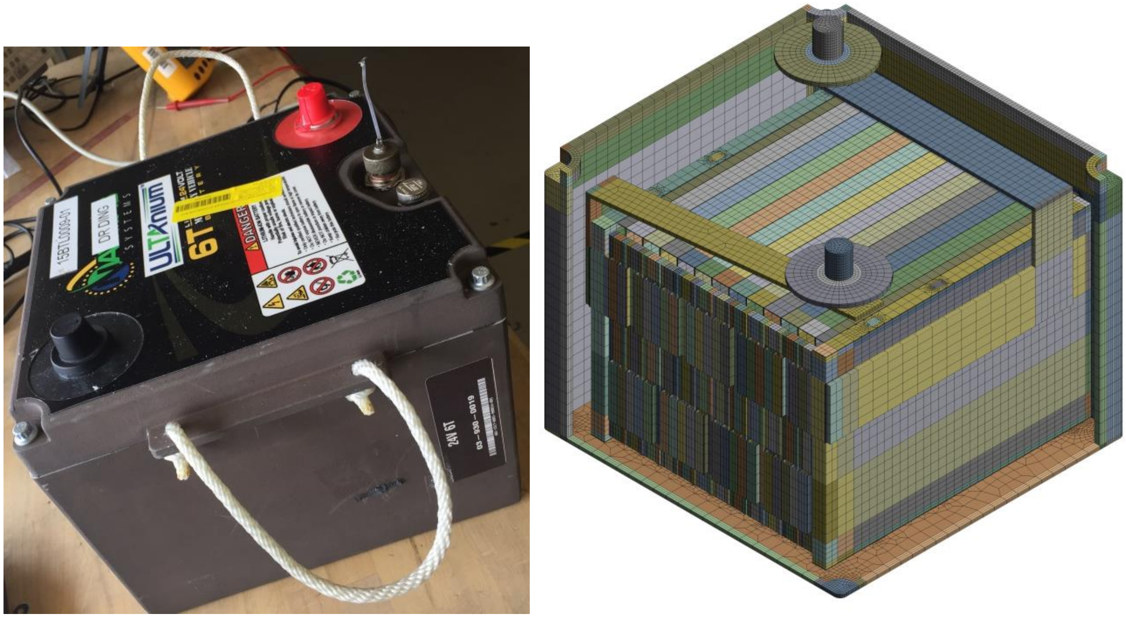

Figure 4. 6T module (left) and its mesh for electrochemical/thermal simulation (right)

Figures Continue on Next Page

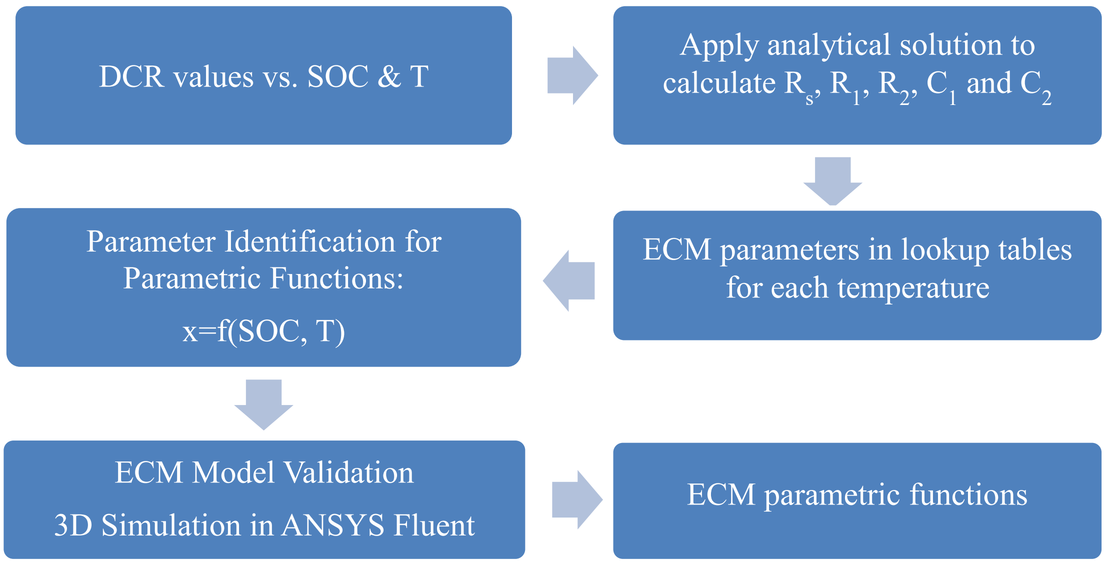

Figure 5. Procedure to identify equivalent circuit model (ECM) parameters from data

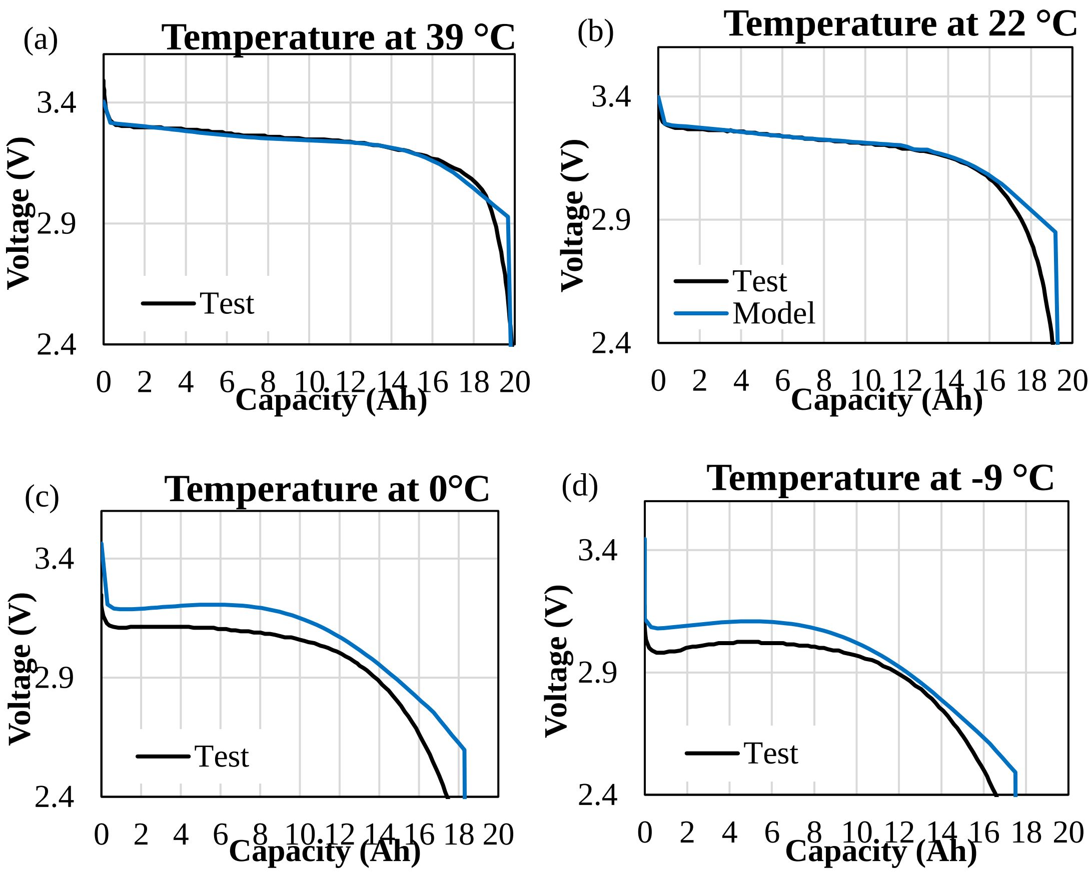

Figure 6. Comparison between single-cell simulated results and experimental results at 39 °C (a), 22 °C (b), 0 °C(c), and -9 °C (d)

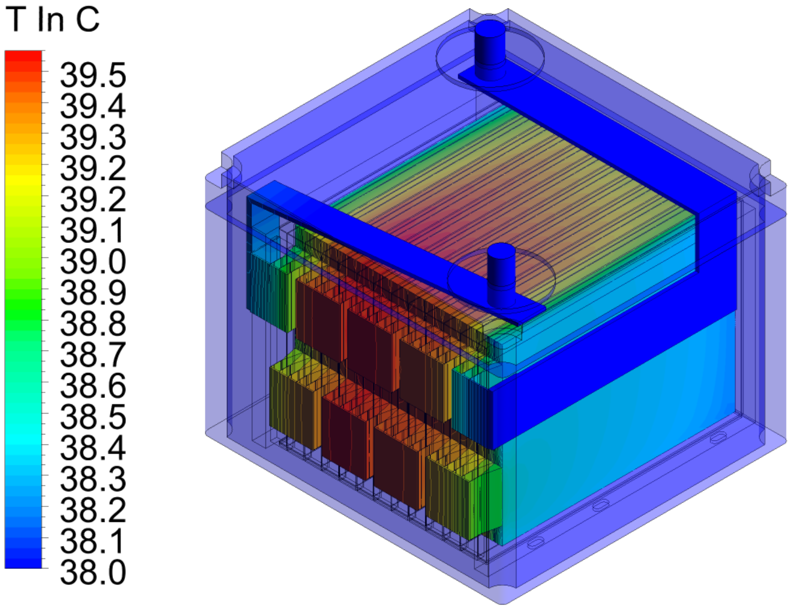

Figure 7. Temperature distribution of 6T module at 50% SOC during 1C discharge at 38 ºC ambient temperature

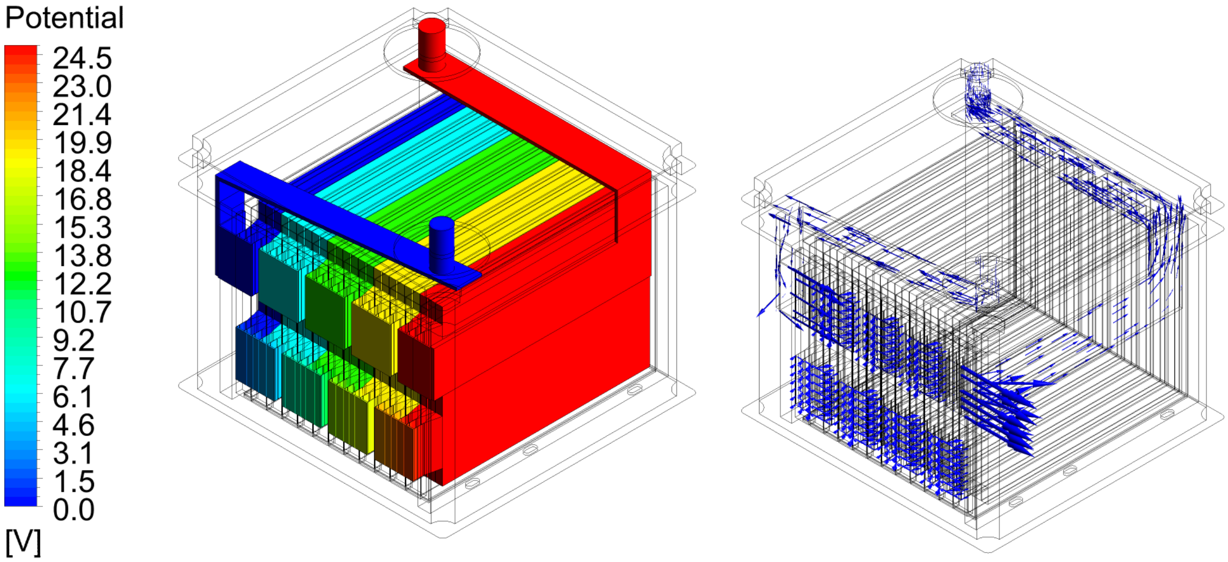

Figure 8. Preliminary 6T simulation results of potential distribution (left) and current flow through 6T busbar (right)

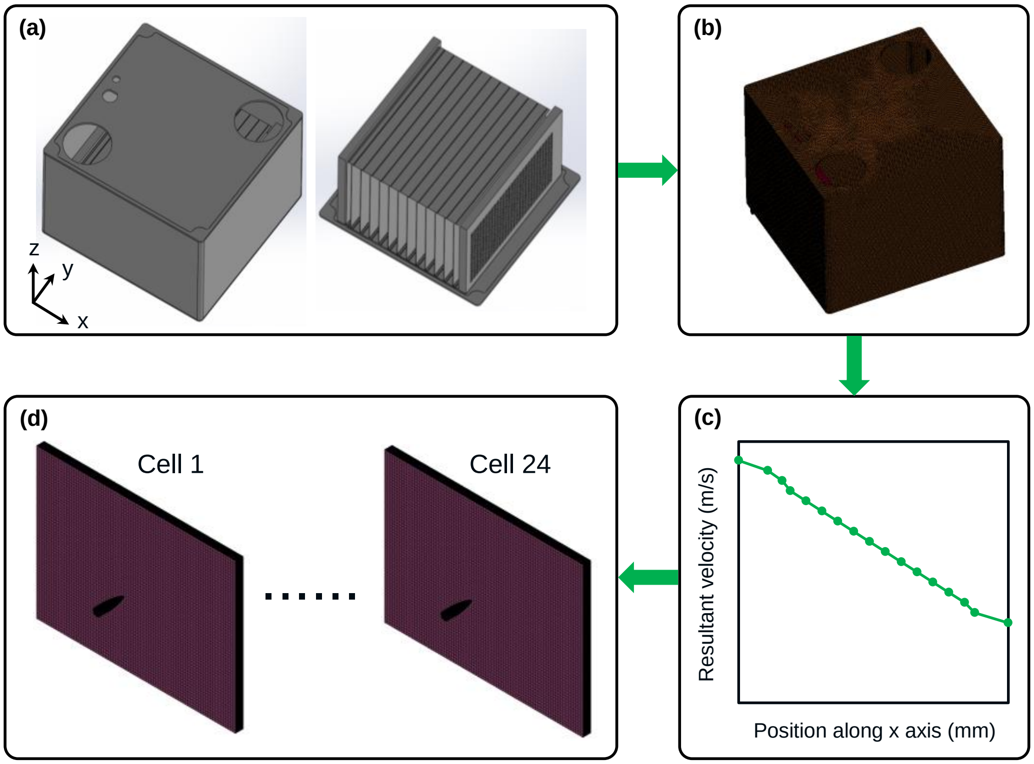

Figure 9. Finite element modeling procedure for bullet penetration of 6T battery. (a) Geometric model of the 6T module. (b) Finite element model of 6T enclosure. (c) Evolution of bullet velocity through each layer. (d) Finite element model of A123 cell.

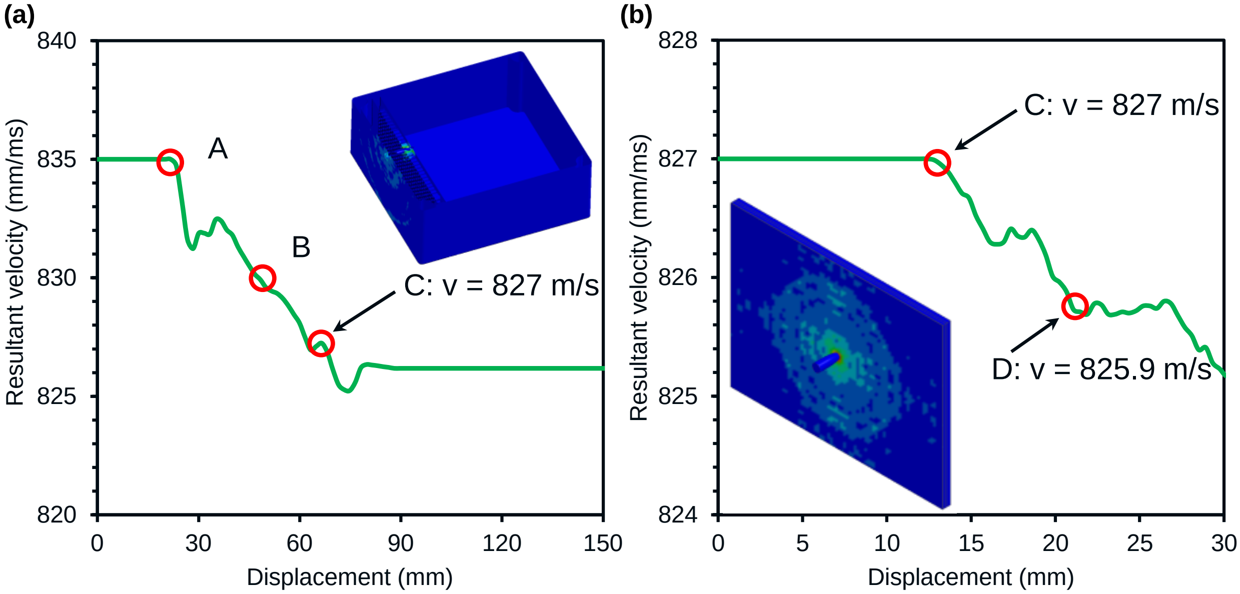

Figure 10. Bullet penetration simulation of 6T battery. (a) Bullet penetration through 6T enclosure and (b) bullet penetration through the first battery cell.

This Page Intentionally Blank

AVPTA Technology Focus Area 6: Energy Storage and Batteries

High Fidelity Fast Running Multiscale Multiphysics Battery Pack Software

DOE-VTO TFA Lead: David Howell
TARDEC TFA Lead: Laurence Toomey

Principal Investigator:
Dr. Shailendra Kaushik
General Motors LLC (Prime)
30500 Mound Road
Warren, Michigan 48092-2031

Project Start: Mar 2017
Estimated Completion: Q4FY19

Objectives:

- To develop multiscale multiphysics battery pack engineering software that significantly surpasses the most advanced software in computational speed by a factor of 100 while resolving complex interplays of physics across length scales ranging from materials (~micrometers) to large automotive battery pack systems (~meters)
- To enhance computational speed and stability while still resolving nonlinearities of the battery's dynamics and enhancing multiphysics integrity of the pack-level model, and enabling model-based diagnostics and prognostics for battery life and safety
- To meet these needs, the project team will perform collaborative research, development, and demonstration in multiple synergistic directions, including cell/module/pack scale-coupling methods, Reduced Order Models (ROM) modeling techniques, battery life models, and User Interface (UI) enhancements
- To enhance the ANSYS Battery Design Tool (ABDT) that was originally developed in previous Computer-Aided Engineering of Batteries (CAEBAT) projects. For clarity in what follows, the ABDT is the software layer that provides a battery-specific UI, automates battery-simulation workflow, and calls proprietary ANSYS products as services.

Strategic Context:

- Energy storage system based on lithium-ion batteries is promising to improve the energy efficiency and functionality of military vehicles through electrification.
- TARDEC energy storage team is interested in enhancing and utilizing computer tools to accelerate development and fielding safe, high-performance, and long-lasting lithium ion battery module for military vehicle applications.

- The tool should be capable of accurately predicting cell and module multiphysics behaviors occurring across a wide range of scale to help the design and evaluation of the batteries in military vehicle environment.

Accomplishments:

- Published the nonlinear multiscale battery model: Fast-varying function voltage (G) and Slow-varying function voltage (H) Multi-Scale Multi-Domain (GH-MSMD) in journal of the Electrochemical Society
- ANSYS DX and ROM team staff in Lyon, France presented an overview of progress made in the development of a ROM Builder, which is planned to be available as part of DX inside ANSYS Workbench in a future release.
- ANSYS Fluent development team in Lebanon, NH began work on implementation of GH-MSMD model as an enhancement to the Fluent battery model.
- ESim developed a Nonlinear State Variable Model (NSVM) representing pseudo-2D electrochemical physics in a reduced order form. The model-to-data and model-to-model comparisons show that the NSVM has excellent accuracy and time efficiency in modeling different battery control modes. ESim have also modeled a blended cathode and capacity fade by Solid-Electrolyte Interface (SEI) formation.
- The National Renewable Energy Laboratory (NREL) is building on the journal article and case studies prepared in previous quarters. NREL has consulted and assisted ANSYS in the implementation of cell-level GH-MSMD algorithms in ANSYS/Fluent
- NREL has performed initial demonstration of interactive MSMD simulation via text user interface and provided guidance to the team on potential routes and considerations for integration of life models within ANSYS.
- ANSYS implementation of the GH-MSMD method is expected to be released in Fluent R19.0

Introduction:

To accelerate the production of safe, reliable, high-performance, and long-lasting lithium-ion battery packs, the automotive industry requires Computer-Aided Engineering (CAE) design tools that accurately represent cell and pack multi-physics phenomena occurring across a wide range of scales. However, due to the lack of battery pack engineering software providing the desired computational speed, flexibility, and solution accuracy, current design and development of automotive battery pack systems heavily rely on costly and time consuming experimental tests. For example, in battery life estimation, General Motors (GM) has instituted multi-parameter Design of Experiments generating test data at cell level and pack level on a reduced basis for each hybrid vehicle program. Generating test data on a pack level has been found to be very expensive, resource intensive, and sometimes unreliable. If a high fidelity fast running multi-physics battery pack model is available, we expect that a model-based approach will replace a significant portion of pack-level aging experiments and reduce 300 pack test-weeks per program.

Approach:

Physicochemical processes in lithium ion batteries occur in intricate geometries over a wide range of time and length scales. As the size of the battery increases, macroscopic design factors in combination with highly dynamic environmental conditions significantly influence the electrical, thermal, electrochemical, and mechanical responses of a battery system. NREL pioneered the Multi-Scale Multi-Domain (MSMD) model, overcoming challenges in modeling the highly nonlinear multi-scale response of battery systems. The MSMD model as shown in Figure1 provides flexibility and multi-physics expandability through its modularized architecture. The project team previously collaborated on combining new and existing battery models into engineering simulation software that provides 3-D battery pack simulation modeling capability. Because of increasing complexities when configuring additional electrical and thermal connections between the cells, the computational cost of simulating a battery pack response is still high: results take weeks, unless low-fidelity sub-models are used to represent the battery's current/voltage response. Therefore, substantial improvement of computational efficiency is needed. Software tools also need improved usability and flexibility to reduce both the computational time and the engineering labor required to keep pace with battery design changes, including geometry and configuration. These improvements would enable the use of models in design and management tradeoff studies of performance/life in large vehicle battery pack systems, which are typically composed of several hundred large-format individual cells.

For large automotive battery pack design and development, the current state-of-the-art battery pack engineering software lacks the combination of sufficient computational speed, physics-based predictive capability and solution accuracy. Led by General Motors (GM), the team comprised of GM, ANSYS, NREL and ESim proposed to develop and implement an innovative nonlinear multi-scale battery model framework in the commercial software package, ANSYS Fluent. The proposed software offers greater computational efficiency while retaining expandability and modularity. In a previous project supported by Department of Energy (DOE), NREL developed a new innovative quasi-explicit nonlinear multi-scale multi-physics framework, GH-MSMD. The new framework uses time-scale separation and variable decomposition to eliminate several layers of nested iteration but keeps the modular framework architecture that is critical to battery behavior simulations. Fast electronic charge balance is differentiated from processes related to slow ionic movements. During the preliminary benchmark test carried out at the Electrode Domain Model (EDM) level, the GH-MSMD implementation demonstrates significant computational speed improvement compared to the original MSMD. Figure 2 presents the comparison of electrical and thermal response predicted by 4 different model combinations, simulating a battery for a mid-size Plug-in Hybrid Electric Vehicle PHEV10 sedan driving a US06 cycle for 20 minutes. The model outputs from different models are nearly identical. The most efficient GH-MSMD model option runs the 1200 second simulation in only 0.74 seconds, while the original MSMD runs the same case in 654 seconds. Based on the encouraging preliminary benchmark result at the EDM level, we propose to improve computational speed of the pack-level simulation by a factor of 100 from the state-of-the-art models.

Due to the pace of battery design change, the physical complexity of packs, and the number of user application scenarios that need to be studied, system-simulation with ROM remains an essential research need. Addressing ROM limitations will complement the expected progress from GH-MSMD, in a multi-pronged attack on the computational-efficiency challenge. It is increasingly evident that more advanced ROM techniques – available from the general literature – need to be integrated into the CAEBAT software tools to have the maximum impact on battery innovation. One particular area of importance is macro-modeling approaches for designs in which parameters other than battery state of charge and coolant flow rate vary. The designer needs to approximate the electrical and thermal performance of the pack while varying design parameters such as the geometry and physical properties. Extending the system modeling with parameterized ROM techniques will allow manufacturers to look at many "what-if" scenarios, and perform optimization and sensitivity analysis, after a single ROM-building process. Effective parallelization and intelligent sampling of the parameter space are the key elements that need to be investigated and developed. This ROM can be built from a Fluent analysis, driven by the ANSYS DesignXplorer (DX) software tool with its design of experiments and response surface processes. It will be exposed both as a generator of fast approximate predictions in ANSYS Workbench, and as a reusable model for use in systems-engineering analysis tools, vehicle simulators, or even real-time battery management systems with hardware in the loop. In addition, state-of-the-art ROMs typically lose validity when severe nonlinearities arise in the system. Because vehicle batteries are often used in a regime where nonlinearity becomes significant (e.g., continuous high-rate charge/discharge or low-temperature cycling), a nonlinear ROM, which is fast enough while coupling kinetic, thermodynamic, and transport equations over complex component geometries, has been desired. The team is exploring a new ROM that retains acceptable accuracy under severe nonlinear conditions at a computational cost comparable to existing ROMs. The project team will further investigate Partial Orthogonal Decomposition (POD) and Discrete Empirical Interpolation Method (DEIM) ROMs where the battery electrochemical behavior is coupled with the thermal behavior. We have implemented DEIM for one- and two-cell batteries. Applying it to larger batteries will require either a method for connecting such small DEIM models together, or obtaining the connectivity information from Fluent and applying DEIM directly to the full geometry of a multi-cell battery.

Finally, new modeling approaches developed in CAEBAT I are being investigated for application at the electrode domain level to enhance computational efficiency and track changes in battery cell performance during lifetime of the cell. Developed by ESim, a new nonlinear state variable implementation of the Newman P2D electrochemical model will help accelerate studies of non-uniform usage of a battery for temperature gradient or non-optimized electrical design. The merit of this novel application of ROM will be researched and evaluated. During CAEBAT I, ESim further extended an existing Equivalent Circuit Model (ECM) to include capacity fade due to cycling of cells by adding a branch for the capacity loss on charge due to the solid electrolyte interface (SEI) formation reaction at the anode. Figure 3 presents this ECM, where an SEI formation branch has been added in parallel with the anode branch.

Remainder of Page Intentionally Blank

Results and Discussion:

Within FY17, NREL documented and published the GH-MSMD modeling approach in The Journal of the Electrochemical Society [1]. Figure 4 shows an example EDM simulation. NREL is supporting GH-MSMD implementation in ANSYS Fluent and has introduced the GH-MSMD method to project team members. NREL has also performed preliminary evaluation of the ANSYS interactive system interface. MATLAB® is selected to run ANSYS Fluent as a server for interactive simulation demonstration to accomplish a model feasibility study on fast, high-fidelity model-based diagnostics and prognostics of pack-level life and safety.

ANSYS has begun implementation of the GH-MSMD method in Fluent. The essential idea of the GH-MSMD method is similar to the circuit model used in Fluent. It assumes that at each level (pack domain, electrode domain, cell domain), the potential change can be written as $\Phi= G+Hi$. G and H at the higher level can be constructed from the G and H at the lower level. As a result, a battery pack's electric load condition can be quickly distributed to the lower hierarchical level and avoid the need for inner iterations. In NREL's GH-MSMD paper [1], this method was applied to the Newman P2D model. Focusing on the cell-level during the first year, the team identified several opportunities to implement GH concepts. When solving electrochemical physics at the 3D cell level, the GH method allows transfer current to be distributed non-uniformly throughout the cell and still maintain good computational efficiency. The need to repeatedly solve cell potential distribution is eliminated. Thanks to algebraic relationships, the Newman P2D electrochemical sub-model is solved only once per time step, instead of once per iteration in the direct method. Figure 5 shows the GH-MSMD flow-chart and Figure 6 shows the updated Fluent user interface, where the GH-MSMD model will be available by enabling cell clustering as an enhancement to the Fluent reduced-order method. It is compatible with all the electrochemical sub-models including the Newman, Tiedemann, Gu and (NTGK), ECM, Newman's P2D and the user-defined electrochemistry model. These enhancements are planned to be released in Fluent R19.0 in January 2018.

During the 2017, the Non-linear State Variable Modeling (NSVM) life model with a SEI formation mechanism was validated with the test data. In order to simulate the specific formation of a LG cell, ESim extended the NSVM to address the NCA/LMO blended chemistry in the cathode, some preliminary results are presented in this report.

Life model using Deshpande's mechanisms:

The results from NSVM life model are compared to experimental data Figure 7. The model shows very good consistency with test data for early stage of battery life (up to 200 cycle).

Model for NCA/LMO blended cathode:

In the previous NSVM model, the anode and the cathode contain only one active material in each; however, the LG cell used by GM has a blended NCA/LMO cathode. Therefore, ESIm modified their NSVM code to include additional particle diffusion and kinetic equations for the additional active material in the cathode. Particle diffusion in the active materials in the cathode are described by the following equations:

$$\frac{\partial c_{s,i}}{\partial t} = \frac{D_{s,i}}{r^2}\frac{\partial}{\partial r}\left(r^2 \frac{\partial c_{s,i}}{\partial r}\right) \qquad (i = \text{NCA, LMO})$$

$$\left.\frac{\partial c_{s,i}}{\partial r}\right|_{r=0} = 0 \qquad -D_{s,i}\left.\frac{\partial c_{s,i}}{\partial r}\right|_{r=R_{s,i}} = \frac{j_{s,i}}{F} \tag{1}$$

The Butler-Volmer equations for blended cathode are given by:

$$j_{s,i} = j_{0,i}\left[\exp\left(\frac{0.5F}{RT}\eta_i\right) - \exp\left(-\frac{0.5F}{RT}\eta_i\right)\right] \qquad (i = \text{NCA, LMO}) \tag{2}$$

where the exchange current densities are defined as follows:

$$j_{0,i} = Fk_{s,i}c_{s,i}^{0.5}\left(c_{s,\max,i} - c_{s,i}\right)^{0.5} c_L^{0.5} \qquad (i = \text{NCA, LMO}) \tag{3}$$

and the overpotentials are expressed by:

$$\eta_i = \phi_s - \phi_L - U_i \qquad (i = \text{NCA, LMO}) \tag{4}$$

The open circuit potential profiles for NCA and Lithium Manganese-Oxide (LMO) materials are presented in Figure 8:

A practical drive cycle was simulated for this blended cathode model, and the voltage profile is shown in Figure 9:

Due to the difference in transport and kinetic behavior, there are imbalances between the two cathode materials. For example, the two materials have different rates in discharge; as a result, LMO is discharged much faster than NCA and is depleted at around 60% Depth of Discharge (DOD), then only NCA is discharged during the next stage as shown in Figure10.

Conclusions:

The project is on track to finish by the end of 2019. GH-MSMD implementation in Fluent is ongoing. Initial implementation has shown up to 20x computational speedup capturing 3D electrochemical physics. Non-linear, dynamic ROM for fast simulation of battery packs using deep neural networks has begun and preliminary results show promise for additional computational speedup of 3D thermal/flow physics. Novel approaches including an additional branch in the equivalent circuit model to represent SEI layer growth show promise to efficiently model battery life and extract relevant model parameters from aging test data.

References:

[1] G.-H. Kim, K. Smith, J. Lawrence-Simon, C. Yang, “Efficient and Extensible Quasi-Explicit Modular Nonlinear Multiscale Battery Model: GH-MSMD”, J. Electrochem.Soc., 164(6), A1076-A1088 (2017)

[2] M Guo, X Jin, and R E White. "Nonlinear State-Variable Method (NSVM) for Li-Ion Batteries: Finite-Element Method and Control Mode." J. Electrochem. Soc. 164.11 (2017): E3200-E3214.

[3] M Guo, X Jin, and R E White. "Nonlinear State-Variable Method for Solving Physics-Based Li-Ion Cell Model with High-Frequency Inputs." J. Electrochem. Soc. 164.11 (2017): E3001-E3015.

Figures and Tables:

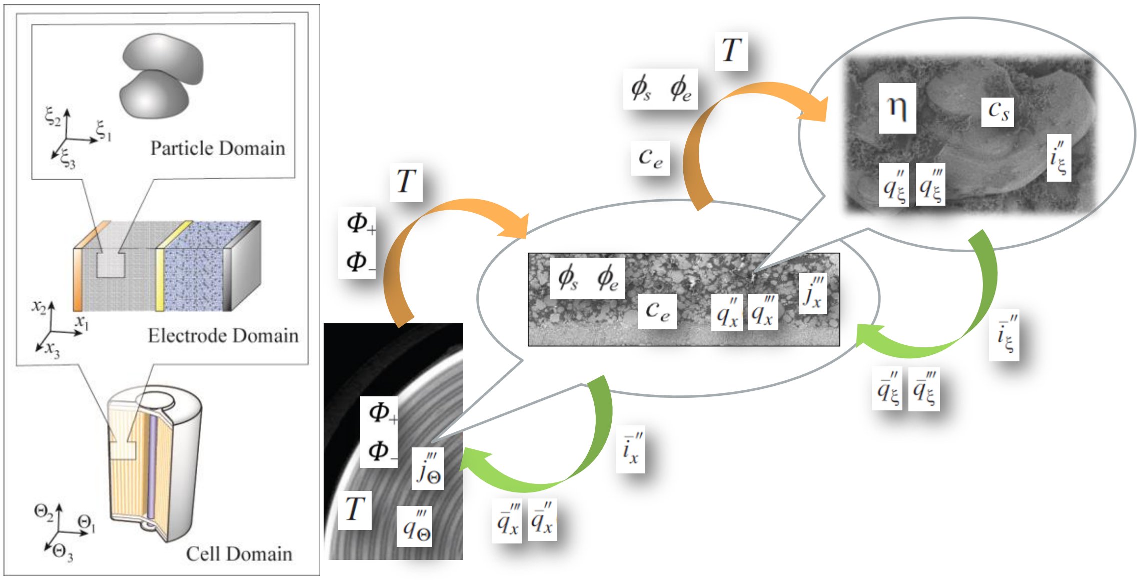

Figure 1. A diagram of intra- and inter-domain coupling protocols used in NREL’s MSMD framework, integrating widely varied scale battery physics in a computationally efficient manner with hierarchical modular architecture

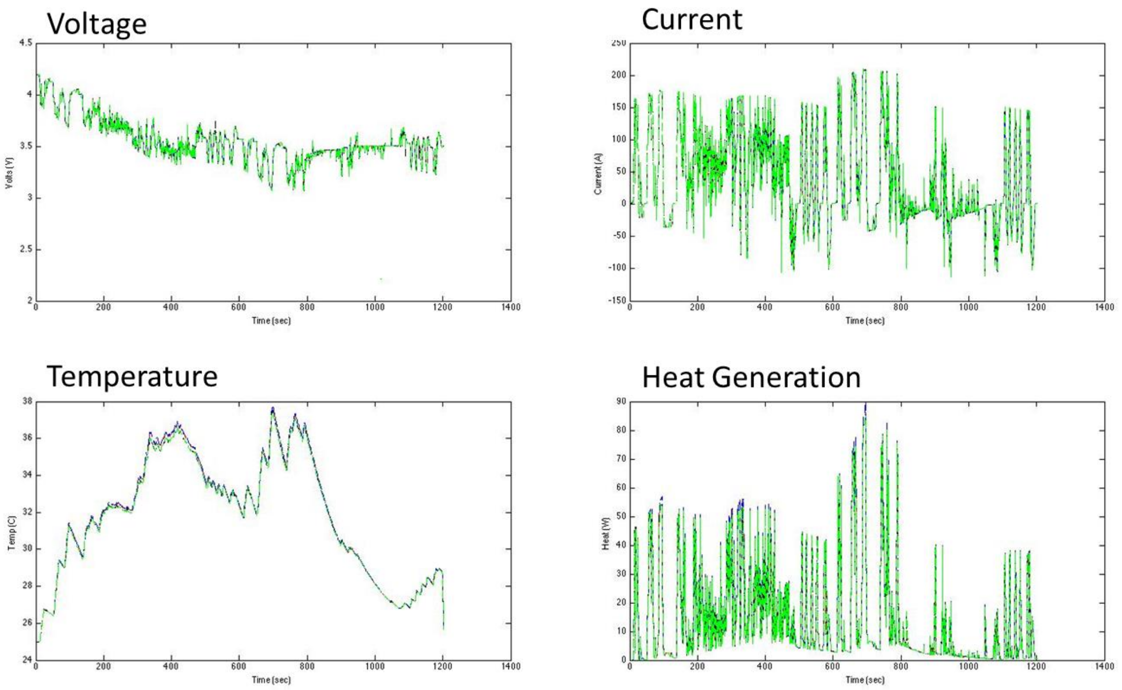

Figure 2. Comparison of electrical and thermal response of a battery for mid-size sedan PHEV10 US06 20 minutes driving power profile from the 4 different model combinations

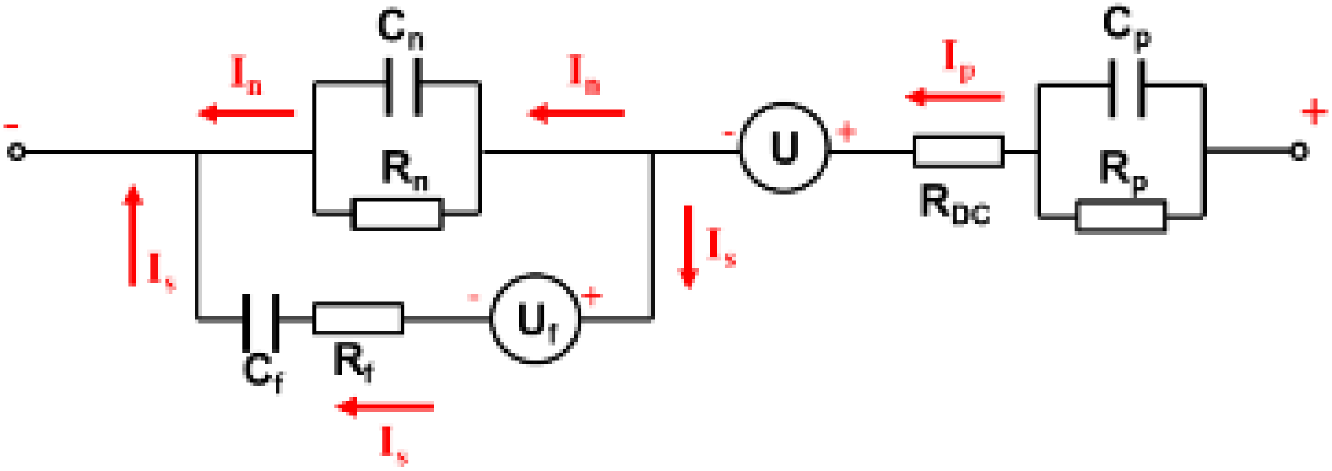

Figure 3. Equivalent circuit model with an SEI formation branch

Figures Continue on Next Page

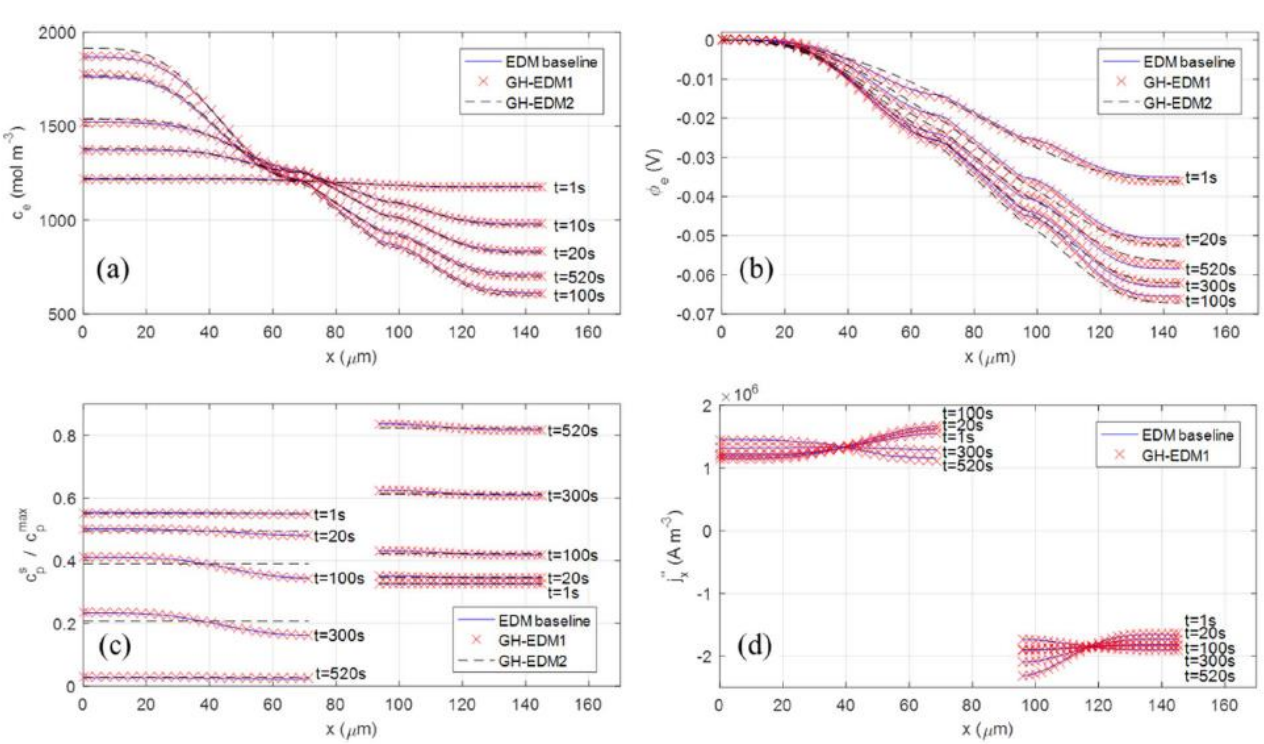

Figure 4. GH-MSMD electrode-domain model (EDM) simulations from Kim, J. Echem. Soc., 2017. (a) Electrolyte salt concentration, (b) electrolyte phase potential, (c) solid surface concentration, and (d) volumetric current density during 5C discharge at 25°C.

Figures Continue on Next Page

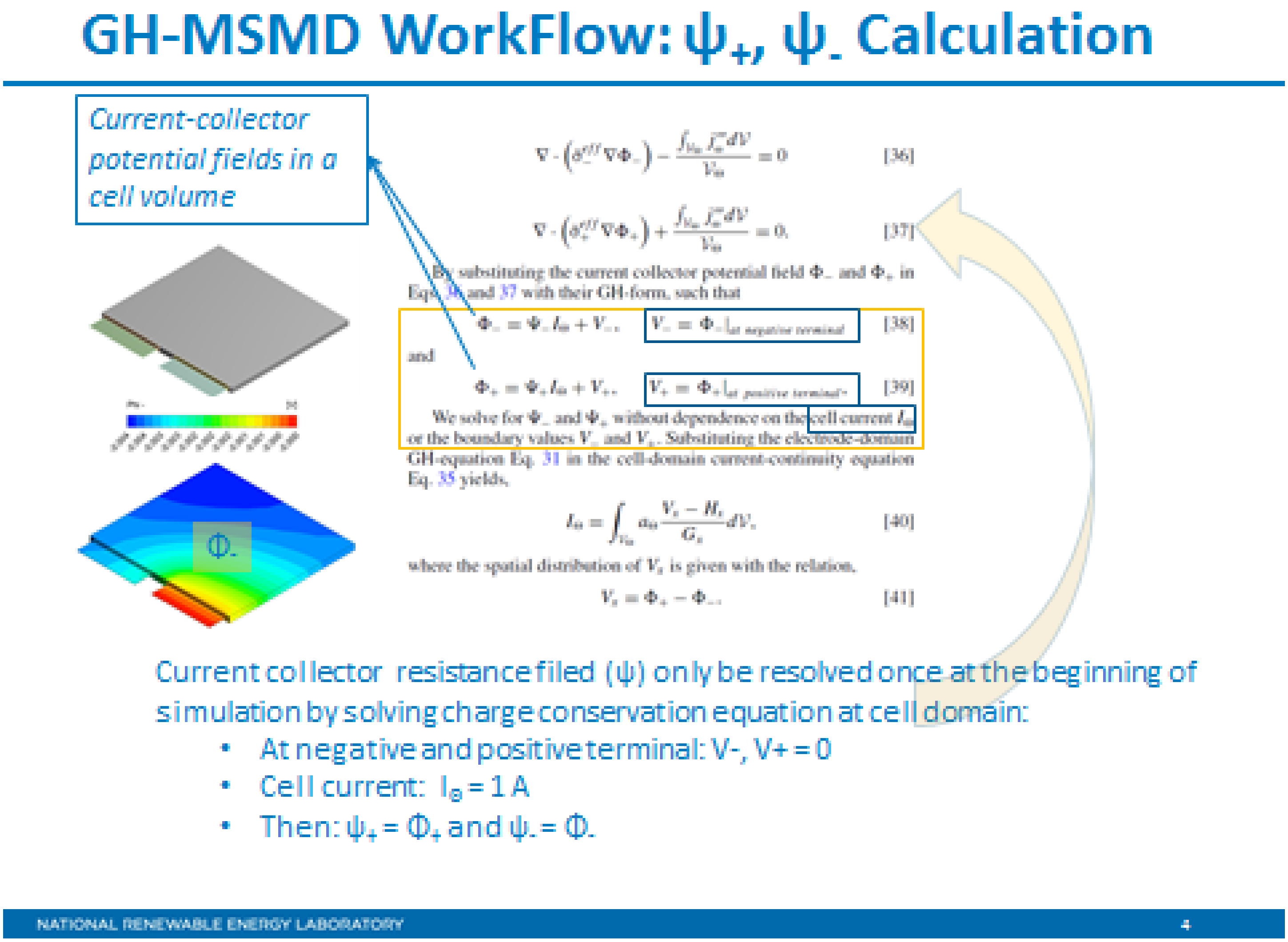

GH-MSMD WorkFlow: ψ₊, ψ₋ Calculation

Current-collector potential fields in a cell volume

$$\nabla \cdot \left(\sigma_-^{eff} \nabla \Phi_-\right) - \frac{\int_{V_{ec}} j_{ec}''' dV}{V_{ec}} = 0 \qquad [36]$$

$$\nabla \cdot \left(\sigma_+^{eff} \nabla \Phi_+\right) + \frac{\int_{V_{ec}} j_{ec}''' dV}{V_{ec}} = 0, \qquad [37]$$

By substituting the current collector potential field Φ_- and Φ_+ in Eqs. 36 and 37 with their GH-form, such that

$$\Phi_- = \Psi_- I_{ec} + V_-, \qquad V_- = \Phi_-|_{at\ negative\ terminal} \qquad [38]$$

and

$$\Phi_+ = \Psi_+ I_{ec} + V_+, \qquad V_+ = \Phi_+|_{at\ positive\ terminal}. \qquad [39]$$

We solve for Ψ_- and Ψ_+ without dependence on the cell current I_{ec} or the boundary values V_- and V_+. Substituting the electrode-domain GH-equation Eq. 31 in the cell-domain current-continuity equation Eq. 35 yields,

$$I_{ec} = \int_{V_{ec}} a_{ec} \frac{V_s - H_s}{G_s} dV, \qquad [40]$$

where the spatial distribution of V_s is given with the relation,

$$V_s = \Phi_+ - \Phi_-. \qquad [41]$$

Current collector resistance filed (ψ) only be resolved once at the beginning of simulation by solving charge conservation equation at cell domain:

- At negative and positive terminal: V-, V+ = 0
- Cell current: $I_a = 1$ A
- Then: $\psi_+ = \Phi_+$ and $\psi_- = \Phi_-$

NATIONAL RENEWABLE ENERGY LABORATORY 4

Figure 5. GH-MSMD Work-flow as implemented in Fluent

Figures Continue on Next Page

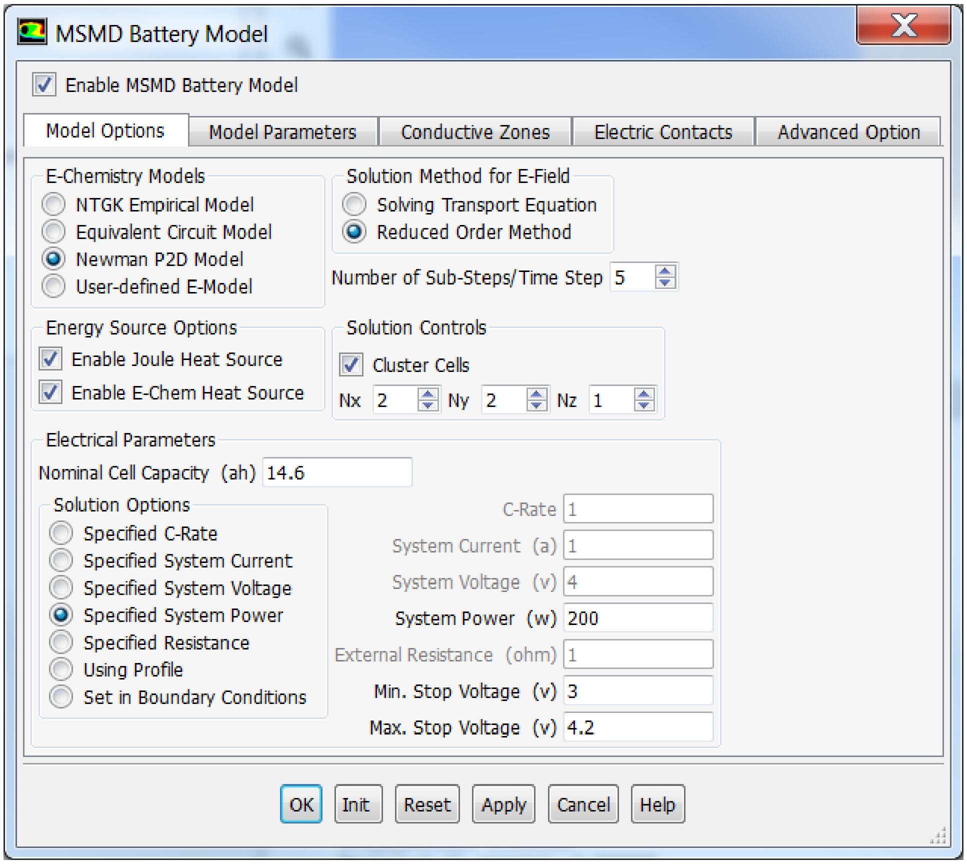

☑ Enable MSMD Battery Model

E-Chemistry Models
○ NTGK Empirical Model
○ Equivalent Circuit Model
● Newman P2D Model
○ User-defined E-Model

Solution Method for E-Field
○ Solving Transport Equation
● Reduced Order Method

Number of Sub-Steps/Time Step 5

Energy Source Options
☑ Enable Joule Heat Source
☑ Enable E-Chem Heat Source

Solution Controls
☑ Cluster Cells
Nx 2 Ny 2 Nz 1

Electrical Parameters
Nominal Cell Capacity (ah) 14.6

Solution Options
○ Specified C-Rate
○ Specified System Current
○ Specified System Voltage
● Specified System Power
○ Specified Resistance
○ Using Profile
○ Set in Boundary Conditions

C-Rate 1
System Current (a) 1
System Voltage (v) 4
System Power (w) 200
External Resistance (ohm) 1
Min. Stop Voltage (v) 3
Max. Stop Voltage (v) 4.2

Figure 6. Updated Fluent MSMD Battery Model panel

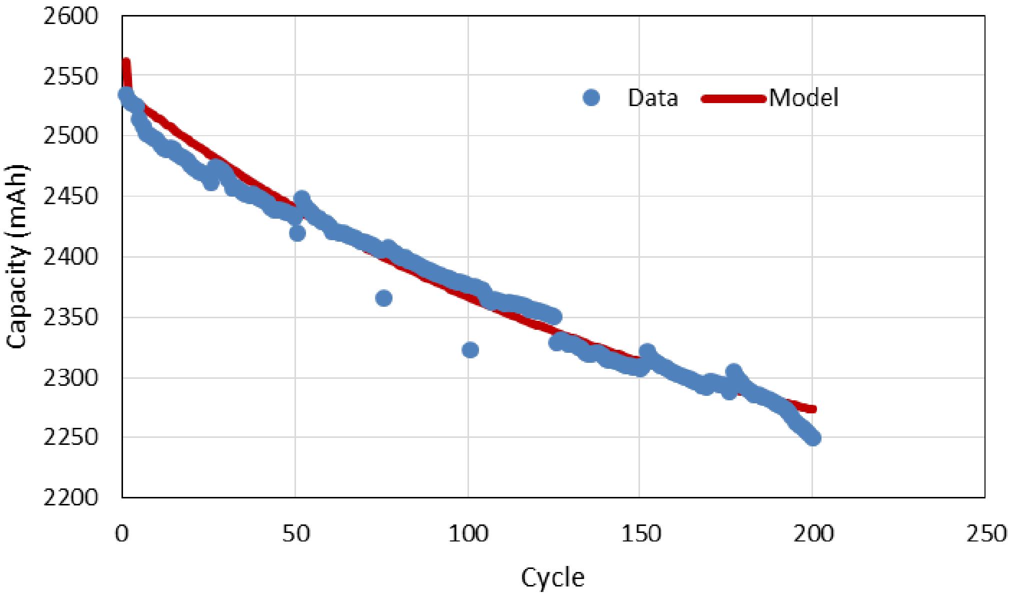

Figure 7. Simulated vs experimental cycling curves

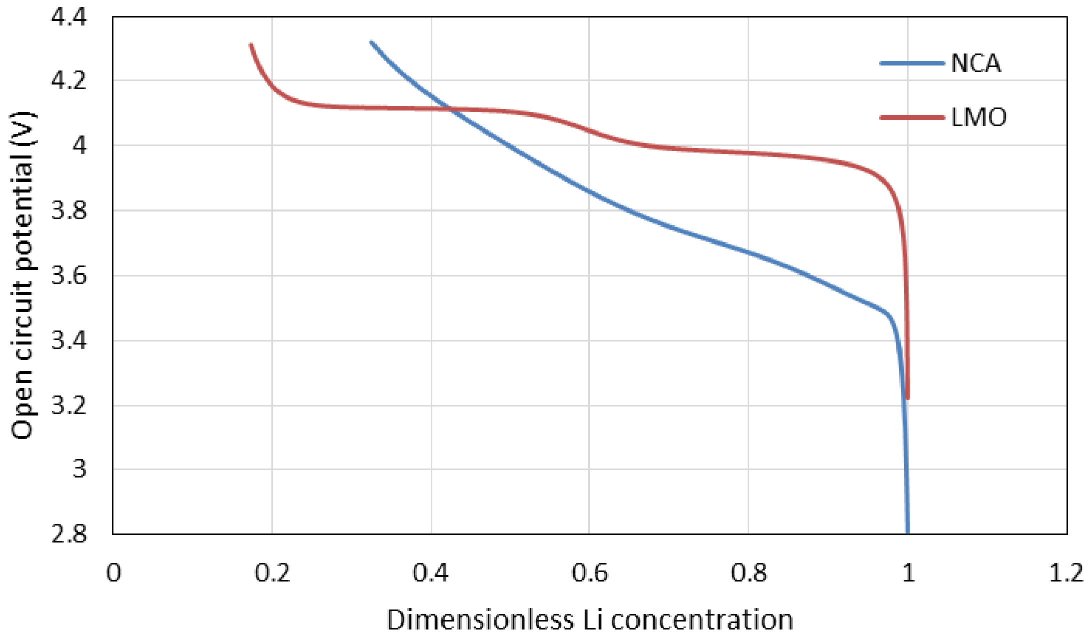

Figure 8. Open circuit potentials for NCA and LMO

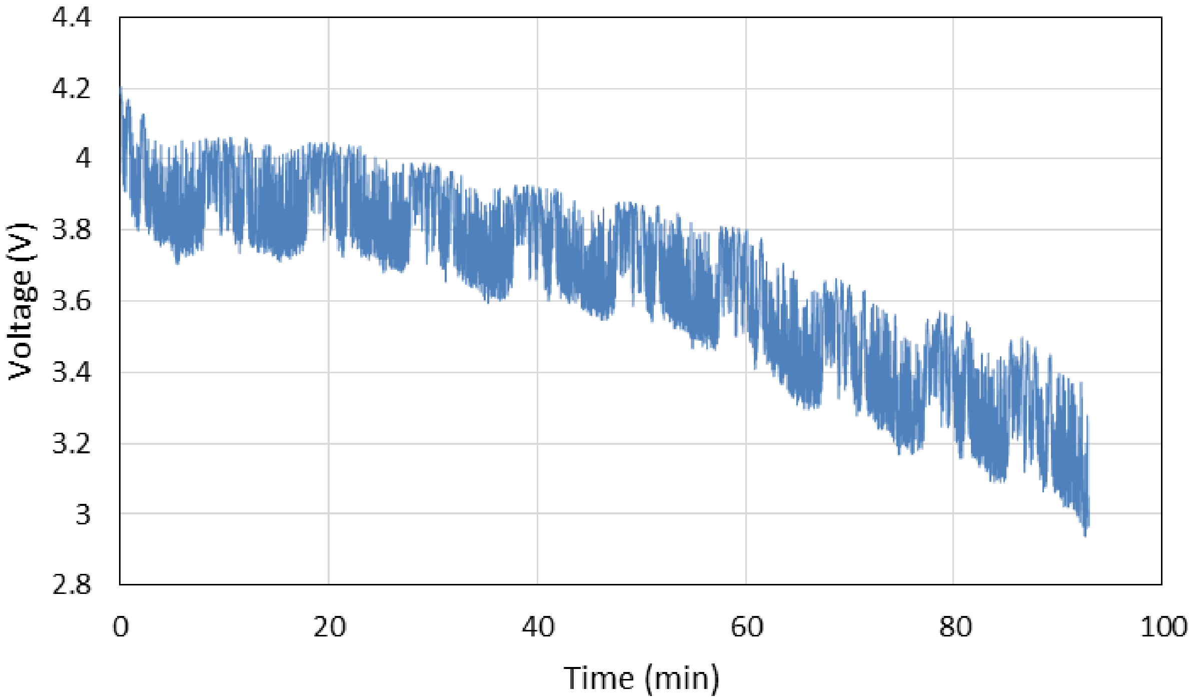

Figure 9. Voltage profile for a practical drive cycle

Figures Continue on Next Page

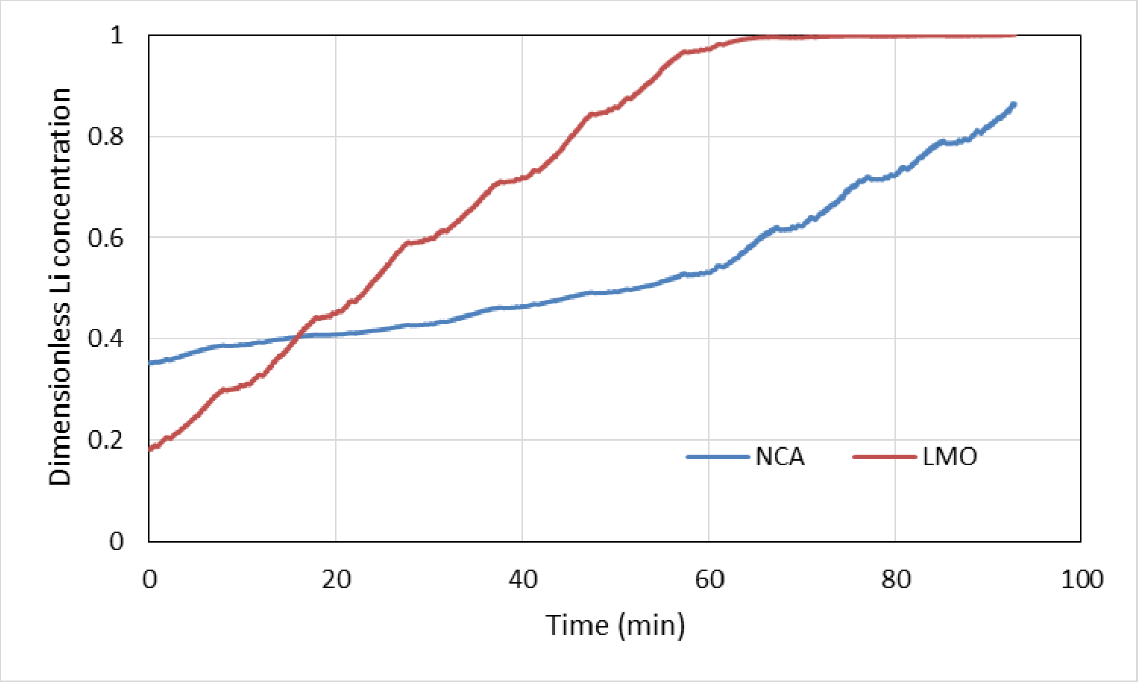

Figure 10. Li concentration in two cathode materials during drive cycle

Remainder of Page Intentionally Blank

This Page Intentionally Blank

AVPTA Technology Focus Area 6: Energy Storage and Batteries

Development and Validation of a Simulation Tool to Predict the Combined Structural, Electrical, Electrochemical and Thermal Responses of Automatic Batteries

DOE-VTO TFA Lead: David Howell
TARDEC TFA Lead: Laurence Toomey

Principal Investigator:
Dr. Chulheung Bae
Ford Motor Company
Energy Storage Research
2101 Village Road
Dearborn, MI 48152

Project Start: Jan 2016
Estimated Completion: Q1FY19

Objective:

- To develop and validate a simulation tool with unprecedented fidelity to predict the combined Structural, Electrical, Electrochemical and Thermal (SEET) response of automotive batteries to crash-induced crush and short circuit.

Strategic Context:

Lithium-ion batteries are promising for both military and commercial vehicle applications by improving energy efficiency and functionality of vehicles through electrification. Computer aided tools will help to accelerate development and fielding of safe, high-performance, and long-lasting lithium ion battery modules for both applications. The simulation tool should have unprecedented fidelity to predict the combined SEET response of automotive batteries to crash-induced crush and short circuit.

Accomplishments:

- The electrochemical properties of type D and E cells (Type D cell vendor A and Type E cell is from vendor B) were obtained; and model prediction of the cell voltage profile during cycling matches measurements.
- Mechanical, Electro-Magnetic (EM) and thermal solvers developed and refined for composite t-shell elements, and model integration completed.

- Simulations using composite t-shell elements were developed, producing results nearly identical to traditional solid element models and to experiment results while significantly reducing computational time in structural analysis.
- Beta version assumptions developed.
- A test site was selected, and initial cell validation testing begun.

Introduction:

This is the second year of a three-year project to develop a practical simulation tool to predict the combined SEET responses of automotive batteries to crash induced crush and short circuit, and validate it for conditions relevant to automotive crash. The expected benefits of the simulation tool are to reduce development time and cost by reducing the number of physical prototypes required, as well as improve the abuse response of battery systems. The project plan including major constituents and progression based on case studies is shown in Figure 1.

Approach:

Develop material constitutive models and Finite Element Method (FEM) element formulations that capture the mechanical response of cell components, including the case material, electrodes, separator, and their interactions with electrolyte.

Clearly identify the required input parameters for the constitutive models, FEM element formulations, and exothermic, electrochemical reaction state equations governing multi-physics phenomena during crush-induced electrical short, thermal ramp, and overcharge conditions.

Design and execute a test matrix encompassing automotive crash strain rates, at a number of kinetic energy levels and physical orientations likely to occur in vehicle impacts.

Develop integrated modeling tools which demonstrate high-fidelity predictions of the onset of thermal runaway from the experimental test matrix using commercially available cells, modules, and packs, spanning multiple chemistries relevant to automotive applications.

Maintain high-fidelity predictions while exploring methods to reduce the computational complexity of the model, and deliver a practical tool that is integrated with the laboratory's Open Architecture Software (OAS), for a broad customer base within automotive product development.

Results and Discussion:

The second year saw significant progress in many areas leading to a workable, validated model. Work continued in refining the mechanical, EM and thermal solvers with composite t-shell elements, all of which are now essentially complete and in use. It was shown that using composite t-shell elements in the mechanical solver can save computational time significantly while achieving almost the same result as using standard solid elements. Since in impact events the mechanical solver takes the majority of the simulation time, using composite t-shell elements has a potential to reduce the total simulation time considerably, which is critical in large-scale simulations such as module or pack level simulations. It was also shown that simulation results using composite t-shell elements are almost identical to results using solid elements in the EM and thermal solvers (see Figure 2). Because of that, composite t-shell elements can now be applied to all the solvers that are needed in the proposed battery safety model. It allows us to use one mesh for the entire models and saves time in the model development processes. (Note that in previous reports and presentations we used both composite t-shell and layered solid elements in reference to the same mesh. In this report, we use only the composite t-shell term.)

The electrochemical properties of type D and E cells have been obtained from the cycling test data via optimization processes. With these properties, the model prediction of the cell voltage profile during discharging and charging matches measurements very well. We built models for type D and E cells, applying the same boundary conditions as experiments in order to check if experimental results can be captured by simulations. The comparison of cell voltage profile during charge and discharge at different temperatures with different initial State of Charge (SOC) is shown in Figure 3, where it can be seen that the model results match experimental measurements well. This indicates that the parameters used in Randle circuit models for both types of cells may capture the battery behaviors over a wide range of conditions.

Additional simulations for shear and crush were run on Type D cells using composite t-shell elements (Figure 4) with very good agreement with experimental data for load/displacement (Figure 5). We have performed the simulation for the shear test using the composite t-shell element as shown in the right hand side of Figure 4. The dimension for the cell is 164 mm X 220 mm X 5.58 mm. Due to symmetric boundary conditions, we modelled only the half of the cell in x direction and a portion of the cell (10 mm in length) in y-direction. Nodes on the left hand side are fixed while the right hand have symmetric boundary condition. Top nodes are moved with a fixed velocity till displacement of 1.5mm. We have used nine elements across the thickness and each element has 16 integration points comprising 4 integration points for positive electrode (cathode), negative electrode (anode) and separator, two integration points are used to represent current collectors. All the components are modelled using MAT-24 material model, parameters for all the components are given in Table 1. The number of composite t-shell elements is 1188 and it took 554 second to complete the simulation on 16 processors. These simulations worked better – had better agreement, fewer elements, less computation time – than simulations with standard solid elements.

Both Type D & E cells were tested under shear conditions at Ford, and then shipped to the Oak Ridge National Laboratory (ORNL) for x-ray computed tomography analyses. Type D cell analysis results indicated that excessive damage was observed in the shear-stressed area and 2 – 3 step shearing might provide details on the progress of the cell component deformation. Additional shear tests were then run again to detectable short circuit, and also stopped at displacements less than creating a short.

Work continued using microphotographs of cell separators to determine statistics of the void fractions, which were then used to create 3D reconstructions. During this year, new models were created and refined and fibrils were added to better simulate type D & E cell separators. Simulations based on the new models compared well with experimental results.

Required platens and indenters were constructed at Intertek, and quasi-static crush testing started. Several Type D and E cells were tested but there were no shorts induced at the highest loading with the current equipment. New load cells, platens, and indenters were designed, purchased or constructed, and testing will resume in the fourth quarter. Fabrication of fixtures for the high-speed impact tests should also be completed and testing started in the fourth quarter.

A test matrix was developed for the cells, and a test site was selected. A preliminary version of the software has been developed and demonstrated for external short circuit and crush leading to internal short circuit scenarios. Techniques such as the use of composite t-shell elements and macro scale meshes were developed to reduce simulation complexity, and demonstrated significant reductions in calculation times. In the coming year, validation experiments will be performed and simulations will be carried out to confirm the model predictions align with physical experiments.

Conclusions:

The second year has been successful, with the project essentially on track and nearly all milestones accomplished. Cell characterization experiments were completed, as were the multi-physics solvers. Model integration was completed and the Beta version assumptions developed. Validation testing was started, but is behind schedule. Spending continues to be below estimated. It is expected that the final year will result in a validated, practical simulation tool that can be used to predict battery response to abuse.

References:

None

Figures and Tables:

Table-1: Parameter for component of the cell.

Component	Thickness (mm)	Elastic Modulus (Gpa)	Yield Strength (Gpa)	Tangent Modulus (Gpa)
Anode	0.064	0.45	0.04	0.01
Separator	0.023	0.50	0.045	0.01
Cathode	0.053	0.55	0.04	0.01
Aluminum Current Collector	0.015	70	0.24	0.1
Copper Current Collector	0.009	110	0.24	0.1

Figures Continue on Next Page

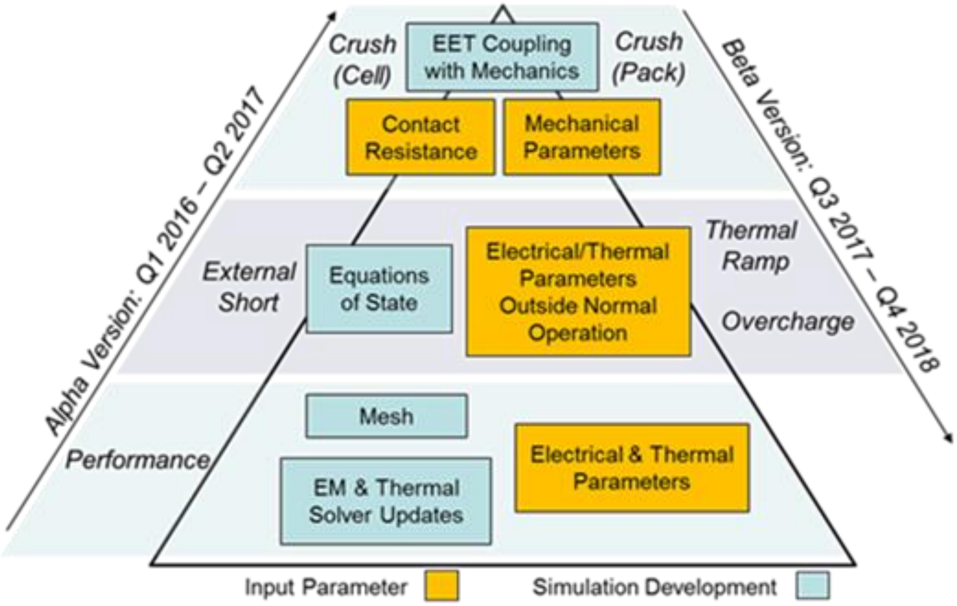

Figure 1. Project schematic showing major constituents and progression of Alpha and Beta versions.

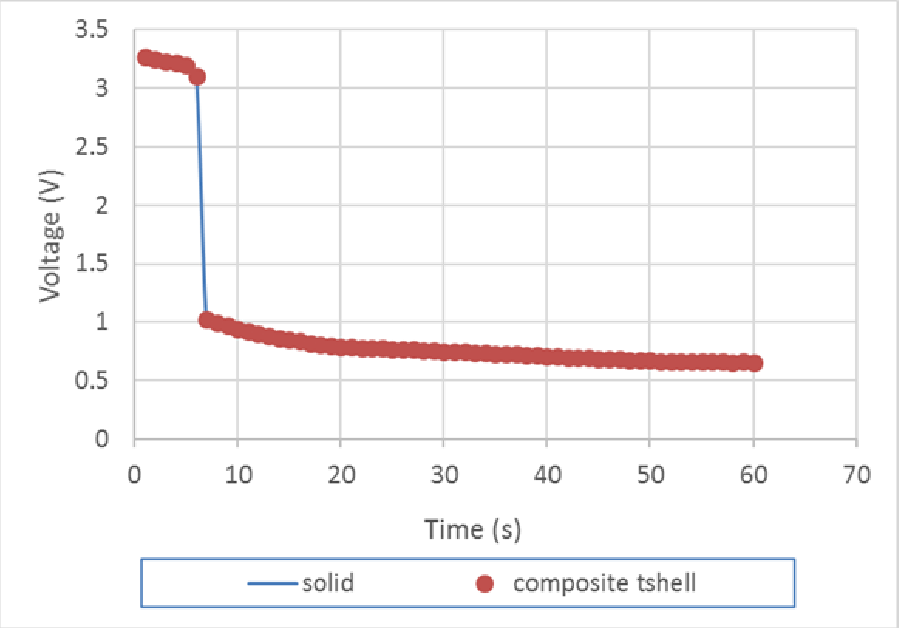

Figure 2. Comparison of voltage evolution in two models.

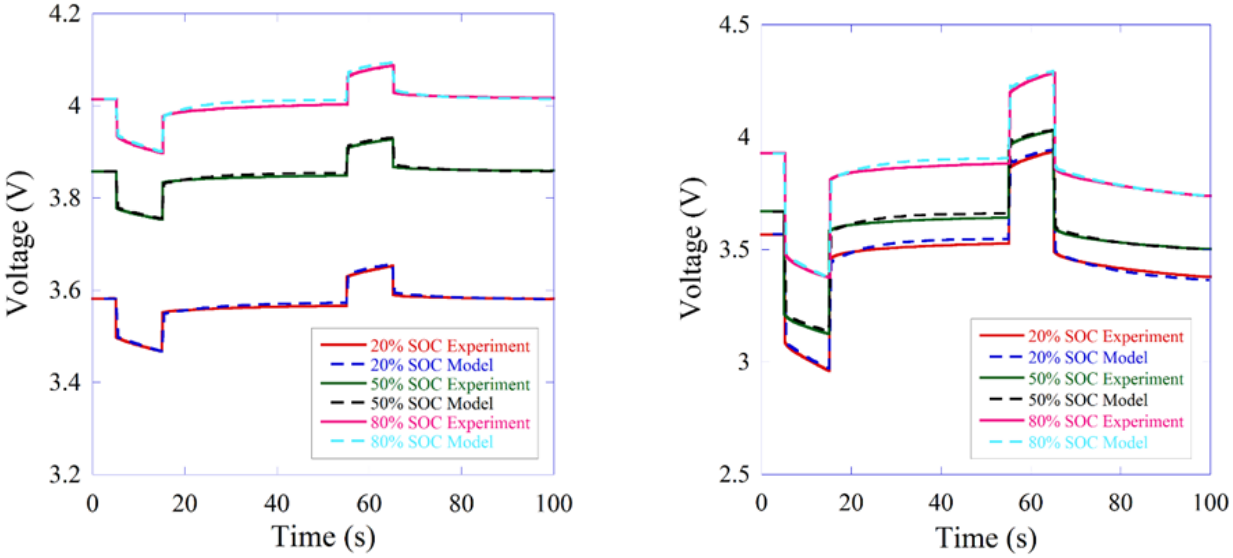

Figure 3. Compare model predictions and measurements of the voltage profile of atype D (left) and type E (right) cell when it is discharged and charged with different initial SOCs.

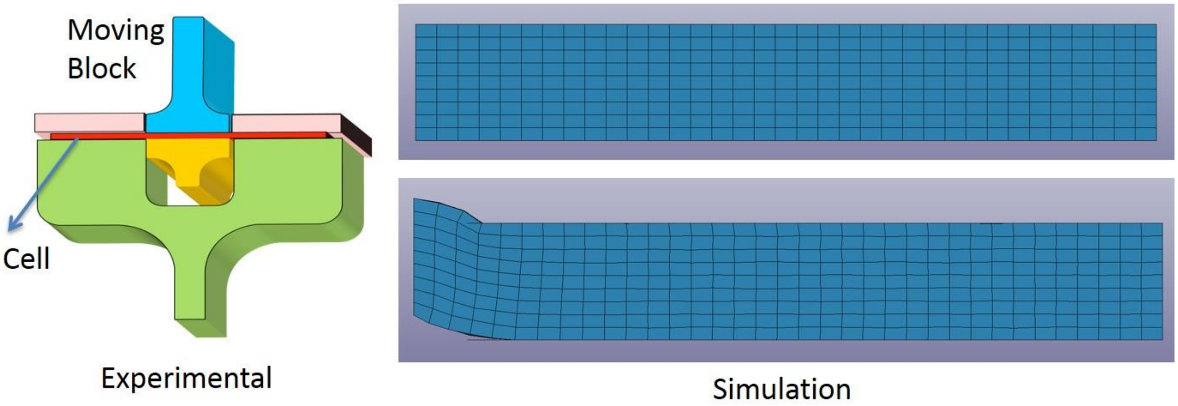

Figure 4. Experimental and Simulation setup for Type D Cell.

Figures Continue on Next Page

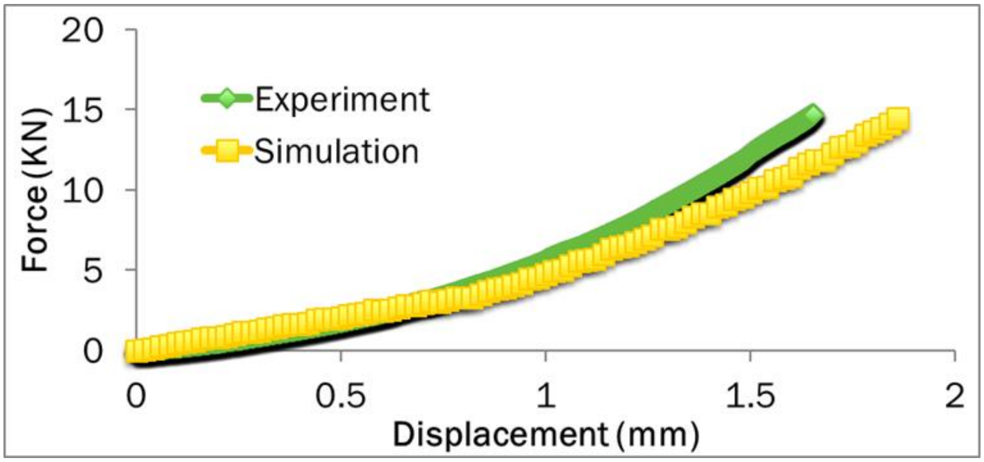

Figure 5. Load displacement curve obtained by experiment and simulation.

Remainder of Page Intentionally Blank

This Page Intentionally Blank

AVPTA Technology Focus Area 6: Energy Storage and Batteries

Advanced Lithium Ion Battery Technology – High Voltage Electrolyte

DOE-VTO TFA Lead: David Howell
TARDEC TFA Lead: Laurence Toomey

Principal Investigator(s):
Dr. Ron Hendershot
Daikin America, Inc.
2749 Highway 20 West
Decatur, AL 35601

Project Start: Oct 2016
Estimated Completion: Q4FY19

Objectives:

- Understand lithium ion battery gassing mechanisms and kinetics as a result of electrolyte decomposition
- Examine both physical and chemical aspects of film formation on the anode and cathode in lithium ion batteries
- Observe any chemical and structural changes at the electrode surfaces under various operating conditions

Strategic Context:

- Developing an electrolyte for lithium ion batteries capable of long-term operation at high voltage (> 4.5 V) will increase power density and improve energy efficiency to both new and retrofitted ground systems
- Minimizing cell decomposition as a result of gas generation will enable safer operation of high-powered vehicles and devices in addition to extending cycle life

Accomplishments:

- Expansion of battery cycling capabilities from 20 to 84 channels and installation of new scientific equipment (e.g. GC/MS)
- Established a baseline of existing data and literature review for the current state of the art performance parameters
- Identified gases present in lithium ion batteries as a function of various parameters: cathode material, electrolyte composition, and voltage
- Increased the capacity retention at high voltage with the addition of Fluoro-Ethylene Carbonate (FEC) to the electrolyte

Introduction:

The use of electrolytes containing small fluorinated molecules to enable stable high voltage (> 4.3 V) battery operation is the focus of this project. Previously, Daikin has shown that it is possible to operate lithium ion batteries utilizing several different cathode chemistries up to 4.5 V. This is accomplished by reducing the gas generation originating from electrolyte decomposition at high voltage. The primary mechanism for this is not completely understood, but the hypothesis is that the fluorinated molecules form a film on the highly oxidizing cathode. It is known that battery cycle performance above 4.5 V drops significantly, however the source of the observed performance loss is not yet understood. The target for this project is to achieve 300 cycles above 80% capacity retention at 4.6 V. A better understanding of gas evolution, which happens above 4.3 V and the failure mode above 4.5 V, is sought in order to propose mitigation strategies which will facilitate better high voltage performance in lithium ion batteries.

The battery industry trend for cathode materials is toward reducing the overall cobalt content (i.e. higher nickel) for a variety of reasons. Some of which include: increasing cost, loss of supply, and human rights issues. The experiments proposed for this project will encompass a range of cathode materials with successively higher nickel content. This will be performed in order to comprehend how fluorinated electrolyte interacts with various cathode surfaces. This is with the anticipation that the lithium ion battery industry will move towards nickel-rich cathodes, which can operate at higher voltage in order to achieve more energy-dense batteries.

Approach:

The baseline of current best-practice fluorinated electrolyte was determined by reviewing already obtained data from high-voltage lithium ion batteries from a previously Department of Energy (DOE)-funded project (DOE EE0006437). In parallel, an up-to date literature and patent review has also been performed to explore other cutting edge developments in 2017. Three electrolytes were selected as standards for this project: 1.2 M $LiPF_6$ Ethylene-Carbonate (EC)/Ethyl-Methyl-Carbonate (EMC) 80:20 (v/v %), 1.2 M $LiPF_6$ EC/EMC/Fluoro-Ether (FE) 20:60:20 (v/v %) and 1.2 M $LiPF_6$ FEC/EMC/FE 20:60:20 (v/v %). These represent electrolytes with zero, one and two fluorinated solvents added, respectively. All electrolytes also contain Propane Sultone (PS) (1% w/w) as an additional anti-gassing additive. 200 mAh dry wound cells have been purchased as test vehicles. The cathode chemistries studied (with increasing mole fractions of nickel are: $LiCoO_2$ (LCO), $LiNi_xMn_yCo_zO_2$ (NMC xyz = 111, 532, 622) and $LiNi_{0.8}Co_{0.15}Al_{0.05}O_2$ (NCA) all paired with artificial graphite anodes. Analysis of the gases produced at high voltage (> 4.3 V) will be completed and compared to cells cycled at a baseline voltage of 4.2 V, which is the current battery industry standard. A post mortem analysis of the gas sampled cells will be conducted for qualitative and quantitative gas analysis. In addition, the cathodes and anodes will be removed for surface analysis to observe Solid Electrolyte Interphase (SEI) film formation and changes in material properties. A mass balance approach to the cells will be used in order to propose performance limiting factors and strategies to overcome them.

Remainder of Page Intentionally Blank

Results and Discussion:

Setup of Experimental Tools, Review State of the Art and Establish Study Baselines:

Work in the first year (FY 2017) has been divided into two tasks which progress against the first four milestones: 1) establishing a baseline based on knowledge learned from first DOE funding opportunity and 2) initiating setup of instruments and samples for gas analysis.

Final cell test results from Argonne National Laboratory were received at the end of March. The cycle testing results are shown in Figure 1 for three groups:

a. Group 1 hydrocarbon electrolyte cycled to 4.5 V, (black trace)
b. Group 2 fluorocarbon best practice electrolyte cycled to 4.5 V, (red trace)
c. Group 3 fluorocarbon best practice electrolyte cycled to 4.6 V, (blue trace)

The results confirm previous Daikin internals results which indicate that fluorocarbon electrolyte performs better than hydrocarbon up to 4.5 V but there is a performance decrease when the upper voltage is extended to 4.6 V. This result fixed the study voltages to 4.2 (both electrolytes work), 4.5 (only fluorinated electrolyte works) and 4.6 V (neither electrolyte works) as initially proposed.

Additional baseline experiments were performed in order to adjust experimental parameters to generate gas in a reasonable timeframe for analysis. Figure 2 displays the volume change in pouches containing NMC111 charged cathodes with graphite anodes stored with electrolyte at 60°C. The targeted temperature settings were established at 35, 45 and 50°C.

Gas Composition as a Function of Voltage and Cathode:

In order to determine the gas composition as a function of various operating conditions ([FEC], voltage, cathode material, etc.), we constructed ninety (LCO, NMC622) 200 mAh cells for an extended Open Circuit Voltage (OCV) test to be carried out at various temperatures for analysis. These cells underwent initial formation then were charged to constant voltage to the desired voltage (4.2, 4.5, and 4.6 V) and placed into ovens at 35, 45, and 55°C. Following this extended aging period with intermittent volume measurements, the cells were discharged and punctured with a gas tight syringe for headspace analysis.

Gas analysis and the determination of components was performed using Gas Chromatography with Thermal Conductivity Detector (GC-MS/TCD) instrument. Figure 3 depicts the full TCD chromatograms (left) and 0-10 minutes (right) of both LCO and NMC622 cells with 10% FEC. The peaks in the TCD chromatograms were confirmed through integration with Mass Spectrometric (MS) detection. It was necessary to compare the retention times of detected species in different cells in order to confirm their assignment and reproducibility.

Table 1 summarizes GC-MS/TCD qualitative results from a calendar (4.6 V, 55°C) life test. The cells underwent formation (2 cycles), were charged to constant test voltage of 4.6 V, and then placed in a 55°C oven. The cell volume and OCV were monitored over a period of 3-4 weeks.

Two different concentrations of FEC (v/v %) were tested during the extended aging experiment. The LCO cathode cells with 10 % FEC exhibited the largest amount of gas produced, in addition to the only battery evolving the larger hydrocarbon gases. In all batteries, CO_2 and CO are the largest components of the analyzed gas. Also present are quantifiable amounts of methane, ethane, and O_2. The additional gases (PF_3, etc.) are present in trace, but measureable quantities. Although the NMC 622 cells produce quantifiable amounts of H_2, we cannot rule out the presence in LCO cells due to detection limits (> 8.5 v/v %) while using helium as the carrier gas in a GC-MS/TCD instrumental setup.

Although the molar quantification of detected gases is ongoing, the integrated TCD intensities can be compared to determine the ratio of gas generation. Of the cells investigated to date, the cells with the highest nickel % (NMC622) generate larger amounts of both fluorinated gases (CH_3F and CH_5F), however did not generate flammable hydrocarbons such as butane, propane, and propene. Further investigation into the origin of higher hydrocarbons in LCO cells is underway.

The presence of PF_3 in the LCO cell at 4.6 V with 10% FEC was an unexpected development, and can be attributed to decomposition of the $LiPF_6$ salt. The mechanism for the formation of PF_3 in not currently understood.

Gassing Kinetics of FEC:

Cycle life testing with intermittent gas measurement experiments were performed on cells containing either LCO or NMC622 cathodes to understand the effect of FEC on battery cycling and gassing. The baseline electrolyte was 1.2 M LiPF6 EC/EMC/FE (20:60:20) + 1% PS. A series of test electrolytes were made by replacing EC with FEC in 5% increments with the final end member electrolyte being 1.2 M LiPF6 FEC/EMC/FE (20:60:20) + 1% PS. Figure 4 depicts the discharge capacity versus cycle number of both NMC622 and LCO cells at 4.6 V and 4.2 V. As expected, discharge capacity at 4.2V was retained throughout 200 cycles, with all cells ranging from 93-95% after cycling at 0.7C. In addition, there was no noticeable effect on the capacity of batteries with the addition of FEC for 4.2 V cycling (Figure 4).

Addition of FEC into the electrolyte resulted in better cycle performance in both chemistries. However, LCO cells cycled at 4.6 V hit the 80% cutoff at < 50 cycles regardless of the FEC content of the electrolyte and ceased operation after 100 cycles (Figure 4 left). However, the NMC622 cells when cycled at 4.6 V showed remarkable improvement with added FEC. Only three electrolytes (0, 5, 15% FEC) are shown for clarity. The noticeable cycling improvement is first evident with 10% FEC, with marginal improvements up to 20%. The NMC622/graphite cell (blue trace, Figure 4 left) cycled at 4.6 V is trending toward project target of 300 cycles. This data along with the gassing and OCV data above suggest that the performance drop in the LCO system at high voltage is due to degradation of the cathode but additional experiments to examine the cathode structure/chemistry need to be completed for confirmation.

Gassing Kinetics Based on Cathode Composition:

Gassing kinetics of two cathode chemistries (LCO and NMC622) have been determined through volume change measurements over a period of 3-4 weeks, with cells stored at 45 °C after formation and final charge to 4.6 V. The data shown in Figure 5 (left) shows the volume change versus time (days) of both LCO and NMC622 cells with two different electrolytes: 1.2 M $LiPF_6$ EC/EMC/FE (20:60:20) + 1% PS and 1.2 M $LiPF_6$ EC/FEC/EMC/FE (10:10:60:20) + 1% PS. The measured OCV versus time of these cells is also depicted in Figure 5 (right).

As seen in Figure 5, there is more gas generated in the LCO cells at 4.6V (left), which is consistent with the OCV drop (right). A decrease in measured OCV indicates that the cathode is being reduced. The cathode can be reduced through multiple mechanisms, one of which includes the oxidation of the graphite anode. One other mechanism includes oxygen defect formation in the cathode material due to crystal structure instability. While additional FEC seems to delay OCV loss, it does not impact gas generation to the same degree.

Conclusions:

Significant work at Daikin in the first year involved setup and validation and training for equipment needed to complete this project. This included expanding our cell cycling capability from 20 to 104 channels and commissioning of several new pieces of equipment (e.g. GC/MS).

An examination of both the existing data and current literature was completed to set baselines for this study. Third party data from final cells of previous Daikin project confirm the there are two battery performance failure points. The first occurs above 4.3 V, which is attributed to electrolyte decomposition resulting in gas generation. It has been shown that the use of fluorinated electrolyte greatly diminishes the decomposition reaction, resulting in enhanced performance. The second failure point occurs above 4.5 V. The baseline experimental voltages for this project have been set at 4.2, 4.5 and 4.6 V in order to study chemical and physical changes which occur when at or near these failure points.

Gas composition has been established for both the LCO and NMC622 cathode materials. Both contain significant amounts of CO, CO_2, CH_4 and O_2 along with select fluorinated hydrocarbons attributed to the decomposition of FEC in the electrolyte.

For both chemistries studied, the addition of FEC to electrolyte results in increased cycle life and capacity retention. However, that benefit for LCO cells is not sufficient to permit viable high voltage operation. The full cycling performance benefit of FEC in the electrolyte is realized at a 10% (v/v %), and can be marginally increased with additional FEC. The data obtained thus far for LCO cells (OCV loss, gas evolution, etc.) suggests that decreased performance is due a non-electrolyte component failure, but rather the result of an inherent property of the cathode material.

References:

[1] Petibon, R.; Dahn, J. R. et al, *J. Electrochem. Soc.*, **2016**, *163*, A1146-A1156

[2] Xiong, D. J.; Dahn, J. R. et al, *J. Electrochem. Soc.*, **2017**, *164*, A340-A347

[3] Onuki, M. et al, *J. Electrochem. Soc.*, **2008**, *155*, A794-A797

[4] Self, J.; Dahn, J. R. et al, *J. Electrochem. Soc.*, **2015**, *162*, A796-A802

Figures and Table:

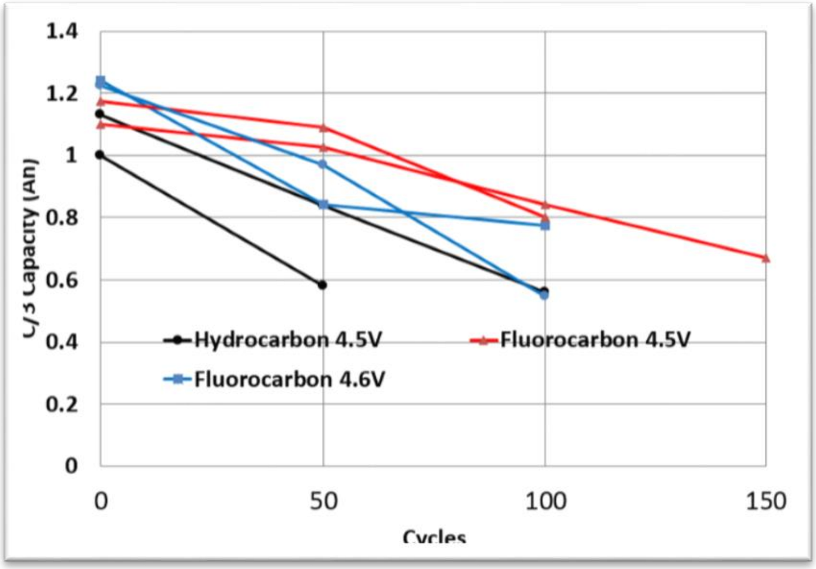

Figure 1. Cycle life (C/3) discharge for a) Hydrocarbon electrolyte charged to 4.5 V (black), 2) fluorocarbon electrolyte charged to 4.5 V (red), and fluorocarbon electrolyte charged to 4.6 volt (blue)

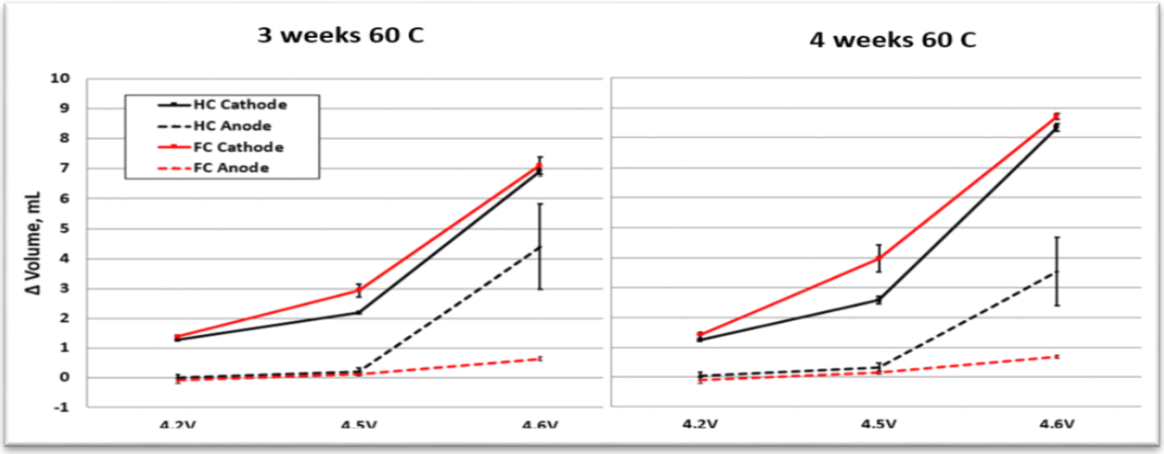

Figure 2. Gas volume change at 3 weeks (left) and 4 weeks (right) for NMC111 cathodes with graphite anodes when exposed to electrolyte at 60°C

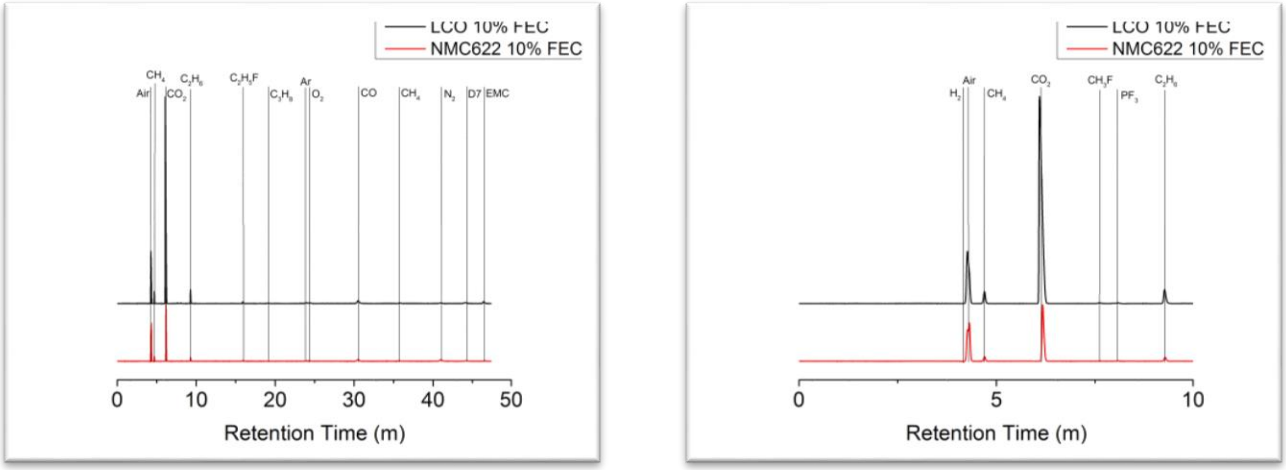

Figure 3. TCD chromatogram overlays of 4.6V LCO and NMC622 cells with 10% FEC concentration in the electrolyte. On the left is the full spectrum, whereas on the right focuses on 0-10 minutes. H_2 is seen in the NMC622 cell and PF_3 in the LCO cell.

Table 1 Gas Composition of LCO and NMC622 Cells as a Function of FEC Concentration Determined by GC-MS/TCD.

[FEC]	CH_4	C_2H_2	C_2H_4	C_2H_6	C_3H_6	C_4H_{10}	CH_3F	C_2H_5F	CO	CO_2	O_2	H_2	PF_3
LCO 10%	X		X	X	X	X	X	X	X	X	X		X
LCO 20%	X	X		X		X	X	X	X	X	X		
NMC622 10%	X		X	X			X	X	X	X	X	X	
NMC622 20%	X	X		X			X	X	X	X	X	X	

Figures Continue on Next Page

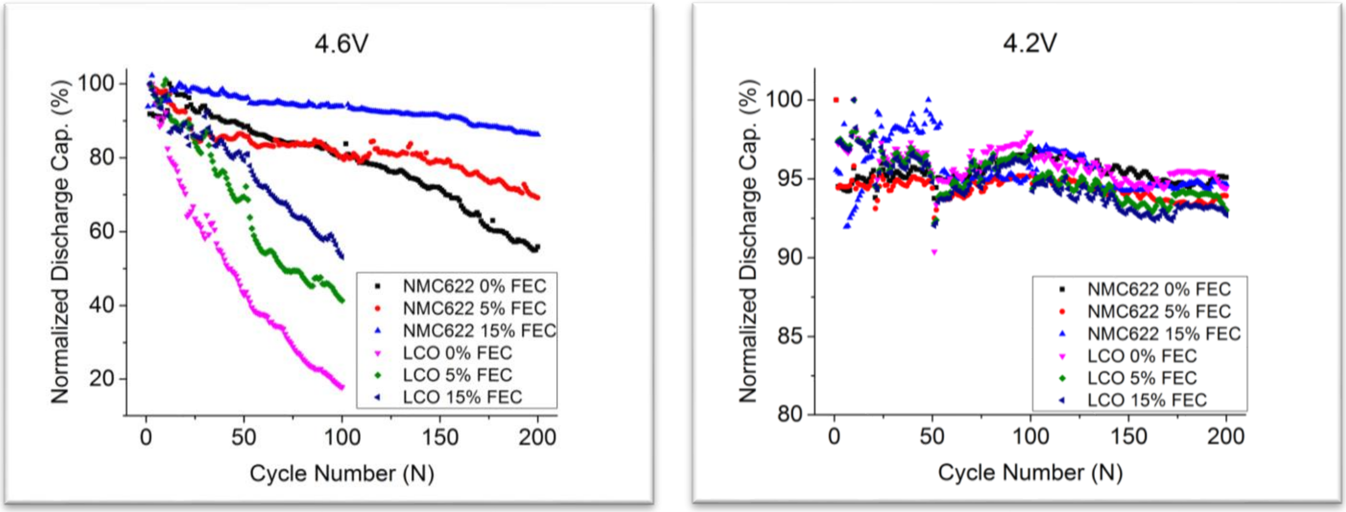

Figure 4. Normalized discharge capacity (%) versus cycle number (N) of NMC622 and LCO cells cycled at 4.6V (left) and 4.2V (right). LCO cells ceased operation after 100 cycles at 4.6V, whereas NMC622 cells completed the desired 200 charge/discharge cycles. Electrolyte is 1.2 M $LiPF_6$ [EC/FEC]/EMC/FE (20:60:20) + 1% PS.

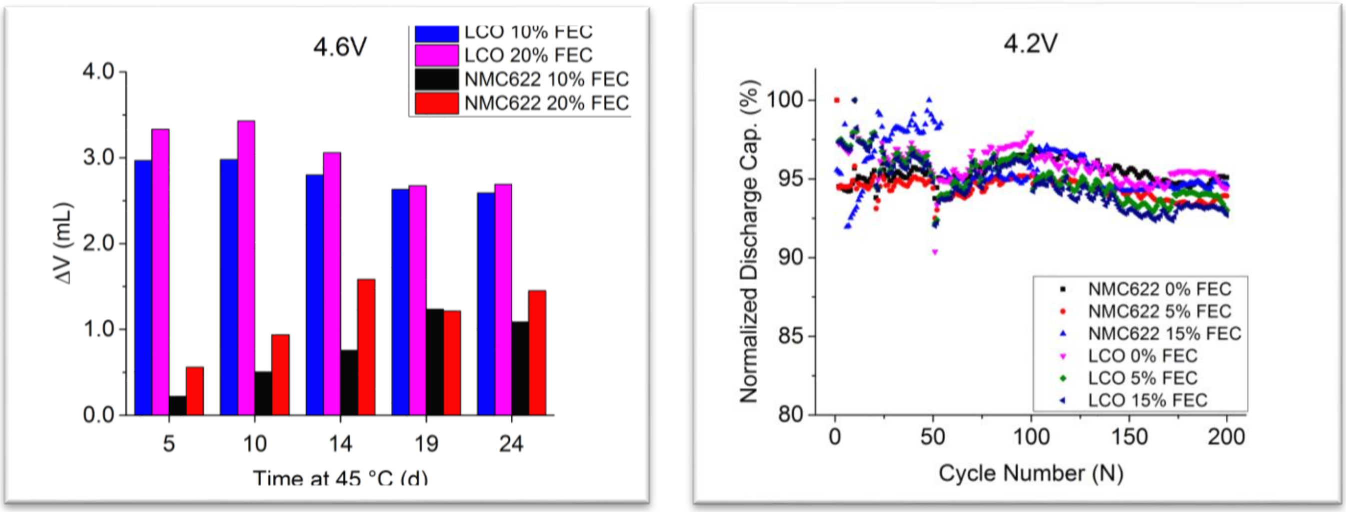

Figure 2 Volume measurements versus time in 4.6V NMC622 cells during an OCV calendar life test at 45 °C as a function of FEC concentration (left). Measured OCV versus time in 4.6V NMC622 and LCO cells during the same calendar life test also as a function of FEC

AVPTA Technology Focus Area 6: Energy Storage & Batteries

Beyond Li-Ion: Overcoming Interface Impedance in Solid-State Batteries

DOE-VTO TFA Lead: David Howell
TARDEC TFA Lead: Laurence Toomey

Principal Investigator:
Dr. Eric Wachsman
University of Maryland
1206 Engineering Laboratory Building
University of Maryland
College Park, MD 20742

Project Start: Oct 2014
Project Completed: Q3FY17

Objectives:

- Develop a multifaceted and integrated (experimental and computational) approach to solve the key issue in Solid-State Li Batteries (SSLiBs), interfacial impedance.
- Develop methods to decrease the impedance across interfaces with the solid electrolyte
- Demonstrate a high power/energy density battery employing the best of these methods.

Strategic Context:

- Generate a leap-ahead technology used for military vehicles to support the future power for TARDEC and the Army by enabling the development of advanced battery systems with significant increases in energy density
- Improve Battery safety characteristics to support vehicle silent watch and enable other high energy requiring applications.

Accomplishments:

Computational understanding of SSE-electrode interface:

- Achieved fundamental understanding of interfacial impedance as demonstrated by consistency between computational and experimental results.
- Developed computational models to investigate stability and interfacial ion transport with varying types of interlayers
- Predicted formation of protective interfaces between garnet and S and Lithium-Nickel, Cobalt and Manganese (NMC) cathodes

For garnet-cathode interface:

- Demonstrated that gel electrolyte can reduce the interfacial resistance by over 4 orders of magnitude achieving an interfacial Area Surface Resistance (ASR) of ~67 Ohm-cm^2 for planar cathode/garnet interface.
- Demonstrated that increasing surface area can effectively decrease the interface resistance, achieving a 52% decrease in interfacial ASR.
- Aqueous interface lead to 7.5 Ohm-cm^2 cathode/garnet interfacial resistance planar cathode/garnet interface. Therefore, we met the ~10 Ohm-cm^2 garnet/cathode goal.

For Li-garnet interface:

- Demonstrated gel electrolyte, Si, and Al can reduce interfacial resistance to 200 Ohm-cm^2, 127 Ohm-cm^2, and 75 Ohm-cm^2, respectively for planar Li metal-garnet interface.
- Further demonstrated that ALD-Al_2O_3 can reduce interfacial resistance to ~1 Ohm-cm^2 for planar Li metal-garnet interface. Therefore, we met the ~10 Ohm-cm^2 garnet/anode goal.

Full Cell demonstration:

- Fabricated and tested SSLiBs with Li-NMC Chemistry.
- Fabricated and tested SSLiBs with Li-S Chemistry.
- Achieved full cell (Li-NMC) performance of 352Wh/kg.
- Achieved full cell (Li-NMC) performance of 200 cycles.
- Achieved full cell (Li-S) performance of 272 Wh/kg and 50 cycles.

Introduction:

Solid state garnet-electrolyte lithium ion batteries have tremendous potential due to their inherent safety, high voltage stability, and reasonably high conductivity. However, the interfacial impedance between solid state electrolytes and electrodes is currently too high. This work focuses on reducing the interfacial impedance, by making controlled structures on the garnet electrolyte surface, and introducing conductive and conformal interfacial layers between the garnet and the electrodes. These results, informed by computational modeling, address the primary issue and significantly advance solid-state Li-battery technology.

Approach:

The above-listed Objectives were accomplished by optimizing the garnet surface structure and electrode material, and investigating high conductivity conformal interfacial layers.

Effect of interfacial structure on impedance

While we and others have made tremendous advances in understanding interfacial resistance in Solid Oxide Fuel Cells (SOFCs), to date no one has applied these techniques to SSLiBs. Therefore, we used SOFC techniques to develop a fundamental understanding of interfacial impedance in terms of intrinsic charge transfer rates, ionic and electronic transport, and effect of interfacial structure.

Electrochemical Impedance Spectroscopy (EIS) of solid electrolyte and electrode or interfacial layer pellets were performed to identify the mechanistic frequency dependence of EIS response for each material as well as blocking electrode and DC measurements to separate out ionic vs. electronic conductivity for each material. Then bilayer electrolyte and electrode/interfacial layer pellets with smooth and controlled interfaces were fabricated and tested with EIS.

This allowed for determination of the specific interfacial impedance, which could then be resolved as an additional EIS frequency response. This interfacial impedance was used to calculate the charge transfer reaction rate across the electrolyte/electrode and electrolyte/interfacial layer interfaces. Bilayered pellets with tailored nano/micro-rod interfaces have been fabricated (by templated deposition and additive manufacturing) with different rod length to diameter aspect ratios. The EIS data from these cells is deconvoluted and compared with known ionic and electronic transport rates, and charge transfer rates, to create fundamental models of interfacial impedance as a function of 3-dimensional interfacial structure.

Investigate interfacial modifications and cell performance

Four types of materials as interfacial layers in SSLiBs were investigated.

Type 1 used nonflammable organic electrolytes such as perfluoropolyethers (PFPE) based electrolytes. It has been confirmed that such organic electrolytes cannot catch fire and are intrinsically safe. Although, PFPE-based electrolytes have very low ionic conductivity (~10^{-5} S/cm) and cannot meet the power density requirement in the Funding Opportunities Announcement (FOA) by itself, PFPE based organic electrolyte can greatly improve the interfaces across electrolyte grain boundaries, or electrolyte/electrode interface for enhancing the battery performance.

Type 2 also used a polymer electrolyte or gel electrolyte, which is bis(trifluoromethane)sulfonimide lithium salt (LiTFSI) in poly(vinylidene fluoride-co-hexafluoropropylene) (PVDF-HFP). Although the polymer or gel electrolyte has a much lower ionic conductivity, its thickness is small as an interface layer and thus its contribution in overall impedance was expected to be negligible.

Type 3 investigated thin inorganic layers formed by Atomic Layer Deposition (ALD) and other thin film deposition techniques to form a nano-thin conducting phase between the garnet and the electrode.

Type 4 used a soft conformable materials such as β-Li_3PS_4 (LPS) or liquids to bridge the gap between the garnet and electrode material.

For each approach, half cells were fabricated to investigate interfacial impedance and their changes during cycling. SSLiB interfaces are typically planar resulting in high impedance due to low specific surface area, and attempts to make 3D high surface area interfaces can also result in high impedance due to poor contact (e.g, pores) at the electrode-electrolyte interface that hinder ion transport or degrade due to expansion/contraction with voltage cycling. We have investigated the fundamentals of solid-solid interfacial impedances in FY15 and investigated interfacial modification (layers between SSE and electrode) to see if we can extend these structure-property relationships to higher performance in FY16. In FY17 we applied these interfacial modifications to develop solid-state batteries. The objective of FY17 was accomplished by developing full cells based on the interfacial impedance reducing techniques and the structurally optimized garnet SSEs. We developed high energy density batteries based on multi-layer garnet, Li metal anode, and two different types of cathodes: $Li(Ni_xMn_yCo_{1-x-y})O_2$ (NMC) and sulfur. For each type of battery chemistry, the battery morphologies, electrochemical stabilities, and cycling performances were evaluated.

Throughout this work, there was collaboration with Dr. Kang Xu at the US Army Research Laboratory with preparation of liquid electrolytes. SSEs and electrode materials were synthesized in University of Maryland Energy Research Center, and characterized in the Nanocenter and FabLab at University of Maryland. Fabrication of the SSLiBs was accomplished using the comprehensive state-of-art multilayer ceramic fabrication facilities. The facilities include tape casting, screen printing, and furnaces for fabrication, as well as extensive electrochemical testing capabilities.

Results and Discussion:

Cathode interface resistance

Characterization of electrolyte/cathode interface impedance

We tested the impedance of LLCZN solid state electrolyte, and its interface impedance with Li2FeMn3O8 (LFMO) electrodes. The LLCZN ($Li_{6.8}La_{2.95}Ca_{0.05}Zr_{1.75}Nb_{0.25}O_{12}$) garnet was synthesized by conventional solid state reactions. The starting materials, Li(OH), $La(OH)_3$, $Ca(OH)_2$, ZrO_2, and Nb_2O_5 were mixed by planetary ball-milling, and then calcined at 700°C for 48 h. The calcined LLCZN powder was mixed with additives (both Al_2O_3 and Li_3BO_3, only Al_2O_3 or only Li_3BO_3) by planetary ball-milling. The mixture was die-pressed at 10 MPa into a pellet and sintered in air. EIS of LLCZN electrolyte and LFMO cathode was tested with Solartron 1260 impedance analyzer at room temperature using gold paste current collectors. EIS plots were collected at 50 mV voltage signal over a frequency range of 10 Hz -20 MHz.

Figure 1a is the EIS curves of thick and thin LLCZN electrolyte samples. A semicircle and Warburg-type impedance appeared at high and low frequency regions, respectively. The high-frequency semicircle is the sum of bulk and grain boundary responses. The low-frequency tail corresponds to the capacitive behavior of gold blocking electrode. The total lithium-ion conductivity of LLCZN electrolyte is estimated from the intercepts from the semicircle at low frequency side. The thin pellet shows a slightly lower total conductivity than the thick pellet sample. Figure 1b is the EIS curves of thick and thin LFMO cathode samples at initial state (0%SOC). The Nyquist plot contains one depressed semicircle in the high frequency and another semicircle in the medium frequency ascribed to the resistance of Li^+ diffusion through the SEI layer and charge transfer reaction, respectively. The EIS plot indicates similar conductivity exhibited by both the thick and thin pellets of LFMO.

Knowing the frequency response of both LLCZN electrolyte and LFMO cathode we then analyzed the system consisting of electrolyte, cathode and their interface. Finely polished electrolyte and cathode with gold electrode on outer side were tightly pressed together. The electrolyte/cathode system was then characterized by EIS. Figure 1c shows the Nyquist plots of LLCZN electrolyte/LFMO cathode system. Both thick and thin pellet samples were examined to identify the interfacial effect in the system. The impedance arc is the total resistance of LLCZN electrolyte, LFMO cathode and their interface. The arc in the medium-low frequency range is the dominant interfacial resistance between LLCZN electrolyte and LFMO cathode. The high frequency response in the magnified plot is the sum of LLCZN electrolyte resistance and LFMO cathode resistance. This process was repeated with other cathode materials beyond LFMO.

The garnet/cathode interface impedance was lowered by making structured garnet surfaces. Sintered dense garnet discs were sanded to 150 µm and polished. To make the column structures, polymer mesh was glued on disc surface as a template, after that a garnet slurry was drop coated to fill the open area. The coated sample was dried in oven and sintered at 800°C for 2h. Figure 2a shows the structured garnet surface. The white shinning areas are the deposited column structures.

Symmetric cathode/electrolyte/cathode cells were made by screen printing thick cathode slurry on the garnet discs. LFMO cathode was sintered at 500°C for one hour. Silver paste was used as current collector. Thickness of the cathode was about 20µm. EIS plots were collected at 50 mV voltage signal in a frequency range of 10 Hz -10 MHz at room temperature. Figure 2b is the EIS response of cathode coated as-polished and structured garnet discs which exhibits lower interfacial resistance, compared to that with smooth surface due to the larger interfacial cathode/electrolyte contact area provided by the surface column structure.

Synthesis and characterization of nonflammable PFPE-based interface (Type 1)

PFPE-DMC was prepared from Fluorolink D10 and triethylamine in 1,1,1,3,3-pentafluorobutane at 0 °C under nitrogen atmosphere, followed by dropping a solution of methyl chloroformate in 1,1,1,3,3- pentafluorobutane. After the mixture was stirred at 25 °C for 12 h, the PFPE-DMC product was obtained by filtering and washing with water and brine, followed by evaporation under reduced atmosphere. The PFPE-DMC electrolyte was then produced by dissolving Lithium bis(Trifluoromethanesulfonyl)Imide into PFPE-DMC. The synthesis method of PFPE-DMC is shown in Figure 3a.

A Li/PFPE/Ti structure in a CR2025 coin cell was used to test Cyclic Voltammetry (CV) of the PFPE/LiTFSI electrolyte. The area of the cell is 1.98 cm^2 (radius=5/16 inch), and the area of Ti cathode is 0.712 cm^2 (radius=5/32 inch). The voltage range was -0.3~4.2 V, and the voltage scan speed was 1 mV/s.

The CV results are shown in Figure 3b. The reaction current density is less than 0.002 mA/cm^2 in 0.3~4.2V region, which is very small. And after the first few cycles, the CV curve becomes stable. The two facts show that the PFPE electrolyte is electrochemically stable between 0-4V. Also, for the PFPE electrolyte, no obvious peaks appear in the voltage region of -0.3 ~ 4.2 V, which means that the Li stripping occurs at a higher voltage than 4.2 V, and the Li platting occurs at a lower voltage than -0.3 V. The electrochemical stability of PFPE/LiTFSI in the voltage range of 0~4.2 V ensures that this electrolyte is stable in the reactions of LLCZN garnet electrolyte lithium ion batteries, and can be used as the interfacial layer between garnet and cathode.

Synthesis and characterization of gel based interface (Type 2)

A Poly(Vinyli-Dene Fluoride-co-HexaFluoroPropene) (PVDF-HFP) based gel polymer was prepared (Figure 4) from 0.25 g PVDF-HFP dissolved into a mixture of 4.75 g acetone and 0.25 g DI water (95:5, m/m) under continuous stirring. The solution was cast onto an Al foil and the solvent evaporated at ambient temperature. After drying under vacuum at 100°C a homogeneous free standing membrane was obtained. The as-prepared porous membrane was immersed into 1 M LiTFSI in a mixture of 1:1 volume ratio of tetraethylene glycol dimethyl ether and n-methyl-(n-butyl) pyrrolidinium bis(trifluoromethanesulfonyl)imide (Py14TFSI) at room temperature for 30 mins in an argon-filled glovebox.

CV testing cell was set up by sandwiching the gel electrolyte membrane between lithium and titanium disks and sealing the configuration in CR2032 coin cells. The CV (Figure 4b) at a scan rate of 1 mV/s suggests a stable electrochemical window up to 4.2 V. The sharp peak at -0.2 V corresponds to the Li plating, while the peak around 0.1 V is due to the Li stripping.

Figure 5a is the electrochemical impedance spectroscopy (EIS) plot of a cathode/garnet/cathode symmetric cell without any interfacial layer modification. The total resistance of cathode/garnet/cathode symmetric cell without gel interfacial layer is ~106 $Ohm\text{-}cm^2$ due to the poor contact between garnet and $LiFePO_4$ cathode material, the difficulty of charge transfer through the interface between two solid materials, the non-conductive binder, and the rough surface of the garnet pellet.

Figure 5b is the EIS plot of cathode/garnet/cathode symmetric cell with gel interface. The impedance curve has three components. In the high frequency region (f >9 kHz) is an incomplete semi-circle, corresponding to the bulk and grain boundary impedance of the garnet electrolyte. In the middle frequency region (7 Hz <f< 9 kHz) is a combination of two semi-circles corresponding to interfacial charge transfer impedance between garnet and cathode, including impedance on the gel/garnet and cathode/gel interfaces, as the impedance of the gel layer itself is very small. In the low frequency region (f <7 Hz) is a straight line, corresponding to diffusion impedance of the cathode.

The interfacial resistance is obtained by subtracting the garnet resistance obtained separately by EIS of garnet samples from the total symmetric cell resistance, then dividing by two as there are two interfaces, e.g.,:

- Thickness of garnet pellet is 500 µm, and garnet conductivity is $2.1*10^{-4}$ S/cm (Figure 5c). Therefore, Area Specific Resistance (ASR) of garnet pellet is 239 Ohm-cm^2.
- The total symmetric cell resistance (Figure 5b) is 600 Ohm-cm^2. Therefore, the ASR of one interface is (600-239)/2 =180 Ohm-cm^2, which is ~4 orders of magnitude less than the same symmetric cell without the interfacial layers.

To further reduce the garnet/cathode interfacial impedance the procedure was improved by making a gel/cathode composite, instead of using separate gel layers, thus reducing the gel thickness and improving the contact between gel and cathode. Figure 5d shows the structure of symmetric cell using $LiFePO_4$/gel cathode on both sides of garnet, and Figure 5e shows the impedance of this structure. The corresponding interfacial ASR is now reduced to only 67 Ohm-cm^2 for one interface (using same approach described above).

Synthesis and characterization of aqueous interface (Type 4)

To further reduce the cathode/garnet interfacial resistance we evaluated an aqueous solution interface (e.g., Type 4). We anticipated a lower cathode/garnet interfacial resistance with the aqueous interface compared with the gel interface as the aqueous solution has higher conductivity and fluidity than the organic electrolyte used for the gel interfaces. Figure 6a shows a schematic of the symmetric cell with the aqueous cathode/garnet interface. The cathode material ($LiFePO_4$, Carbon black and PVDF) was coated on a carbon cloth. Then these electrodes were immersed into a saturated aqueous LiCl solution to wet them and then the two electrodes and a garnet pellet were pressed together.

As shown in Figure 6b, the EIS semi-circle of the cell yields a resistance of 253 Ohm-cm^2, which after correcting for garnet ASR and dividing by 2 for the dual interfaces results in a single cathode/garnet interfacial resistance of only 7.5 Ohm-cm^2, 5 orders of magnitude lower than the non-interfacial layer cell, and achieving the Q4FY16 and budget period 2 Go/NoGo milestones.

Characterization of structured garnet interface

A 3D garnet surface structure can dramatically increase the effective surface area relative to the planar areal surface area. 3D structured garnet line patterns were printed on surface polished garnet pellets and sintered to form structured ionic conductive paths with varying line spacing (Figure 7). Cathode slurries ($LiFePO_4$, Carbon Nano-Tube (CNT), and gel) were coated on both flat and structured garnet surfaces. EIS of the symmetrical cells was obtained at room temperature.

The depressed arcs, which can be assigned to Li^+ diffusion and charge transfer steps, became much smaller after effective extension of surface area. The 3D printed lines (40μm height and 70μm width) increased the effective sample surface areas from 36 mm^2 for polished pellet to 39.9, 42.3 and 48 mm^2 with increasing line density, resulting in 22%, 35% and 52% reduction of interfacial resistance (from the intercept of real axis high frequency arc (Figure 7a)) proportional to the increase in effective surface area (Figure 7b). Therefore, as expected the 3D printed structures reduced the cathode-electrolyte interfacial resistance linearly with increasing effective surface area.

Anode interface impedance:

Characterization of gel electrolyte interface

Figure 8a shows that the total resistance of a Li/garnet/Li symmetric cell (formed by melting Li metal on the garnet surfaces) without an interfacial layer is about 3000 Ohm-cm^2. Figure 8b shows the EIS plot of Li/gel/garnet/gel/Li plot has four components. In the high frequency region is an incomplete semi-circle, from the garnet impedance. In the middle frequency region are two semi-circles, due to interfacial charge transfer impedance between garnet and Li metal, which mainly comes from impedance on the gel/garnet and Li/gel interfaces, as the impedance of the gel layer itself is very small. In the low frequency region is a tail, corresponding to diffusion impedance of the interface of gel/stainless steel outside of the lithium metal. Correcting for garnet impedance, the ASR with the gel interlayer is reduced to 200 Ohm-cm^2 for one interface; however, this is done without melting the Li metal as was done for the other cell.

Characterization of Si interface

LLZ and Si-coated LLZ was sandwiched by two Li metal electrodes to assemble symmetric cells (Figure 9a and 5b). Prior to the electrochemical measurements, all the cells were heated at ~200°C for twenty minutes in a glovebox since thermal treatment promotes superior contact between Li and LLZ. Due to the high reactivity of molten Li, lithiated Si will be formed in situ between the Li metal and the Si-coated LLZ. The Nyquist plots of symmetric cells in Figure 9c exhibit two distinct semi-circles: one at high frequency and another at low frequency. The Li/LLZ/Li symmetric cell delivers a large resistance of 2064 Ohm-cm^2, where the interfacial resistance between Li and LLZ was calculated to be 925 Ohm-cm^2.

The first semi-circle at relatively high frequency was used to analyze the interfacial resistance between the Li metal electrode and the LLZ solid electrolyte with/without Si coating. As shown in Figure 9d, the overall resistance of the LLZ (bulk and grain boundary) measured using Au electrodes is 215 Ohm-cm^2. As shown in Figure 9e, the first semi-circle of the Li/LLZ/Li cell yields a resistance of 2064 Ohm-cm^2, which can be divided into two parts: one is the resistance of the LLZ (bulk and grain boundary) and the other is the Li metal-LLZ interfacial resistance. Thus, the overall Li metal-LLZ interfacial resistance is 1849 Ohm-cm^2. Since two Li metal-LLZ interfaces are present in the Li/LLZ/Li symmetric cells, the single Li metal-LLZ interfacial resistance is approximately 925 Ohm-cm^2. On the other hand, the Si-coated LLZ cell displays a much smaller resistance of 469 Ohm-cm^2 in the first semi-circle. By subtracting the resistance of the LLZ (215 Ohm-cm^2) and dividing by two, the Li metal/Si-coated LLZ interfacial resistance can be calculated: 127 Ohm-cm^2, which is about 7.3 times lower than bare LLZ.

Characterization of Al interface

Two symmetric cells, Li | Garnet SSE | Li and Li | Al-Garnet SSE-Al | Li, were prepared and tested directly in an argon-filled glovebox. The two cells showed large differences in total resistance, which depend on both the garnet's total resistance and the interface charge transfer resistance, as shown in the Nyquist plots (Figure 10a and 10b). The Li | Garnet SSE | Li cell had a total resistance of ~2000 Ohm-cm^2. However, the Li | Al-Garnet SSE-Al | Li cell exhibited a resistance of ~300 Ohm-cm^2, which is almost one order of magnitude smaller than the uncoated SSE. The small partial semicircle at high frequency can be assigned to the total resistance of the garnet material. The large semicircle at medium frequency and low frequency correspond to the charge transfer resistance, which is the combination of the solid-state electrolyte resistance as well as the Li interfaces within the symmetric cells. The decreased size of the semicircle indicates that the interfacial resistance was significantly reduced using the Al coating. The total garnet resistance was ~150 Ohm-cm^2 and remained unchanged during the Li melting process. By subtracting the garnet ASR, the Li | Garnet SSE | Li cell charge transfer resistance was ~1900 Ohm-cm^2 at 20°C. For the Li | Al-Garnet SSE-Al | Li cell, the charge transfer resistance was decreased to ~150 Ohm-cm^2. Note that the interfacial resistance corresponds to two symmetric interfaces. Therefore, the interfacial resistance is ~950 Ohm-cm^2 and ~75 Ohm-cm^2 for Li | Garnet SSE and Li | Al-Garnet SSE-Al, respectively.

Characterization of ALD Al_2O_3 interface

To make Li/garnet/Li symmetric cell with ALD Al_2O_3 interface, a ~ 5-6 nm thick ALD-Al_2O_3 coating was applied to the garnet surface. Then a piece of Li metal foil was pressed on the garnet pellets and heated at 250°C for 1 hour under a small pressure. A control sample was made using bare LLCZN pellets in the same way.

Figure 11a shows the schematic of the interface between garnet and Li metal. The SEM images in Figure 11b clearly demonstrated that the enhancement of interfacial contact by applying ALD Al_2O_3 ultrathin layer on garnet interface. Inset are photo images to show the surface wetting of garnet and the Atomic Layer Deposition (ALD) treated garnet.

To quantify the effect of ALD on the improvement of garnet/Li interface, symmetric Li/garnet/Li cells were prepared and evaluated by EIS (Table 1 and Figure 11). As shown in Figure 11c, two distinct arcs were seen in each sample. The bulk garnet ASRs, obtained from the high frequency intercept, are 26 and 28 Ohm-cm^2 for cells with and without ALD coating, respectively. The first arc represents most likely the overlap of the grain boundary and interface impedances, which were 176 Ohm-cm^2 and 3500 Ohm-cm^2 for cells with and without ALD coating, respectively. Interfacial

ASR was calculated by subtracting the garnet impedance measured with Au electrodes (~108 Ohm-cm^2) and dividing this result by two before normalizing to the electrode surface area. It can be seen that the ALD treatment decreased the interfacial ASR by EIS from 1750 Ohm-cm^2 to 34 Ohm-cm^2. However, DC cycling (Figure 11e) further reduced the interfacial impedance. The total ASR from DC cycling is calculated as 110 Ohm-cm^2, which after subtracting 108 Ohm-cm^2 for the garnet contribution leaves 1 Ohm-cm^2 for each Li-garnet interface.

Modeling of interfacial coating layers on garnet-electrode interfaces:

First principles modeling of garnet solid electrolyte materials was performed on both tetragonal and cubic LLZ phases. The ordering of Li was determined using computational methods, and the ground state ordering of Li was determined. The Li grand canonical phase diagram of the Li-La-Zr-O system based on first principles computation methods and electrochemical stability of garnet against Li metal was determined (Figure 12).

In addition, first principle models were constructed to evaluate the structure and energetics of the electrolyte-electrode interfaces between garnet and Li metal. We found that Li metal has a very weak interfacial binding with Li_2CO_3, which are found on the garnet surfaces, and Li metal binds strongly with oxide materials that may form on the garnet surfaces. The weak interface binding may lead to forming interfacial gaps and intervals, thus a low contact area and a high interfacial resistance. Stronger interface binding would lead to enhanced interfacial contacts with larger contact area and good interfacial conductance.

We developed a computational model for garnet-electrode interfaces (Figure 13). The comprehensive interface model is based on a large variety of inputs provided by a range of first principles computation and actual experimental parameters to model the interface properties. The interface model has been developed and demonstrated for garnet materials with electrode materials, such as $LiCoO_2$ and LFMO. The interphase layers between the garnet and the electrode were determined using grand potential phase diagram at the applied voltage of the battery at the input for the model. The formation of the interphase was found to be thermodynamically favorable for the interfaces of garnet with anode and cathode. In addition, the properties of the materials comprising the interphase, such as defect and migration energy, were also evaluated in first principles calculations. The effects of the space-charge layer were incorporated as a part of interface model. Using all these predicted input parameters, the conductivity and interfacial resistance of the interfacial layer were determined. The model is now ready to be applied to any composition of garnet solid electrolyte in contact with any electrode materials. The inputs for the interface model are generated by the first principles computation and experimental parameters. The model was able to demonstrate that a poor interfacial layer causes high interfacial resistance in all-solid-state batteries.

We applied first principles calculations to investigate the interface stability between garnet and formed Li-Al alloys (Figure 14a). We considered the interface as a pseudo-binary of Li-Al alloy and garnet, then constructed the related phase diagram to identify possible thermodynamically favorable reactions. The compositional phase diagrams were constructed, and the mutual reaction energy of the pseudo-binary calculated using same approach defined in our previous work (Figure 14b). We found that three kinds of Li-Al alloy showed mutual reactions with garnet because of the slightly thermodynamic "welding" at their interface. Since the calculated reaction enthalpy is only around -60 ~ -40 meV/atom, the small reaction energy indicates that the interfacial reactions are likely to be limited and the formed interface could be relatively thermodynamic stable. Therefore, the interface between Li-Al alloy and garnet may exhibit good chemical stability, which might facilitate Li ion transport through.

We apply the computational scheme to investigate interfacial chemical compatibility of these two interfaces with the coating layer with the SE and LCO, respectively. The previously demonstrated coating layer materials, such as $Li_4Ti_5O_{12}$, $LiTaO_3$, $LiNbO_3$, Li_2SiO_3, and Li_3PO_4, have excellent chemical stability with the LCO and $L_{0.5}CO$ with zero or negligible decomposition energy (Table 2). In addition, all coating layer materials show relatively better stability with the sulfide SE comparing to the original sulfide SE-LCO interfaces, which have the interfacial reaction energy of ~ -500 meV/atom. As a result, the interface with the coating layer has significantly improved stability and suppresses the formation of thick interphase layer. In addition to stabilizing the interface, the coating layer of only a few nanometers is significantly thinner than the decomposition interphase layer of ~10 to 100 nm. The reduced thickness of the coating layer may significantly reduce the high interfacial resistance caused by the thick decomposition interphase layer.

In addition, we also computationally investigated other compounds (listed in Figure 15 and Table 2) based on the same cations, such as Ti, Nb, Si, Ta, and P, as potential coating layer materials. All these lithium metal oxide materials have a wide electrochemical window (Figure 15a). The compounds with higher Li content generally show lower reduction potential, and the compounds with lower Li content or higher O content show higher oxidation potential. Most of these compounds have excellent chemical stability against LCO and $L_{0.5}CO$ cathode materials with zero or small (Table 2). All these coating layer materials significantly improve the stability of sulfide SE-LCO interfaces. The chemical stability between LLZO-coating layer interfaces varies significantly with the compositions of the coating layer materials. The other Li-rich coating layers, such as Li_4TiO_4, Li_2TiO_3, Li_8SiO_6, Li_4SiO_4, Li_5TaO_5, and Li_3TaO_4 may work better with LLZO than those previously demonstrated for sulfide SEs, such as $Li_4Ti_5O_{12}$, $LiTaO_3$, and Li_2SiO_3.

Computational modeling study for interface for Li-S and Li-NMC SSLiBs:

Thermodynamic computation predicted potential reaction and interphase formation between LLZO and Li polysulfides in all-solid-state Li-S batteries (Figure 16a). Li_2SO_4 is identified as a dominant reaction product, which is confirmed in the XPS spectra (Figure 16b). The formed interphase layer may serve as a protection layer between garnet solid electrolyte and S cathode. The Li-ion transport mechanism in these interphase layers would be crucial for assessing interfacial ion transport. First principles computation based on nudged-elastic-band methods were performed to identify the Li^+ transport pathway (Figure 16c) and migration energy barrier (Figure 16d) of ~0.6-0.8eV, showing reasonable Li^+ interfacial transport across the formed interphase layers in Li-S solid-state battery.

Thermodynamic computation also predicted potential reaction and interphase formation between LLZO and NMC cathode in solid-state Li-ion batteries, and such reaction is energetically more favorable at high applied voltages. As potential formed products, the interphase equilibria include Li_6ZrO_7, $La_2Zr_2O_7$ and various Li/La transition metal oxides. The Li^+ transport was studied in Li_6ZrO_7, a dominant interphase product, using first principles computation. The Li-ion transport pathway is shown in Figure 16e. The migration energy barrier (Figure 16f) of ~0.2-0.8eV suggests decent Li-ion transport across the interface from garnet electrolyte and NMC cathode in an all-solid-state Li-ion battery.

In summary, our developed computation models reveal the interphase layer formation between garnet solid electrolyte and S or NMC cathode materials in all-solid-state Li batteries. The formation of such layers serves an important protection role at the electrolyte-cathode interfaces. The Li-ion transport in these interphase layers are crucial for the battery performance. First principles calculations revealed Li-ion diffusion mechanisms and showed decent Li-ion transport in these materials and across the interfaces.

Fabrication of Full Cell SSLiBs:

SSLiBs with Li-NMC chemistry

Solid-state batteries consisting of Li metal anode, NMC cathode, and garnet-type $Li_7La_3Zr_2O_{12}$ (LLZO) solid electrolyte were fabricated and evaluated. The LLZO solid electrolyte has a bi-layer dense-porous structure with thicknesses of 20 µm and 50 µm, respectively (Figure 17a). Li metal anode is hosted in the porous layer of garnet electrolyte (Figure 17b). NMC cathode is laminated on the dense layer. Figure 17c is the Electrochemical Impedance Spectroscopy (EIS) of the battery. The interfacial resistance is around 250 Ohm-cm^2, which is at the same level as our results for the gel interface previously reported. It proves that the bi-layer garnet and Li anode have a good interfacial contact. The cyclic voltammetry (CV) test result (Figure 17d) shows that there is an oxidation peak around 4.2V, which is the charging voltage plateau, and there is a reduction peak around 3.4 V, for the discharging plateau. Outside this voltage range, there is no reaction current. The conclusion is that a battery with a NMC cathode and bi-layer garnet electrolyte can have stable cycling performance up to ~4.5V.

Cycling performances of Li/NMC cells with NMC mass loadings of 13.5 and 32 mg/cm^2 are shown in Figure 18. Figure 18a is the voltage profile of a cell with 13.5 mg/cm^2 NMC loading cycled at 0.1 C rate (1 C = 170 mA/g). Figure 18b shows the capacity and Coulombic efficiency of this cell. The capacity is stable at 175 mAh/g over 30 cycles. The energy density of the cell is calculated to be 232 Wh/kg. Capacities and Coulombic efficiencies of high rate cycling for this cell are in Figure 18c. The Coulombic efficiency is over 99% during the 200 cycles, and the battery shows 80% capacity retention at 0.2 C after 200 cycles at varying rates up to 0.5 C. Figure 18d shows the voltage profiles of a cell with a high-mass-loading (32 mg/cm^2) NMC cathode. The cell is cycled at 0.05 C rate in 2 ~ 4.6 V voltage window. The capacity is 175 mAh/g, and the battery energy density is 357 Wh/kg, calculated based on the masses of the cathode, Li anode and electrolyte.

SSLiBs with Li-S chemistry

Solid state lithium batteries with a sulfur (S) cathode, bi-layer garnet SSE, and Li metal anode were fabricated (Figure 19a). The structure of the bi-layer garnet and the S cathode is shown by the scanning electron microscope (SEM) image (Figure 19b). The S fills the pores of garnet in the porous layer, as confirmed by the Energy-Dispersive X-ray Spectroscopy (EDS) in Figure 19c. Li metal anode was coated on the dense side of the bi-layer garnet, with a polymer interface for better contact. The cycling performance is shown in Figure 19d. The Coulombic efficiency remains > 99%, confirming that no shuttling effect occurs in the cell. The bilayer Li-S cell with a S mass loading of 7.5 mg/cm^2 has an energy density of 280 Wh/kg on the basis of the cathode, Li anode and electrolytes.

We also demonstrated Li-S batteries based on tri-layer garnet SSE. The tri-layer SSE is composed of a porous-dense-porous structure. The thickness of each porous layer is 70 µm and the thickness of the dense layer is 30 µm. Li metal anode is stored in one porous layer, and sulfur cathode is stored in the other porous layer. Mass loadings of lithium and sulfur are 4.3 mg/cm^2 and 5.4 mg/cm^2, respectively. The battery performance is shown in Figure 20. The voltage profiles in Figure 20a show a typical Li-S two plateau behavior with a high capacity of ~1200 mAh/g. The cell shows high capacity retention and nearly 100% Coulombic efficiency during 50 cycles (Figure 20b). The total energy density of the tested cell is 272 Wh/kg as calculated from the integrated cycling curve, measured masses of sulfur, carbon, garnet electrolyte, and lithium metal anode.

Conclusions:

Over the course of this project, we developed a computational approach to model the interfacial behavior of LLZ garnet SSE with different electrodes. Using the model, we achieved a fundamental understanding of interfacial impedance as demonstrated by consistency between computational and experimental results. We then developed computational models to investigate stability and interfacial ion transport with varying types of interlayers at the electrolyte/electrode interface. Our results the predicted the formation of protective interfaces between garnet and S and NMC cathodes.

We experimentally investigated multiple techniques to decrease the impedance at the garnet-cathode interface. We demonstrated that a gel electrolyte can reduce the interfacial resistance by over 4 orders of magnitude achieving an interfacial ASR of ~67 Ohm-cm^2 for planar cathode/garnet interface. We also showed that increasing surface area can effectively decrease the interface resistance, achieving a 52% decrease in interfacial ASR. The aqueous interface lead to a 7.5 Ohm-cm^2 cathode/garnet interfacial resistance planar cathode/garnet interface meeting the ~10 Ohm-cm^2 garnet/cathode goal.

At the lithium metal-garnet interface, we demonstrated that gel electrolyte, Si, and Al can reduce interfacial resistance to 200 Ohm-cm^2, 127 Ohm-cm^2, and 75 Ohm-cm^2, respectively for planar Li metal-garnet interface. We further showed that ALD-Al_2O_3 can reduce interfacial resistance to ~1 Ohm-cm^2 for planar Li metal-garnet interface, meeting the ~10 Ohm-cm^2 garnet/anode goal.

Using the above techniques, informed by the computational modeling, we fabricated and tested SSLiBs with both Li-S and Li-NMC chemistries. We achieved an energy density of 272 Wh/kg and 50 cycles with the Li-S chemistry. With the Li-NMC chemistry, we achieved a very high energy density of 352 Wh/kg. The Li-NMC chemistry was also shown to cycle for over 200 cycles.

References:

[1] W. Luo, Y. Gong, Y. Zhu, Y. Li, Y. Yao, Y. Zhang, K. K. Fu, G. Pastel, C. F. Lin, Y. Mo, E. D. Wachsman, L. Hu, Reducing Interfacial Resistance between Garnet-Structured Solid-State Electrolyte and Li-Metal Anode by a Germanium Layer. *Adv. Mater. 29* (22), 1–7, (2017).

[2] B. Liu, K. Fu, Y. Gong, C. Yang, Y. Yao, Y. Wang, C. Wang, Y. Kuang, G. Pastel, H. Xie, E. D. Wachsman, L. Hu, Rapid Thermal Annealing of Cathode-Garnet Interface toward High-Temperature Solid State Batteries. *Nano Lett.* 9. 4917-4923 (2017).

[3] K. Fu, Y. Gong, B. Liu, Y. Zhu, S. Xu, Y. Yao, W. Luo, C. Wang, S. D. Lacey, J. Dai, Y. Chen, Y. Mo, E. Wachsman, L. Hu, Toward Garnet Electrolyte–based Li Metal Batteries: An Ultrathin, Highly Effective, Artificial Solid-State Electrolyte/metallic Li Interface. *Sci. Adv.* 3, e1601659 (2017*).*

[4] K. Fu, Y. Gong, S. Xu, Y. Zhu, Y. Li, J. Dai, C. Wang, B. Liu, G. Pastel, H. Xie, Y. Yao, Y. Mo, E. Wachsman, L. Hu, Stabilizing the Garnet Solid-Electrolyte/polysulfide Interface in Li-S Batteries. *Chem. Mater.* 29, 8037–8041 (2017).

[5] K. Fu, Y. Gong, S. Xu, Y. Zhu, Y. Li, J. Dai, C. Wang, B. Liu, G. Pastel, H. Xie, Y. Yao, Y. Mo, E. Wachsman, L. Hu, Transient Behavior of the Metal Interface in Li Metal-Garnet Batteries. *Angew. Chemie Int. Ed.* 1–7 (2017).

[6] C. Wang, H. Xie, L. Zhang, Y. Gong, G. Pastel, J. Dai, B. Liu, E. D. Wachsman, L. Hu, Universal Soldering of Lithium and Sodium Alloys on Various Substrates for Batteries. *Adv. Energy Mater.* 1701963 (2017).

[7] C. Yang, K. Fu, Y. Zhang, E. Hitz, L. Hu, Protected Lithium-Metal Anodes in Batteries: From Liquid to Solid. *Adv. Mater.* 29, 1–28 (2017).

[8] B. Liu, Y. Gong, K. Fu, X. Han, Y. Yao, G. Pastel, C. Yang, H. Xie, E. D. Wachsman, L. Hu, Garnet Solid Electrolyte Protected Li-Metal Batteries. *ACS Appl. Mater. Interfaces* 9, 18809–18815 (2017).

[9] Y. Zhu, X. He, Y. Mo, First Principles Study on Electrochemical and Chemical Stability of the Solid Electrolyte-Electrode Interfaces in All-Solid-State Li-ion Batteries, *J. Mater. Chem. A*, 4, 3253-3266 (2016).

[10] Y. Zhu, X. He, Y. Mo, Origin of Outstanding Stability in the Lithium Solid Electrolyte Materials: Insights from Thermodynamic Analyses Based on First-Principles Calculations, *ACS Appl. Mater. Interfaces*, 7, 23685-23693 (2015).

[11] F. Han, Y. Zhu, X. He, Y. Mo, C. Wang, Electrochemical Stability of Li10GeP2S12 and Li7La3Zr2O12 Solid Electrolytes", *Adv. Energy Mater.*, 6, 1501590 (2016).

[12] W. Luo, Y. Gong, Y. Zhu, K. Fu, J. Dai, S. D. Lacey, C. Wang, B. Liu, X. Han, Y. Mo, E. D. Wachsman, L. Hu, Transition from Super-lithiophobicity to Super-lithiophilicity of Garnet Solid Electrolyte, *J. Am. Chem. Soc.*, 138, 12258-12262 (2016).

[13] X. Han, Y. Gong, X. He, G. T. Hitz, J. Dai, Y. Mo, V. Thangadurai, E. D. Wachsman, L. Hu, Negating Interfacial Impedance in Garnet-Based Solid-State Li-Metal Batteries, *Nat. Mater.*, 16, 572-580, (2017). DOI: 10.1038/NMAT4821

[14] K. Fu, Y. Gong, G. T. Hitz, D. W. McOwen, Y. Li, S. Xu, Y. Wen, L. Zhang, C. Wang, G. Pastel, J. Dai, B. Liu, H. Xie, Y. Yao, E. D. Wachsman, L. Hu, Three-Dimensional Bilayer Garnet Solid Electrolyte High Energy Density Lithium Metal-Sulfur Batteries, *Energy Environ. Sci.*, 10, 1568-1575, (2017). DOI: 10.1039/c7ee01004d

Figures and Tables:

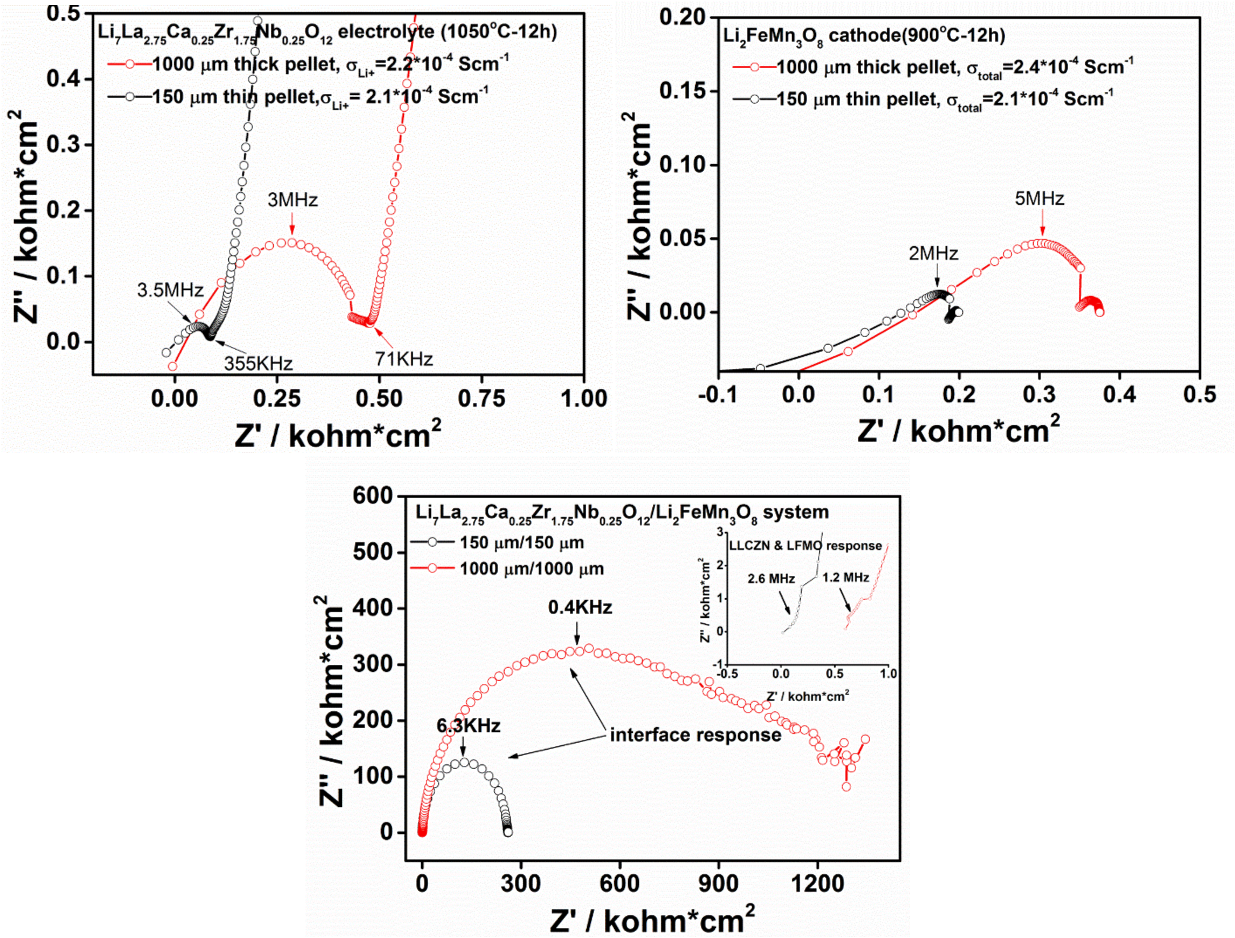

Figure 1. (a) EIS of thick and thin LLCZN pellets, (b) thick and thin LFMO pellets, and (c) thick and thin LLCZN/LFMO pellets.

Figures Continued on Next Page

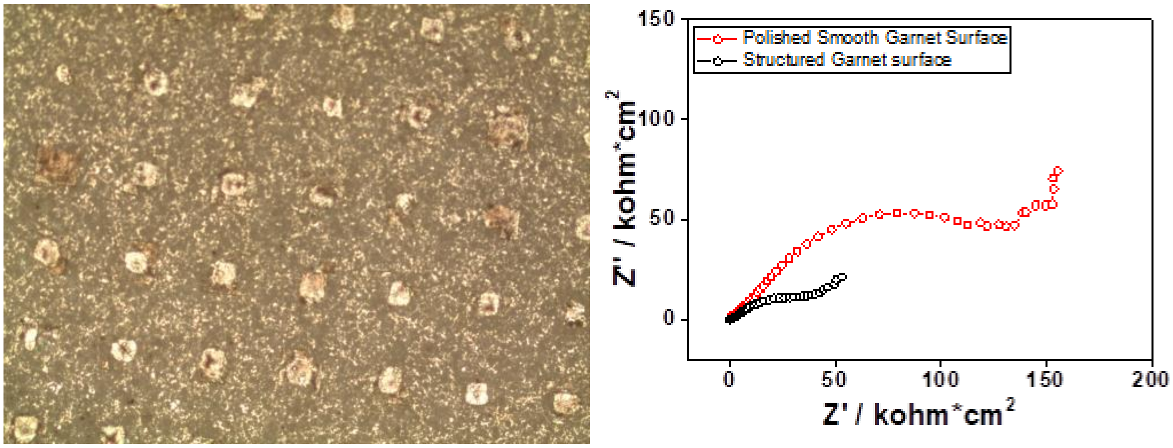

Figure 2. (a) Photograph of structured garnet surface, bright white spots are garnet columns. (b) EIS of polished smooth garnet surface and structured garnet surface.

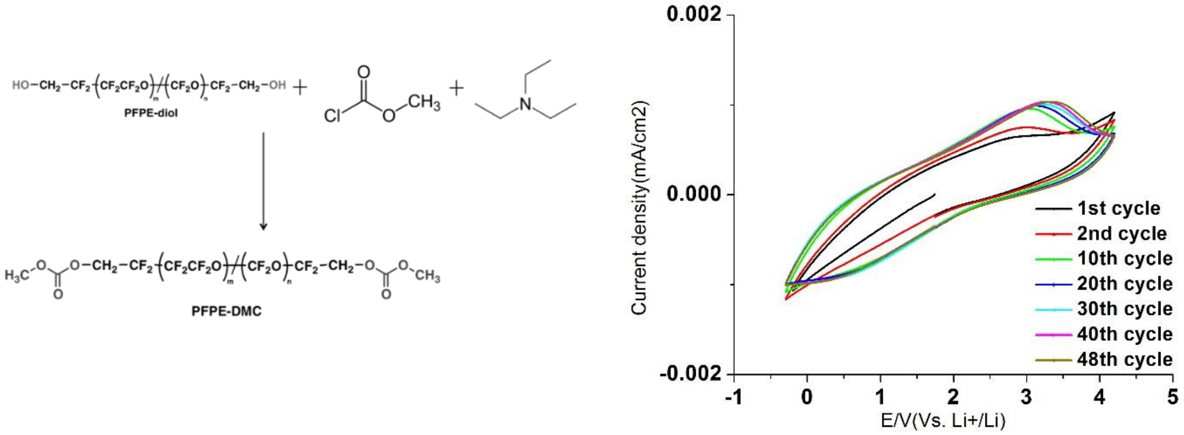

Figure 3. (a) Synthesis procedure of PFPE-DMC. (b) Cyclic voltammetry study of LiTFSI-PFPE electrolyte.

Figures Continue on Next Page

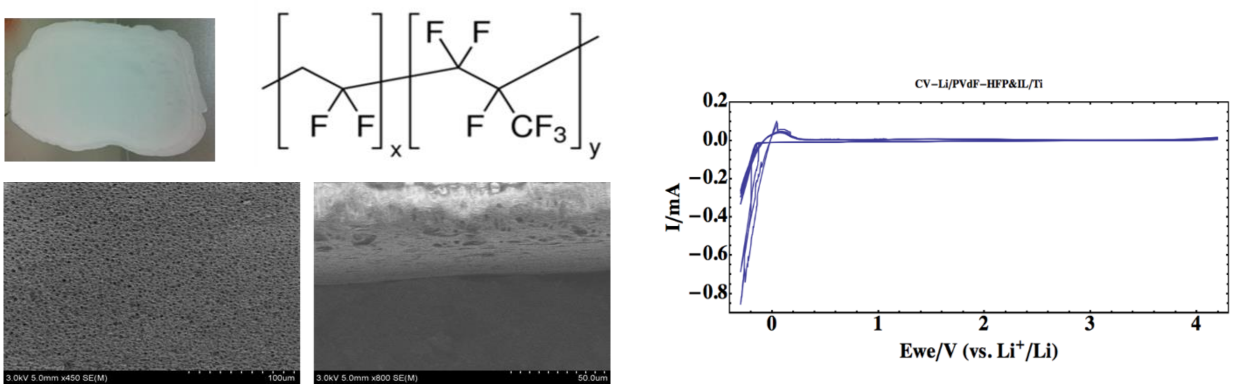

Figure 4. (a) Photograph, (b) structure, (c) top and (d) side SEM images of PVDF-HFP gel membrane. (e) Cyclic voltammetry study of Li|PVDF-HPF+IL|Ti.
(g) EIS of LLCZN/LFMO interface without (black)
(h) and with (red) PVDF-HFP gel electrolyte interface.
(i)

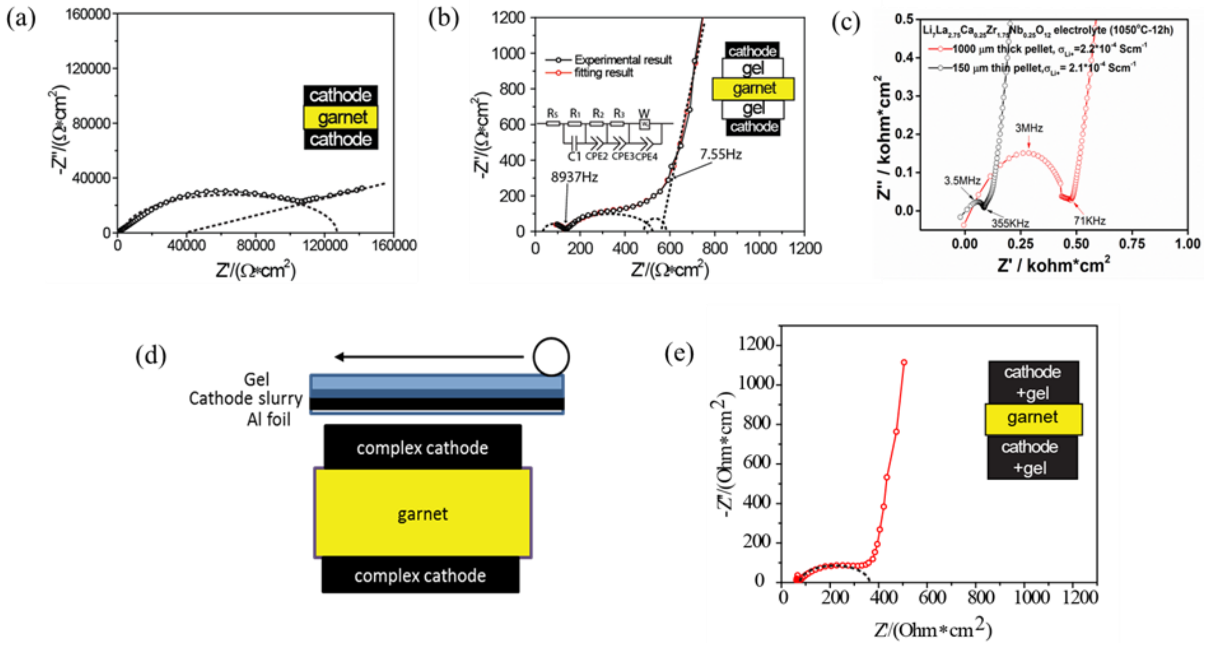

Figure 5. (a) EIS plot of cathode/garnet/cathode symmetric cell without gel electrolyte.
(b) EIS of cathode/gel/garnet/gel/cathode symmetric cell and the equivalent circuit.
(c) EIS of garnet itself. (d) Schematic of making garnet cell with mixed cathode.
(e) EIS of symmetric cell with mixed cathode and gel.

Figures Continue on Next Page

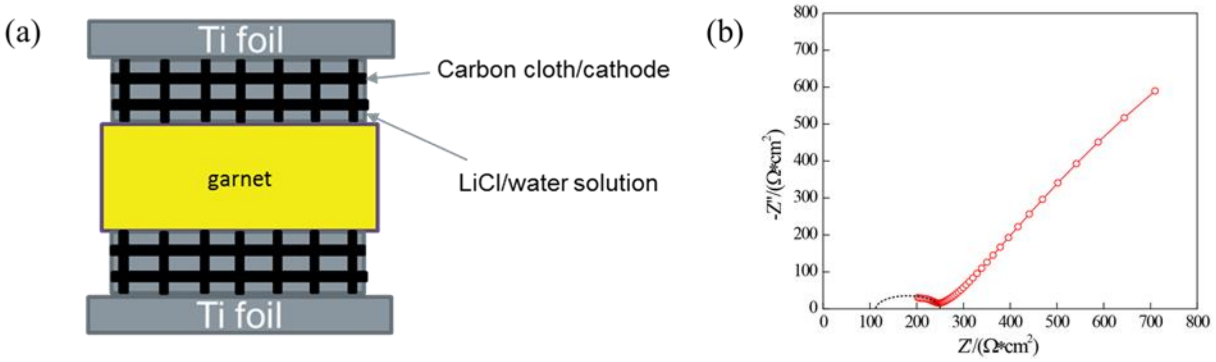

Figure 6. (a) Schematic of a cathode/garnet/cathode symmetric cell with aqueous interface. (b) Impedance of this cell with aqueous interface.

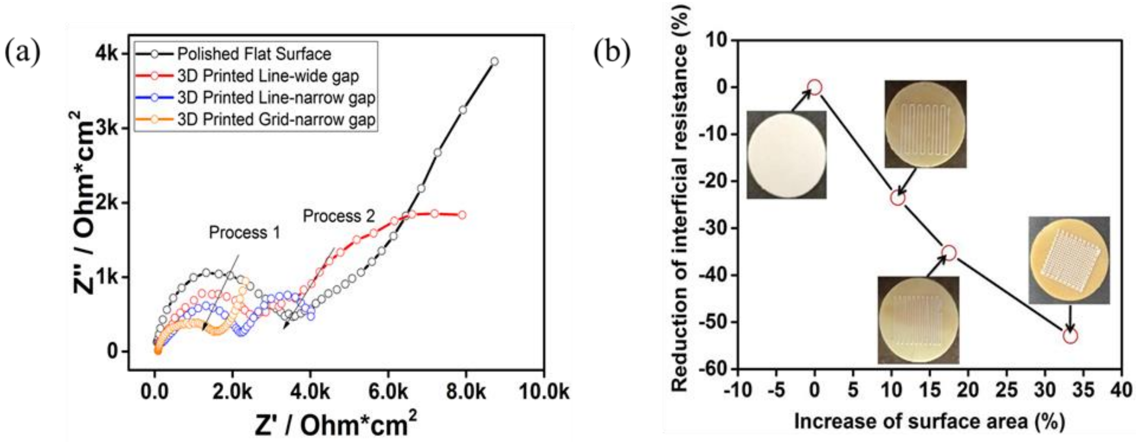

Figure 7. Comparison of cathode/electrolyte interfacial impedance on flat and 3D-structured garnet pellets. (a) EIS plot of garnet without 3D printing and with different 3D printings. (b) Reduction of interfacial resistance with increase in surface area

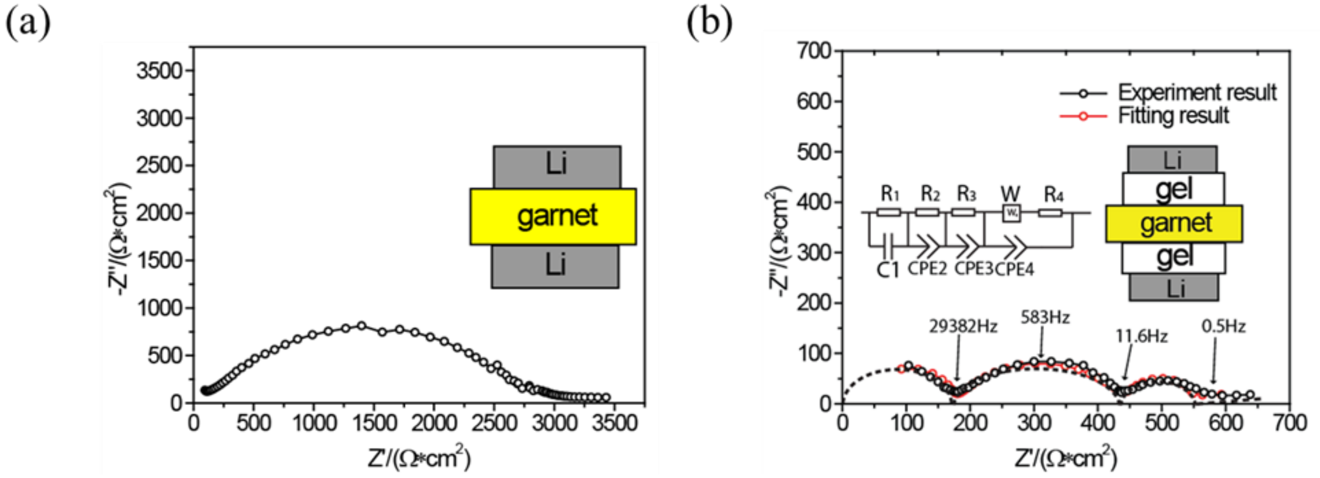

Figure 8. (a) EIS plot of Li/garnet/Li symmetric cell. (b) EIS plot and equivalent circuit of Li/gel/garnet/gel/Li symmetric cell.

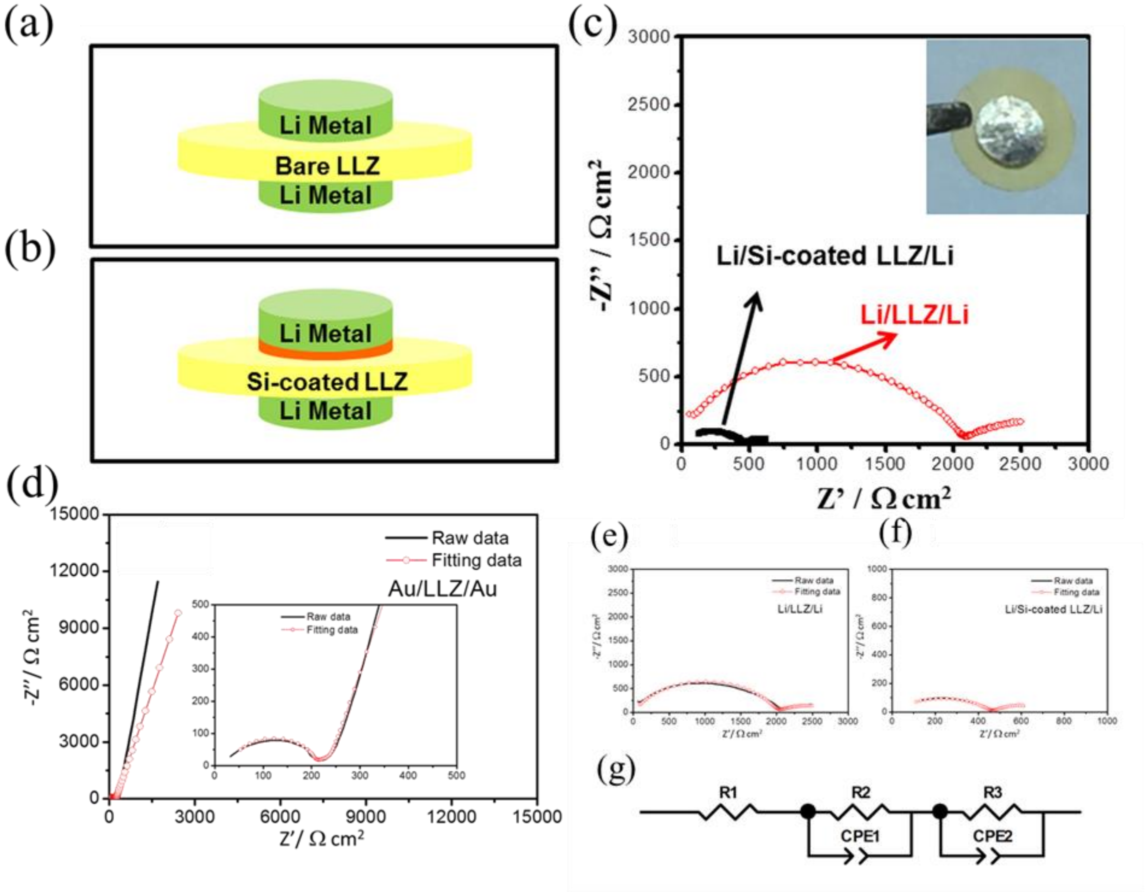

Figure 9. Schematic illustration showing the structure of symmetric cells with (a) LLZ or (b) Si-coated LLZ SSEs. (c) Electrochemical impedance spectroscopy (EIS) measurements of symmetric cells where the interfacial resistance of the Si-coated garnet cell significantly decreased. Inset of (c) is a digital image of a Li/Si-coated LLZ/Li symmetric cell. (d) Nyquist plots of the Au/LLZ/Au symmetric blocking electrode system at room temperature. The solid black line denotes the experimental data while the red line with hollow spheres represents the fitting data using the equivalent circuit modeling. (e-g) Nyquist plots of (e) Li/LLZ/Li and (f) Li/Si-coated LLZ/Li symmetric cells. (g) The equivalent circuit model used in this study.

Figures Continue on Next Page

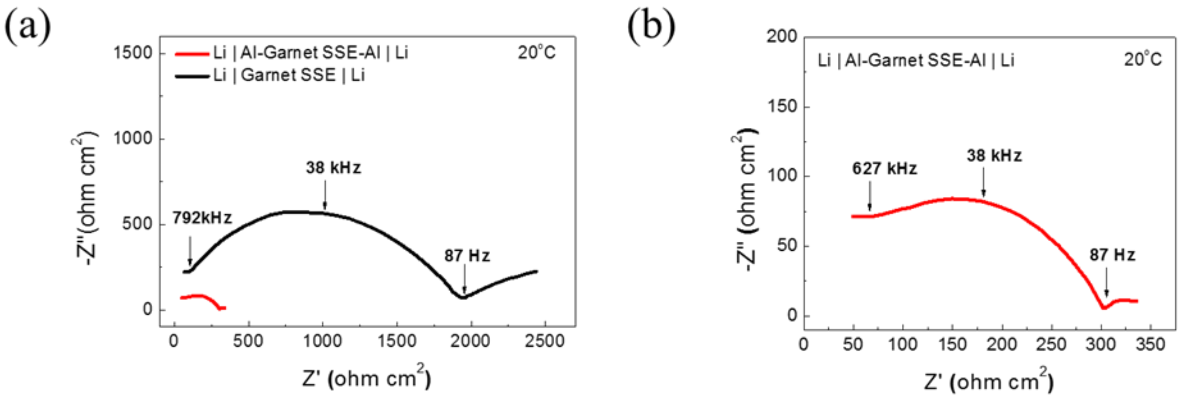

Figure 10. Nyquist plots of Li | Garnet SSE | Li (a) and Li | Al-Garnet SSE-Al | Li (b) in the frequency of 1 MHz to 100 mHz at 20°C.

Table 1. Electrochemical impedance with fitting data for Li/LLCZN/Li cells with and without ALD coating on both sides of the garnet SSEs.

LLCZN SSE	Bulk ASR (Ω-cm^2)	Grain Boundary ASR (Ω-cm^2)	Grain Boundary Capacitance (F)	Interfacial ASR (Ω-cm^2)	Interfacial Capacitance (F)
No ALD	28	4500	$2.09\text{x}10^{-9}$	490	$9.9\text{x}10^{-4}$
ALD	26	150	$3.09\text{x}10^{-9}$	16	$2.8\text{x}10^{-5}$

Figures Continue on Next Page

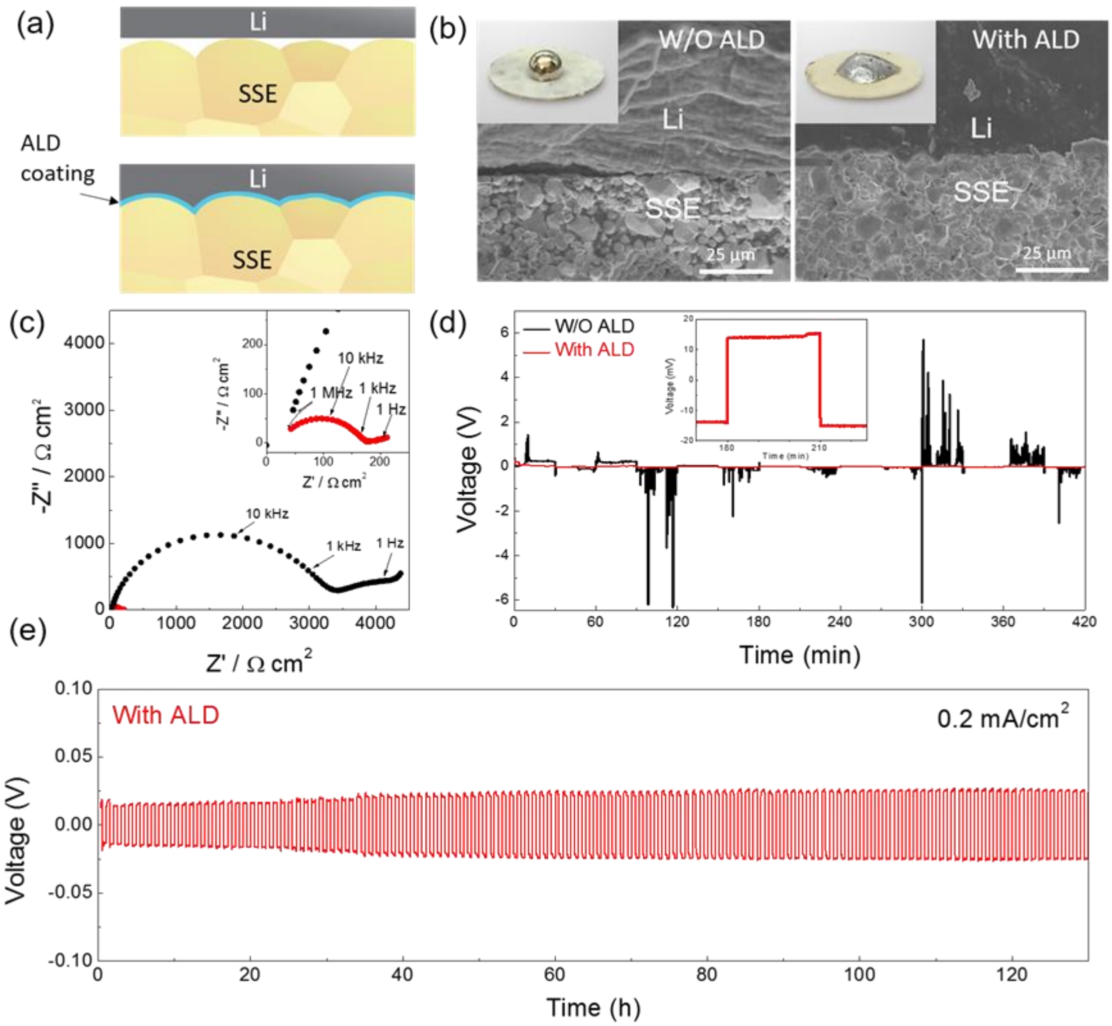

Figure 11. Characterization of garnet solid state electrolyte/Li metal interface. (a) Schematic of the wetting behavior of garnet surface with molten Li. (b) SEM images of the garnet solid state electrolyte/Li metal interface. Without ALD Al_2O_3 coating, garnet has a poor interfacial contact with Li metal. Inset are photo images of contacts between melted Li metal and garnet surface. (c) Comparison of EIS profiles of the symmetric Li non-blocking garnet cells. Inset shows the enlarged impedance curve of the ALD treated garnet cell. (d) Comparison of Li tripping/plating behavior of the symmetric garnet SSE/Li cells. Inset is the one cycle of stripping/plating for the ALD treated garnet cell, exhibiting a low overall impedance and stable interfacial property. (e) Voltage profile of the ALD treated garnet symmetric cell at a current density of 0.2 mA/cm^2.

Figures Continue on Next Page

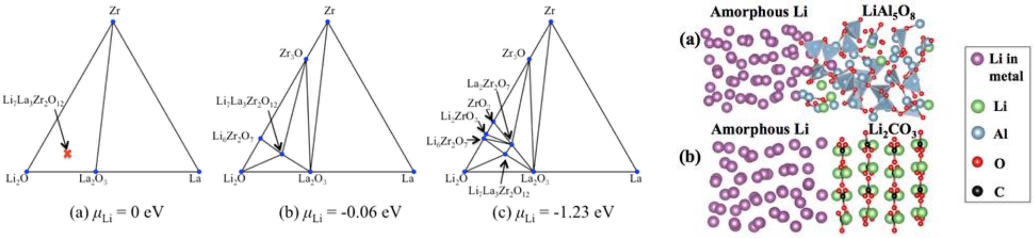

Figure 12. (a) Li grand cannonical phase diagram of Li-La-Zr-O system. (b) Models for the interfaces between Li metal and garnet surface materials.

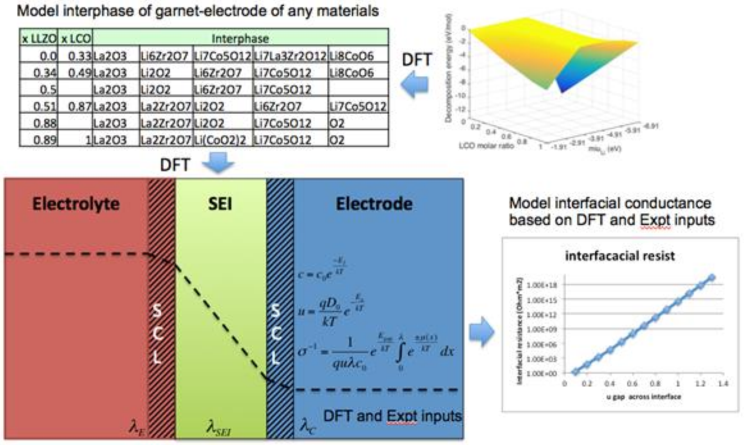
Model interphase of garnet-electrode of any materials

x LLZO	x LCO	Interphase				
0.0	0.33	La2O3	Li6Zr2O7	Li7Co5O12	Li7La3Zr2O12	Li8CoO6
0.34	0.49	La2O3	Li2O2	Li6Zr2O7	Li7Co5O12	Li8CoO6
0.5		La2O3	Li2O2	Li6Zr2O7	Li7Co5O12	
0.51	0.87	La2O3	La2Zr2O7	Li2O2	Li6Zr2O7	Li7Co5O12
0.88		La2O3	La2Zr2O7	Li2O2	Li7Co5O12	O2
0.89	1	La2O3	La2Zr2O7	Li(CoO2)2	Li7Co5O12	O2

Figure 13. Model for garnet-electrode interfaces, which take inputs from first principles calculations and experimental condition parameters.

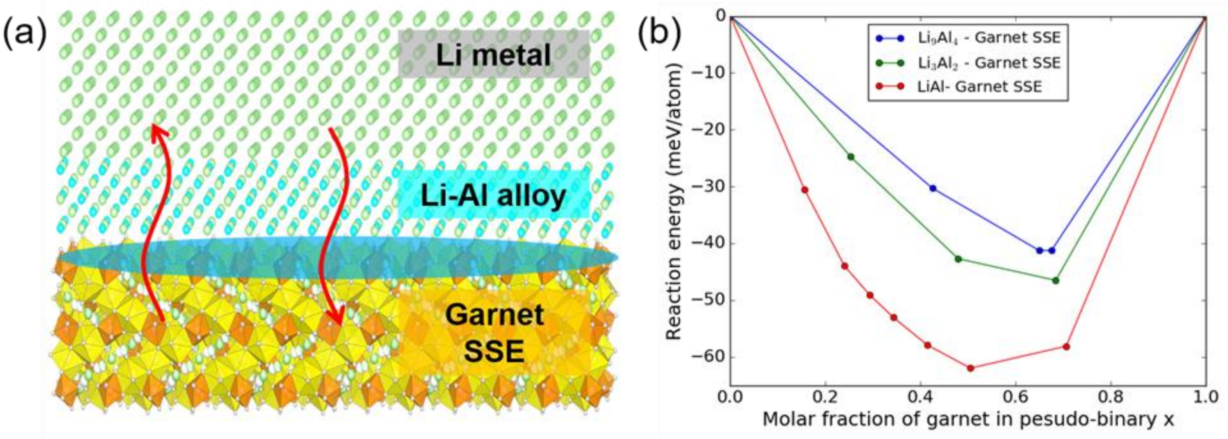

Figure 14. Calculated mutual reaction energy, ΔED, of garnet and Li-Al alloy interfaces.

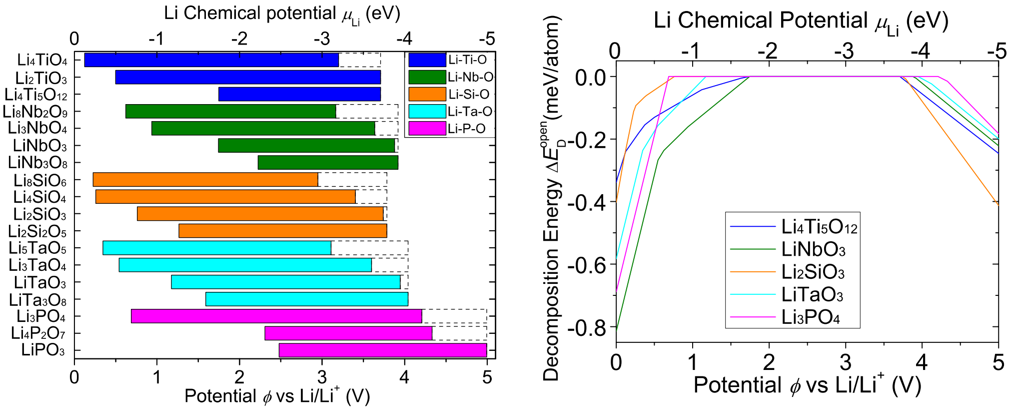

Figure 15. Electrochemical window (left) and the decomposition energy (right) of the proposed and previously demonstrated coating layer materials applied between SE and cathode materials. The dashed line in (a) marks the equilibrium voltage to fully delithiate the materials.

Table 2. The mutual reaction energy (in meV/atom) of the coating layer materials with the SE or LCO materials.

	Li_3PS_4	LLZO	LCO	$L_{0.5}CO$
Li_4TiO_4	-125	0	0	-30
Li_2TiO_3	-75	-5	0	0
$Li_4Ti_5O_{12}$	-80	-75	-1	0
$Li_8Nb_2O_9$	-147	0	0	-20
Li_3NbO_4	-132	-4	0	0
$LiNbO_3$	-155	-76	0	0
$LiNb_3O_8$	-173	-115	-16	0
Li_8SiO_6	-177	0	-3	-50
Li_4SiO_4	-81	-1	0	-12
Li_2SiO_3	-19	-29	0	0
$Li_2Si_2O_2$	-10	-69	-4	0
Li_5TaO_5	-117	0	0	-32
Li_3TaO_4	-64	-3	0	0
$LiTaO_3$	-49	-68	0	0
$LiTa_3O_8$	-64	-105	-22	0
Li_3PO_4	0	0	0	0
$Li_4P_2O_7$	-9	-101	-44	-3
$LiPO_3$	-32	-201	-76	-19

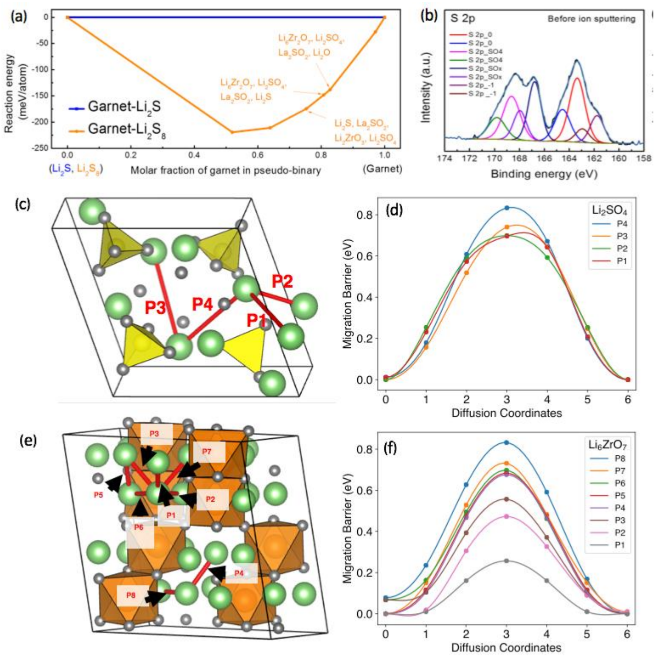

Figure 16. (a) Calculated interphase equilibria and reaction energy between LLZO and Li polysulfides. (b) XPS spectra of garnet interface in Li-S battery. Calculated Li$^+$ transport pathway (c) and energy barriers (d) of Li_2SO_4. Calculated Li$^+$ transport pathway (e) and energy barriers (f) of Li_6ZrO_7.

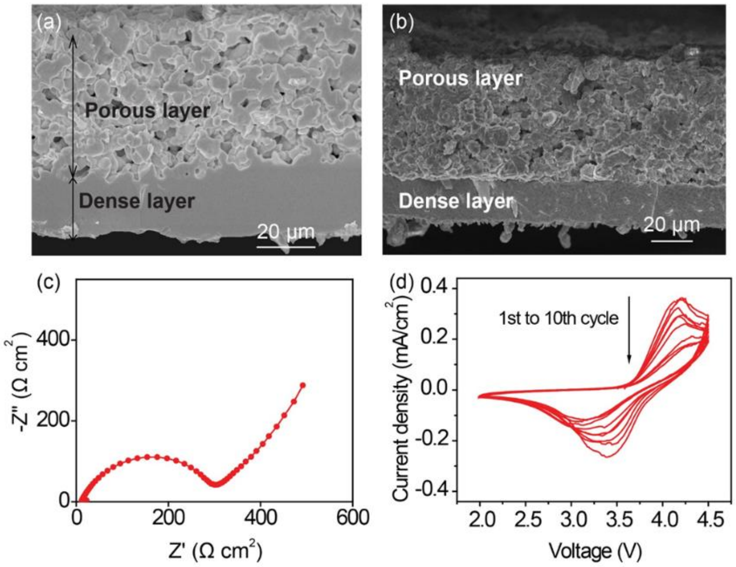

Figure 17. Characterization of bi-layer garnet and performance of Li-NMC battery. (a) Cross sectional SEM image of bi-layer garnet SSE. (b) SEM of garnet SSE with Li metal inside. (c-d) EIS and CV of the Li-NMC battery with garnet SSE.

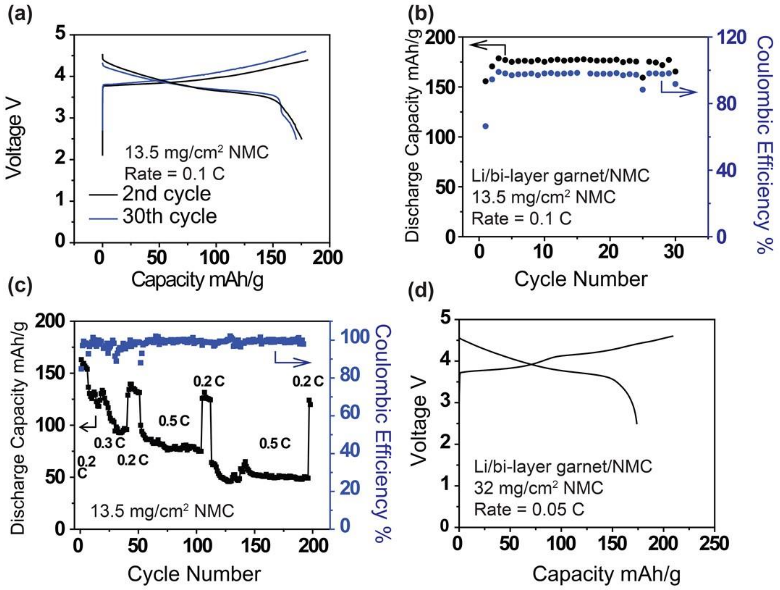

Figure 18. Cycling performances of Li-NMC cells with garnet SSE. (a-b) Voltage profiles and cycling performance of Li-NMC cell with 13.5 mg/cm^2 cathode at 0.1 C rate. Stable capacity at 175 mAh/g was achieved. (c) Cycling performance of Li-NMC cell with 13.5 mg/cm^2 cathode at various rates. High Coulombic efficiency and capacity retention were achieved over 200 cycles. (d) Voltage profiles of a Li-NMC cell with high NMC loading of 32 mg/cm^2 at 0.05 C rate.

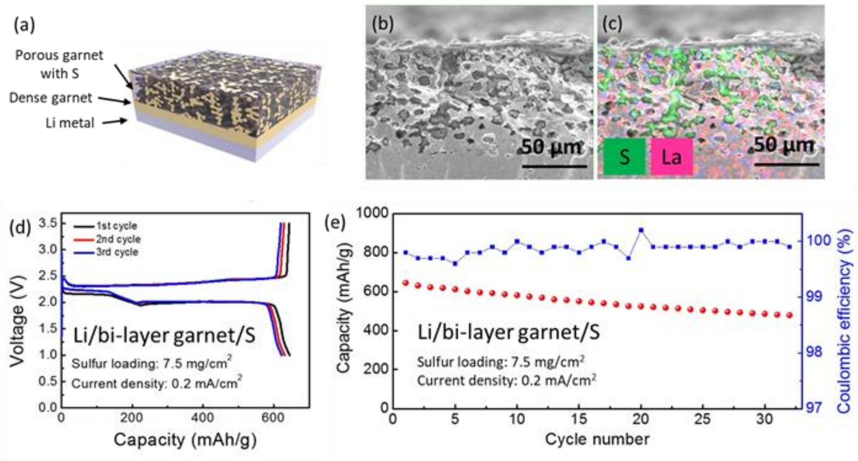

Figure 19. Characterization of bi-layer garnet and performances of Li-S battery. (a) Schematic of Li-S battery based on bi-layer garnet. (b) Cross sectional SEM of bi-layer garnet filled with S. (c) EDS of S (green) and La (red) distribution in bi-layer garnet. (d-e) Voltage profile and cycling performance of the solid state Li-S cell with a loading of 7.5 mg/cm^2 at 0.2 mA/cm^2.

Figures Continue on Next Page

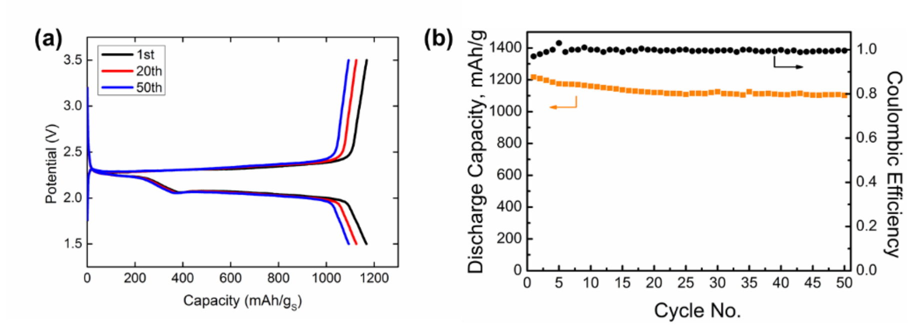

Figure 20. Cycling performances of Li-sulfur cell with garnet electrolytes.
(a) Voltage profiles of the 1st, 20th and 50th cycle of the solid-state Li-S cell.
(b) 1200 mAh/g capacity and low capacity loss were achieved.
(c) (b) Cycling results of the solid state Li-S cell.
(d) High capacity retention was achieved with near
(e) 100% coulombic efficiency.

Remainder of Page Intentionally Blank

Beyond Li-Ion: New Lamination and Doping Concepts for Enhanced Li-Sulfur Battery Performance

DOE-VTO TFA Lead: David Howell
TARDEC TFA Lead: Laurence Toomey

Principal Investigator:
Dr. Prashant N. Kumta
University of Pittsburgh
Attn: Jennifer Woodward
123 University Place
Pittsburgh, PA 15213-2303
Phone: 412-648-0223; Fax: 412-624-3699
Email: pkumta@pitt.edu

Project Start: Oct 2014
Project Completed: Q4FY17

Objective:

- To successfully demonstrate generation of novel sulfur cathodes for Li-S batteries meeting the targeted gravimetric energy densities ≥ 350 Wh/kg and ≥750Wh/l with a cost target $125/kWh and cycle life of at least 1000 cycles for meeting the Electric Vehicle (EV) everywhere blueprint. The proposed approach will yield sulfur cathodes with specific capacity ≥1400mAh/g, at ≥2.2V generating ~460Wh/kg, energy density higher than the target. Full Cells meeting the required deliverables will also be made.

Strategic Context:

- Generate a leap-ahead technology used for military vehicles to support the future power for TARDEC and the Army by enabling the development of advanced battery systems with significant increases in energy density
- Improve Battery safety characteristics to support vehicle silent watch and enable other high energy requiring applications.

Accomplishments:

- Demonstrated capabilities for generation of novel sulfur 1-D, 2-D and 3-D morphologies exhibiting superior stability and capacity (June 2015)

- Identified and synthesized LIC materials for use as coatings for sulfur cathodes (June 2015)
- Identified suitable dopants and dopant compositions to improve electronic conductivity of sulfur (October 2015)
- Demonstrated synthesis of doped LIC membrane with improved Lithium-ion conductivity (December 2015)
- Identified and developed effective coating methods to form a uniform lamina of LIC membrane over sulfur hetero-structures (March 2016)
- Identified suitable dopants and dopant compositions to improve electronic conductivity of sulfur (October 2015)
- Conducted fundamental electrochemical study to understand the reaction kinetics, mechanism and charge transfer kinetics (October 2015)
- Prepared doped LIC with improved ionic conductivity (January 2016)
- Demonstrated synthesis of doped LIC membrane with improved Lithium-ion conductivity (January 2016)
- Developed CFN morphology with a stable cycling performance of ~650 mAh/g for over 300 cycles with < 0.02% fade rate (April 2016)
- Accomplished demonstration of binding of polysulfide with Complex Framework Network (CFN) results in polysulfide retention and hence, improved cycling stability (April 2016)
- Demonstrated the effect of the unique pore size (~2nm) of CFN preventing dissolution of polysulfide from the liquid electrolyte (April 2016)
- Demonstrated stable capacity of ~550 mAh/g over 100 cycles with the application of TMPM improved the specific capacity of commercial sulfur (April 2016)**.**
- Developed novel lithium-ion conducting (LIC) membrane systems using *ab-initio* methods displaying impermeability to sulfur diffusion (December 2014)
- Demonstrated capabilities for generation of novel sulfur 1-D, 2-D and 3-D morphologies exhibiting superior stability and capacity (June 2015)
- Identified suitable dopants and dopant compositions to improve electronic conductivity of sulfur (October 2015)
- Performed fundamental electrochemical study to understand the reaction kinetics, mechanism and charge transfer kinetics (October 2015)
- Prepared doped LIC with improved ionic conductivity (January 2016)
- Conducted study on doping sulfur with dopants of similar size to sulfur with enhanced electronic properties (April 2016)
- Completed developing organic and inorganic Complex Framework Materials (CFM) as effective polysulfide traps (July 2016)
- Design and engineering of high capacity LIC coated sulfur nanoparticles (January 2017)
- Design, development, and application of a Composite Polymer Electrolyte with improved polysulfide trapping properties (January 2017)
- Synthesis of Polysulfide Trapping Agent (PTA) coated Directly Doped Sulfur Architecture Electrodes (April 2017)
- Sulfonic Complex Framework Materials (CFMs) with improved cycling stability and rate capability (July 2017)

- Cost analysis of electrodes, electrolytes, separators, binders and related processes (September 2017)

Introduction:

The increasing demand in the EV industry for low cost, light-weight and high energy storage batteries to meet the EV everywhere grand challenge, the current focus of research has shifted towards the development of lithium sulfur (Li–S) batteries owing to the high theoretical specific capacity exhibited by sulfur compared to other cathode materials currently available. Li–S battery shows a theoretical capacity of 1675 mAh/g corresponding to the formation of Li_2S which makes sulfur a promising electrode to replace the layered transition metal oxides (~150 mAh/g, e.g. $LiCoO_2$, $LiMn_2O_4$) and $LiFePO_4$ (~170 mAh/g) deployed in present LIB systems. Moreover, the abundance of sulfur in the earth's crust, its ubiquitous availability as a byproduct in the extractive mineral and petrochemical industry, combined with ease of processing, makes it a more economical proposition compared to currently existing cathode materials.

Approach:

The above-listed objectives were accomplished by engineering sulfur cathode materials primarily by laminating the electrodes with lithium ion conductor (LIC) coatings to prevent polysulfide dissolution and doping of sulfur to improve the electronic and ionic conductivity. Major technological innovations will be undertaken to accomplish the following objectives in this effort:

Phase – 1 (Year 1): Synthesis, Characterization and Scale up of suitable LIC matrix materials and multilayer composite sulfur cathodes. This phase is completed.

- Identify novel LIC coating materials and morphology for composite multilayer sulfur cathode architectures exhibiting: Specific capacity ≥1000 mAh/g (≥8 mAh/cm^2), cyclability (~1000 cycles), loss per cycle ≤0.05% per cycle, and Coulombic Efficiency (CE): ≥80%.

Phase – 2 (Year 2): Development of LIC coated sulfur nanoparticles, scale up of high capacity engineered LIC coated multilayer composite electrodes and doping strategies for improving the electronic conductivity of sulfur.

- Optimize and scale up of interface engineered multilayer composite LIC coated sulfur cathode architectures exhibiting: Specific capacity ≥1200 mAh/g (≥4 mAh/cm^2), cyclability (~1000 cycles), loss per cycle: ≤0.01% per cycle, and CE: ≥80%.
- Synthesize and scale up of doped sulfur nanoparticles on gram scale and demonstrate improvement in performance, reflected as an increase in sulfur weight percentage and improvement in rate capability of cycling of the electrodes.

Remainder of Page Intentionally Blank

Phase-3 (Year 3): Advanced high energy density, high rate, highly cyclable cell development.

- Tie together the three different trees of development i.e. coating development/sulfur particle development/Carbon Nano-Tube (CNT) based exploration by identifying suitable configuration integrated electrode (I.E.) with maximum sulfur weight percentage demonstrating high capacity ≥1400 mAh/g, cyclability (~1000 cycles), loss per cycle: ≤0.01% per cycle, CE: ≥80%.
- Assemble 4 mAh high energy density Li-S pouch cells and performance testing.

Results and Discussion:

Phase-1 of the current project concluded with the successful identification of effective lithium-ion conducting (LIC) membrane and demonstration of the ability of LIC to shield the polysulfide species from dissolving into the electrolyte. To achieve this target, 4 strategies outlined in the following were employed during Phase-1 of the project: (a) Use of inorganic LICs in the form of pellet coatings (Q1, Q2) (b) fabrication of flexible polymer-sulfur wires (Q2) (c) generation of gel polymer electrolyte (GPE) as an electrolyte medium (Q3) (d) use of complex framework materials (CFM) as trapping agents for sulfur species (Q4). These strategies resulted in improved cycling with scope for further improvement. The aim of Phase-2 studies is to synthesize novel doped LIC materials with high lithium ion conductivity identified in Phase 1, to develop effective coating strategies of these materials and to generate hetero structured composites of sulfur with carbon materials. The following strategies were employed during Phase-2 of the project: (a) Improving ionic conductivity of lithium ion conductors using first-principles driven doping approaches (b) Composite polymer electrolytes demonstrating no capacity loss in commercial sulfur electrodes (c) Sulfur-infiltrated Framework Materials (SFM) with chemical trapping of sulfur (d) Altering the electronic structure of sulfur with size matched dopants. Phase-3 aims at developing doped sulfur architectures, prevention of polysulfide dissolution using a trapping agent and developing surface engineering material. The following strategies were employed during Phase-3: (a) Developing and characterizing a composite polymer electrolyte system with good chemical and electrochemical properties, (b) Designing a Polysulfide Trapping Agent (PTA) coated Directly Doped Sulfur Architecture (DDSA) that can prevent polysulfide dissolution and (c) Complex Framework Material (CFM) with controlled physical and chemical properties to improve the cycling stability of sulfur cathodes.

Developing a Composite Polymer Electrolyte (CPE):

In FY17, polymer based Composite Polymer Electrolytes (CPEs) were prepared by a simple electrospinning technique. Further, three nanoparticulate fillers prepared using a simple sol – gel based nano fabrication technique[1, 2] were used as fillers to augment the mechanical and Li-ion conducting properties of these CPEs among other necessary ionic transport requirements. These nanofiller incorporated CPEs as separator – electrolytes were then tested to demonstrate their improved cycling stability using commercial sulfur as cathodes in Li – S batteries.

The mechanical properties of the CPEs are very important for effective application in batteries as separators. The mechanical properties of the CPEs are expected to be improved due to entanglement of singular fibers aided by the presence of nanoparticle fillers [3]. The mechanical properties of the electrospun membranes were compared with that of solution cast membranes of the same composition to demonstrate the superior properties attained by the electrospinning method. The thickness of both electrospun and solvent cast membranes used for mechanical property measurements was maintained uniformly at 0.035±0.005 mm. The tensile strength of the electrospun membranes is uniformly superior to that of solvent cast membranes (Figure1) due to the enhanced elastic nature of the electrospun membranes as explained by Blond et al on his work comparing the mechanical properties of electrospun and solvent – cast membranes[4].

The Fourier-Transform Infrared Spectroscopy (FTIR) spectrum of the CPE membrane soaked in electrolyte shows peaks corresponding to the polymer and peaks corresponds to the introduction of LiTFSI and SiO_2 and nanofillers[5]. After 100 charge – discharge cycles, both sides of the polymer membrane showed almost the same FTIR pattern (Figure 2a) with peaks indicating the presence of exchangeable protons, from amide group and $-SO_3$ group from LiTFSI[6]. Polysulfide peaks arising due to -S-S- stretching vibrations usually occurring between 500 – 540 cm^{-1}[7, 8]. The absence of these peaks indicates the absence of dissolved polysulfide in the CPE membranes after cycling. The absence of any anomalous peaks further confirms the chemical stability of the polymer membranes even after prolonged cycling. The chemical stability of the CPEs suggests their potential to replace PP separators in commercial sulfur batteries.

In addition to the improved mechanical properties, flame retarding ability of the CPEs is an important factor that determine the safety of the lithium ion battery[9, 10]. The CPEs soaked in electrolyte were thus, subjected to combustion test by exposing them to heat for 60 seconds. Commercial Celgard 2400 PP separators soaked in electrolyte was also exposed to the same conditions, the results of which are shown in Figure 2b. The commercial separator shrunk immediately after exposing to the flame. However, the CPEs remained unaffected by the heat exposure generated by the flame for more than 60s and the dimensions of the CPE membranes also remained unaltered confirming the absence of shrinkage due to the high temperature exposure generated from the flame. These results show that the CPE membranes show better flame retarding properties and thermal stability, which would subsequently make them a safer alternative for use in lieu of commercial separators and electrolytes.

Polysulfide Trapping Agent (PTA) coated Directly Doped Sulfur Architecture (DDSA) electrode:

Phase-3 also involved development of Directly Doped Sulfur Architecture (DDSA) electrode with very high sulfur loadings of ~18 mg/cm^2 significantly higher than that of slurry-coated electrodes. The DDSA electrodes were prepared using electrodeposition technique reported elsewhere[11]. These DDSA electrodes were then coated with a Polysulfide Trapping Agent (PTA) to enhance the cycling stability and capacity retention[12]. The PTAs were selected from the results of a first principles based theoretical study on identifying possible candidates that bind polysulfide chemically. The process of developing the PTA-coated DDSA electrodes with the polysulfide trapping property is depicted in Figure 3. Both the DDSA electrodes and PTA coated DDSA electrodes were tested electrochemically in 2025-coin cells against lithium metal anode. The cycling performance of slurry-coated commercial sulfur cathodes were compared with that of the DDSA and PTA coated DDSA electrodes in Figure 4. The commercial sulfur cathodes started with an initial discharge capacity of 557 mAh/g which faded rapidly to 100 mAh/g in under 60 cycles. However, the DDSA electrodes, despite their high electrode loadings showed a high initial capacity of 1088 mAh/g and maintained a capacity of 809 mAh/g for 200 cycles. The PTA coated DDSA electrode on the other hand, shows excellent electrochemical cycling performance with an initial capacity of 1305 mAh/g that stabilized at 1112 mAh/g for over 200 cycles with less than 0.0014% when cycled at at 0.2C rate (Figure 4). The initial loss in capacity of ~0.2% is likely related to parasitic reactions. Optimization studies to be conducted subsequently in future years will help overcome these reactions.

To explain the exceptional performance of the PTA coated DDSA electrodes, UV-VIS spectroscopy analysis was performed on the electrolytes before and after cycling. The UV-VIS spectrum of DDSA (Figure 5a) showed considerable decrease in the intensities of peaks corresponding to higher and lower order polysulfides as opposed to the slurry coated sulfur cathodes indicating the effectiveness our synthesis technique in improving the cycling stability. The PTA coated DDSA electrodes remarkably showed almost absence of peaks corresponding to higher and lower order polysulfides indicating the binding of polysulfide onto the PTA.

X-ray Photoelectron Spectroscopy (XPS) analysis performed on the PTA coated DDSA electrodes and slurry coated sulfur electrodes after 200 electrochemical charge-discharge cycles are shown in Figure 5b. The XPS spectrum of PTA-DDSA lacks peaks corresponding to higher and lower order polysulfides observed in slurry coated electrode. This confirms the effectiveness of PTA in preventing polysulfide dissolution.

Sulfonic Complex Framework Materials (CFMs)/ Gen-2 CFMs:

A significant portion of Phase-3 involved the development of Gen-2 CFMs to address the problems faced by Gen-1 CFMs developed in Phase-2. The strategy of using a framework material host[13, 14] for sulfur has two principal advantages: (a) the framework material is usually of higher conductivity and hence helps in improving active material utilization[15] and (b) the fine-tuned pores of the frameworks which are in the order of the size of polysulfide species will help in preventing the polysulfides from dissolving into the electrolyte[16]. The Gen-1 CFMs upon testing after sulfur infiltration, demonstrated very stable cycling with fade rates <0.01% loss per cycle after a short initial capacity fade. Despite improvements in stability, these structures exhibit an initial capacity loss, due to the reaction of sulfur with the -CO_3 groups of the CFM as explained using X-ray photoelectron spectroscopy studies[16]. To rationally design sulfur hosts, CFMs free of the reactive -CO_3 groups must be used.

In Phase-3 an air stable for the CFM was prepared by replacing the -CO_3 groups with a sulfonic group. The novel CFMs synthesized using a simple room temperature synthesis process showed a high sulfur loading (~3-4 mg/cm^2) in the electrodes. Figure 6a shows a comparison of the XRD patterns of the experimentally synthesized CFM with the simulated pattern obtained from theoretical crystallographic information file (CIF)[17]. The CFMs showed an initial discharge capacity of 1265 mAh/g and maintained a capacity of 1051 mAh/g for over 100 cyces with 0.0011% fade at 0.2C rate (Figure 6b). This improved specific capacity of the sulfur electrode is attributed to the successful polysulfide trapping by the novel CFMs. Research work is currently on-going to improve the electrochemical performance even further.

Conclusions:

The aim of Phase-3 was to establish methods to improve sulfur cycling characteristics by replacing the commercial separator and electrolyte using a composite polymer electrolyte containing nanoscale filler materials. In addition, the work was directed at developing doped sulfur architectures and complex framework materials. By implementing such approaches various materials have been derived with initial capacities close to 1400 mAh/g with retention of capacity of >1100 mAh/g after 200 cycles. It can also be clearly observed that fade rates have been significantly reduced by using these approaches and exceptionally low fade rates of ~0.0014% loss per cycle have been observed. In particular, in the case of the PTA coated DDSA systems, a complete absence of polysulfides at the separator has been obtained and shown even after 200 cycles.

Publications:

[1] Jampani, P.H.; Gattu, B.; Shanthi, P.M.; Damle, S.S.; Basson, Z.; Bandi, R.; Datta, M.K.; Park, S.K.; Kumta, P.N. Flexible sulfur wires (Flex-SWs) – A Versatile platform for lithium-sulfur batteries, Electrochimica Acta Vol. 212, pp. 286 - 293 (2016)

[2] Shanthi, P.M; Jampani, P.H; Gattu, B; Sweeney, M; Datta, M.K; Kumta, P.N. Nanoporous Non-Carbonized Metal Organic Frameworks (MOFs): Understanding the Origin of Irreversible Capacity loss in Non-Carbonized Carbonate − based Metal Organic Framework (MOF) Sulfur hosts for Lithium − Sulfur battery, Electrochimica Acta, Vol, 229, pp 208–218 (2017)

[3] Jampani, P.H.; Gattu, B.; Shanthi, P.M.; Kumta, P.N. Novel electro-spun sulfur wires for fabricating mattes of lithium-sulfur batteries, International Patent Number: WO 2016/145429 A1, U.S. Provisional Patent, Application Number: PCT/US2016/022283 (Filing date: 03/14/2016)

[4] Shanthi, P. M, Jampani, P.H., Gattu, B.; Datta, M K, Velikokhatnyi, O. I., Kumta, P.N., “Electrospinning of PVdF-HFP: Novel Composite Polymer Electrolytes (CPEs) with enhanced ionic conductivities for Lithium-Sulfur batteries.” U.S. Provisional Appln. Serial No. 62/529,638 (2017).

[5] Jampani, P.H., Shanthi, P. M., Gattu, B., Datta, M K, Velikokhatnyi, O.I., Kumta, P.N., “High capacity, air-stable, Structurally Isomorphous lithium Alloy (SIA), Multilayer Porous Foams (MPFs) and Composite Multilayer Anodes (CMAs) for dendrite-free lithium metal anodes for Li-ion batteries”, U.S. Provisional Patent Appln. No. 62/529,588 (2017).

[6] Shanthi, P.M., Jampani, P.H., Gattu, B., Albuquerque T., Datta, M.K., Kumta, P.N., “Novel electrospun PVdF – HFP Composite Polymer Electrolytes (CPEs) with enhanced Ionic Conductivities for Lithium – Sulfur batteries”, ACS Applied Energy, (2017) under review.

[7] Shanthi, P.M., Jampani, P.H., Gattu, B., Datta, M.K., Velikokhatnyi, O.I., Kumta, P.N., “The effect of Mg, Ca and F doping on the ionic conductivity of Li4SiO4: Experimental and First Principles Investigation”, Solid State Ionics (2017) under review.

References:

[1] K. S. Rao, K. El-Hami, T. Kodaki, K. Matsushige and K. Makino, *Journal of Colloid and Interface Science*, 2005, **289**, 125-131.

[2] X. Chen and S. S. Mao, *Journal of Nanoscience and Nanotechnology*, 2006, **6**, 906-925.

[3] J. R. Kim, S. W. Choi, S. M. Jo, W. S. Lee and B. C. Kim, *Electrochimica Acta*, 2004, **50**, 69-75.

[4] D. Blond, W. Walshe, K. Young, F. M. Blighe, U. Khan, D. Almecija, L. Carpenter, J. McCauley, W. J. Blau and J. N. Coleman, *Advanced Functional Materials*, 2008, **18**, 2618-2624.

[5] N. S. Mohamed and A. K. Arof, *physica status solidi (a)*, 2004, **201**, 3096-3101.

[6] G. M. S. El-Bahy, *Journal of Applied Spectroscopy*, 2005, **72**, 111-116.

[7] N. Biswas, A. J. Waring, F. J. Walther and R. A. Dluhy, *Biochimica et Biophysica Acta (BBA) - Biomembranes*, 2007, **1768**, 1070-1082.

[8] K. Park, J. H. Cho, J.-H. Jang, B.-C. Yu, A. T. De La Hoz, K. M. Miller, C. J. Ellison and J. B. Goodenough, *Energy & Environmental Science*, 2015, **8**, 2389-2395.

[9] K. Matsumoto, S. Sogabe and T. Endo, *Journal of Polymer Science Part A: Polymer Chemistry*, 2012, **50**, 1317-1324.

[10] W. Li, Y. Pang, J. Liu, G. Liu, Y. Wang and Y. Xia, *RSC Advances*, 2017, **7**, 23494-23501.

[11] L. Zhang, H. Huang, H. Yin, Y. Xia, J. Luo, C. Liang, Y. Gan, X. Tao and W. Zhang, *Journal of Materials Chemistry A*, 2015, **3**, 16513-16519.

[12] P. J. Hanumantha, B. Gattu, O. Velikokhatnyi, M. K. Datta, S. S. Damle and P. N. Kumta, *Journal of The Electrochemical Society*, 2014, **161**, A1173-A1180.

[13] Z. Gong, Q. Wu, F. Wang, X. Li, X. Fan, H. Yang and Z. Luo, *RSC Advances*, 2016, **6**, 37443-37451.

[14] S.-R. Chen, Y.-P. Zhai, G.-L. Xu, Y.-X. Jiang, D.-Y. Zhao, J.-T. Li, L. Huang and S.-G. Sun, *Electrochimica Acta*, 2011, **56**, 9549-9555.

[15] J. Jin, Z. Wen, G. Ma, Y. Lu and K. Rui, *Solid State Ionics*, 2014, **262**, 170-173.

[16] P. M. Shanthi, P. J. Hanumantha, B. Gattu, M. Sweeney, M. K. Datta and P. N. Kumta, *Electrochimica Acta*, 2017, **229**, 208-218.

[17] E. L. First and C. A. Floudas, *Microporous and Mesoporous Materials*, 2013, **165**, 32-39.

Figures and Tables Begin on Next Page

Figures and Tables:

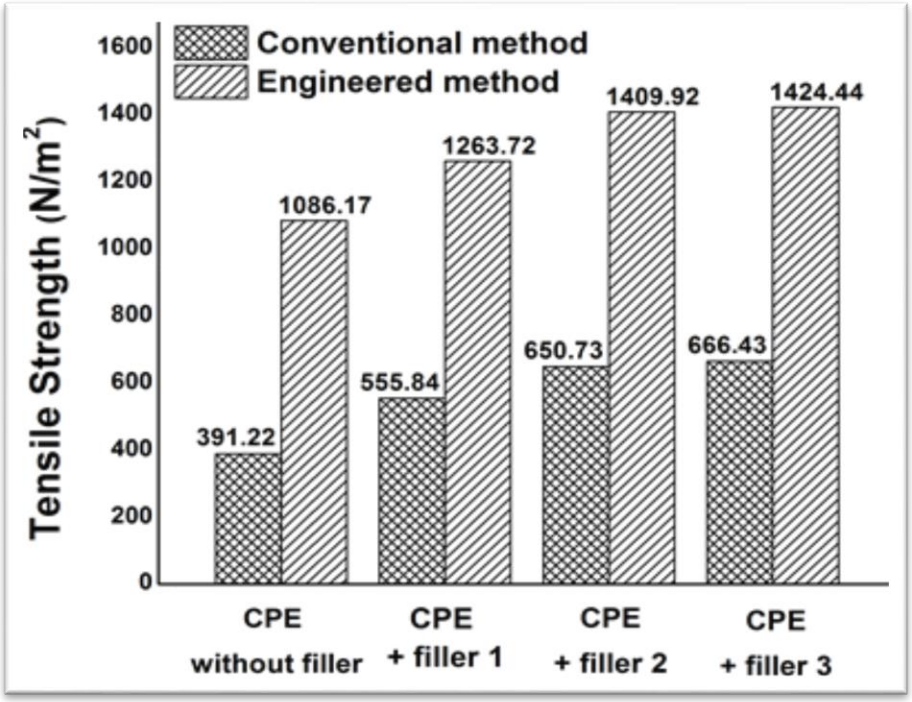

Figure 1. Cycling performance of Sulfur – infiltrated framework material (SFM).

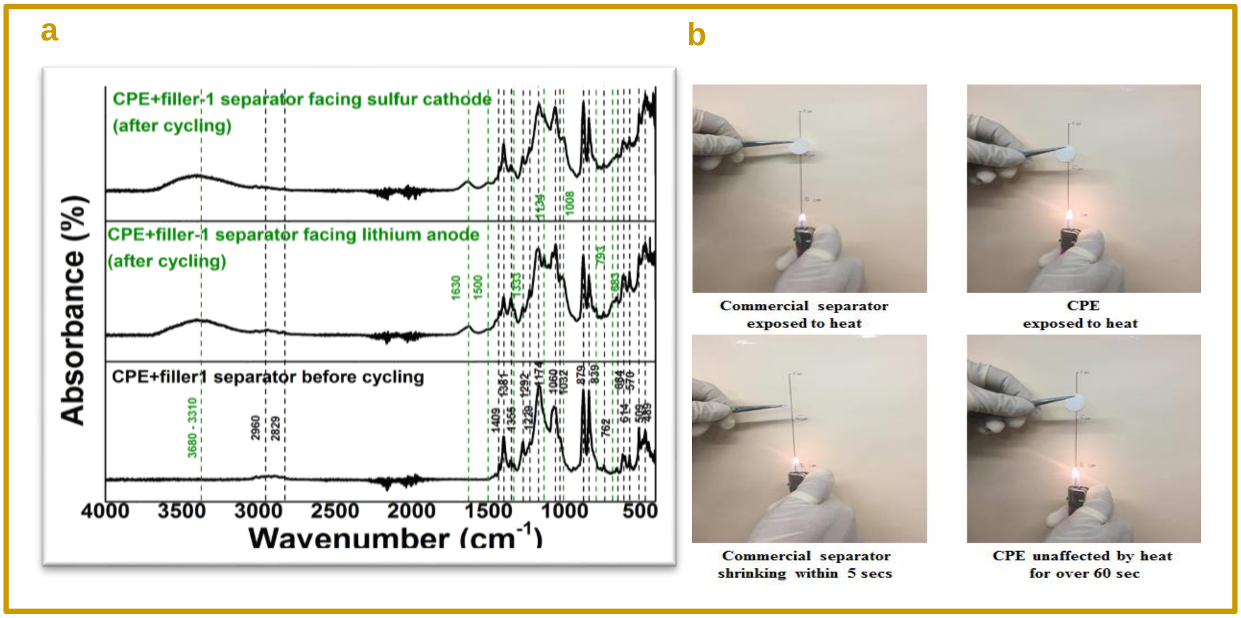

Figure 2a. FT-IR spectra of CPE after cycling and Figure 2b flammability test result of the CPE.

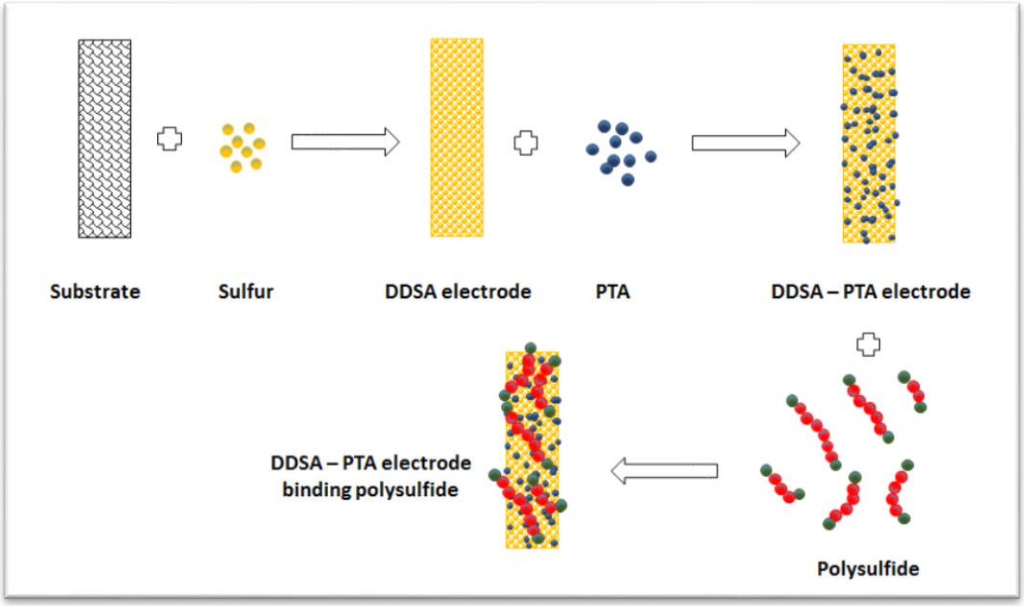

Figure 3: Scheme of interaction of PTA with polysulfide.

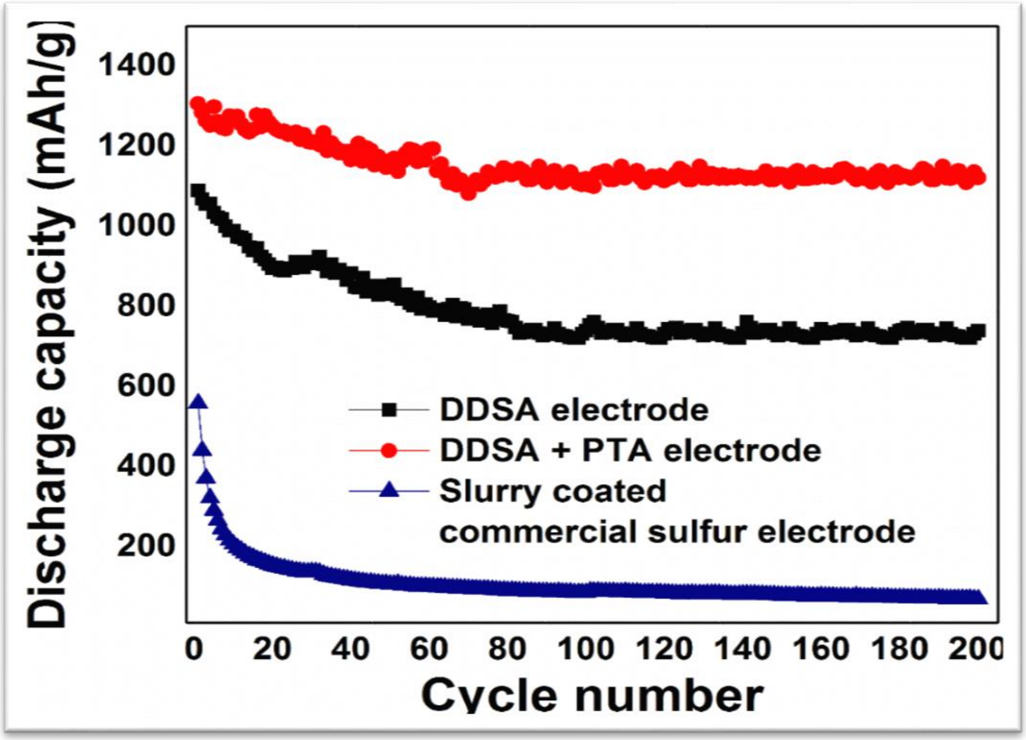

Figure 4: Cycling performance of PTA coated DDSA electrode.

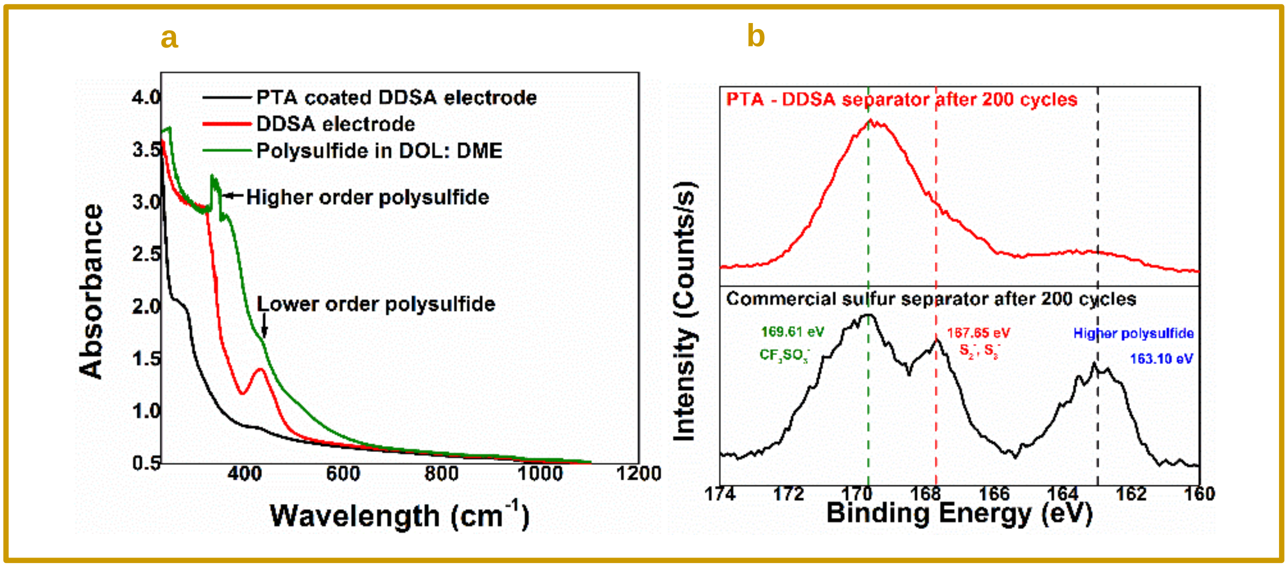

Figure 5a: UV – VIS spectroscopy of PTA coated DDSA electrodes showing absence of polysulfide absorbance and Figure 5b: Comparison of XPS patterns of commercial sulfur and PTA - DDSA separators after 200 cycles.

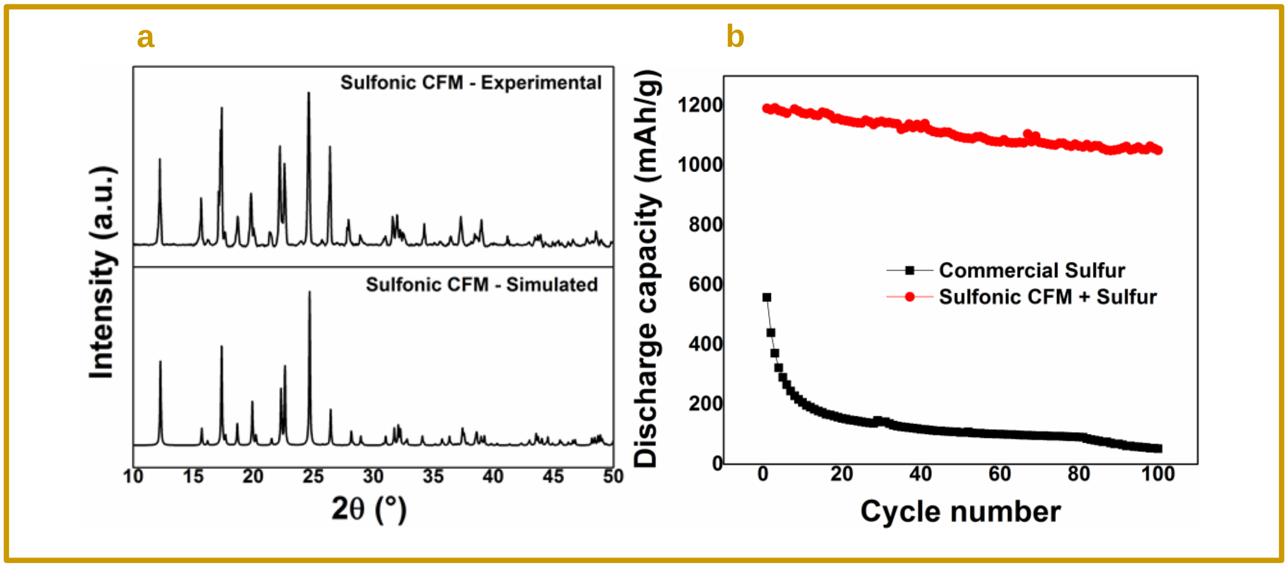

Figure 6a: Comparison of experimental and simulated XRD patterns of sulfonic CFM and Figure 6b: Electrochemical cycling performance of the sulfonic CFM compared with commercial sulfur.

Remainder of Page Intentionally Blank

This Page Intentionally Blank

AVPTA Technology Focus Area 6: Energy Storage & Batteries

Self-Forming Thin Interphases and Electrodes Enabling 3-D Structures High Energy Density Batteries

DOE-VTO TFA Lead: David Howell
TARDEC TFA Lead: Laurence Toomey

Principal Investigator:
Dr. Glenn G. Amatucci
Rutgers, The State University of New Jersey
Energy Storage Research Group
671 US Highway 1
North Brunswick, NJ 08902

Project Start: Oct 2016
Estimated Completion: Q4FY19

Objective:

- Develop and implement a novel *in-situ* formed lithium-metal-based metal fluoride battery that will enable packaged 10mAh batteries of energy density > 1000 Wh/L and specific energy > 400 Wh/kg at 12V

Strategic Context:

- Reduce battery weight and volume burden by developing: 1) electrochemical systems with the highest practical energy density, and 2) unique pathway to high voltage systems enabling high energy density packaged cells
- Develop safe energy storage systems with non-flammable solid state electrolytes that would reduce abuse tolerance during shipping and operation
- Develop safe and cost effective energy storage systems with the elimination of lithium metal during fabrication, handling and shipping
- Develop cost effective fabrication processes with the maskless scalable patterning technique providing potential for high throughput and low material cost that would reduce cost of complex architecture fabrication
- Utilize low cost materials to further decrease overall costs

Accomplishments:

- Achieved self-formed cell-stack with >500 Wh/L at a rate of C/10
- Implemented maskless, scalable patterning technique for the fabrication of the self-forming cells

- Established positive reactive current collector compositions that achieved > 30% of the theoretical energy density
- Established bi-ion solid-state conducting glass compositions with > 1×10^{-4} S/cm conductivity post formation

Introduction:

The ultimate goals of this project are to establish a step change in energy density, cost, safety and high voltage scalability of battery technology compared to the current state of the art secondary battery technologies. This will be accomplished using a secondary battery technology enabled by a novel *in-situ* formed solid-electrolyte battery leading to high energy metal fluoride vs. lithium metal chemistry in a planar battery electrode format. This technology provides many advantages including: 1) enabling the use of lithium metal electrodes via solid-state electrolytes, 2) eliminating Li metal in fabrication and handling of cells, 3) providing the highest practical energy density electrochemical system, and 4) enabling a unique pathway to high voltage systems.

Approach:

The *in-situ* self-formed battery is based on the *in-situ*, electrolytic formation of a Li metal negative electrode and a positive metal fluoride positive electrode from a LiF-based bi-ion conducting glass between a positive and a negative reactive current collector. As depicted in Figure 1, under polarization the LiF-based glass electrolytically decomposes with the release of the F^- and Li^+ ions to react with the positive and the negative reactive current collectors respectively, thereby forming the active electrodes in-situ.

As such, the project is divided into two main tasks that focus on the advance of the self-forming chemistry concurrent to the cell design and fabrication as depicted in Figure 2. The self-forming chemistry task is comprised of three subtasks encompassing the negative and positive reactive current collectors and the bi-ion glass conductor. Whereas the cell design and fabrication targets the development and integration of the bipolar configuration to achieve the 12V single cell goal.

Results and Discussion:

Bi-ion conductor development:

The bi-ion conductor is the heart of the electrochemical system as it enables the first formation cycle and the in-situ formation of the metal fluoride at the positive and lithium metal at the negative. Once the cell is formed, the majority of the subsequent charge/discharge reactions follow a mechanism similar to a lithium battery based on a MF_3 metal fluoride conversion into 3 LiF + M with lithium plating at the negative electrode. The bi-ion conductor will be essentially acting as a solid-state electrolyte development of bi-ion conductor. Therefore, this essential component must have the ability to electrolytically decompose at the positive electrode and release F^- anions to diffuse within the reactive positive current collector. This cannot be restricted to the simple surface decomposition of the bi-ion conductor at the interface as this is not nearly a sufficient amount of F^- to induce the fluorination reaction. Bulk diffusion of F^- and replenishment at the interface is required. The bi-ion conductor also needs to have the capability to conduct Li^+ throughout its bulk to enable continuous Li deposition at the negative electrode. As such, the main goal for FY17 was to establish bi-ion solid-state conducting glass compositions with ionic conductivity $>1x10^{-4}$ S/cm prior to in-situ formation. In order to accomplish this goal, a systematic experimental process was set in place for the fabrication and characterization of bi-ion glass conductors of different composition in order to rapidly determine if they would be good candidates for the *in-situ* self-formed solid-state batteries. After deposition, the compositions were characterized by 1) electrochemical impedance spectroscopy (EIS) to extract the ionic conductivity, 2) a combination of stepped and linear sweep voltammetry to investigate the electrochemical stability, and 3) x-ray diffraction (XRD) to investigate nano-crystallinity. More than 20 compositions and 80 cells were deposited and tested with some of the resulting EIS and direct current conductivity measurements presented in Figure 3. Best results were obtained with dopants which were identified to increase conductivity from $1x10^{-8}$ S/cm to $1x10^{-5}$ S/cm pre-formation and $> 1x10^{-4}$ S/cm at operation voltage were obtained. In addition, all except one composition exhibited electrochemical stability to breakdown in excess of 6 V with no increase of interfacial impedance.

Positive and negative reactive current collector development & design and fabrication: electrodes and cells:

Full solid-state cells were first fabricated in the second quarter using the newly developed bi-ion conductors with conductivities $> 1x10^{-4}$ S/cm at operation voltage, baseline current collector compositions identified in the first quarter, and baseline cell-stack designs established based on calculations and prior work. The viability of the *in-situ* formation of the entire electrochemical cell was demonstrated with limited cycling at output voltages of approximately 2V as shown in Figure 4, and low energy density represented by Generation 1 in the bar graph of Figure 5. Transport is a critical aspect of this program and as such all components' chemistries, electrode and cell design had to be developed in order to maximize it. Our approach consisted of using planar configurations. The electrodes configurations impact diffusion distance, energy density, current density, and effective electron transport through the current collectors. Therefore, the focus of the third quarter was to improve the electrode architecture and combine these upgraded configurations with the improved bi-ion conduction composition described above. All cells were all fabricated with a newly implemented maskless scalable patterning process described in the next section. Figure 5 depicts the consistent progression in energy density that we have been able to achieve with time following this approach. The Generation 2 architecture brought forth an improvement of a factor 4 with respect to the initial Generation 1 design. Greater advance in energy density was obtained with the upgrade of the bi-ion conductor chemical composition using the initial cell configuration leading to a factor 10 improvement compared to Generation 1 with the baseline bi-ion conductor. Finally, combining both approaches further increased the stack energy further by doubling the energy density obtained with the new bi-ion conductor alone (Generation 2 Bi-ion Conductor). Upon formation at 3.5V, 76% of the 500 Wh/L go-no go goal was achieved, while a 4.0V formation brought us closer with

96% of the 500 Wh/L goal. Additional architectural upgrades (Generation 3 and 4) demonstrated an effective path to effectively achieve and even surpass our go-no go goal with up to 570 Wh/L. The corresponding utilization of the reactive positive current collector also consistently increased from 16-20% for Generation 2 Bi-ion conductor to 24% for the Generation 2 Bi-ion conductor + Generation 2 architecture combination. The actual utilization is higher since the calculation assumed dense films, while experimental cells contain porosity.

Maskless scalable patterning implementation:

In order to develop a feasible and economically viable pathway to manufactures using vapor deposition, masks should be eliminated from the process flow. In this spirit, a maskless scalable patterning technique that offers tremendous benefits towards a practical pathway to high throughput, low material loss fabrication of complex architectures was implemented. In addition to the ulterior benefits, this new technique more immediately enables time and cost saving at the program level. This was a significant leap forward as we achieved the implementation of the maskless process one year ahead of time. Moving to the new makless approach helped us to achieve the significant boost in energy density as described as we moved from generation 1 to generation 2. All other fabrications pathways were eliminated to solely pursue the maskless scalable patterning technique throughout the program.

Hybridization:

In the fourth quarter, we shifted our focus toward improving rate capability while architecture and hybridization of transport pathways were investigated in parallel. Each approach contributed in different ways to the advancement of our full cell performance. While further changes to the architecture did not significantly contribute to a steep change in rate capability, overall higher energy and utilization were realized. In contrast, hybridization resulted in greater than an order of magnitude increase in our discharge current densities and enabled us to achieve the C/10 rate capability of our year-end go-no go goal. Figure 6 reveals the cell in-situ formation is followed by a full discharge at C/2 rate. In short, we have demonstrated a path to achieve over an order of magnitude improvement in current density leading to initial results achieving > C/10 discharge rates.

Conclusions:

Consistent progress has been realized during FY17 through advancements in chemistry, cell architecture and hybridization of transport pathways. Bi-ion solid-state conducting glass compositions with > 1×10^{-4} S/cm conductivity after formation were fabricated and successfully integrated into full solid-state cells of stack energy density that increased from 5, to 70 to 120% of the year-end go-no goal 500 Wh/L in the 2nd, 3rd, and 4th quarter, respectively to achieve 570 Wh/L. Whereas, the utilization of the positive reactive collector of these cells increased from approximately 1, to 14, to 24%. These solid-state cells were fabricated using a maskless scalable patterning technique was successfully implemented one year ahead of schedule. Finally, hybridization of transport pathways enabled improvement of current density by one order of magnitude leading to initial results achieving > C/10 discharge rates.

Figures and Tables:

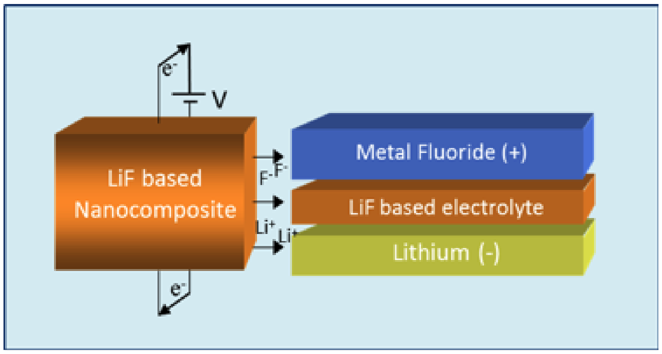

Figure 1. Diagram illustrates the *in-situ* formation of a metal fluoride positive electrode and a lithium metal negative electrode from the electrolytic decomposition of a Li-based bi-ion glass under polarization

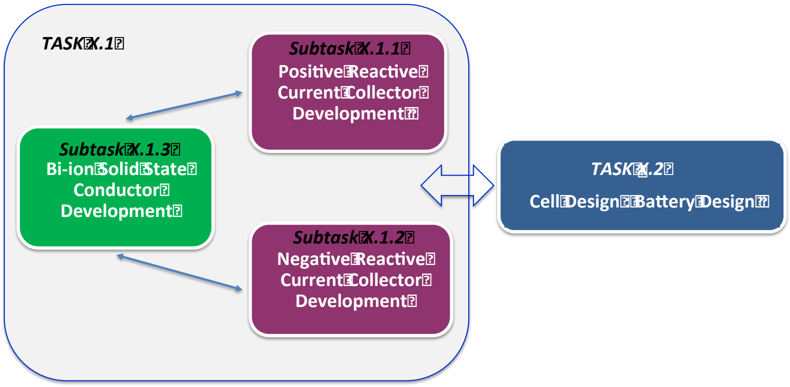

Figure 2. Program approach breakdown

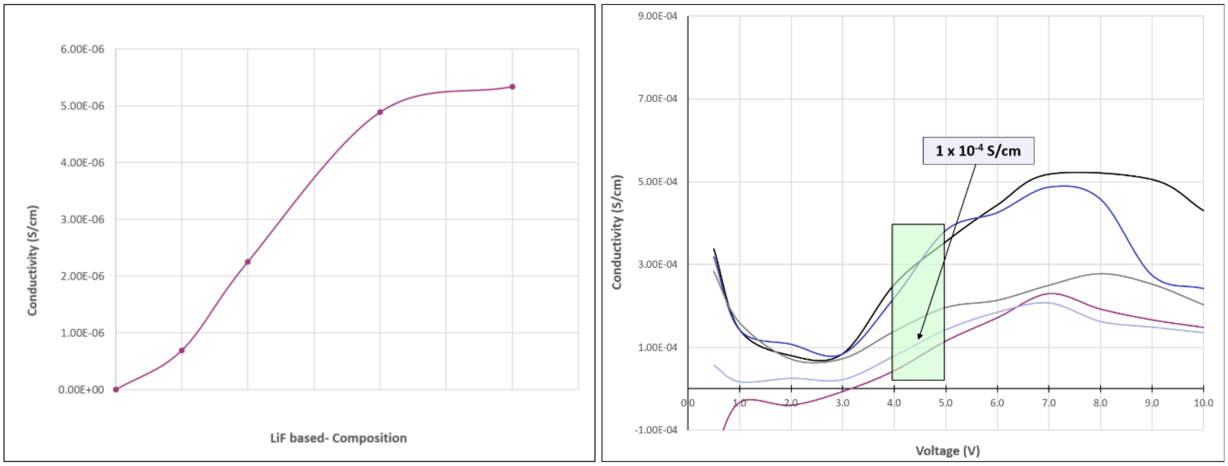

Figure 3. Electrochemical impedance spectroscopy as a function of composition (left) and in-situ direct current conductivity as a function of voltage for several compositions (right)

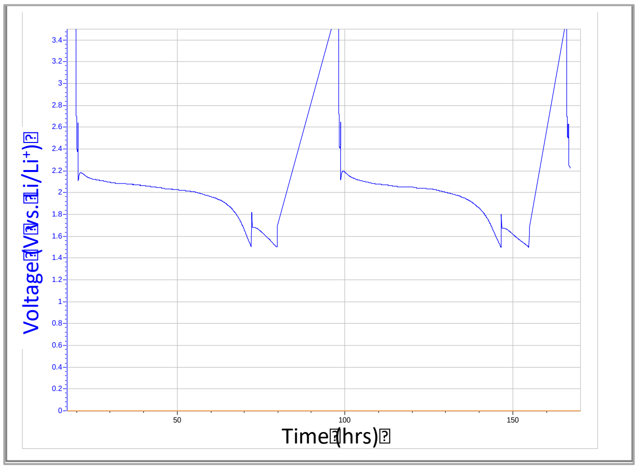

Figure 4. Voltage profile of an *in-situ* self-formed battery fabricated using newly implemented maskless scalable patterning technique

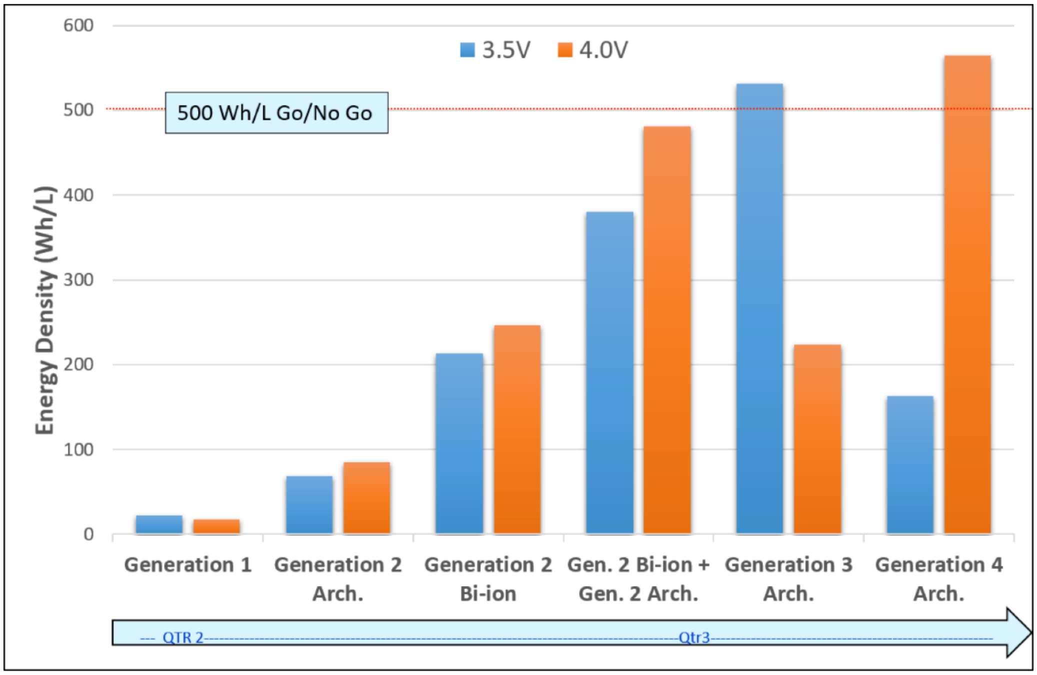

Figure 5. Energy density in the first discharge at slow rate plotted upon formation at 3.5 and 4.0V for various architecture combined with new bi-ion conductor chemistry. Labels indicate approach that gained the generation improvement.

AVPTA Technology Focus Area 7: Analytical Tools (Modeling & Simulation)

Physics-Based Computational Fluid Dynamics (CFD) Sub-model Development

DOE-VTO TFA Lead: Dr. Michael Weismiller
TARDEC TFA Lead: Dr. Vamshi M. Korivi

Principal Investigators:

Dr. Ajay K. Aggarwal,
Dr. Emily Ryan,
Dr. Caroline L. Genzale,
Dr. Sage Kokjohn,
Dr. Seong-Young Lee,
Dr. Seung Hyun Kim,
Dr. Daniel C. Haworth,
Dr. Chia-Fon Lee

Respective Affiliations:

University of Alabama,
Boston University,
Georgia Institute of Technology,
University of Wisconsin-Madison,
Michigan Technological University,
Ohio State University,
Penn State University,
University of Illinois at Urbana-Champaign

Project Start: Jan 2016
Estimated Completion: Q1FY19

Objectives:

Development and validation of more accurate, physics-based mathematical sub models (fuel injection spray, cavitation within fuel injectors, flash boiling, spray/wall interaction, super critical fuel injection, in-cylinder radiation and heat transfer, engine knock and soot emissions) for use in Computational Fluid Dynamics (CFD) software.

Strategic Context:

The impact of transient mixing and charge formation during the initial stages of the fuel injection event for high pressure JP-8 injection is a research gap identified by office of Chief Scientist.

Improvement of these sub models will help develop the fire protection competency of advanced modeling and simulation tools to address emerging threats and technologies due to fuel fires inside the ground combat vehicles.

Accomplishments:

Development and validation of more accurate, physics-based mathematical sub models for use in Computational Fluid Dynamics (CFD) software have been initiated with different universities and a national lab partner for developing following eight sub models. Computational and experimental studies have been initiated for development of these sub models.

- Super critical fuel injection (University of Alabama & Argonne National Labs [ANL])
- Cavitation within fuel injectors (Boston University & Oak Ridge National Labs [ORNL])
- Fuel injection spray (Georgia Tech & ANL)
- Soot emissions (University of Wisconsin-Madison & Sandia National Labs)
- Spray/wall interaction (Michigan Technological University [MTU] & ANL)
- Engine knock (Ohio State University & ORNL)
- In-cylinder radiation and heat transfer (Penn State University & ORNL)
- Flash boiling (University of Illinois at Urbana-Champaign & ANL)

Introduction:

Computational Fluid Dynamics (CFD) Software has led to improved engine designs but not yet realized full potential for attaining the goals of shortened engine development time, reducing fuel consumption, and minimizing exhaust emissions due to predictive accuracies of the sub models used in commercial and government sponsored software.

Also, it is a general consensus among academic, national Labs and industry community that there is lack of experimental data for validation of the new or improved sub-models. Developing accurate sub-models that are physics-based, predictive in nature and validated with experimental data, will require less calibration and tuning than currently available sub-models.

Approach:

Experimental protocols and apparatuses to identify the inaccuracies and formulate a technical approach to overcome.

Publication and Dissemination of information regarding improved sub models for inclusion in all commercial and government sponsored CFD codes.

Results and Discussion:

Summary for each sub model development updates from year II is summarized in following sections I-VIII separately.

Development and Validation of Physics-Based Sub-Models of High Pressure Supercritical Fuel Injection at Diesel Conditions:

The Eulerian-Eulerian (EE) framework is a viable numerical approach for simulating fuel injection at high-pressure diesel engine conditions. The uncertainty is reduced compared to the Lagrangian-Eulerian approach because of the fewer empirical models used. However, the accuracy in calculating thermo-physical properties of pure fluids and their mixture plays a vital role in high- fidelity simulations using the EE approach. Traditional diesel spray CFD models include droplet effects as the fuel exits the injector. Operation above the critical conditions requires different modeling approach because of the absence of surface tension. Proposed research will enable robust experimental validation of developed models and CFD codes to reduce modeling uncertainty, and increase operational flexibility.

Experiments were conducted in a Constant-pressure Flow Rig (CFR) whereby a low-speed flow of heated, pressurized air is supplied to the test chamber, and the fuel is injected against this flow. High-speed Rainbow Schlieren Deflectometry (RSD), a novel optical diagnostics technique pioneered in the University of Alabama laboratory to acquire quantitative scalar measurements in jets and flames, and supersonic flows is utilized to resolve the highly dynamic features of the mixing process. Experiments are conducted initially at conditions approximating the Engine Combustion Network (ECN) “Spray A”, and then at different chamber and fuel injection conditions, and fuel-types, i.e., pure or mixtures of surrogate species, and eventually with the real diesel fuel.

The RSD analysis steps consist of (a) the raw Schlieren images are converted from RGB format as saved by the camera to Hue-Saturation-Value (HSV) format, (b) The hue at each pixel is then converted to ray deflection angle at the pixel location based on a calibration of the rainbow filter, (c) A single image provide the instantaneous value at each pixel location. After performing a number of injection experiments, and ensemble average of 50 images is taken at each injection time. Thus, average deflection angle is obtained at each time step after start of injection by ensemble averaging instantaneous deflection angle at each pixel in the frame over all injections (50 in this case), (d) the average deflection angle is used to estimate the center plane fuel volume fraction in the spray through the Abel inversion process, which converts deflection angle to local fuel fraction. This process requries assumptions of axisymmetry and binary mixing between the fuel and air. Thus, quatitative results are valid only in the vapor region prior upstream of the combustion zone.

Figure I(A) shows the results at 1.3ms a Start Of Injection (SOI) at which time the reaction is underway downstream. The first thing to note is the high deflections in the reaction zone resulting from temperature induced density gradients. This is as opposed to the mixing induced density gradients near the injector. Another interesting feature is the reduction in deflection angle between the near injector spray and the downstream reaction zone. Principal investigators of the project believe this is caused by initial reactions causing slight temperature rise (reducing density to near that of the ambient in this case) prior to subsequent primary ignition. In other words there is a transition region between the dense spray near the

The integration of the developed numerical module for real-fluid thermo-transport property calculations has been completed. Some debugging has been performed to ensure the communication for exchanging values of needed flow variables and fluid properties between the open-source CFD solvers with the real-fluid module is done properly. A 2-D axisymmetric made-up verification test case similar to the Spray A injector was conducted. No successful result was obtained for n-Dodecane/nitrogen mixing case during this report period due to the convergence issue with the open source code employed and work is being done on the open-source code to resolve convergence issue.

A Convergent Science® CFD code CONVERGE® software User Defined Function (UDF) has been developed, which provides an interface between the CONVERGE® solver and user defined real fluid property model. Instead of using an Equation of State (EoS) or assuming ideal gas law, the fluid solver is now able to acquire thermodynamic properties from real fluid property model with given temperature and pressure, or given enthalpy and pressure. Current implementation uses a look-up table that is generated by the real fluid property for testing purpose, which provides internal energy, enthalpy, Cv, Cp, viscosity, conductivity and compressibility factor, as functions of temperature and pressure. Sample results are shown in Figure I (B).

Development & Multiscale Validation of Euler-Lagrange based Computational Methods for Modeling Cavitation within Fuel Injectors:

This project is developing methods for simulating cavitation dynamics in a fuel injector that can be used in preliminary design and for final design analysis, and performing experiments for validation of the models. Research focuses on three specific thrusts: computational model development, small-scale cavitation experiments and High Flux Isotope Reactor (HFIR) imaging of a real fuel injector.

The computational sub-models that are being developed rely on cavitation analysis performed with a high-resolution model of bubble dynamics and uses both a Lagrangian frame solver in the form of the Smoothed Particle Hydrodynamics (SPH) method and the Eulerian CFD solver OpenFOAM. One sub-model will create constitutive relations for inclusion in a CFD solver using an upscaling process based on the results from detailed computational studies of canonical injectors. Detailed simulations of cavitation in nozzles using SPH and OpenFOAM will form a database from which an upscaling method will be used to define a new submodel that can be integrated into a Reynolds-averaged Navier-Stokes (RANS) based multiphase CFD code (much like turbulence models are used in CFD). The second sub-model will consist of the SPH model itself by defining the two-way coupling interface equations for use with unsteady RANS CFD. Using a two-way coupled SPH and CFD approach will create a more detailed and accurate model but will be much more computationally expensive than upscaling and as such is proposed for final design analysis. Development and validation of the SPH tool and the subsequent full simulation capabilities based on the new sub-models relies on outcomes from experimental studies of detailed flow characteristics for canonical and real geometry injectors performed at Boston University (BU) and ORNL. The results from an OpenFOAM (setup at BU) and the BU SPH model are compared to those from Verma et al. (2017) and Klostermann (2013) as showin in Figure II(A).

Experimental efforts have been focused on further developing the technique for determination of void fraction through vibrational analysis. The results reported previously from the acoustic experiments conducted at ORNL assumed an effective stiffness, mode, and moment of inertia. The motivation here is to address some of those assumptions. To measure the dominant vibrational mode of the structure, at Boston University, PIs continued experiments of an impulse excited empty fuel injector with fixed and free end conditions. The response was obtained using Laser Doppler Vibrometery (LDV) in velocity mode and the measurements made along the vertical direction of the fuel injector. Controlled pintle actuation provided impulse excitation. Fig. II (B) is the response of the structure for a pintle opening of 5ms and the measurement was made at the tip (free end). Qualitatively, the response is similar to observations made on the ORNL campaign with initial vibration due to pintle opening and a secondary vibration response due to pintle closing. Additionally, the ring downs show low quality factors, an indicator of high damping. Fig. II (C) shows the results when the max amplitude is evaluated for distances away from the free end. As shown, the dominant mode indeed does appear to be the fundamental mode for a cantilever beam.

Studies from ANL has shown spray decay/dribble outside of fuel injector nozzle occurs after end of injection external of injector. ORNL data corroborates this observation internally as shown in Figure II (D) and offers complementary analysis. The team submitted a proposal for neutron imaging for the use of High Flux Isotope Reactor (HFIR) at ORNL. The proposal was accepted and is scheduled for beam time at the end of November, 2017. Joint Boston University & ORNL imaging campaign includes continuing the dynamic fuel-injection imaging technique.

Development and Validation of Turbulent Liquid Spray Atomization Sub-model for Diesel Engine Simulations:

This research aims to develop a new spray atomization sub-model that will appropriately capture the role of liquid turbulence on diesel jet breakup and enable accurate predictions for multicomponent fuels. A novel joint-facility experimental plan will quantify spatially-resolved liquid volume fraction distribution, SMD, and optical thickness under controlled scenarios to quantify the role of liquid turbulence and aerodynamic forces on spray atomization.

Georgia Tech implemented three benchmark Lagrangian spray breakup models within OpenFOAM. The three benchmark models included: 1) the Kelvin-Helmholtz Rayleigh-Taylor (KH-RT) model – the most widely employ spray model for engine simulations; 2) the Kelvin-Helmoltz Aerodynamic-Turbulence-Cavitation (KH-ACT) model - a newer hybrid physics breakup model available in CFD code CONVERGE®; and 3) the Huh-Gosman model – a turbulent breakup model employed widely by research groups using OpenFOAM in Europe (e.g. Politecnico di Milano). Benchmarking of the three models in predicting the droplet

Sauter Mean Diameter (SMD) along the centerline of Spray A is compared with experimental results. The Huh-Gosman model formulation demonstrated inadequate response to change in ambient density, particularly under low ambient densities. Based on these benchmarking simulations, the Huh-Gosman model formulation was excluded from further development.

Further benchmarking sensitivity studies were conducted to evaluate appropriate model formulations under low ambient density conditions. Georgia Tech found that models that included Kelvin-Helmoltz aerodynamic mechanisms of breakup (i.e., aerodynamic breakup) predicted incorrect response to changes in injection pressure (or velocity) at low ambient densities. That is, aerodynamic models are inappropriate for low ambient densities where aerodynamic forces from gas inertia at the liquid interface are low. There is very little change in the measured centerline SMD when the ambient density (or ambient pressure) is varied at low ambient density conditions (P ambient = 0.1 and 0.2 MPa). Experimental measurements from ANL strongly indicate aerodynamic forces do not govern breakup at these conditions, since the gas inertial force has increased by about 2x without a concomitant change in droplet size. The body of work from Faeth et al. suggests that liquid turbulence governs breakup at these conditions. Based on these analyses, Georgia Tech concluded that for low ambient density conditions, the spray breakup model should be formulation based on liquid turbulence breakup mechanisms alone, and formulated a new breakup model based on the empirical droplet size correlations of Faeth et al.

A new round of x-ray radiography measurements of the fuel distribution near the nozzle were completed at ANL. The year II round of experiments focused on improving measurement deficiencies identified during year I and expanding the matrix of available experimental conditions. In particular, Georgia Tech focused on improving Scattering-Absorption Measurement Ratio (SMR) in the low mass regions of the spray periphery by including a cerium additive in the fuel and took measurements from multiple viewing angles to better assess spray asymmetries. Demonstration of these improvement measurements is shown in Figure III (B). Spray asymmetries are now well resolved by the multiple viewing angles and a significant density of measurement points is seen clustered at the spray periphery that better quantify the mass distribution in these regions.

Development and Validation of a Lagrangian Soot Model Considering Detailed Gas Phase Kinetics and Surface Chemistry:

The objective of this project is to develop and validate a new, Lagrangian based soot model. This model will include a detailed reaction mechanism including Polycyclic Aromatic Hydrocarbon (PAH) chemistry up to benzopyrene. Particle modeling will be separated from gas-phase modeling through the use of Lagrangian soot parcels that contain a soot population. Particle nucleation will be modeled considering PAH dimerization. Once primary particles are formed, they will be transferred out of the gas phase and tracked using statistical soot “parcels”. The soot parcels will include a full soot population and description of the soot aggregates. The soot population in each soot parcel will evolve according to Smoluchowski’s population balance equation using a Monte-Carlo particle technique. The population balance solver will consider surface chemistry, collision, condensation, and wall interactions. The model will be rigorously validated through comparisons with existing constant volume vessel experiments and engine experiments.

In year II, expanded Lagrangian parcel model to include storage for soot population data (solving soot mass, diameter and number in each parcel) and the model has shown functionality with two-way coupling between stochastic solver and CFD. Quantitative fuel-vapor concentrations were measured using toluene fuel-tracer fluorescence under non-reacting conditions. Under combusting conditions, Planar Laser-Induced Fluorescence (PLIF) imaging was used to track formaldehyde and Hydroxide (OH) throughout the combustion process. Quantitative fuel-vapor concentrations were measured using toluene fuel-tracer fluorescence under non-reacting conditions. Under combusting conditions, planar laser induced fluorescence (PLIF) imaging was used to track formaldehyde and OH throughout the combustion process. All optical imaging is shown with cameras viewing into the outer region of the combustion chamber as shown by the camera field of view in Figure IV (A). Compared simulated results to measurements from the literature to ensure models are capable of reproducing measured fuel distribution. Overall good agreement is found between measured bulk combustion characteristics and ignition locations as shown in Figure IV (B).

Experiments were planned on one of University of Wisconsin-Madison heavy-duty research engines; however, a cylinder head failure delayed testing. To avoid project delays, experiments were moved to a small bore engine → new heavy-duty head casting is complete and undergoing final machining. Addition of small-bore experiments will allow assessing the models on additional platforms and provide some assessment of engine size effects. Initial round of Laser Diagnostics (LD) experiments complete. Data analysis is underway (two-stage micro-diluter and scanning mobility particle sizer) to measure soot particle size distribution.

Evaporation Sub-Model Development for Volume of Fluid (VOF) Method Applicable to Spray-Wall Interaction Including Film Characteristics with Validation at High Pressure Temperature Conditions:

The goals of this research project are to develop, implement and validate a Volume-Of-Fluid (VOF) approach for modeling evaporation, which is integrated into CFD codes to provide accurate and predictive simulation of spray-wall interactions without extensive need of parameter tunings. This is accomplished by development and inclusion of an evaporation sub-model in existing VOF modeling framework. This sub-model will be validated through extensive experimentation of the spray-wall interaction and film formation, spreading and vaporization dynamics.

- Designed and fabricated mounting fixture for new Bosch injector. Finished temperature calibration test with close-loop temperature control system and data acquisition system.
- Completed Rate-Of-Injection (ROI) test for the new single-hole injector and spray-wall impingement test with diesel and n-heptane on a new quartz window (front/side/bottom views).

- Finished film thickness measurement calibration using Refractive Index Matching (RIM) method.
- Completed the critical heat flux measurements at three different locations as shown in Figure V (A) in the impinging plates under various conditions including injection pressure, surface temperature and ambient density.
- Completed LE CFD simulations validation with MTU single-hole nozzle experiments.
- Investigated the effect of injected parcels on the statistical significance of extracted data in Lagrangian-Eulerian simulations.
- Extended Yarin and Weiss's theory to Lagrangian-Eulerian sprays for the prediction of droplet splash and formalized a rigorous mathematical formulation of the droplet impingement frequency for such applications.
- Implemented and preliminary tested the modified spray-wall interaction model into Converge code.
- Performed DNS runs of surface impingement of single and multi-train of droplets and validated the results with experiments of Yarin and Weiss as shown in Figure V (B).
- Validated numerical contact angle model with MTU single droplet impingement experimental results in DNS framework.
- Continued working on developing the DNS framework of spray-wall-interaction and evaporation model.
- Developed a benchmark test for evaluating the accuracy of evaporation modeling in finite domains and transient regimes.

Development of a Physics-Based Combustion Model for Engine Knock Prediction:

The objective of the research is to develop a new, physics-based Large Eddy Simulation (LES) combustion model for engine knock prediction, which 1) accurately describes turbulence-chemistry interactions during end-gas ignition and spark-ignited flame propagation and 2) enables the use of a detailed (reduced) chemical mechanism in engine large eddy simulations.

In year II, the Principal Investigator (PI) has performed the validation of end-gas ignition Conditional Moment Closure (CMC) using DNS data. As continued efforts of budget Period I, 2-D reduced chemistry DNS of end-gas ignition has been performed with various levels of temperature inhomogeneity and better grid resolution, 3-D two-step chemistry DNS has been completed, and larger-scale DNS of a premixed flame with the increased ratio of turbulence integral length scale to flame thickness at a higher Reynolds number has been performed. The end-gas ignition CMC has been validated using the ignition DNS database. The performance of CMC can substantially depend on the choice of a conditioning variable.

The emphasis of the analysis has thus been placed on the effects of the conditioning variable on reaction rate estimation in CMC. The sensible enthalpy and the total enthalpy are employed as the conditioning variable for the end-gas ignition problem to capture the effects of temperature fluctuations on the ignition processes. The results show that the sensible-enthalpy based CMC performs well in estimating heat release and species reaction rates. It is also found that the total-enthalpy-based CMC can lead to the substantial errors for this ignition problem with near stoichiometry Primary Reference Fuel (PRF)/air mixtures. PI has also performed the validation of the mixing sub-models used in CMC. A mapping method for the mixing models of the sensible enthalpy is developed and being validated. Figure VI (A) shows the predicted in-cylinder pressure and mean temperature as a function of the crank angle degrees.

The experimental results to date consist of two campaigns to isolate conditions of knock. PRF grade isooctane was used in these campaigns with various levels of boost. The airflows were selected as they probed the low temperature chemistry reactions of the fuel, and were used to understand if any effects this process had on knock and knock fundamentals. To augment the experimental conditions, kinetic simulations were performed using ANSYS Chemkin software. All ignition delay simulations were performed under adiabatic conditions using the closed homogeneous reactor simulation with a constant volume. All ignition delay calculations were performed for stoichiometric engine conditions with air. The gasoline surrogate mechanism from Lawrence Livermore National Laboratory, containing 1,389 species and 5,935 reactions, is used.

The contours in the figure highlight the amount of Pre-Spark Heat Release (PSHR) that occurred, which is labeled and plotted as PSHR percent relative to the total heat release energy. The kinetically controlled PSHR combustion process can be shown that PSHR is a result of low temperature chemistry reactions. The ramifications of this are poorly understood, and are thought to be present in the unburned zone of Spark Ignition (SI) combustion. Therefore this experimental data is a diagnostic tool for understanding this complex process that is often overshadowed by the much more energetic deflagration process in apparent heat release analysis. Using the present data to understand the effects of low-temperature reactions on knock and how fluid mechanics effects can and or do influence these processes is of interest. The resulting matrix of points for the 804 g/min airflow condition are illustrated in the contour plot of Figure VI (B).

Development and Validation of Predictive Models for In-Cylinder Radiation and Wall Heat Transfer (Figure VII):

Objective of the proposed research is to develop predictive CFD models for radiation and wall heat transfer, and made openly available. The models will explicitly account for couplings between different modes of heat transfer. New experimental data and high-fidelity simulation-based data for model development and validation will be generated and made available.

Identified two key datasets as shown in Figure VII (A) for validation of wall boundary layer wall heat transfer models, one from DNS and one from experimental measurements. Performed the first spectrally resolved measurements of Radiative Intensity (RI) in an optical engine, and initiated quantitative comparisons between computed and measured spectral radiative intensities. A high-fidelity Photon Monte Carlo (PMC) radiation model with Line-By-Line (LBL) spectral resolution was exercised to guide the design of engine experiments to be performed at ORNL. Exercised PMC/LBL radiation model to guide the design of the engine experiments to be performed at ORNL, which focus on the potential influence of radiative heat transfer on knock.

At the University of Michigan, initial spectrally resolved Infrared (IR) radiation measurements were made in an optical engine. A complication is the quartz cylinder liner that is used in the experiment, which has complex spectral absorption and reflection characteristics at the IR wavelengths of interest. To better understand the optical qualities of the quartz, measurements were made in a simpler flame configuration: a Hencken burner. There spectral radiation measurements were made with and without the quartz as shown in Figure VII (B) & (C). This provided insight into the spectral radiation characteristics of the quartz, and guidance on what adjustments will be needed on the experimental and simulation sides to allow accurate quantitative comparisons of spectral infrared radiation to be made. Simulations of the Hencken burner have been performed, and computed radiation spectra have been extracted to compare with the experimental measurements.

A highly simplified model for radiative heat transfer in engines and other high-pressure turbulent combustion systems was proposed. The model is based on observations from Photon Monte Carlos (PMC) / LBL computed spectral radiation characteristics in high-pressure turbulent spray flames and in engines. There it has been found that, to a good approximation: 1) the system is optically thin with respect to broadband soot radiation; 2) the system is optically thick at the primary carbon dioxide band (~4.2 μm), and little carbon dioxide radiation reaches the walls; and 3) the system is of intermediate optical thickness at the primary carbon dioxide/water vapor overlap band (~2.8 μm), and most of the radiation that reaches the walls is from water vapor. A simple box model for spectral radiation properties has been constructed that captures these key features, and this is combined with a simple Radiative Transfer Equation (RTE) solver: a first-order spherical harmonics method, which requires the solution of a single elliptic partial differential equation for each band. Results from the simplified model have been compared with those from PMC/LBL. For the conditions tested, results from the simplified model are quite close to those from PMC/LBL, at a small fraction of the computational cost of PMC/LBL.

Model Development for Multi-Component Fuel Vaporization and Flash Boiling:

Main objectives of the proposed research are to develop multi-component fuel droplet and wall film vaporization sub-models using both discrete and continuous thermodynamics methods; develop a sub-model for multi-component flash boiling; integrate sub-models into multi-dimensional engine models; validate numerical models with measurements acquired from a droplet chamber and a spray chamber under a wide range of ambient temperature and pressure conditions.

During Fiscal Year 2017, a new solver using discrete multi-component method is developed, and it is validated for droplet vaporization in quiescent ambient conditions by comparing simulation results with measurements obtained in the experimental portion of this work. The model is tested for both single- and multi-component fuel droplets. Measurements are done using the bended single-filament droplet suspension technique developed in the PI’s lab. The droplet vaporization evolution and the droplet interior temperature acquisition are carried out separately due to the significant heat conduction through the thermocouple to the droplet, especially at the low ambient temperature conditions. Results shown in Figure VIII (A) are the variation of the normalized time history of diameter squared of droplet consisting of ethanol and isooctane. The evolution of droplet size predicted by the model agrees well with the experiment for all four test conditions. Increasing ethanol content increases droplet lifetime considerably.

An Eulerian-Lagrangian-Spray-Atomization model is designed and implemented by the Argonne National Laboratory collaborator to examine flash boiling characteristics. The injection system of interest is the Spray G moving needle, which has been studied extensively previously for non-flash boiling conditions. The proposed approach extends from single-component fuel to blended fuel vaporization and flashing in the Lagrangian framework. Blends of iso-octane and ethanol were considered. Both non-flashing (Spray G case) and moderate flashing (Spray G2 case) conditions are tested under conditions that are similar to those stated on Spray G ECN webpage. The specific details of these tests are: Spray G: Pchamber = 600 kPa, Tchamber = 573 K Tfuel = 363 K; Spray G2: Pchamber = 53 kPa, Tchamber = 293 K and Tfuel =363 K. In case of Spray G, the fuel does not superheat, so the result is a non-flashing spray. For the Spray G2 case, moderate flashing can be expected. The peak injection pressure is around 20 MPa, with an injection duration of 0.78 ms. The rate-of-injection based blob injection methodology is used. For blended fuels the mass fractions of the constituent species in the injected parcels are specified in the simulation setup along with the physical thermodynamic and transport properties of ethanol and iso-octane. The density contours at 10 mm downstream of injector tip are shown in Figure VIII (B). The effect of fuel physical properties is considerable. Nonetheless, it is vital to carry out further study and compare with experimental data when available. During the current reporting period, the developing flash boiling model has been incorporated into high-fidelity VOF framework in CONVERGE, and droplet vaporization model has been implemented in KIVA for spray simulation testing. The newly implemented Eulerian-Lagrangian-Spray-Atomization (ELSA) model was tested for the Spray G moving needle cases, and the new solver is developed for droplet vaporization using discrete multi-component method underwent the validation process for wider range of varying temperature and pressures.

Conclusions:

Both Computational and experimental efforts are underway for developing eight different sub-models. Four project leads are using open source software for development and four universities are working with a commercial software vendor to implement these sub models. After FY18 quarter I, Go or No-Go decisions will be made for budget period III which is the last year for the project.

References:

None

Figures Begin on Next Page

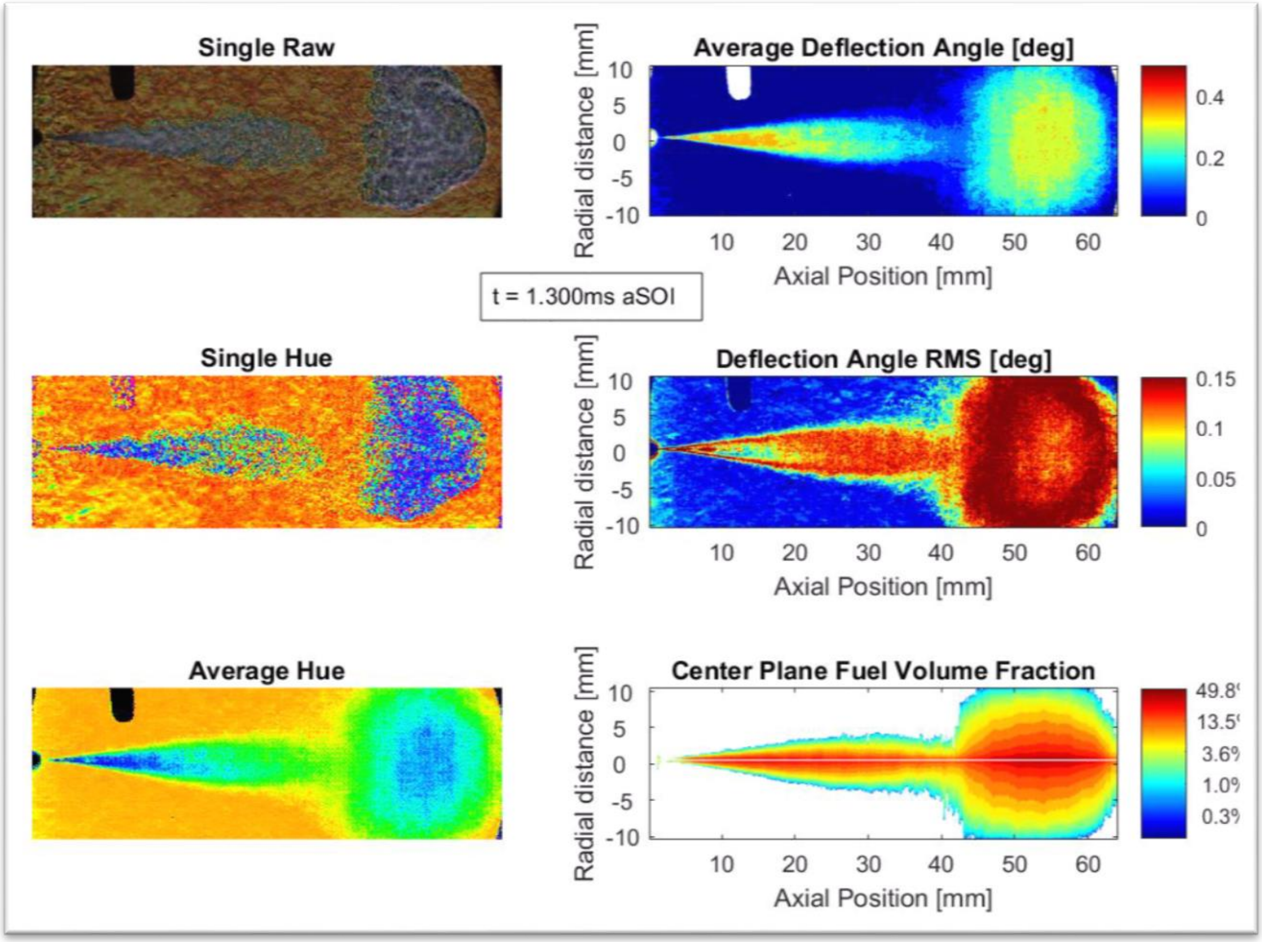

Figure 1 (A). Rainbow Schlieren Deflectometry (RSD) images during combustion at 1.3ms after start of injection (aSOI) for *n*-heptane injected at 1000 bar for 4ms into ambient air at 30 bar and 825 K. A total of 50 injections were captured in this case.

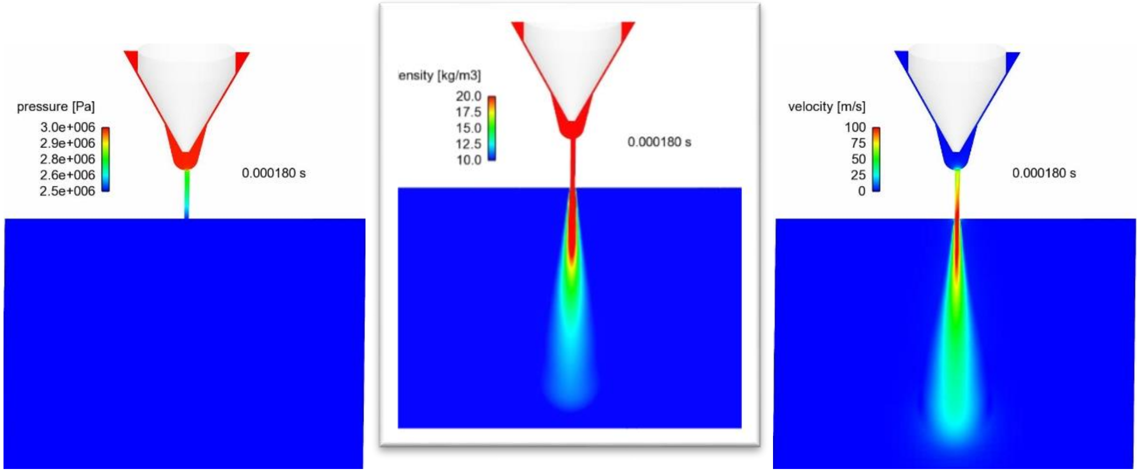

Figure 1 (B). 2D distributions of pressure, density and velocity at 0.18 ms after start of injection.

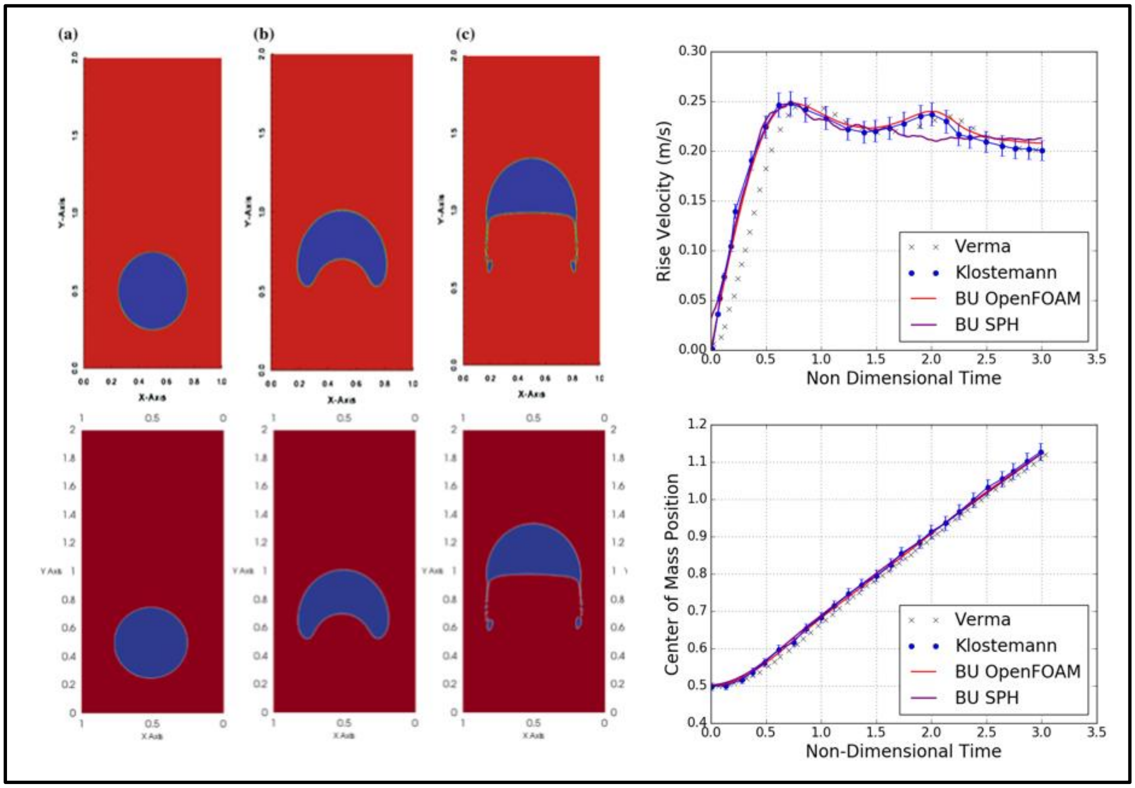

Figure 2 (A) OpenFOAM (setup at BU) and the BU SPH model comparison with Verma et al. (2017) and Klostermann (2013).

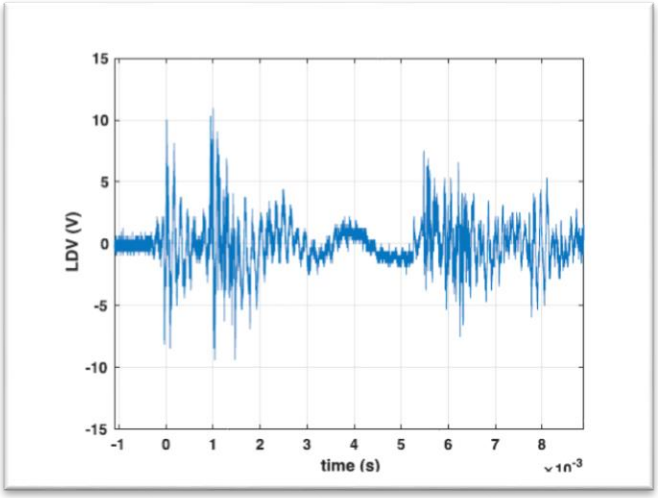

Figure 2 (B). LDV signal of fuel injector tip excitation from Pintle opening and closing.

Figures Continue on Next Page

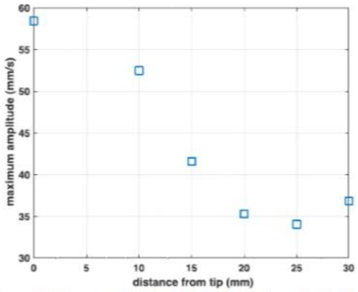

Figure 10 Max amplitude of LDV at the tip and 10, 15, 20, 25, and 30mm away from the free end.

Figure 2 (C) Max amplitude of LDV at the tip and 10, 15, 20, 25, and 30 mm away from the free end.

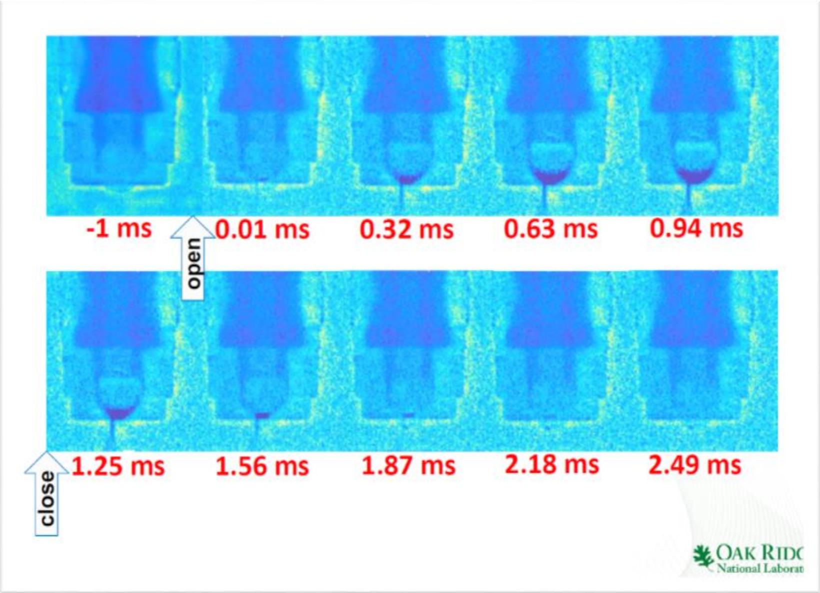

Figure 2 (D) Time-stamped images show composite injection event and illustrate fuel in sac long after pintle closes (flash conditions)

Figures Continue on Next Page

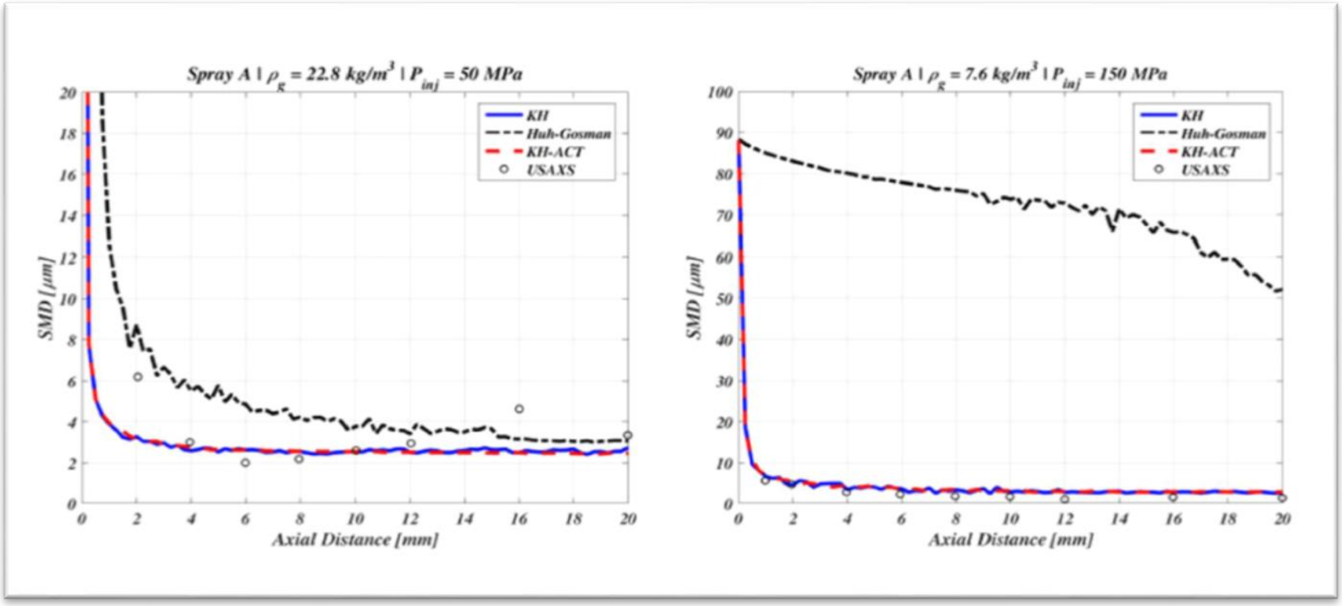

Figure 3 (A). Performance benchmarking of existing Lagrangian breakup models against recent Measurements of SMD along the centerline of Spray A. Benchmarked models include: 1) Kelvin-Helmholtz (KH), 2) Huh-Gosman, and 3) Kelvin-Helmholtz Aerodynamic-Cavitation-Turbulence (KH-ACT).

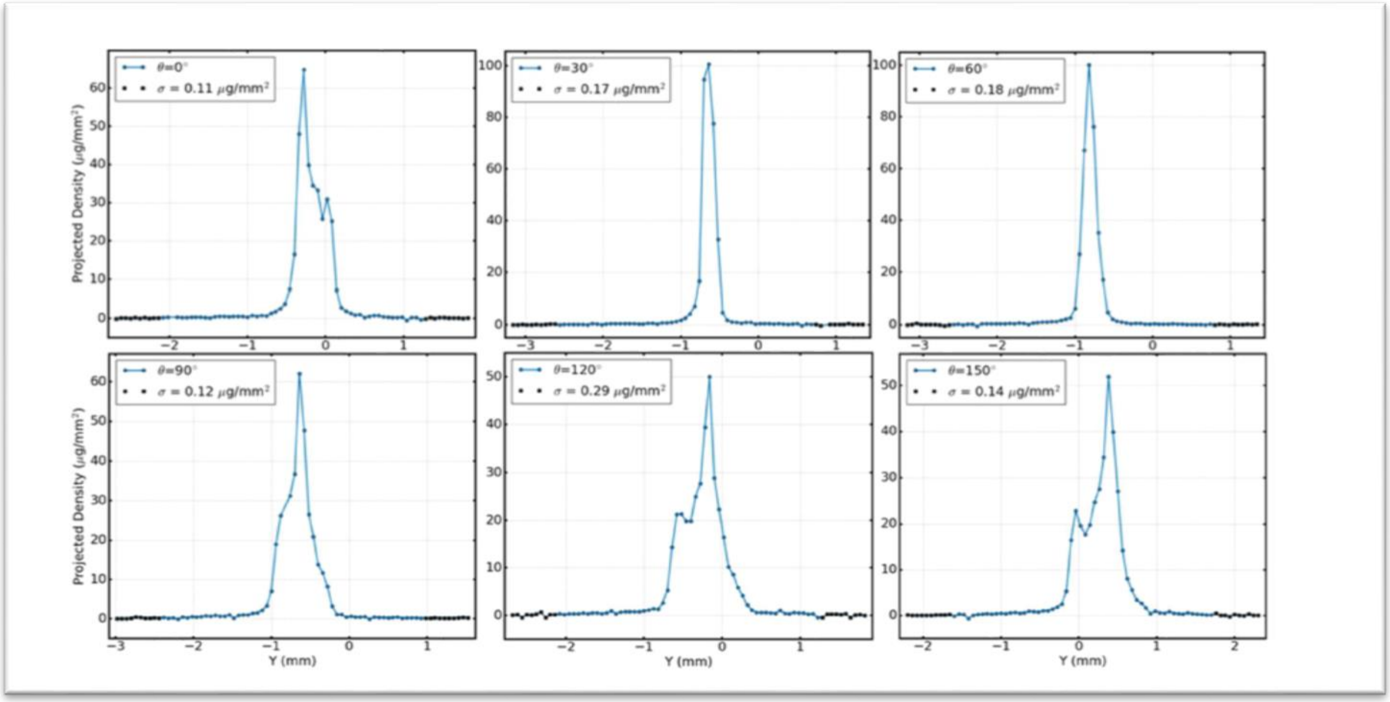

Figure 3 (B). Projected mass distributions of the injected fuel from Spray D 20 mm from the nozzle, showing cross sections of the spray from six lines of sight. Pinj = 150 MPa, Rhoambient = 1.2 kg/m3.

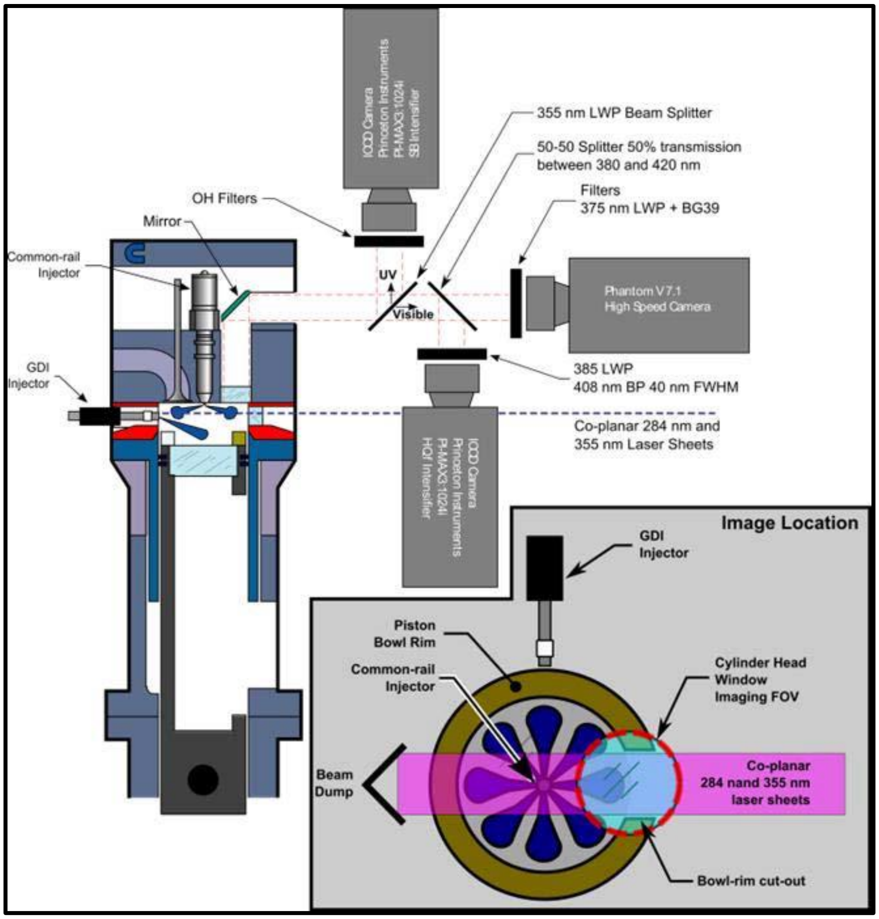

Figure 4 (A). Imaging setup for simultaneous CH2O PLIF and OH PLIF measurement.

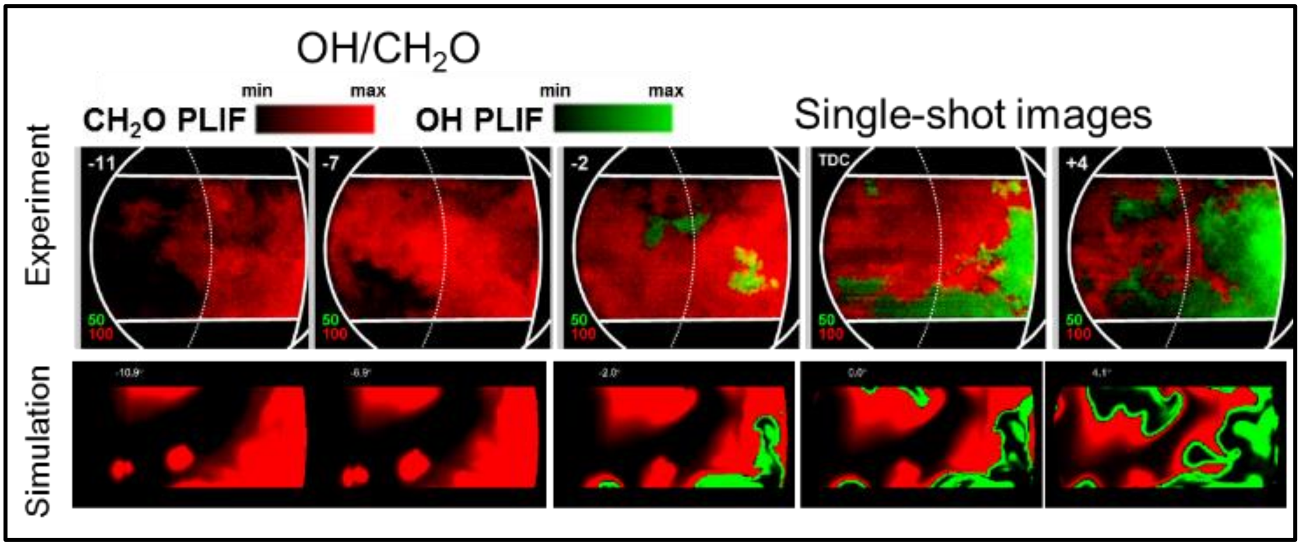

Figure 4 (B). Comparison of measured (top) and predicted (bottom) formaldehyde (CH2O) and hydroxyl (OH).

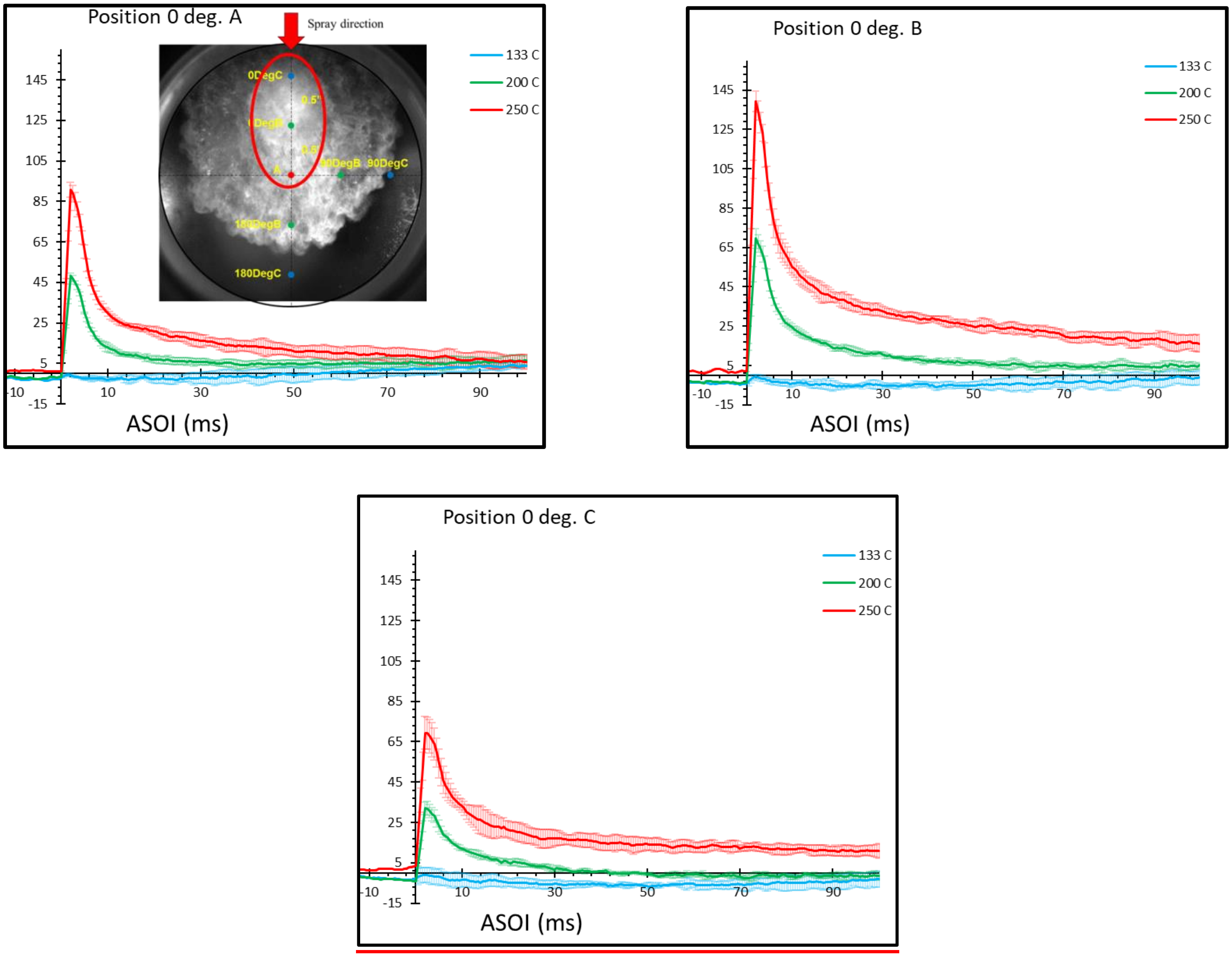

Figure 5 (A). Effects of the surface temperature on the heat flux at three different locations.

Figures Continue on Next Page

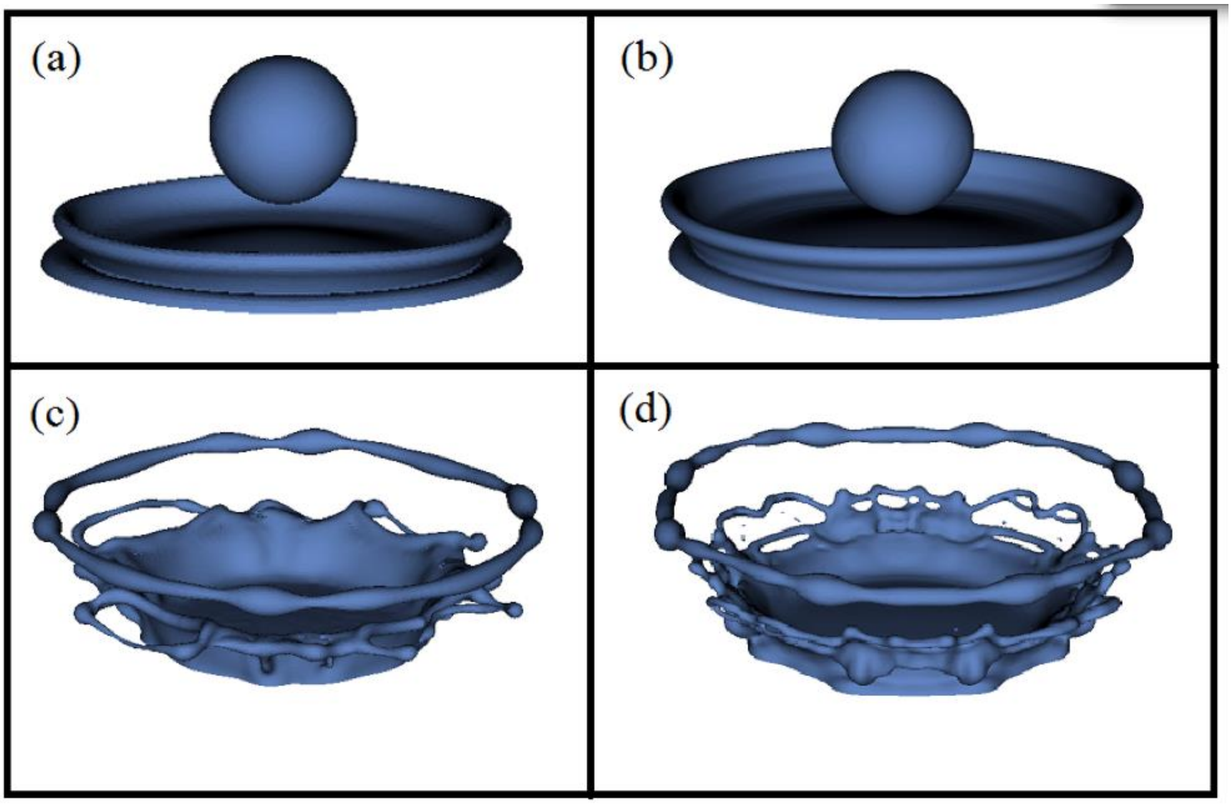

Figure 5 (B). DNS results of the surface impingement of a train of 109 micron ethanol drops at non-splashing (top row) and splashing (bottom row) regimes at grid resolution of (a, c) 2.5 microns, and (b, d) 1.25 microns. Simulation results agree well with the experiments of Yarin and Weiss.

Figures Continue on Next Page

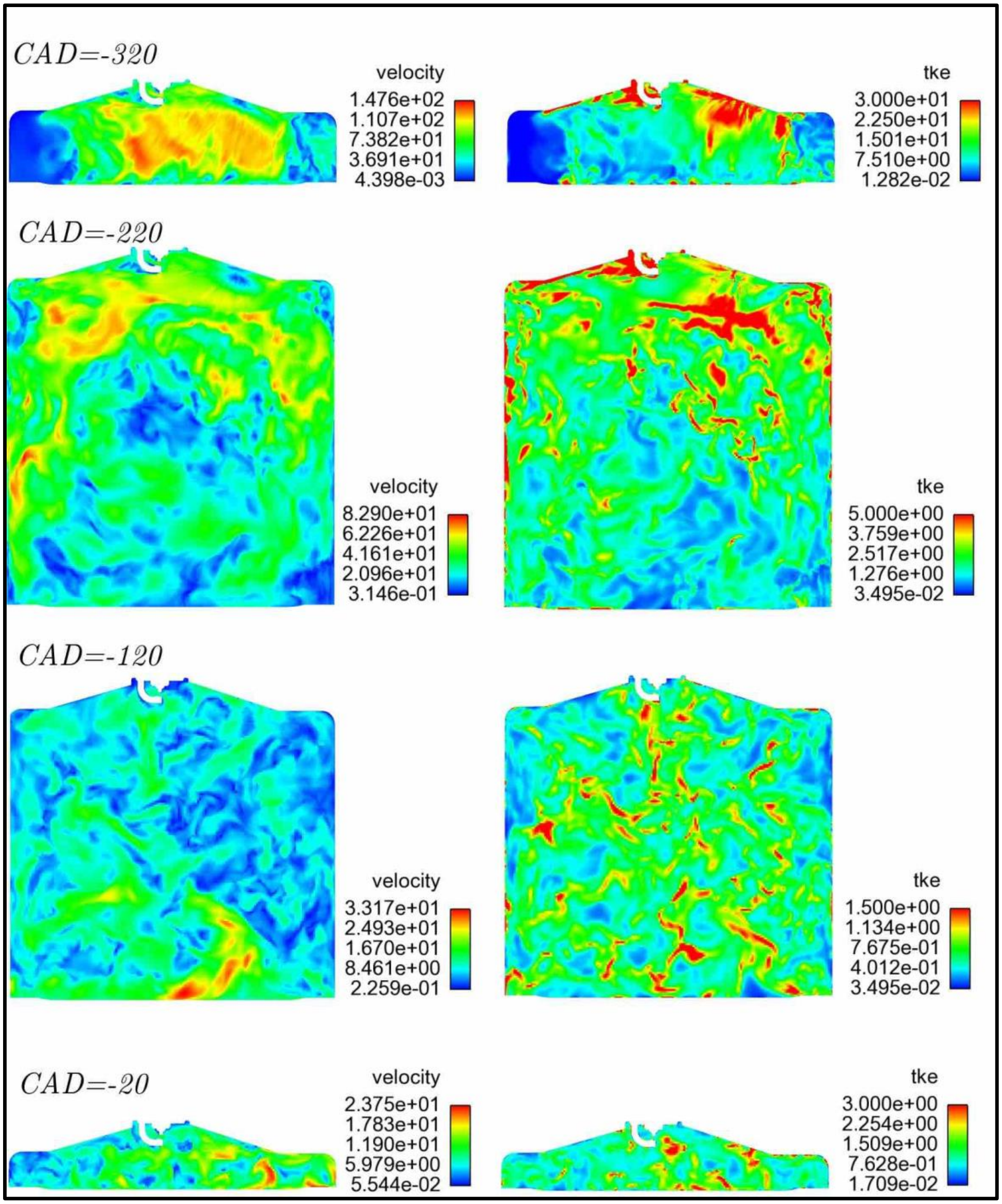

Figure 6 (A). Velocity and sub-grid turbulent kinetic energy fields at four crank angle degrees in LES of the example SI engine

Figures Continue on Next Page

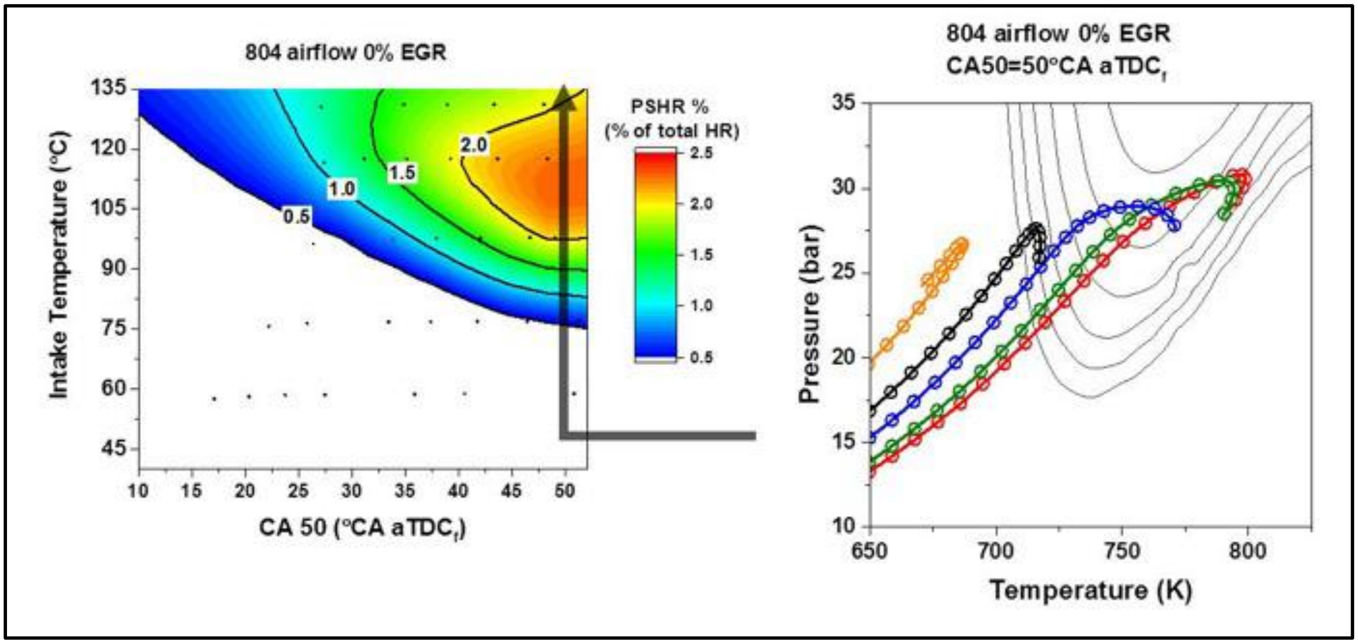

Figure 6 (B) (Left) Pre-Spark Heat Release contours generated from experimental data at 804 airflow operation 0% EGR for various intake temperatures and combustion phasing. (Right) intake temperature sweep at constant CA50 combustion phasing of 50_CA TDC.

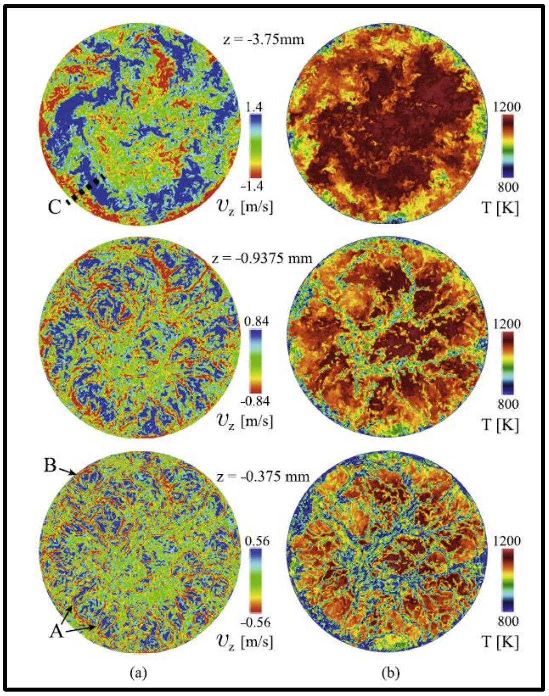

Figure 7 (A) Axial velocity (left) and temperature contours (right) on horizontal slices at z = -3.75 mm and z = -0.9375 mm (distances below the head) at 346° ATDC. (This is Figure 4 of Schmitt et al., 2016.)

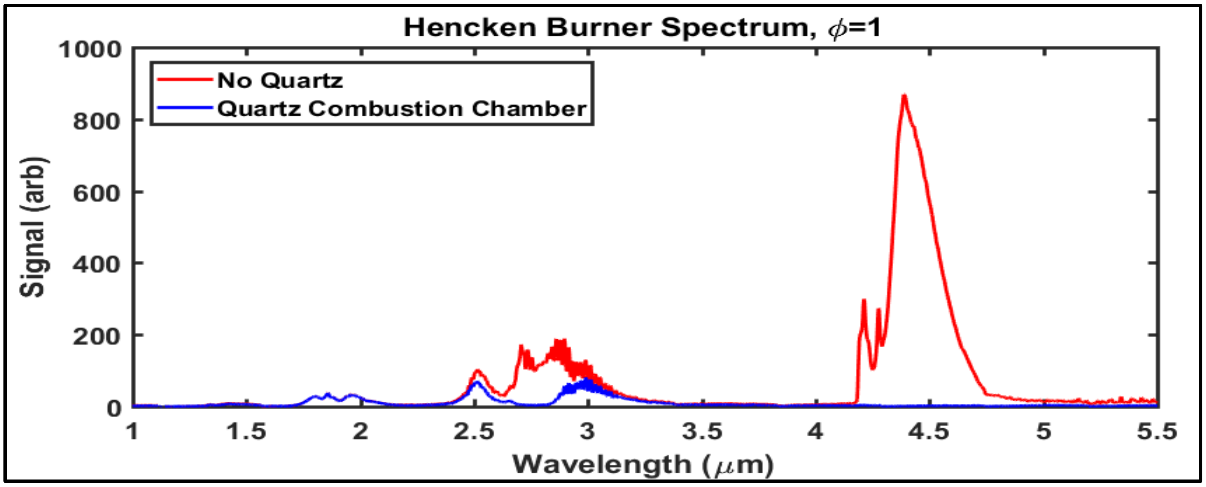

Figure 7 (B). Measured infrared spectra for a one atmosphere stoichiometric methane-air Hencken burner flame with and without quartz.

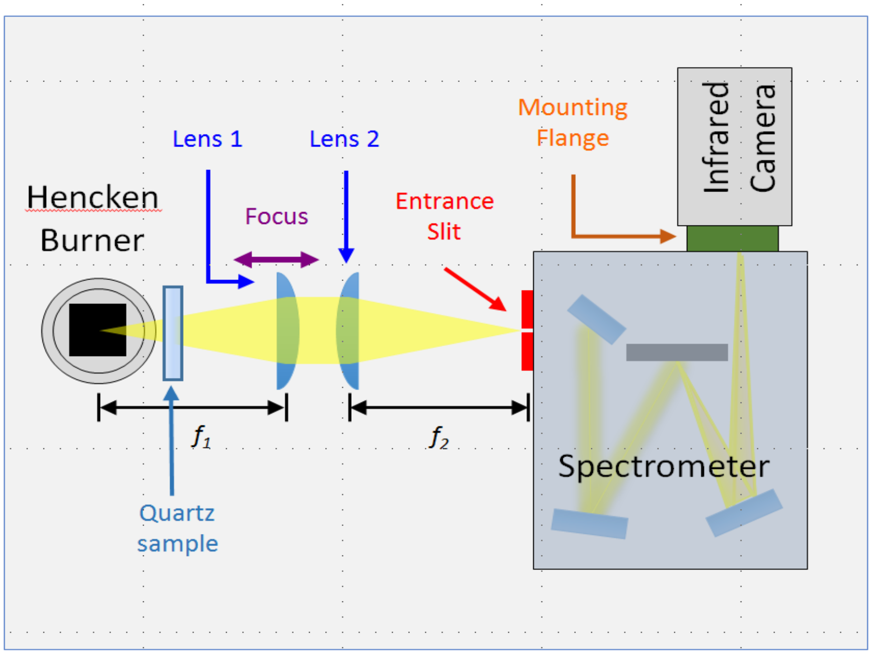

Figure 7 (C). Schematic of the experimental setup for the Hencken burner spectral radiation measurements at the University of Michigan.

Figures Continue on Next Page

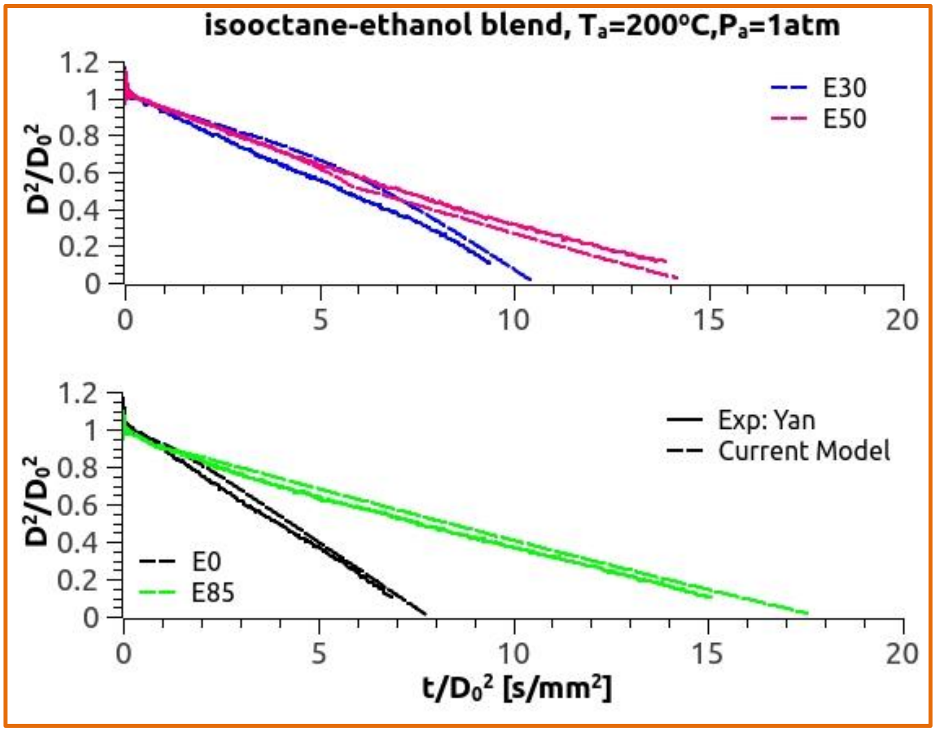

Figure 8 (A). Temporal history of multi-component droplet vaporization for ethanol/isooctane binary system under atmospheric pressure at 200°C. (E0 = pure ethanol; E85 = 85% ethanol, 15% iso-octane by volume)

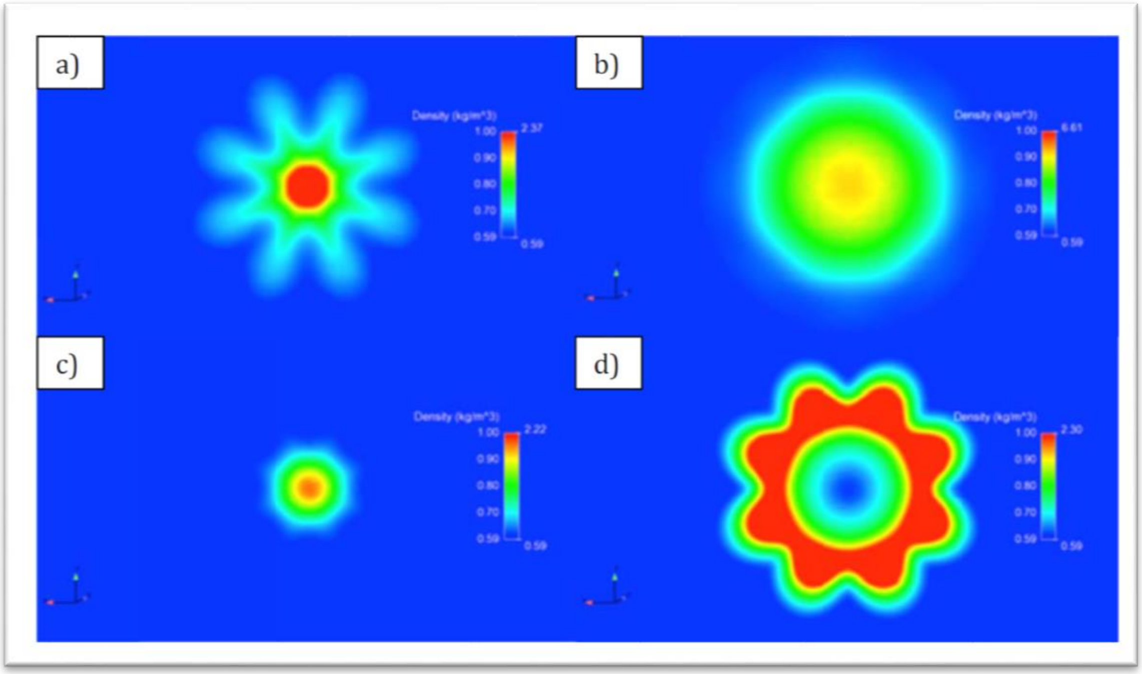

Figure 8 (B). Density Contours (a-iso-octane, b-ethanol, c-E30, d-E85) across a horizontal plane placed 10 mm downstream of the injector tip when subjected to spray G2 condition.

AVPTA Technology Focus Area 9: Autonomy-enabled Technologies

DOE-VTO TFA Lead: David Anderson
TARDEC TFA Lead: Dr. Rob Karlsen

There was no project activity under this TFA during FY17.

Remainder of Page Intentionally Blank

This Page Intentionally Blank

AVPTA "Extended Enterprise" Activities

Optimization of Scalable Military Fuel Cell Hybrid Vehicles

Principal Investigators:
Dr. Denise Rizzo
U.S. Army TARDEC
Systems Integration & Engineering
Analytics - Vehicle Performance &
Tradespace

Dr. Jason Siegel
University of Michigan
Mechanical Engineering Department
Ann Arbor, MI

Project Start: Jan 2017
Estimated Completion: Q1FY19

Objectives:

- Develop scalable tools to address optimization electrified Proton Exchange Membrane Fuel Cell (PEMFC) powertrains ranging from 300W robots to 250kW vehicles
- Optimize sizing of battery and fuel cell systems, coupled with the control strategy for power split for military load profiles and understand the impact of different mission profiles
- Address PEMFC challenges unique to military application, such as heat rejection in armored vehicles with low surface area, startup from sub-zero temperatures, and operation at dry ambient conditions.

Strategic Context:

- Squad Maneuver Equipment Transport (SMET)
- SCARAB
- Next Generation Combat Vehicle (NGCV)
- Electric Tank

Remainder of Page Intentionally Blank

Accomplishments:

- Developed the scalable vehicle models required to convert speed and grade information into electric power requirements.
- Developed the velocity trajectory optimization using Dynamic Programming for the electric powertrain to understand the role of regenerative braking and battery sizing. Submitted a conference publication to the 2018 American Controls Conference as an invited session in energy storage and conversion titled "Role of Regenerative Braking in Velocity Trajectory Optimization of an Electric Powertrain."
- Developed a scalable PEMFC stack model and tuned the polarization curve to match the terminal voltage of both the 250W Ballard air cooled PEMFC stack for mobile robot application and the 15kW Hydrogenics PEMFC stack powering the M RZR fuel cell vehicle at TARDEC.
- Presented results on dynamic programming, and Equivalent Consumption Minimization Strategy (ECMS) for online power split leveraging models and load profiles for the small robot application at the University of Michigan (U of M) Automotive Research Center (ARC) Annual Program review in May.
- Parameterized fuel cell air blower model to understand main parasitic losses for an air cooled fuel cell system.
- Performed offline optimization of the air flow rate, for cooling fans, coupled with the power split strategy for the PackBot robot using the 250W Ballard stack. Results to be presented at the 2018 SAE WCX (nee World Congress).

Introduction:

Given the high power demand requirements of military drive cycles and extreme environmental conditions in temperature and humidity, modeling and simulation tools are needed to perform Right sizing and power control for Proton Exchange Membrane (PEM) Fuel Cells (FC) running on hydrogen and hybridized with a lithium ion battery pack. This research aims to address the optimal sizing of Lithium ion battery and PEM FC stack for:

A1) Various Military Cycles (with high power demand)
A2) Powertrains ranging from 300W robots to 250kW vehicle
A3) Startup from freezing temperatures
A4) Operating at dry ambient conditions

When hybridizing a power train, it is challenging to size the Energy Buffer (EB) or lithium ion battery because the drive cycle, the control policy, and the hardware architecture all affect the optimal size. The type and characteristics of the energy buffer used also affect the EB sizing, for example reduced performance of the lithium ion batteries at cold temperatures limits their power capability. When increasing the EB size in hybrid electric vehicles, the total vehicle weight increases, which affects the fuel consumption [1] and maneuverability. In order to prepare the PEMFC stack for startup from harsh environmental conditions such as subfreezing temperatures [1], [3], [4] , energy intensive purging strategies are required as part of the shutdown process to ensure excess water is removed from the stack. Therefore the startup and shutdown energy requirements should also be considered as part of the sizing study. These requirements have not been previously addressed in the sizing literature or how to handle the warm-up from cold temperatures when considering the temperature dependent performance of both the battery and PEMFC system.

The problem outlined above involves design of the power split for the fuel cell and battery and joint systematic sizing of both FC and battery for various vehicle sizes and drive cycles. The objective of the research is to develop scalable physics-based models of the PEMFC system and balance of plant components, including Hydrogen storage, that capture the relevant tradeoffs in designing hybrid systems. This will likely include performance (power output), fuel consumption, startup time, volume and weight. Figure 1 below shows the Balance of Plant (BOP) components required to support operation of the PEMFC stack. The major parasitic losses are associated with the pumps and air compressor. The advantage to using physics-based models is that they can be upgraded to include degradation (lifetime) concerns under dry ambient conditions, limited cooling scenarios or during fast startup.

Approach:

There are 3 main technical challenges that we plan to address during this research

1) Coupling of electrical, thermal, and water management systems of the PEM Fuel Cell during warmup from low temperatures and potential to exchange thermal energy with the battery to enhance battery warmup.
2) Complexity of combined sizing, optimal power split and trajectory optimization problem
3) Unknown impact of power-split and sizing on the degradation rates of the Battery and Fuel Cell (Stretch Goal).

Our goal is to develop a scalable reduced-order model for the hybrid system that can predict dynamic battery and fuel cells temperatures and terminal voltages within 5% error during a military drive cycle.

We aim to demonstrate via simulation that > 5% Increase in vehicle range can be achieved through hybridization and right sizing of components.

We will apply scalable physics-based models of the fuel cell integrated with existing scalable electro-thermal models of the lithium ion battery including phonological models of the degradation rate parameterized from experimental data. Based on these physical models we can develop reduced-order models which capture the dominant trends relevant to component sizing and system performance.

For scaling of the battery in the hybrid system we can use a modular approach, adding cells in parallel and series, and changing the chemistry and electrode thickness to yield cells with different power/energy ratio.

The U of M team will work with TARDEC engineers to collect baseline performance data on the available 10kW and 20kW PEMFC stacks needed to parameterize the fuel cell stack and Balance of plant models. Once this data has been collected and used to parameterize the physics based PEMFC model, we will validate the model performance on additional data sets. The parametrized PEMFC model will then form the base for studying sizing of fuel cell/energy of storage, Cooling/heating requirements and parasitic loads (e.g. air compressor). These results will be shared with our industry partner to get feedback and additional validation where possible.

An Equivalent Consumption Minimization Strategy (ECMS), will first be applied as the baseline to determine performance under various battery sizes and initial temperatures. The equivalence factor converts battery power to an equivalent fuel power that must be added to the actual fuel power to attain a charge-sustaining control strategy [1]. We will investigate opportunity to leverage excess heat from the PEMFC system during warmup [5] to aid/speed battery warmup, and study the impact on overall system efficiency through this thermal coupling of components.

Results and Discussion:

The Results and Analysis from recent SAE WCX18 submission:

Military vehicles are typically armored, hence the open surface area for heat rejection is limited, Hence, the cooling parasitic load for a given heat rejection can be considerably higher and important to consider upfront in the system design. Since PEMFCs operate at low temp, the required cooling flow is larger to account for the smaller delta temperature to the air. This research aims to address the combined problem of optimal sizing of the lithium ion battery and PEM Fuel Cell stack along with development of the scalable power split strategy for small a PackBot robot. We will apply scalable physics-based models of the fuel cell stack and balance of plant that includes a realistic and scalable parasitic load from cooling integrated with existing scalable models of the lithium ion battery. This model allows the combined optimization that captures the dominant trends relevant to component sizing and system performance. The baseline optimal performance is assessed using dynamic programming for a reduced order model, by assuming a static cooling load required to maintain the stack at the operating temperature with peak efficiency. Pseudo-spectral optimization methods, which enable fast computation even for larger number of states in the model is then used to consider the additional control of the cooling system. If the fuel cell operates always with net power above the peak efficiency point, a simple rule based strategy can nearly recover the optimal fuel consumption achieved with dynamic programming, however for stack operation at powers near and below the peak eff point, the simple rule based strategy performs almost 20% worse than the optimal.

Fuel Cell Model:

The fuel cell voltage, and hence power can be parameterized by the operating temperature, T_{fc}, current I_{fc}, and oxygen partial pressure in the cathode $P_{O_2,ca}$. In the case of an air breathing PEMFC, we can assume the oxygen partial pressure is the same as ambient conditions, or 0.21 atm. Fuel cell polarization curves are typically functions of the current density $i = I_{fc} / A_{fc}$, where A_{fc} is the stack active area in cm^2. An empirical relationship for the cell voltage is then given by:

$$V_{cell} = \mathrm{E}(T_{fc}, P) - \frac{\mathrm{R}T_{fc}}{\alpha \mathrm{F}} \sinh^{-1}\left(\frac{i + i_{\mathrm{loss}}}{2 i_{oc}}\right) - i\mathrm{R}_{\mathrm{mb}} + \mathrm{B}_{\mathrm{c}} \log\left(1 - \frac{i}{i_{\max}}\right)$$

$$E(T_{fc}, P) = \frac{-\Delta G(T_{fc})}{\mathrm{nF}} + \frac{\mathrm{R}T_{fc}}{\mathrm{nF}} \log\left(\frac{\mathrm{P}_{\mathrm{H}_2} / P^0 \sqrt{\mathrm{P}_{\mathrm{O}_2} / P^0}}{P_V / P^{sat}(T_{fc})}\right) \qquad (0.1)$$

$$\frac{-\Delta G(T)}{\mathrm{nF}} = -\frac{\Delta H(T) - T\Delta S(T)}{\mathrm{nF}} = 1.256 - 2.26\mathrm{E}\text{-}4 \times T$$

Where P^0 is the reference pressure at 1atm and $P^{sat}(T)$ is the saturation pressure and assuming product water in the vapor phase [14]. For further details about the polarization curve, including the parameters see the appendix. The fuel cell polarization curve, and gross power are plotted in Figure 1. The fuel cell voltage varies slightly, decreasing with temperature as shown. The optimal stack operating temperature for the Ballard 1020ACS Stack was found experimentally in [18], however the authors did not consider the parasitic loss of the fan. The effect of increased membrane resistance due to drying at high temperatures, and flooding at low temperature are not included in the present model [8], [11], [12], [14], [16] but will be the focus of subsequent work.

The fuel cell heat generation is given by:

$$Q_{gen} = (E^{th} - V_{cell}) I_{fc} N_{cells} \qquad (0.2)$$

Where N_{cells} is the number of series cell in the stack and Eth=1.256V. The fuel cell stack temperature dynamics can be modeled by the following differential equation,

$$mcp \frac{d}{dt} T_{fc} = Q_{gen} / N_{cells} - Q_{cool} \qquad (0.3)$$

Where, *mcp* is the heat capacity of a single cell and the cell heat removal rate, Q_{cool}, is given as a function of the per cell flow rate,

$$Q_{cool} = 1/h\left(T_{fc} - T_{amb}\right)\left(W_{air} / N_{cells}\right)^{1/1.35} \qquad (0.4)$$

where W_{air} is the total stack air cooling rate in Standard Liters Per Minute (SLPM), and T_{amb} is the ambient temperature of the cooling air. The heat transfer coefficient h=26 is taken from the operation manual for the Ballard Mark 1020 fcs stack assumed for this simulation.

Finally, electrical power required for the cooling fan can be calculated from the following empirical fan curve,

$$\mathrm{P_{cool}} = \left(\mathrm{k_1{+}k_2\ \Delta P_{ca}\ W_{air}/N_{cells}}\right)\mathrm{N_{cells}} \qquad (0.5)$$

Where the constants $k_1=1$ and $k_2=10^{-3}$ describe the base electrical power of the fan and the work required to overcome the pressure drop across the stack, $\Delta \mathrm{P_{ca}}$ (Pa), for a given flow rate $\mathrm{W_{air}}$ (SLPM).The pressure drop across the stack, $\Delta \mathrm{P_{ca}}$ is given by

$$\Delta \mathrm{P_{ca}} = f\,\frac{4L}{D_h}\left(\frac{1}{2}\rho_{air}U^2\right);\ 4.65U \qquad (0.6)$$

Where f is the friction factor, and $f\,\mathrm{Re}=14.2$ for a square cross section [13], L=60mm is the channel length $D_h=0.66$mm is the hydraulic diameter, ρ_{air} is the air density, $U = W_{air}/N_{cells}/A_{CS}/1000/60$ is the velocity of air (m/s) in the cathode channels and $A_{CS} = 125\ \mathrm{mm}^2$ is the total cross sectional area of the channels. At 100 SLPM of air flow per cell the channel velocity is around 13.3 (m/s). Under these assumptions, a pressure drop of 50 Pa is predicted by equation (0.6) and a power consumption of 6W for the fan, or 14% of the peak cell power (43W). The Reynolds number $\mathrm{Re} = \frac{UD_h}{\upsilon_{air}};\ 430U$ indicates that laminar flow is a reasonable assumption for the cathode air channels below about 35 SLPM/cell.

Since the fuel cell generates significant heat, requiring a large cooling flow rate, the model should account for the auxiliary loads for the cooling systems. The system efficiency defined as

$$\eta = \left(P_{fc} - P_{cool}\right) \big/ \left(I_{fc}E^{th}N_{cells}\right)\ . \qquad (0.7)$$

Where the stack power is the power per cell multiplied by the number of series connected cells in the stack,

$$P_{fc} = I_{fc}V_{cell}N_{cells}\ . \qquad (0.8)$$

The auxiliary loads, $\mathrm{P_{cool}}$, are non-zero, even at zero fuel cell gross output power, therefore the system efficiency is low for small net fuel cell power as shown in Figure 2. Hence, the low power operation, below 10% of the peak power should be avoided similar to idle condition in internal combustion engines. The system is representative of the National Renewable Energy Laboratory (NREL) targets for FC efficiency given in [15], where the maximum efficiency is at 25% of the maximum load. Also shown in Figure 2 is the optimum efficiency as a function of fuel cell net power, representing the corresponding steady state temperature which yields that efficiency. We can approximate the fuel cell efficiency from this steady state line and that curve is used as the baseline efficiency of the fuel cell for the initial optimization study. The fuel cell manufacture also specifies a maximum temperature of 70 degrees Celsius, which is used as a constraint in our optimization routines.

Battery Model:

A simple one-state Open Circuit Voltage-Resistance (OCV-R) type battery model is assumed, where the open circuit voltage is assumed to be a linear function of SOC for simplicity. The cell voltage is given by

$$V_b = N_s \left(V_{OC}(SOC) - I_b R_b \right) \tag{0.9}$$

Where R_b is the battery internal resistance, Ns is the number of series cells N_p is the number of parallel cells, I_b is the per cell battery current and SOC is the battery state of charge given by the following differential equation.

$$\frac{d}{dt} SOC = \frac{I_b}{3600 Q_b} \tag{0.10}$$

where Q_b is the battery capacity in Ah and V_{oc} is the battery open circuit voltage, assumed to be a linear function of SOC without loss of generality for simplicity

$$V_{OC}(SOC) = \left(V_{max} - V_{min} \right) SOC + V_{min} \tag{0.11}$$

Where V_{min}=3 and V_{max}=4.2 (V) are the cell minimum and maximum voltage. The battery current I_b, can be determined from the power by

$$I_b = \frac{V_{OC}(SOC) - \sqrt{V_{OC}(SOC)^2 - 4 R_b P_b \big/ \left(N_p N_s \right)}}{2 R_b} \tag{0.12}$$

Where

$$P_B = P_{load} + P_{cool} - P_{fc} \tag{0.13}$$

Component Sizing:

The main system design parameters are the number of battery cells and series connected fuel cells, which we call the sizing problem. The base system design can be determined from the simple rule based strategy in equation (0.15) and(0.16), where the total trip energy is divided between the battery and fuel cell. The number of series connected FCs for the base system design is Ncells=3, chosen to put the average fuel cell output power near the peak system efficiency, and the number of batteries in series Ns=8 and parallel (Np=3) were chosen to meet the remaining load requirements. The battery temperature should also be considered as a design requirement, with a not to exceed temperature, which would limit the choice of cells based on their internal resistance or number of cells in parallel. The topic of battery temperature will be addressed in a subsequent work.

Optimal Control Strategy:

Dynamic Programming

To find the optimal split between the battery and fuel cell that minimizes fuel consumption in the fuel cell, Dynamic Programming (DP) is used in this paper. The Bellman Principle for minimizing a given cost function is the basis for DP [19]. For implementation of the DP algorithm, the open source software DPM is utilized which can handle the non-linear fuel cell model [20]. The algorithm produces an optimal input sequence which that will minimize our given cost function of fuel consumption, which is proportional to the stack current.

$$J = \int W_{H_2} = \int I_{fc} N_{fc} M_{H_2} / 2F \qquad (0.14)$$

The DP was set up with one input of fuel cell power and one state of battery State of Charge (SOC). In this way, the optimal FC power could be determined while adhering to the battery SOC constraints as well as minimizing hydrogen consumption. Within the model, once the FC power is determined, the corresponding current and voltage were found by interpolating on the polarization curve. Only the initial part of the polarization curve up to maximum fuel cell power is considered in the interpolation.

The remaining power demand of the drive cycle is to be met by the battery. The maximum battery power is limited by the resistance and the open circuit voltage which depends on the battery SOC. These are regulated in DP using the infeasibility conditions. Hence, from the battery power, the battery current can be determined which updates the battery SOC for the next time step.

Since DP is a numerical method the optimal results depend on the discretization. For this problem, the boundary line method was used that ensures all feasible inputs are considered by predetermining the boundary line between feasible and infeasible spaces [21]. For discretization, the input and state grids were increased till an optimal solution was found and using finer grids did not improve the optimal solution. For a one state, one input problem, DP is computationally quite efficient and can determine the solution fairly quickly, within a few minutes. On the other hand, increasing states or inputs can exponentially increase computation time.

Dynamic Programming Results

The DP results for the optimal power split is shown in Figure . The simulations for a given power demand were carried out for three different ranges of battery SOC which limited battery energy to approximately full, half and a quarter of the total. As can be seen clearly, as the battery energy reduces, the power demand from the fuel cell increases, as expected. But surprisingly, the optimal fuel cell power is shown to be almost constant for a given battery energy. The variation in load demand was handled completely by the battery, while the fuel cell supplied almost constant power. This behavior was replicated across 6 different drive cycles with significantly varying power demand as well. In all cases, the final SOC was constrained between the limits given below but the optimal SOC trajectory always ended up discharging the battery energy as much as possible.

The almost straight line behavior could therefore be approximated with a simple rule based solution which we define as follows

$$FC_{energy} = Total_{energy} - Battery_{energy} \tag{0.15}$$

$$FC_{power} = \frac{FC_{energy}}{\text{TripTime}} \tag{0.16}$$

For the cases shown in Figure 3, the difference between the fuel consumption from DP is given in the table below

Table 1. Battery to trip energy ratio and the difference in H2 consumption between optimal DP solution and the rule-based strategy.

SOC Range	Battery to Trip Energy Ratio	% Difference in H2 consumption from constant FC power strategy
Full (10-90%)	0.66	0.036
Half (50-90%)	0.34	0.004
Quarter (70-90%)	0.17	0.097

Clearly, the simple rule based solution, is able to match the optimal DP solution quite well for all cases and therefore, the simple rule given in equation (0.16) can quickly determine the optimal power split between the two power sources.

The reason for the fuel cell power being almost constant across the power demand is due to the relatively linear fuel cell efficiency with respect to fuel cell power as shown in Figure 4.

From Figure 4, it is clear that switching between different fuel cell powers, changes the fuel cell efficiency linearly and therefore, a constant FC power would be the approximate mean power and by extension a mean efficient point. Hence, overall the fuel consumption is almost the same.

However, these results were shown for only the cases, where the fuel cell operates in region where the power is greater than the peak efficiency point. In the cases where the fuel cell power demand was around the 20 W (7W/cell), the power demand would change due to the non-linear efficiency curve.

The optimal power split in navigating such a trajectory is shown below in Figure 5. In this example, the optimal strategy for the fuel cell is to switch between zero fuel cell power and a constant power that corresponds to the maximum efficiency point. All negative power in the power trajectory are absorbed in the battery to recharge it, while during positive power demand, the fuel cell power is almost constant except for some points. The reason for operation at a higher power is due to limited battery energy despite long charging, where the battery power has to be supplemented by less efficient higher fuel cell power.

Now since the change in efficiency is significantly different and non-linear, the simple rule based solution from equation (0.16) is not able to match the DP results at all and shows a 20.9% higher hydrogen consumption. The increased consumption of hydrogen is due to operation in the less efficient operating points of the fuel cell where the losses due to auxiliary loads significantly reduce efficiency. The results are shown below in Figure 6.

Figure 6 shows the operating points of the DP optimization and the rule-based constant fuel cell power case. While the figure does not show the time of operation, we can confirm from Figure 5 that the maximum time of operation is spent at the maximum efficiency point of ~ 25-30 W. As explained before some operating points do move into the higher fuel cell power at slightly lower efficiency. At all other times, the fuel cell is switched off. The constant power case operates at almost half the power and a much lower efficiency. In doing so, it is also switched on during the regions of negative power demand thus it burns hydrogen in a less efficient manner to only charge the battery. The final battery SOC is same between the DP and rule-based solution, but hydrogen demand for the rule based is significantly higher.

Optimal Control Strategy – Thermal Effects

In the previous results, we see that using a simple rule-based strategy produces a solution that nearly replicates the optimal solution found using DP, if the fuel cell power demand is more than 30 W (10W/cell). However, our results were based on fixed approximation of auxiliary loads, without considering the actual temperature of the fuel cell (only the power required to maintain the optimal temperature for a given load). In the next section we address the fuel cell thermal dynamics and control of the cooling fan using to account for the actual losses from the cooling system as the fuel cell heats up producing useable electric power.

The system efficiency to maintain a given temperature at a given current is shown in Figure 2. The efficiency curve is similar to the NREL curve as the fuel cell efficiency increases up to 10W/cell and then starts to decrease with increasing net power draw. Also, with increasing temperature, the fuel cell stack efficiency increases till the optimal temperature and then falls significantly due to the increased air flow required to cool the cell and the additional resistive losses due to drying of the membrane. From the efficiency contour shown in Figure 2, we can see that the fuel cell system is most efficient at low loads between 5-15 W/cell and medium temperatures between 45-65 ^{o}C. The portion shown in white is the region of negative steady state efficiency. This means that at these points, the cooling load to maintain temperature in steady state, is higher than the power produced by the fuel cell. Transient operation during warmup occurs here, but without using the fan to maintain temperature a high efficiency can be achieved at these operation points.

Trajectory Optimization using MathWorks® MATLAB® General Purpose Optimal Control Software (GPOPS)

The issue with including a thermal model is that it increases the model inputs to two by having the input of cooling air flow and the number of states to two by adding the state of fuel cell temperature. DP is very sensitive to these dimensions, and problems which could previously be solved in a few minutes now increased computation time to a few hours. Hence, a more efficient optimization algorithm was sought.

Pseudo spectral methods that use a direct collocation method to approximate a state using a global polynomial are used for these optimizations [22]. In particular, the commercially available GPOPS software, that utilizes the Legendre-Gauss-Radau (LGR) points for the approximation was used in this paper [23]. The model layout for GPOPS is very similar to DP and has been shown to approximate the DP solutions quite well [24]. The main advantage of using GPOPS is that it is able to reduce computation time significantly from hours to a few 100 s.

The results for the optimal power split and control of the fan are shown in Figures 7-9 for three distinct simulation cases highlighted in Table 2 corresponding to the Half (50-90% SOC) and Quarter (70-90% SOC) battery simulations, where the final SOC was increased to reduce the available battery energy. The ratio of battery to trip energy is a useful figure of merit for battery sizing. Figure 7 shows the results for a medium sized battery, the battery trip to energy ratio for the half sized battery about 0.347, requiring 66% of the energy to come from the fuel cell, however due to IR losses in the battery, the actual energy is a little bit higher for highly dynamic cycles.

Since the battery resistance is relatively low compared to the fuel cell, the transients of the load power are mostly handled by the battery. The fuel cell operates near constant power, with slightly higher power in the initial phase when the temperature is low, and the efficiency is relatively high (compared to the steady state efficiency) since the fan does not need to operate to cool the cell. At the end of the cycle, again the cooling rate is decreased to save energy, permitting the cell to warm slightly nearing the peak allowable temperature. In future work the shutdown requirements, including purging will be included in the optimization to capture their impact on energy utilization and final SOC.

The quarter battery simulation shows very poor system efficiency as the FC is required to handle a higher fraction of the load and hence operates at higher temperatures. Increasing the number of cells in the FC stack from 3 to 7 reduces the power per cell and brings the stack operating power back near the peak efficiency point as shown in Figure 8. This highlights the importance of combined battery and FC stack sizing for plug in hybrid vehicle applications even where the battery energy is less than half of the total trip energy.

Table 2. Battery to trip energy ratio. Average dynamic efficiency and H2 consumption.

Battery Capacity	Battery to Trip Energy	Average Eff	FC average Power (W)	H2 Consumed
Full (1.9 Ah)	0.6751	54.6722	33.5243	1.1220
Half	0.3631	49.0459	65.6476	2.4536
Half	0.3375	48.2568	68.4135	2.5934
Quarter	0.1876	42.1410	83.4637	3.6386
Quarter	0.1877	54.4481	83.6864	2.8158

Conclusions:

This work highlights the importance of combined sizing and power split for PEMFC hybrid systems where the battery supplies less than 50% of the total trip energy. The relative internal resistance of the battery vs. fuel cell determines the load following response vs load leveling. In the case simulated here, the low battery resistance resulted in a nearly constant FC power output when using a simple 1-state battery model with static FC efficiency and dynamic programming. Including the dynamics of FC temperature resulted in an improvement in system efficiency, due to the reduced cooling requirement during stack warmup as compared to the rule-based strategy and dynamic programming results with a static FC model. The rule based strategy however can be effective when the fuel cell operates with powers above the peak system efficiency, where the efficiency decreases gently with increasing power and is almost linear. The effects of battery temperature and battery thermal limits will be considered in future work as well as adding a physics based model of membrane hydration and flooding to guide the optimal power split.

References:

[1] R. K. Ahluwalia, X. Wang, J-K Peng, and C. F. Cetinbas “Fuel Cells Systems Analysis” DOE Hydrogen and Fuel Cells Program 2016 Annual Merit Review and Evaluation Meeting. Washington, D.C. June 6-10, 2016.

[2] Antonio Sciarretta; Lino Guzzella, “Control of hybrid electric vehicles” IEEE Control Systems, Volume: 27, Issue: 2 Pages: 60 - 70, 2007.

[3] Ahluwalia, R.K., and Wang, X. (2006) Rapid self-start of polymer electrolyte fuel cell stacks from subfreezing temperatures, J. Power Sources, 162, 502–512.

[4] Fangming Jiang, Chao-Yang Wang, and Ken S. Chen “Current Ramping: A Strategy for Rapid Start-up of PEMFCs from Subfreezing Environment” J. Electrochem. Soc. 2010 157(3): B342-B347;

[5] E. A. Muller, A. G. Stefanopoulou, and L. Guzzella. Optimal power control of hybrid fuel cell systems for an accelerated system warm-up. IEEE Transactions on Control Systems Technology, 15(2):290-305, March 2007.

[6] E. Khmelnitsky, “On an optimal control problem of train operation,” Automatic Control, IEEE Transactions on, vol. 45, no. 7, pp. 1257–1266, Jul 2000.

[7] A. Albrecht, P. Howlett, P. Pudney, X. Vu, P. Zhou, “The key principles of optimal train control— Part 1: Formulation of the model, strategies of optimal type, evolutionary lines, location of optimal switching points,” In Transportation Research Part B: Methodological, vol. 94, pp 482-508, 2016

[8] F. Nandjou, J.-P. Poirot-Crouvezier, et al. “Impact of heat and water management on proton exchange membrane fuel cells degradation in automotive application” Journal of Power Sources (326) 2016.

[9] K. Boice, A. Leo, et. al.“Baseline Field Testing of BB-2590 Lithium-Ion Batteries using an iRobot FasTac 510 Robot.” U.S. Army Tank Automotive Research, Development, and Engineering Center, Technical Report no 21320. Sept 2010.

[10] Setareh Shahsavari, Andrew Desouza, Majid Bahrami, Erik Kjeang, “Thermal analysis of air-cooled PEM fuel cells,” In International Journal of Hydrogen Energy, Volume 37, Issue 23, 2012, Pages 18261-18271, ISSN 0360-3199,

[11] J. B. Siegel, Y. Wang, A. G. Stefanopoulou and B. A. McCain, "Comparison of SOFC and PEM Fuel Cell Hybrid Power Management Strategies for Mobile Robots," Vehicle Power and Propulsion Conference (VPPC), 2015 IEEE, Montreal, QC, 2015, pp. 1-6..

[12] J. B. Siegel, S. Yesilyurt, A. G. Stefanopoulou "Modeling and experiments of voltage transients of polymer electrolyte membrane fuel cells with the Dead-Ended anode". Journal of Fuel Cell Science and Technology, vol. 9, 2012.

[13] Adrian Bejan “Convection Heat Transfer, Fourth Edition” John Wiley & Sons, 2013.

[14] Matthew M. Mech “Fuel Cell Engines” Wiley; (2008)

[15] Zolot, M., Anthony J. Markel, and Ahmad A. Pesaran. “Analysis of fuel cell hybridization and implications for energy storage devices.” National Renewable Energy Laborary, 2007. 4th Annual AABC June 2004.

[16] L. Yang, A. Karnik, B. Pence, M. T. B. Waez and N. Ozay, "Fuel cell thermal management: Modeling, specifications and correct-by-construction control synthesis," 2017 American Control Conference (ACC), Seattle, WA, 2017, pp. 1839-1846.

[17] Patterson, M. A. and Rao, A. V. 2012. GPOPS-II: A MATLAB software for solving multiple-phase optimal control problems using hp–adaptive Gaussian quadrature collocation methods and sparse nonlinear programming. ACM Trans. Math. Softw. 41, 1, Article 1 (October 2014), 37 pages.

[18] You Zhiyu, Xu Tao, Liu Zhixiang, Peng Yun, Cheng Weirong, “Study on Air-cooled Self-humidifying PEMFC Control Method Based on Segmented Predict Negative Feedback Control,” In Electrochimica Acta, Volume 132, 2014, Pages 389-396, ISSN 0013-4686,

[19] Bellman R. Dynamic programming. Courier Corporation; 2013 Apr 9.

[20] Sundstrom, O.; Guzzella, L., "A generic dynamic programming Matlab function," Control Applications, (CCA) & Intelligent Control, (ISIC), 2009 IEEE , vol., no., pp.1625,1630, 8-10 July 2009

[21] Sundström, O., D. Ambühl, and L. Guzzella. "On implementation of dynamic programming for optimal control problems with final state constraints." Oil & Gas Science and Technology–Revue de l’Institut Français du Pétrole 65.1 (2010): 91-102.

[22] Patterson, Michael A., and Anil V. Rao. "Exploiting sparsity in direct collocation pseudospectral methods for solving optimal control problems." Journal of Spacecraft and Rockets 49.2 (2012): 364-377.

[23] Patterson, Michael A., and Anil V. Rao. "GPOPS-II: A MATLAB software for solving multiple-phase optimal control problems using hp-adaptive Gaussian quadrature collocation methods and sparse nonlinear programming." ACM Transactions on Mathematical Software (TOMS) 41.1 (2014): 1.

[24] W. Zhou, C. Zhang, J. Li and H. K. Fathy, "A Pseudospectral Strategy for Optimal Power Management in Series Hybrid Electric Powertrains," in IEEE Transactions on Vehicular Technology, vol. 65, no. 6, pp. 4813-4825, June 2016.

[25] S. Onori, L. Serrao, G. Rizzoni, "Hybrid Electric Vehicles Energy Management Strategies" Springer-Verlag London 2016

Figures:

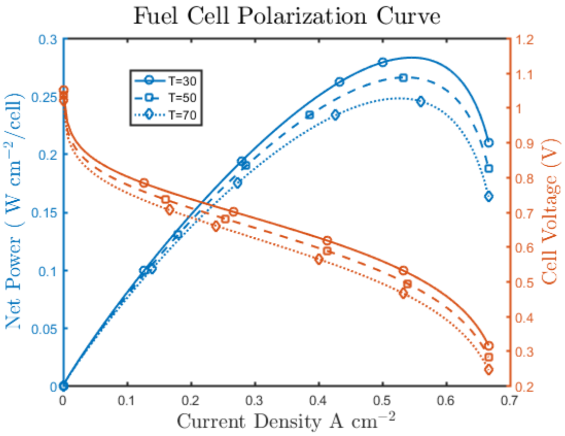

Figure 1: Fuel cell polarization curve and power output per cell normalized by cell active area. The fuel cell output power increases with current, and peaks when the voltage drops below a critical value.

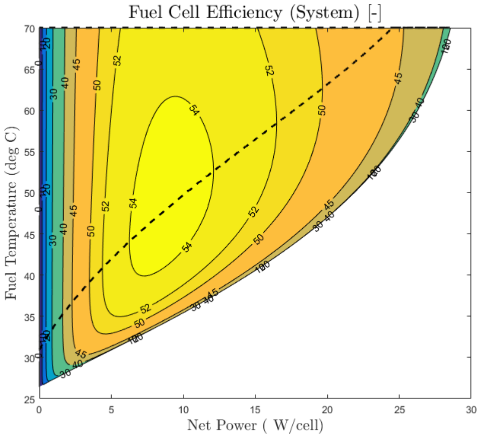

Figure 2: Fuel cell system efficiency including power to drive the fan and regulate the stack at a given temperature. The black dashed line indicates the optimum efficiency line for the system as a function of net power and the corresponding stack temperature. The white region in the lower right hand corner of the figure is the set of net power and temperature for which are infeasible. That is the cooling power is greater than the stack output at these low temperatures and high operating current.

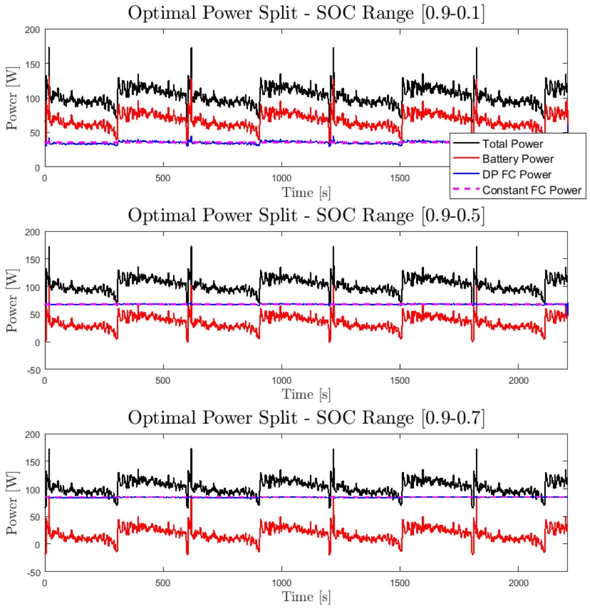

Figure 3. Optimal power split between the fuel cell and battery for a given power demand as shown above. Three different SOC ranges are shown that limit the battery energy to approximately full, half and quarter.

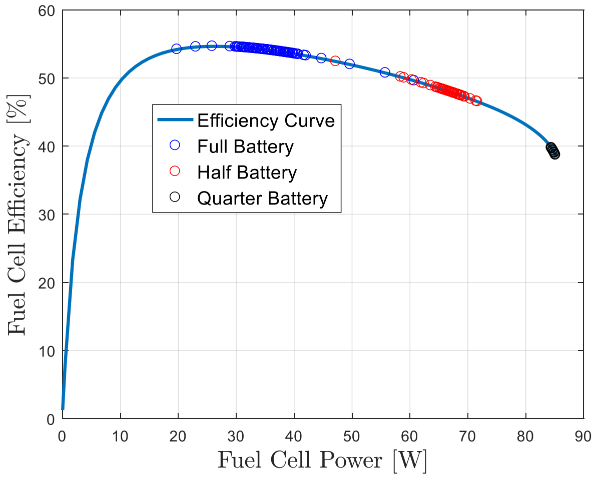

Figure 4. Operating points of fuel cell on the efficiency curve for different battery energy with a 3 cell stack.

Figures Continue on Next Page

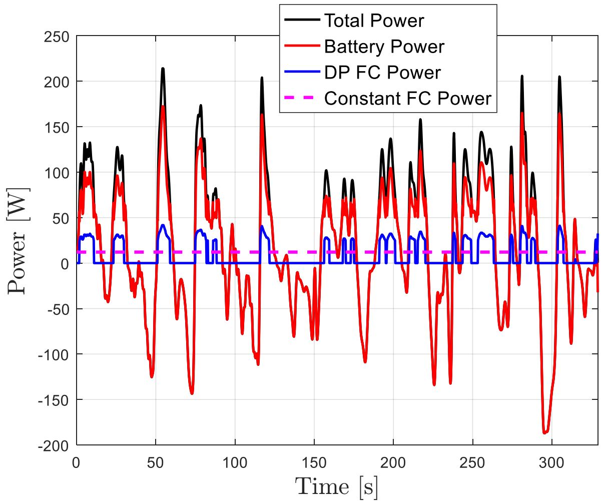

Figure 5: Optimal power split between battery and fuel cell for traversing the Churchill B cycle with the given power demand.

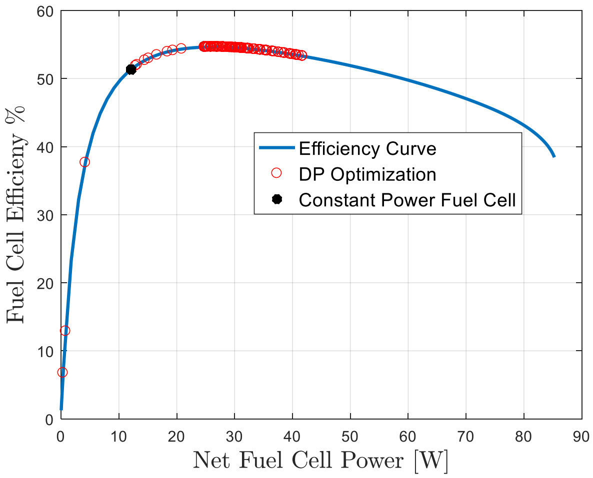

Figure 6: Optimal operating points of the Fuel Cell found from DP with the constant operating point of the rule based solution.

Figures Continued on Next Page

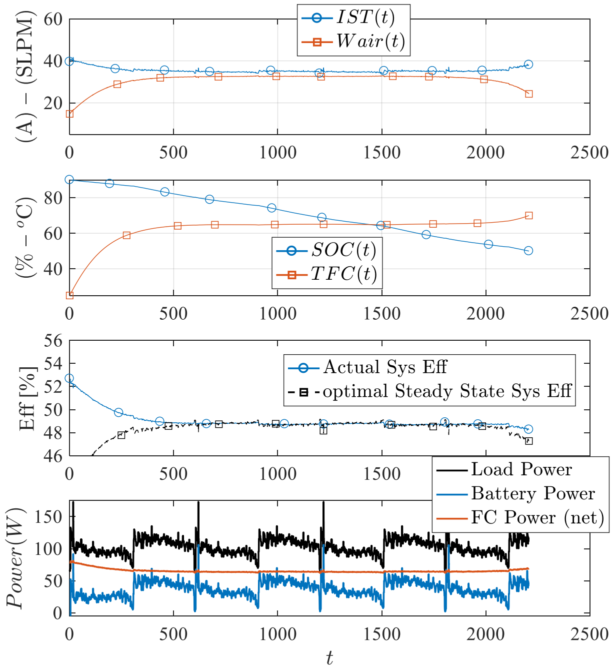

Figure 7: Optimal system trajectory for a medium sized battery. The fuel cell and battery delivery roughly equal power to the load.

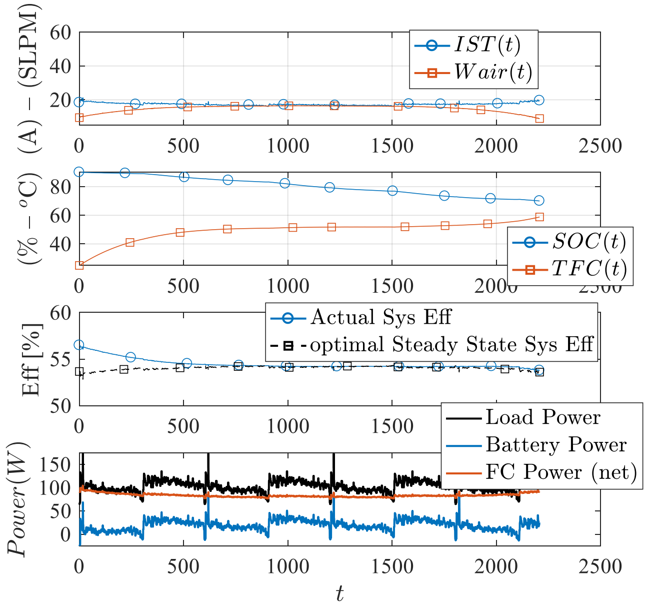

Figure 8: Optimal sized fuel cell stack for reduced battery size. Increasing the number of cells in the stack from 3-7 reduces the cooling requirement and allows the cell to operate at the peak efficiency point.

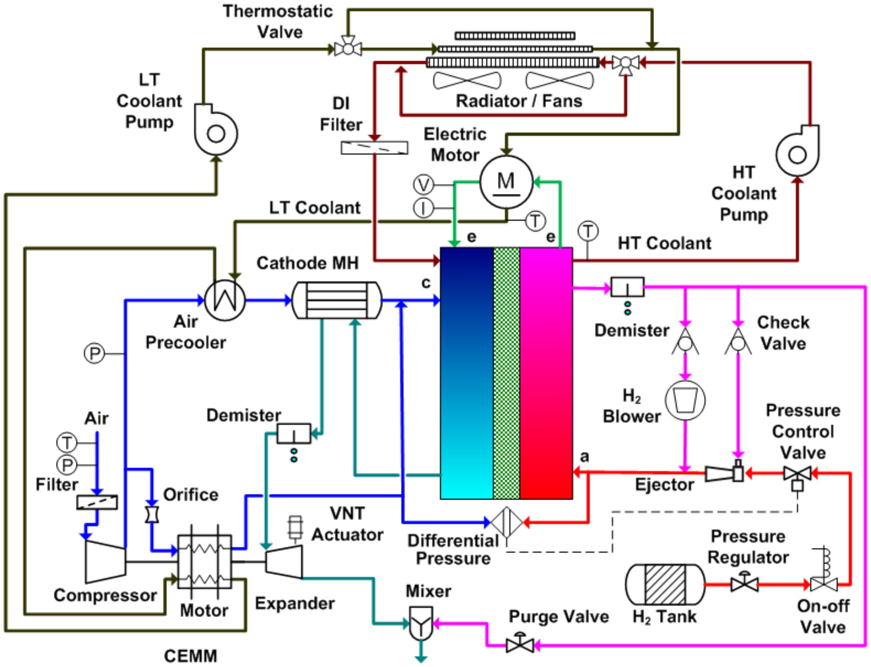

Figure 9: Argonne National Lab proposed target system architecture from 2016 DOE Annual Merit Review.[1]

<u>Remainder of Page Intentionally Blank</u>

AVPTA "Extended Enterprise" Activities

Wrought FeMnAl Study

Principal Investigator:
Dr. Katherine Sebeck
U.S. Army TARDEC
Product Lifecycle Engineering - Materials

Project Start: Oct 2016
Estimated Completion: Q4FY20

Objectives:

- Evaluate new class of lightweight steel alloys for use in armor.
- Support effort to transition production of material from lab scale to commercial production.
- Identify thermomechanical processing to optimize hardness and high-strain performance.
- Identify suitable welding and machining processes for wrought FeMnAl
- Characterization of material properties to support modeling and simulation efforts
- FY17: planning and initial material procurement

Strategic Context:

- 10-15% weight reduction over current wrought armor steel with no change in thickness
- Interest from Program Manager Main Battle Tank Systems (PM MBTS) Product Manager (PdM) Abrams to reduce weight of turret and hull.
- Coupled to other efforts to transition production of materials from lab scale to commercial production.

Accomplishments:

- A project plan has been developed with the Lightweight Innovation for Tomorrow (LIFT) consortium for production of wrought FeMnAl
- Fund sent to Office of Naval Research (ONR) and placed on LIFT contract
- Developed Statement of Work with Oak Ridge National Lab (ORNL) to develop FY18 efforts for welding evaluations.
- Identified two possible routes to develop Johnson-Cook material cards to support Modeling and Simulation (M&S) efforts with TARDEC Analytics
- Developed Scope of Work with Edison Welding Institute for weldability development
- Developed Statement of Work with Pacific Northwest National Lab (PNNL) for FY18 material fatigue evaluation to support M&S efforts

Introduction:

Increasing weight to protect against changing threats is a challenge across all Army ground vehicle platforms, with major consequences for platforms such as the Abrams Main Battle Tank. (Gerth & Howell, What is a Ton of Weight Worth?, 15-17 Nov., 2016) [1] As additional capabilities are developed without weight as an explicit requirement, this weight creep continues. For legacy vehicle systems, the available light-weighting solutions are limited by current form, fit and function requirement.

FeMnAl is a high-Mn, high-Al steel alloy that has a 10% lower density with similar mechanical performance to existing armor steels. Prior to integration onto existing vehicles, it is necessary to mature the manufacturing process of this material, as well as conduct studies to better understand best practices for joining, machining, corrosion prevention and design implementation. The base material has previously been evaluated in the Ph.D. thesis of Lieutenant Colonel (LTC) Ryan Howell. (Howell R. A., 2009). This work is leveraging funding from PdM Abrams and Army ManTech to increase the production scale pursued. General Dynamics Land Systems has identified this material as one of the largest potential ways to reduce weight on the Abrams platform. (General Dynamics Land Systems, 2016)

Approach:

The primary objective of FY17 was to develop plans for future years, and begin the actions necessary for material procurement. Using leveraged funding, two 45T heats of materials were cast and hot-rolled to plate by Ellwood Quality Steels (EQS) and ArcelorMittal (AM). The material produced in the second heat will help feed FY18 activities.

The planning strategy centered on defining 8 major areas of development, and identification of associated data points and activities necessary to support development and integration of this material. The eight major areas are:

- Manufacturability
- Blast Data (see “Lightweight Blast Applique” – Appendix A)
- Ballistic Penetration
- Machinability
- Weldability
- Modeling and Simulation
- Corrosion
- Stiffness/Mobility

The AVPTA effort will address work in each area. For each development area, internal capabilities were evaluated. If TARDEC facilities were unavailable or at capacity, TARDEC Materials Application and Integration (MAI) reached out to other DoD facilities or DoE labs. Manufacturability is largely to be pursued with industrial partners, but will also be supported by small-scale lab work. Critical path analysis of the schedule indicates that the longest timeline is with corrosion testing. Efforts are underway to pull forward the start of corrosion and coating testing and development.

Results and Discussion:

Working in conjunction with PdM Abrams, the Army Research Laboratory (ARL), EQS and AM, two industrial heats of material were poured and rolled. During the first heat, a standard steel teeming flux was used to cover the molten metal and limit contact with the atmosphere. However, due to the high SiO_2 content of the fluxes, a reaction occurred between the molten Al and the SiO_2, resulting in a conversion of Al -> Al_2O_3, and a significant reduction of the total Al content of the melt. This reduced Al content turned out to be sufficient to inhibit the age hardenability of the materials

During the second heat of material, the teeming flux was changed, and four different compositions were compared. All demonstrated improved results compared to the previous effort, with the best surface finish from a uniquely developed flux. In addition to the same size ingots produced in the first heat, a larger 840 mm x 1200 mm x 2540 mm ingot was also produced. Unfortunately, this ingot fractured due to thermal stresses during cooling, which is not uncommon in high alloy steels. An intermediate size will be investigated in future heats.

The first two ingots were rolled at 1150°C, which resulted in significant cracking, and rolling was halted at a thickness of 25 mm. After discussion, the remaining two ingots were divided on two processing paths: one was rolled at 1250°C, and the other was first forged, and scheduled to be rolled at 1250°C. This will allow direct comparison of material strength between the hot-rolled and the forged condition. The plate rolled at 1250°C is 40 mm thick, and currently in heat treatment. This plate is shown in Figure 1.

To address the various development areas, discussions were held with internal labs, other DoD labs, and DoE labs to find the best fit. Fatigue analysis of production representative material is planned with PNNL for FY18. ORNL will conduct rolling simulations via Gleeble, as well as studies of the carbide strengthening mechanisms. ONR will conduct Gleeble simulations of weldability, which will help inform work at Edison Welding Institute to develop welding parameters and select welding consumables. ARL will work on coatings and corrosion, as well as development of constitutive models for use in M&S to be performed at TARDEC.

Conclusions:

FY17 was the first year of a four year effort, with a major effort on thorough planning, and leveraging of additional resources. Two heats of material were produced with leveraged funds, providing significant learning towards best production practices for high-Mn, high-Al steels. Collaborative plans were defined for FY18, using material produced in FY17, as well as continuing plate production from leveraged funding in FY18.

References:

[1] R. J. Gerth and R. A. Howell, "What is a Ton of Weight Worth?," in *Ground Vehicle Survivability Training Symposium*, Ft. Benning, GA, 15-17 Nov., 2016

[2] S Army PM Abrams, *Abrams Special Topic: Transportability IPT Briefing,* 2015.

[3] R. A. Howell, *Microstructural Influence on Dynamic Properties of Age Hardenable FeMnAl Alloys,* Rolla: Missouri S&T, 2009.

[4] General Dynamics Land Systems, *Lightweighting IPR - Value Engineering for Abrams Briefing,* Sterling Heights: TARDEC, 2016.

Figure:

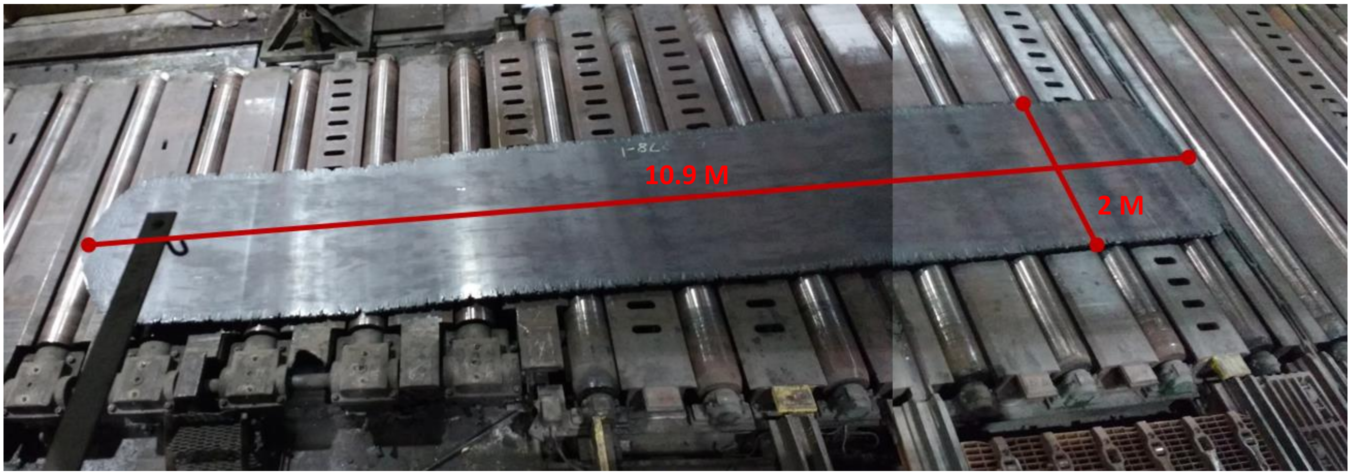

Figure 3. FeMnAl Ingot #A1132-04 38mm thick plate immediately post rolling, approximate dimensions in red.

Remainder of Page Intentionally Blank

AVPTA “Extended Enterprise” Activities

Cast FeMnAl Study

Principal Investigator:
Dr. Katherine Sebeck
U.S. Army TARDEC
Product Lifecycle Engineering - Materials

Project Start: Oct 2016
Estimated Completion: Q2FY18

Objectives:

- Determine weld materials and process for joining cast FeMnAl steel
- Support development and adoption of a 3rd generation Advanced High Strength Steel (AHSS)

Strategic Context:

- 10-15% weight reduction over current cast armor steel with no change in thickness
- Interest from Program Manager Main Battle Tank Systems (PM MBTS) Product Manager (PdM) Abrams to reduce turret weight.
- Coupled to other efforts to transition production of materials from lab scale to commercial production.

Accomplishments:

- Plate procured from Waukesha Foundry
- Start of work with Oak Ridge National Laboratory (ORNL) to conduct weld wire evaluation
  - To be completed in FY18 with no additional funding
- Create weld samples with TARDEC Center for System Integration (CSI)
  - Nondestructive evaluation showed no defects in weld
- Mechanical evaluation of base cast material, welded plate by TARDEC Materials Characterization and Failure Analysis (MCFA).

Introduction:

Increasing weight to protect against changing threats is a challenge across all Army ground vehicle platforms, with major consequences for platforms such as the Abrams Main Battle Tank. (Gerth & Howell, What is a Ton of Weight Worth?, 15-17 Nov., 2016) (US Army PM Abrams, 2015) However, for legacy vehicle systems, the available solutions are limited by current form, fit and function requirement. FeMnAl is a high-Mn, high-Al steel alloy that has a 10% lower density with similar mechanical performance to existing armor steels. Prior to integration onto existing vehicles, it is necessary to understand the joining processes required for vehicle manufacturing. The base material has previously been evaluated in the Ph.D. thesis of LTC Ryan Howell. (Howell R. A., 2009)

Approach:

Cast plates of 13 mm and 25 mm thickness were procured from Waukesha Foundry. These plates were to be heat-treated by a subcontractor to meet the hardness properties laid out in MIL-STD-12560, but as-received, the plate hardness values were below target. Base material hardness, tensile and impact properties were evaluated following appropriate ASTM International (formerly American Society for Testing and Materials) standard practices. Electron Dispersed Spectroscopy (EDS) was used to evaluate the local compositional variations of the material. Samples were also prepared for metallographic analysis.

Plates were distributed to ORNL and CSI for weld testing. TARDEC CSI began with several bead-on-plate tests, using a 316L stainless filler wire, and testing various current configurations. ORNL has to-date tested bead-on-plate with a 308 stainless wire and a wire developed jointly with TARDEC for current armor steels.

Results and Discussion:

The following is a high level summary of the work completed under this AVPTA effort. More complete reports of base plate properties are available upon request. (Toppler & Tzelepis, 11 September 2017) (Toppler & Tzelepis, 21 April 2017) Upon completion of the work current funded at ORNL in Q2FY18, a final report will be prepared. Preliminary data will be available in Q1FY18.

Base Plate Analysis:

In August 2016 plates were cast by Waukesha Foundry. Plate chemistry was within targeted values, with ~8.9 wt. % Al, 1 wt. % C, and 28-30 wt. % Mn. All plates were solution annealed at 1065°C: however, not all plates were aged at 540°C for five hours as specified. When the plates were received by TARDEC, hardness testing showed plates were well under expected values. Plates were then returned to the foundry for further processing, but once again returned soft. TARDEC conducted internal heat treatment experiments using a small open-atmosphere furnace, and noted that some decarburization at the surface should be expected. This is shown in Figure 1. However, no evidence of this effect was observed in the returned castings.

It was also noted that the castings contained significant porosity, both near the surface and within the core. Analysis of the exposed pores showed a significantly high Mn concentration relative to the bulk material. Figure 2 compares the EDS peaks of pores exposed by surface polishing (top) with bulk material exposed by surface polishing (bottom).

The average hardness value for the 13 mm plate as heat-treated was Brinell Hardness Number (HBN) 253 HBN, while the solutionized 1” plate, which was only 95 HBN. Limited

Charpy testing at -40°C was possible for these castings: when pores were revealed at the surface by machining operations, cracks would propagate from the pore. These pre-cracked samples appeared several days after sample preparation, but prior to testing. An average breaking energy of 50J was measure for the 13mm plate. Only two samples were successfully tested from the 25 mm plate, with 45J and 79J measured energies. Of these two samples, the lower impact energy test showed significant internal porosity and incomplete separation. The fracture surface is presented in Figure 3.

Tensile testing was conducted at two strain rates. Representative curves are shown in Figure 4, along with images of the samples post fracture. The tensile strength is insensitive to strain rate, with an average of 710MPa.The elastic modulus is ~183Gpa for 0.1/s strain rate, and ~150 Gpa for 0.001/s strain rate. The presence of pre-existing cracks, such as seen in 2Y (Figure 4), resulted in reduced total elongation. Some minor corrosion can be observed in the pre-existing crack region. In all samples, porosity is seen within the gauge, likely limiting the total elongation achieved.

Residual stresses were determined to be a major issue with the plate cast. In addition to the intra-granular fracture propagating between pores, post-tensile testing, significant deflection of the samples was observed. This amount of deflection was measured, and presented in Figure 5. Further analysis is ongoing to use X-ray diffraction for more complete analysis of the residual stress state. This behavior, in conjunction with the porosity throughout the piece, indicates poor filling during the casting process, and a need for improved processing parameters, such as pre-heat temperature, position of gate, and size of risers.

Preliminary Welding Results:

TARDEC CSI tested basic welding conditions using a 316L stainless wire. ORNL tested 308 stainless, and a Low-Temperature Phase Transformation (LTPT) wire previously developed jointly by TARDEC MCFA and ORNL for armor steel applications. All wires should good fusion via both visual inspection and non-destructive evaluation. The 316L plate was sectioned and prepared for metallographic analysis. Figure 6 shows two different magnifications. While good fusion was observed, a mushy region is observed at the line between the base metal and the filler metal.

Closer inspection via scanning electron microscopy (Figure 7) shows hallmark indications of inter-dendritic shrinkage. It is hypothesized that the use of a low silicon weld material results in reduced fluidity of the weld pool, and poor filling of pores during solidification. ORNL is testing higher silicon weld fillers. A fillet weld break test (specimen in Figure 8) of two 13mm thick plates joined with 316L stainless failed in the weld material, indicating good mechanical fusion.

It was observed during welding that the weld pool was less fluid than typical for steels, and there was a layer that floated to the surface. Analysis of this surface material was conducted with Scanning Electron Microscopy (SEM) and Energy Dispersive Microscopy (EDS). Results are presented in Figure 9.

Initial mechanical test plates were prepared using lab-scale wrought FeMnAl material, due to the problems with the base material detailed above. However, as the chemistry is the same between the cast and wrought, it still informative regarding the weldability of this alloy. Tensile testing has been completed, with all sample failing within the weld material. Charpy specimens are under preparation. Completion of mechanical test plates for 316, 308, and LTPT wires is expected in Q1FY18. ORNL continues to test additional wires, and welding procedures to identify best practices.

Conclusions:

While this project successfully welded cast FeMnAl, there clearly remains significant work to more robustly optimize the casting process itself. There are active conversations with PdM Abrams to identify specific parts of interest, as casting optimization is a function of the component geometry. Further work to identify best welding practices is ongoing. Follow-on work with wrought plate will include ballistic evaluation of welds.

References:

[1] R. J. Gerth and R. A. Howell, "What is a Ton of Weight Worth?," in *Ground Vehicle Survivability Training Symposium*, Ft. Benning, GA, 15-17 Nov., 2016.

[2] US Army PM Abrams, *Abrams Special Topic: Transportability IPT Briefing,* 2015

[3] R. A. Howell, *Microstructural Influence on Dynamic Properties of Age Hardenable FeMnAl Alloys,* Rolla: Missouri S&T, 2009.

[4] I. J. Toppler and D. A. Tzelepis, *Materials Characterization of One Inch Thick Cast FeMnAl Plate,* Warren: RDTA-SIE-ES-PLE-MCFA, 11 September 2017.

[5] I. J. Toppler and D. A. Tzelepis, *Material analysis of FeMnAl Cast Plate,* Warren: RDTA-SIE-ES-PLE-MCFA, 21 April 2017.

Figures Begin on Next Page

Figures:

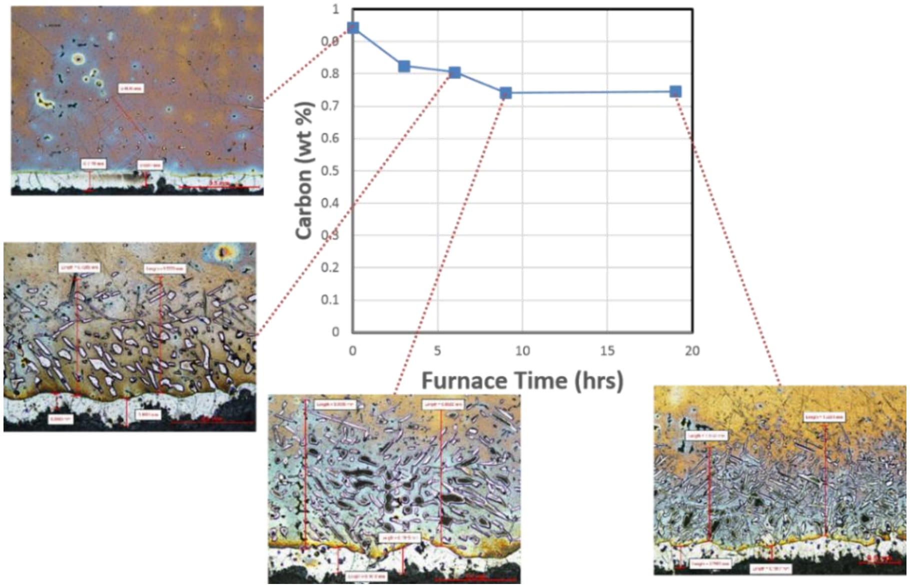

Figure 1. Decarburization layer observed in cast samples treated in 1100°C over, no atmosphere control, water quench. Carbon levels measured with LECO Carbon/Sulfur analyzer.

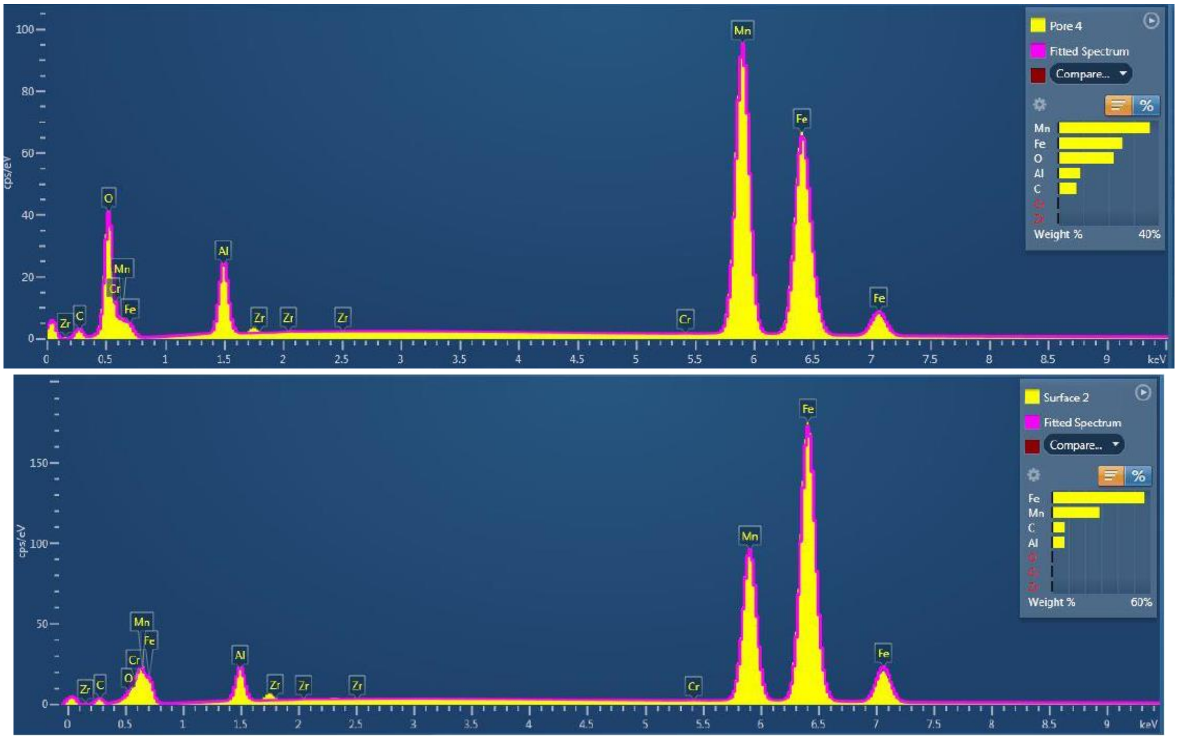

Figure 2. EDS peaks of and elemental analysis of Mn concentration for (top) pores and (bottom) bulk material exposed after surface polishing.

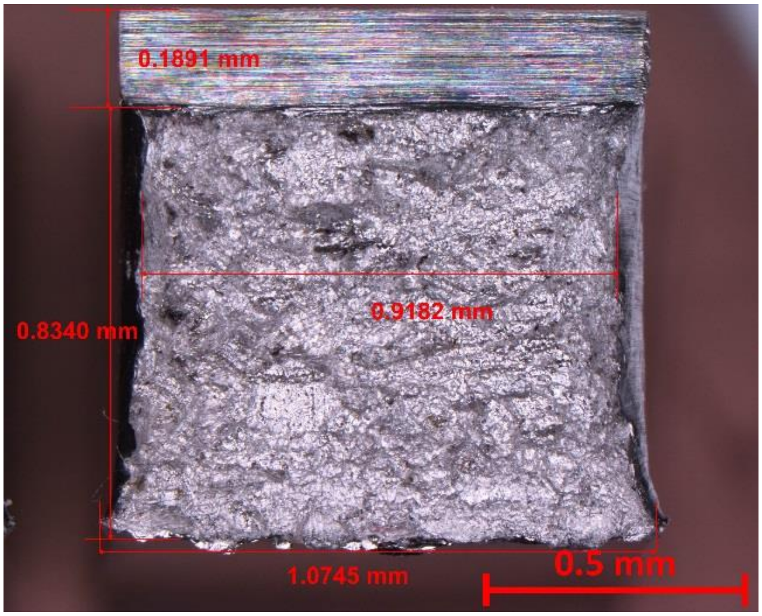

Figure 3. Charpy test specimen from 25 mm cast FeMnAl showing significant porosity. Sample did not completely separate at -40°C

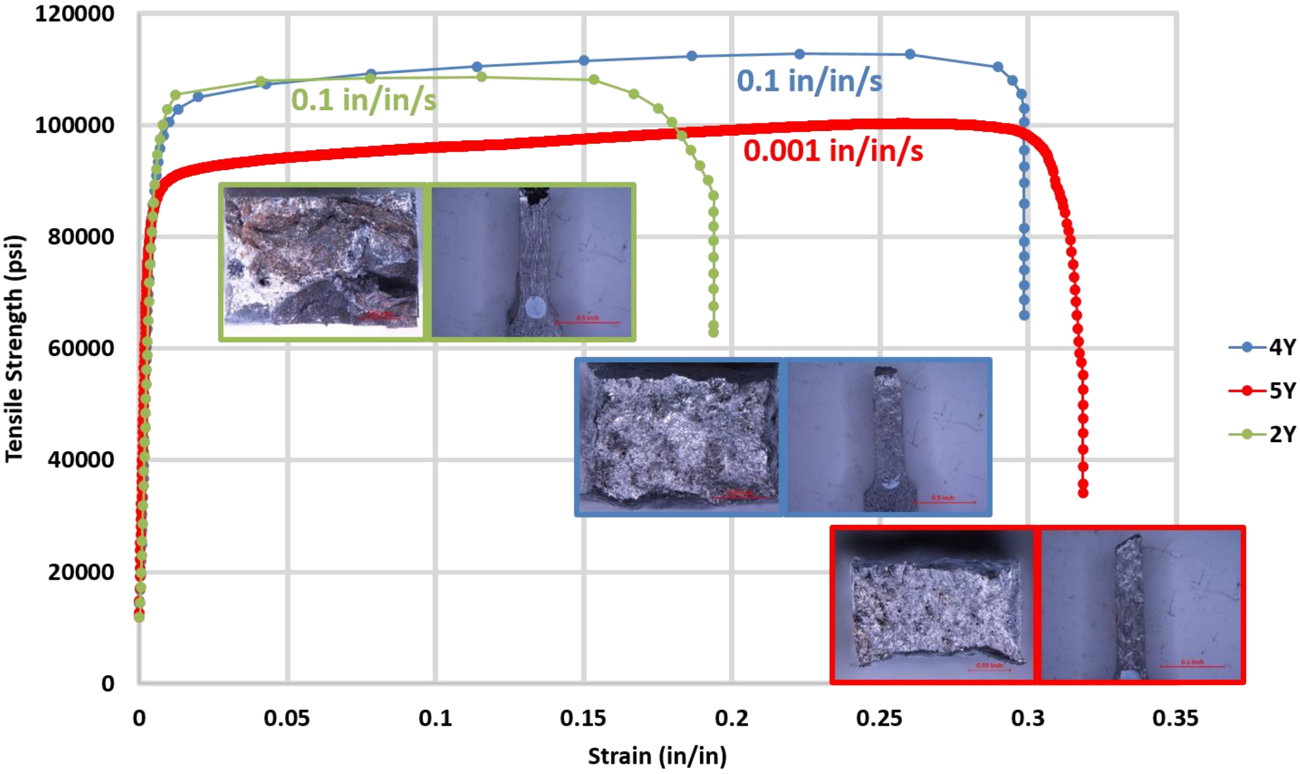

Figure 4. Tensile test of 13 mm thick cast plate at 0.1 in/in/s (green, blue) and 0.001 in/in/s (red).

A pre-existing crack was present in sample 2Y (green), resulting in premature failure.

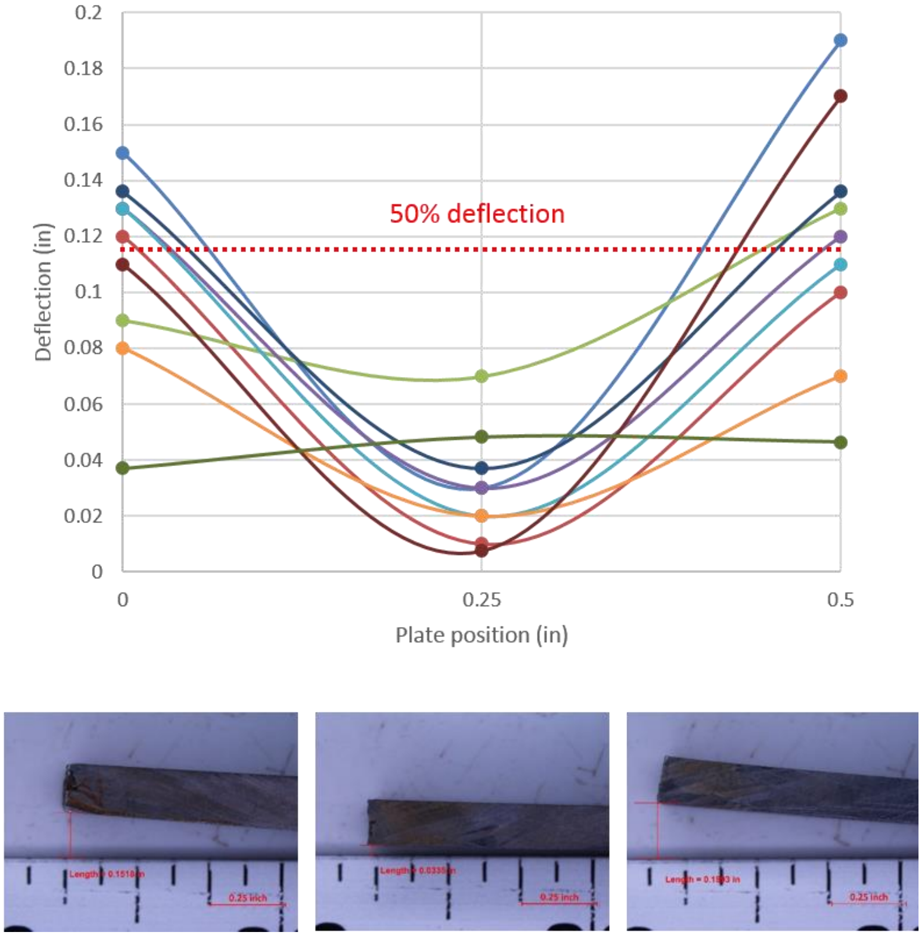

Figure 5. Deflection post-tensile testing for top, middle and bottom samples trough plate thickness, demonstrating the residual stresses present in the 13 mm thick cast plate.

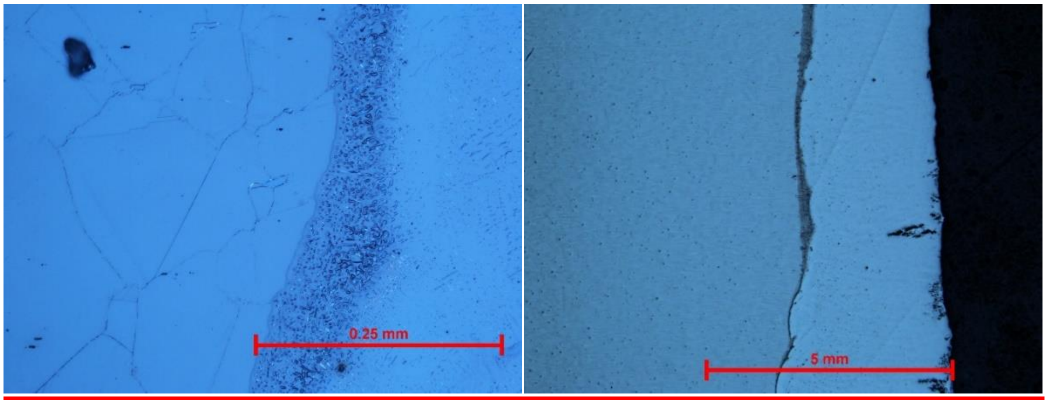

Figure 6. Metallographic images of fusion zone between 316L stainless wire and cast FeMnAl for initial bead-on-plate pass.

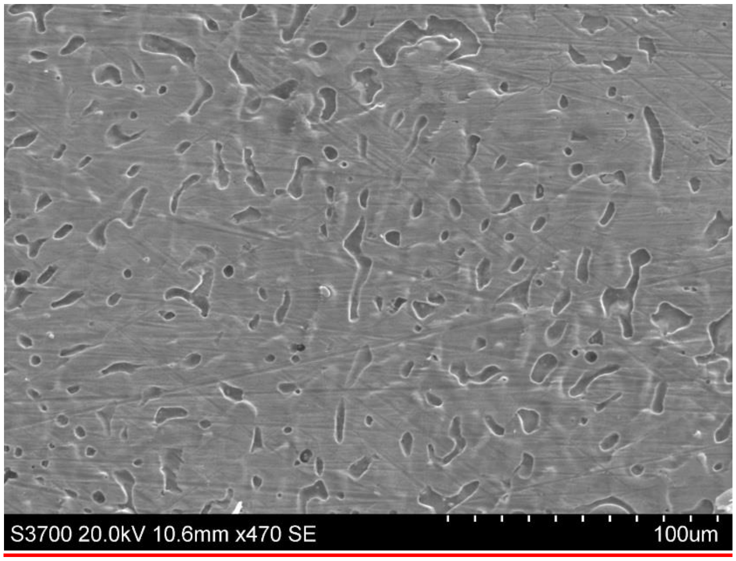

Figure 7. Scanning electron micrograph of fusion zone, demonstrating interdendritic shrinkage behavior.

Figure 8. Welded T-joint used for break test.

Figures Continued on Next Page

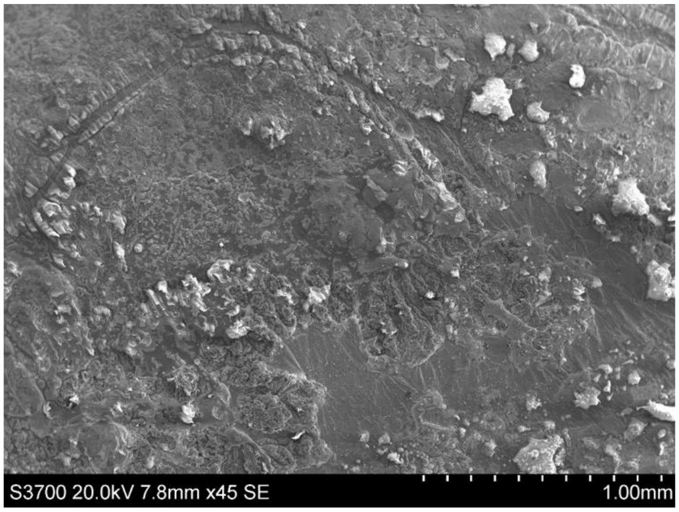

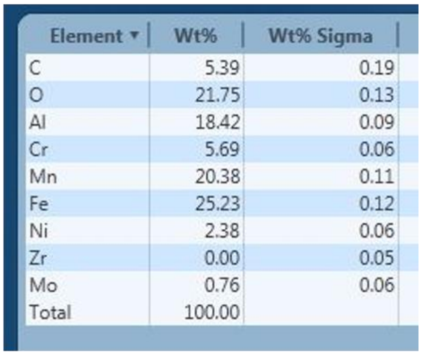

Element	Wt%	Wt% Sigma
C	5.39	0.19
O	21.75	0.13
Al	18.42	0.09
Cr	5.69	0.06
Mn	20.38	0.11
Fe	25.23	0.12
Ni	2.38	0.06
Zr	0.00	0.05
Mo	0.76	0.06
Total	100.00	

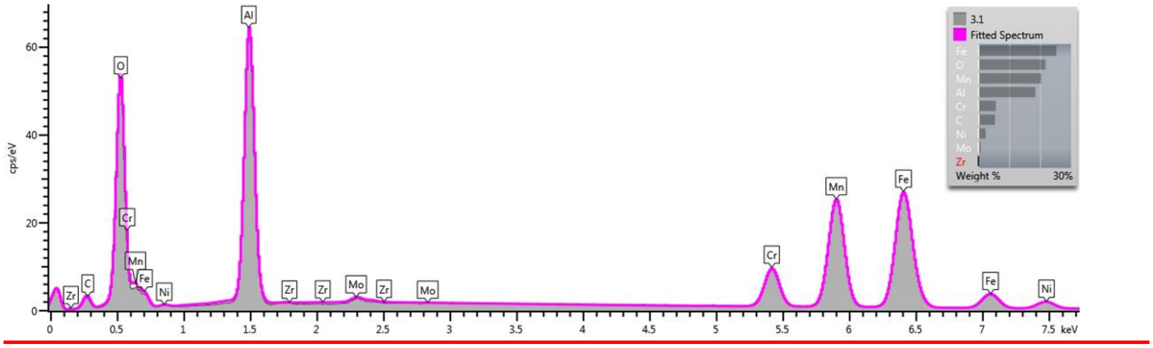

Figure 9. SEM and EDS analysis of weld surface oxide formation, showing large amounts of Al2O3 at the surface.

Remainder of Page Intentionally Blank

This Page Intentionally Blank

Appendix A

AVPTA "Extended Enterprise" Activities

Lightweight Blast Applique

Principal Investigator:
Dr. Katherine Sebeck
U.S. Army TARDEC
Product Lifecycle Engineering - Materials

Project Start: Oct 2016
Project Completed: Q4FY17

Objectives:

- Demonstrate a lighter Rolled Homogeneous Armor (RHA)-equivalent performer
- Characterization of a castable blast shield
- Demonstrate a weight savings of up to 10% for Abrams blast applique without degradation in performance

Strategic Context:

- 10-15% weight reduction over current wrought armor steel with no change in thickness
- Interest from Program Manager Main Battle Tank Systems (PM MBTS) Product Manager (PdM) Abrams to reduce weight of the turret and hull.
- Coupled to other efforts to transition production of materials from lab scale to commercial production.

Accomplishments:

- Production of 4'x4' plates completed by Waukesha Foundry
- Blast testing completed by Southwest Research Institute (SwRI)
- Simulation of blast completed by TARDEC Analytics (to be submitted for LS-Dyna User Meeting Conference Proceedings)

Introduction:

RHA has been the workhorse for majority of the military ground vehicles. A new class of FeMnAl-C steel alloys is being explored as potential lighter weight alternative for RHA. FeMnAl steel's low mass density, high strength and excellent ductility have led to strong interest in further maturation of this material. FeMnAl alloy has 10% lower mass density and a comparable yield strength to that of RHA makes it suitable for blast and ballistic armor application.

In order to evaluate the performance of FeMnAl compared to RHA, blast tests were performed with the SwRI landmine blast test fixture.

Approach:

SwRI performed four blast tests with their Landmine Test Fixture to explore the blast behavior of a FeMnAl-C steel (FeMnAl) as compared to RHA, Class 1 steel (RHA). TARDEC supplied two nominally 48-inch by 48-inch FeMnAl plates for these tests. One plate was nominally 1-inch thick, the other nominally 1.1-inches thick. SwRI purchased two 48- inch by 48-inch by 1-inch RHA plates. The four blast tests were conducted on April 13, 2017 and TARDEC's Michael Foley was in attendance.

Simulations were conducted by TARDEC Analytics. A hybrid Arbitrary Lagrangian Eulerian - Smoother Particle Hydrodynamics Smoothed Particle Galerkin (ALE-SPG) simulation approach is used in this analysis due to the nature of the test set up as shown in Figure 1. The soil pots were constructed using 30-inch diameter sections of cardboard tubing (Sonatube). The Sonatube was cut to a length of 16 inches and attached to a base of ¾-inch plywood by use of "2x4" (1.75" x 3.75") pine lumber cross ties. A prepared soil mixture filled into the soil pot. High Explosive (HE), Soil and Air is modeled as ALE and the Sonotube cardboard and plywood below the ALE soil is represented as Lagrange and the soil below the plywood is represented by SPG formulation.

Results and Discussion:

The cast plates produced by Waukesha Foundry were tested with a 6" standoff, after pre-computation results and first RHA plate showed minimal static deflection expected from a 10" standoff, in order to improve results of the digital image correlation system. The dynamic and static deflection results are presented in Table 1. The FeMnAl plates had a slightly higher maximum dynamic deflection than the RHA plates, and a significant increase in the permanent deflection. As can be seen in the maximum deflection versus time in Figure 2, very little elastic recovery is observed. Inspection of the plates showed substantial porosity throughout the piece. It is expected with better refinement of casting practices, this permanent deflection could be substantially reduced

Post-test analysis of the plates showed cracking from the stress of the ballistic tests, presented in Figure 3. Though the plates did not fail, these cracks are under further investigation by TARDEC's Metallurgy Lab and could be the result of improper hardening and poor process control during casting resulting in a notably porous product.

Due to the incomplete mechanical test data on the FeMnAl base material, the simulation effort used a modified RHA card with available data. Future work includes a more complete development of appropriate equations of state for this new material. However, TARDEC Analytics was able to use the high speed footage obtained in this test to make significant improvements to the model of the SwRI landmine fixture, capturing the failure of the plywood and Sonatube pot, which result in large piece that increase the total impulse delivered to the test plate.

Conclusions:

Two cast FeMnAl plates were tested and compared to RHA for their ability to withstand blast loading. While the deflection was higher, the FeMnAl plates performed as expected given the quality of the castings. Further development of casting processes is necessary prior to additional testing. While this test is promising, improved material quality and additional testing is necessary to conclude whether FeMnAl is capable of replacing RHA in blast appliques.

References:

None

Figures and Table:

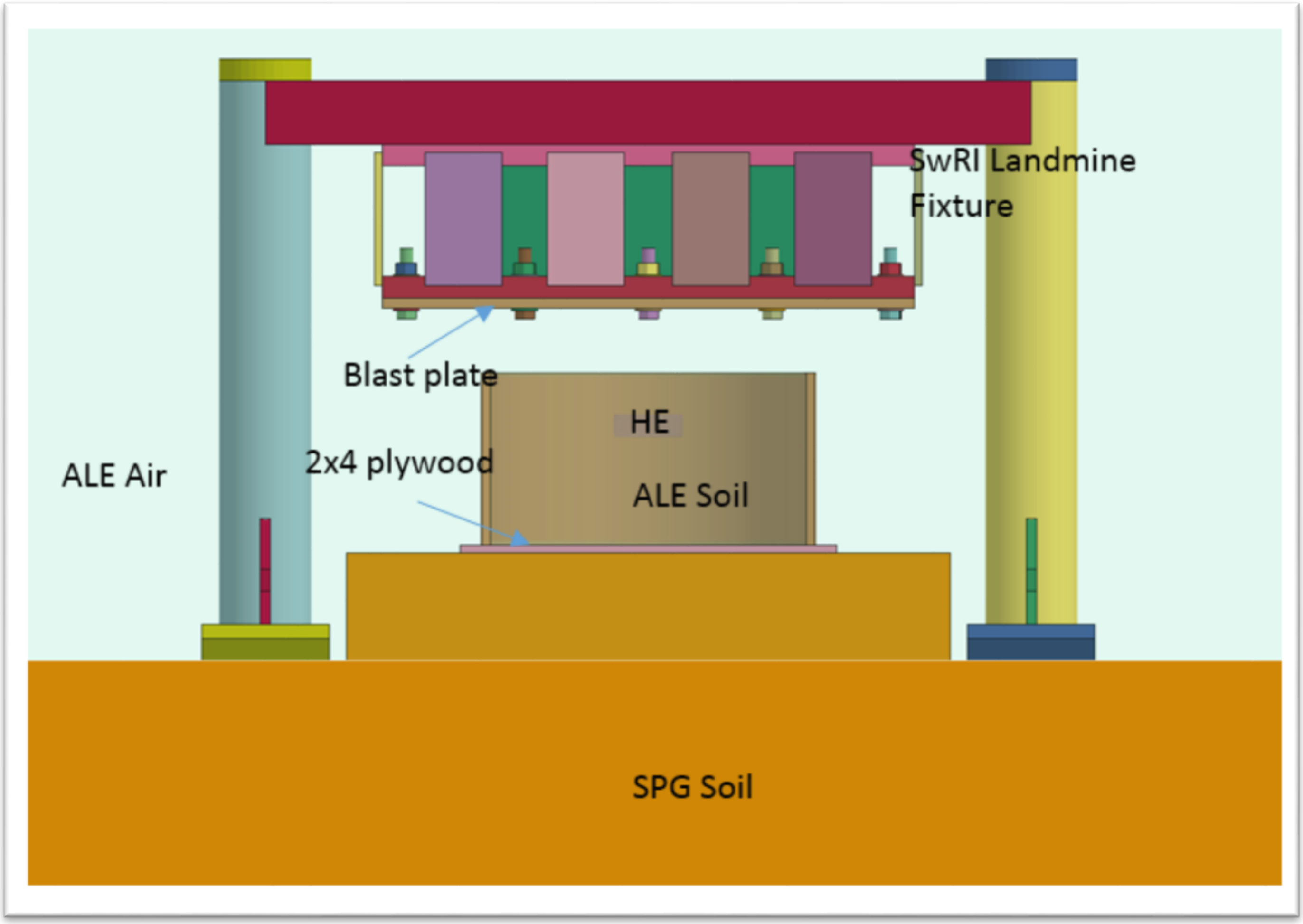

Figure 1. SwRI Landmine fixture and blast plate setup used for simulation

Table1. Summary of blast test data for RHA and cast FeMnAl plates. All tests were performed with the same charge level and depth-of burial.

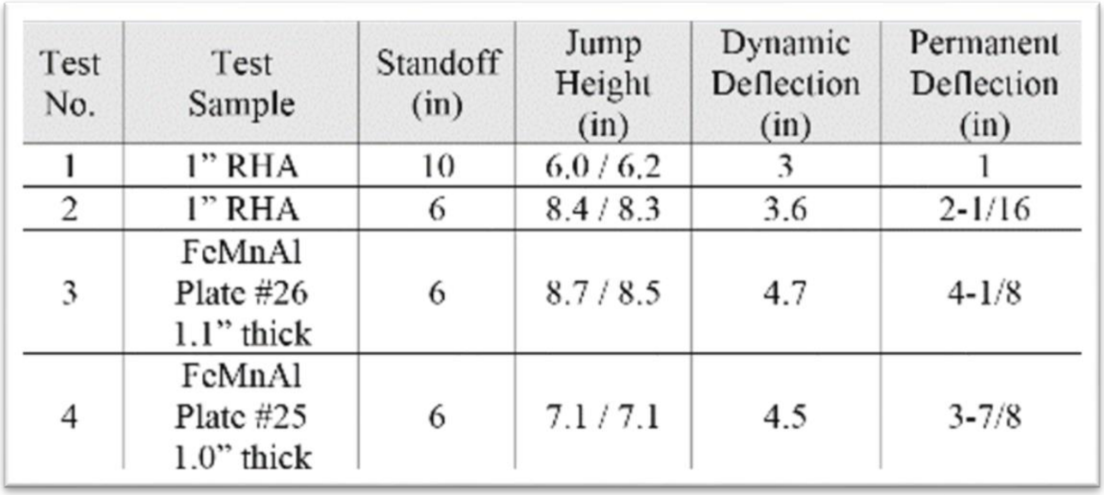

Test No.	Test Sample	Standoff (in)	Jump Height (in)	Dynamic Deflection (in)	Permanent Deflection (in)
1	1" RHA	10	6.0 / 6.2	3	1
2	1" RHA	6	8.4 / 8.3	3.6	2-1/16
3	FeMnAl Plate #26 1.1" thick	6	8.7 / 8.5	4.7	4-1/8
4	FeMnAl Plate #25 1.0" thick	6	7.1 / 7.1	4.5	3-7/8

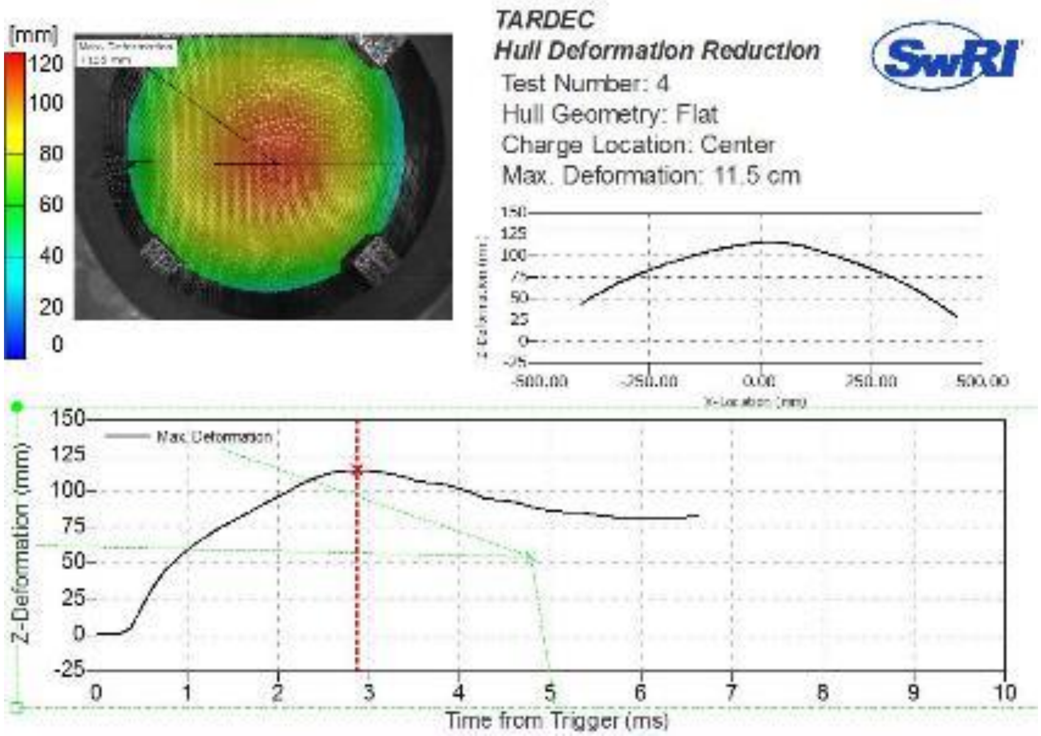

Max Deflection vs Time (ms)

Figure 2. Deflection history of Plate #25, showing the localization of deformation (upper left), overall deformation shape (upper right) and maximum deflection versus time in ms (bottom).

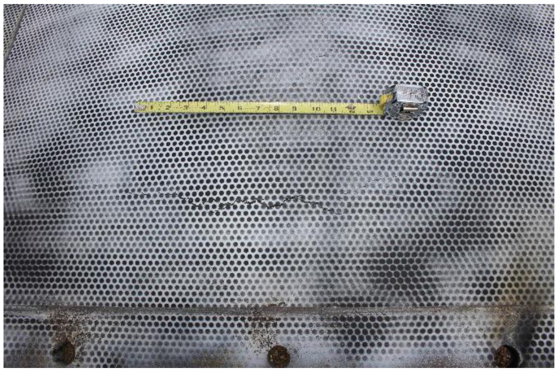

**Figure 3. Post test cracking of Plate #26.
This crack does not go through the piece.**

Remainder of Page Intentionally Blank

This Page Intentionally Blank

APPENDIX B

Memorandum of Understanding
Between
U. S. Department of Energy
And
U. S. Department of Defense

Concerning Cooperation in a Strategic Partnership to Enhance Energy Security

I. Purpose

The purpose of this Memorandum of Understanding (MOU) is to identify a framework for cooperation and partnership between the Department of Energy (DOE) and the Department of Defense (DOD), hereafter referred to as the Parties, to strengthen coordination of efforts to enhance national energy security, and demonstrate Federal Government leadership in transitioning America to a low carbon economy. This MOU covers, but is not limited to, efforts in the areas of energy efficiency, renewable energy, water efficiency, fossil fuels, alternative fuels, efficient transportation technologies and fueling infrastructure, grid security, smart grid, storage, waste-to-energy, basic science research, mobile/deployable power, small modular reactor nuclear energy, and related areas.

II. Legal Authority

DOE enters into this MOU under the authority of section 646 of the Department of Energy Organization Act (Pub. L. 95-91, as amended; 42 U.S.C. § 7256). DOD enters into this MOU under the authority of DOD Instruction 4000.19 "Inter-Service and Intra-Governmental Support" August 9, 1995.

III. Background

In the 2010 Quadrennial Defense Review, the DOD expressed an intent to partner with other U.S. agencies to research, develop, test, and evaluate new sustainable energy technologies. The DOD aims to speed innovative energy and conservation technologies from laboratories to military end users, and it uses military installations as a test bed to demonstrate and create a market for innovative energy efficiency and renewable energy technologies coming out of DOE laboratories, among other sources. The DOE is currently supporting a range of projects aimed at improving energy efficiency and renewable energy efforts across the military services.

Energy security for the DOD means having assured access to reliable supplies of energy and the ability to protect and deliver sufficient energy to meet operational and Installation energy needs. Energy efficiency can serve as a force multiplier, increasing the range and endurance of forces in the field while reducing the number of combat forces diverted to protect energy supply lines, as well as reducing long-term energy costs. DOD is also increasing its use of renewable energy supplies and reducing energy demand to improve energy security and operational effectiveness, reduce greenhouse gas (GHG) emissions in support of U.S. climate change initiatives, and protect the DOD from energy price fluctuations. Solving military challenges through innovation has the potential to yield spin-off technologies that benefit the civilian community as well.

The DOE is the lead Federal agency responsible for the development and deployment of advanced energy technologies, yet DOD will need to invest in many of these same energy technologies as well as other energy technologies which may be unique to DOD's operational requirements. Partnering with DOD provides DOE the opportunity to accelerate the deployment of its technologies and expertise toward the critical economic and energy security needs of the United States and to promote scientific and technological innovation.

The Parties acknowledge the significant positive collaboration that already exists between DOE and DOD and intend through this MOU to strengthen and broaden that cooperation.

IV. Activities

Specific activities covered under this MOU include, but are not limited to:

A. Evaluate energy systems and technology management solutions that meet DOD objectives including developing energy technologies that meet DOD energy requirements. Work collaboratively to identify a strategy for their development and deployment.

B. Maximize DOD access to DOE technical expertise and assistance through cooperation in the deployment and pilot testing of emerging energy technologies. Technology areas may include, but are not limited to, energy efficiency, renewable energy, water efficiency, fossil fuels, alternative fuels, efficient transportation technologies and fueling infrastructure, grid security (e.g., superconductivity, power, electronics, microgrids, cyber, EMP), smart grid, storage, waste-to-energy, basic science research, mobile/deployable power, small modular reactor nuclear energy, and related areas.

C. Expand cooperation related to energy management practices and knowledge exchange, working to ensure that Federal leadership is in compliance with all statutory and Executive Order goals and objectives, particularly in the area of GHG reductions. Encourage the sharing of data, including, but not limited to, data on internal energy management projects and technical assistance projects.

D. Collaborate on science and technology (S&T) projects at research institutions sponsored by either agency. Synchronize research and development (R&D) of new knowledge and technologies to expand complementary efforts.

E. Develop joint initiatives for major energy technology research, development and demonstration programs of mutual interest to DOD and DOE, such as pilot or demonstration facilities which address military needs and also may address national security needs that transcend military requirements. DOD installations may serve as test beds for such technical demonstrations.

F. Develop human capital within DOE and DOD through teaching and education. Work to integrate respective agency energy training and knowledge exchange practices.

G. Encourage professional exchanges and formal liaison relationships between all DOE and DOD components including, but not limited to, laboratory, headquarters, military installations, combatant command headquarters, and forward operating bases.

H. Collaborate on issues regarding nuclear power, except naval nuclear propulsion, including developing a business, licensing and regulatory strategy as appropriate, and evaluating the integration of energy technologies with other industrial applications that support DOD objectives for energy security and GHG reduction. Collaboration will include NRC review and licensing of nuclear power plants that are deployed for DOD purposes, and are located on or adjacent to DOD U.S. installations.

V. Implementation

DOE and DOD intend to develop and conduct cooperative activities relating to identified high priority energy strategic needs, where such cooperation contributes to the efficiency, productivity, and overall success of the activity. The Parties intend for the activities to be executed under the MOU to be established by a joint DOE/DOD senior-level Executive Committee. This Executive Committee will be co-chaired by a designee of the Under Secretary of Defense (Acquisition, Logistics and Technology) and a designee of the Deputy Secretary from DOE. The Executive Committee will be responsible for the operations and governance of this MOU. Under the direction of the Co-Chairs, the Committee will include representatives from each of the principal DOE offices, specifically, the Office of the Under Secretary for Science, the National Nuclear Security Administration, and the Office of the Under Secretary for Energy. From the Department of Defense representatives will include the Deputy Under Secretary of Defense (Installations and Environment) and the Director of Operational Energy Plans and Programs. Additional members from both Agencies that may be involved in issues or functions of this MOU may be added. Upon agreement of both Departments, the Co-Chairs will appoint a team to develop, within 60 days, a charter and operating structure, membership, products, and decision processes.

The Executive Committee may establish working groups of Federal employees to perform and execute necessary activities contemplated by this MOU at their discretion. The Executive Committee and its working groups may make consensus recommendations based on their collaboration.

The Executive Committee will determine an appropriate regular meeting schedule, not to be less than four times annually. The Co-Chairs will be responsible for the development and distribution of agendas, presentations, and minutes of each meeting. Action items will be clearly identified and tracked in the minutes.

The Co-Chairs will be responsible for any reporting to the appropriate Departmental Secretarial Officers and will outline accomplishments, issues, redirections, and change assessments. The reporting will be coordinated by the Co-Chairs as appropriate.

The Co-Chairs will be responsible for any reports or presentations that are requested by other organizations, subject to the necessary review of each Party.

VI. Funding

Each party intends to coordinate their individual funding and resource decisions in order to maximize the benefits of cooperation under this MOU. Any transfer of funds or sharing of resources between the parties will be pursuant to a separate or pre-existing agreement.

VII. General

Work under this MOU will be jointly planned and monitored by the DOD and DOE.

In the event any activity undertaken by the agencies to implement the purposes of this MOU involves access to and sharing or transfer of technology subject to patents or other intellectual property rights, such access and sharing or transfer will be provided on terms which recognize and are consistent with the adequate and effective protection of intellectual property rights.

This MOU is strictly for internal management purposes for each of the Parties. It is not legally enforceable and shall not be construed to create any legal obligation on the part of either Party. This MOU shall not be construed to provide a private right or cause of action for or by any person or entity.

This MOU in no way restricts either of the Parties from participating in any activity with other public or private agencies, organizations, or individuals.

This MOU is intended to complement, and not to duplicate, cooperation by the Parties under the Memorandum of Understanding between the Department of Energy (National Nuclear Security Administration)/(Office of Science)/(Office of the Under Secretary) and the Department of Defense (Acquisition, Technology and Logistics) concerning Cooperation in a Strategic Partnership to Enhance National Security of January 26, 2009.

All agreements herein are subject to, and will be carried out in compliance with, all Federal applicable laws, regulations and other legal requirements.

This MOU is neither a fiscal nor a funds obligation document. Nothing in this MOU authorizes or is intended to obligate the Parties to expend, exchange, or reimburse funds, services, or supplies, or transfer or receive anything of value.

VIII. Contacts/Designated Representatives

Under Secretary for Science
U.S. Department of Energy
Washington, DC 20585

Under Secretary for Energy
U.S. Department of Energy
Washington, DC 20585

Under Secretary for Nuclear Security
U.S. Department of Energy
Washington, DC 20585

Deputy Under Secretary of Defense
Installations and Environment
U.S. Department of Defense
Washington, DC 20301

Director of Operational Energy Plans and Programs
U.S. Department of Defense
Washington, DC 20301

Deputy Assistant to the Secretary of Defense for Nuclear Matters
U.S. Department of Defense
Washington, D.C. 20301-3050

IX. Duration of Agreement

This MOU is effective on the date of the final signature and will remain in effect until it is terminated by mutual agreement of the Parties or by either Party providing ninety days written notice to the other. This MOU may be modified at any time by written agreement of the Parties. Nothing in this MOU shall be interpreted to limit or otherwise affect any authorities, powers, rights, or privileges accorded to DOD or DOE or any of the officers, employees, or organizational units under any statute, rule, regulation, contract, or agreement.

Daniel B. Poneman Deputy Secretary of Energy	William J. Lynn III Deputy Secretary of Defense
JUL 22 2010	JUL 22 2010
Date	Date

APPENDIX C

The Deputy Secretary of Energy
and
The Under Secretary of the Army
CHARTER
Advanced Vehicle Power Technology Alliance

I. DESIGNATION

By authority of this charter, effective on July 18, 2011, the Advanced Vehicle Power Technology Alliance (AVPTA) was established. AVPTA shall be active until the charter is rescinded, repealed, terminated, or suspended.

II. MISSION

The AVPTA is a partnership between the Department of the Army (DA) and the Department of Energy (DOE) in accordance with Section IV. E of the Department of Defense (DoD) and DOE Memorandum of Understanding (MOU) Concerning Cooperating in a Strategic Partnership to Enhance Energy Security, for the establishment of a joint technology research initiative in the area of ground vehicle power technology research, development, and transition. The seven focus areas of science and technology are: (1) advanced combustion engines and transmissions, (2) lightweight structures and materials, (3) energy recovery and thermal management, (4) alternative fuels and lubricants, (5) electrified propulsions systems, (6) energy storage & batteries, and (7) autonomy-enabled technologies. Where requirements are common, the two Departments will leverage resources to improve transition of technologies into both the commercial and military marketplace. The AVPTA leverages industrial research and development involving commercial automotive and defense ground vehicle manufacturers to transition technologies and increase precompetitive research and development.

III. RESPONSIBILITY

The AVPTA is designated as the DA's and DOE's primary point of contact for automotive power technology in the seven focus areas of science and technology. Consistent with applicable law, regulation, and policy the AVPTA may conduct its activities in accordance with such agreements as are deemed necessary for its efficient operation.

IV. AUTHORITY

The AVPTA is jointly led by the Director, U.S. Army Tank Automotive Research, Development and Engineering Center, and the Department of Energy Director, Vehicle Technologies Office (hereinafter "Directors"). Both Directors maintain authorities over their respective budgets. The AVPTA conducts activities in accordance with the DoD-DOE Energy Security MOU. DOE entered into the MOU under the authority of section 646 of the DOE Organization Act (Pub. L. 95-91, as amended; 42 U.S.C.). The Army entered into the MOU under the authority of DoD Instruction 4000.19, "Inter-Service and Intra-Governmental Support," April 25, 2013. The Directors are the principal and primary points of contact for the prioritization of automotive/ground vehicle power and energy technologies in the seven focus areas of science and technology.

V. COORDINATION

The AVPTA shall, as appropriate, coordinate activities and actions with associated government agencies, industries, and academia with a focus on efficient vehicle power systems. The AVPTA will conduct a yearly meeting to coordinate science and technology (S&T) activities, and will align S&T projects and products where requirements are similar. A yearly meeting will be conducted to assess results, update requirements, and determine new joint efforts. The AVPTA will report results to the Under Secretary of the Army and the Deputy Secretary of Energy.

VI. ADVISORY BOARD

The Directors may establish a Senior Advisory Board with other government agencies to review strategic planning and make recommendations on future activities. All activities associated with the Senior Advisory Board will comply with the Federal Advisory Committee Act (FACA), 5 U.S.C. App. 2 and implementing regulation and policy, as applicable. As authorized by law, regulation, and policy, the Senior Advisory Board may seek the individual advice of non-Government employees (e.g., individual members of industry or academia) to secure facts and other information to assist the Senior Advisory Board's review.

VII. LEGAL AUTHORITY

The Directors will ensure that AVPTA activities are conducted in a manner consistent with all applicable laws, regulations, and policies. In particular, the appropriate agency counsel will review in advance all interaction with industry, academia, or other non-governmental entities to confirm that any necessary enabling authorities exist and to ensure compliance with the FACA and implementing regulations and policies.

VIII. TERMINATION AND REVIEW

This charter shall terminate automatically on the 5-year anniversary date unless the undersigned expressly approves it for renewal. Directors will review this charter biannually on its anniversary date to ensure currency, completeness, and adequacy. Changes to mission and/or responsibilities will require the review by, and approval of, the Secretary of the Army and the Secretary of Energy.

Elizabeth Sherwood-Randall

Elizabeth Sherwood-Randall
Deputy Secretary of Energy

Patrick J. Murphy
Under Secretary of the Army

Remainder of Page Intentionally Blank

This Page Intentionally Blank